SOLID-STATE THERMOACOUSTICS: THEORY, FORMULATION, AND DEVICE OPTIMIZATION

by

Haitian Hao

A Dissertation

Submitted to the Faculty of Purdue University

In Partial Fulfillment of the Requirements for the degree of

Doctor of Philosophy

School of Mechanical Engineering

West Lafayette, Indiana

August 2021

THE PURDUE UNIVERSITY GRADUATE SCHOOL
STATEMENT OF COMMITTEE APPROVAL

Dr. Fabio Semperlotti, Co-chair
School of Mechanical Engineering

Dr. Carlo Scalo, Co-chair
School of Mechanical Engineering

Dr. J. Stuart Bolton
School of Mechanical Engineering

Dr. Xianfu Xu
School of Mechanical Engineering

Dr. Vikas Tomar
School of Aeronautics and Astronautics

Approved by:
Dr. Nicole Key

To my parents.

ACKNOWLEDGMENTS

First of all, I would like to thank my advisors Dr. Fabio Semperlotti and Dr. Carlo Scalo for their invaluable guidance and support. I cannot count how many times I walked into Prof. Semperlotti's office, or he walked into mine, brainstorming all aspects of my research. His availability and willingness to advise and discuss are critical to the completion of all projects we have worked on together. I also learned a lot from Prof. Scalo. It was his vivid explanation of the principle of thermoacoustics that drew my interest in this subject. All the tricks about numerical modeling that I have learned from him will be a great asset to my career. I would like to thank Prof. J. Stuart Bolton for his acoustic courses that lay the foundation of my acoustic studies. In addition, the constant support for my career development from Prof. Bolton is greatly appreciated. My gratitude also goes to the other members of my committee: Dr. Xianfan Xu and Dr. Vikas Tomar, and the colleagues and friends in the acoustic program at Herrick Labs.

Finally, I want to extend my special thanks to my parents. I would never expect to get a PhD degree without their constant love, support, and encouragement to continue pursuing my education. Last but not least, my girlfriend Yue is sincerely appreciated for her love and patience throughout my education and job hunting process.

TABLE OF CONTENTS

LIST OF TABLES

LIST OF FIGURES

ABSTRACT

Thermoacoustic (TA) oscillations have been one of the most exciting discoveries of the physics of fluids in the 19th century. Since its inception, scientists have formulated a comprehensive theoretical explanation of the basic phenomenon which has later found several practical applications to engineering devices. The most common devices are the so-called TA engines (prime movers) and refrigerators (heat pumps). These devices are distinguished by the direction in which they perform energy conversion. While a traveling sound wave propagates through a TA regenerator with a positive temperature gradient, the gas parcels experience a Stirling-like thermodynamic cycle, so that thermal energy can be converted into acoustic power cyclically. The most fascinating feature of TA engines is its capability of utilizing low-grade external heat sources, such as industrial waste heat and solar thermal energy to produce acoustic power, which can be easily converted into electricity using piezoelectric elements. The absence of moving parts in TA engines is another advantage over conventional heat engines, which demonstrates the potential for developing low-cost and reliable power generators.

To-date, significant research efforts have been made to develop TA coolers and electric generators, but all studies have concentrated on fluid media where this mechanism was exclusively believed to exist. This research extends the idea of thermoacoustic instability to solid media and lays the theoretical foundation of Solid-State Thermoacoustics (SSTA). This new paradigm uncovers the fundamental idea that a self-sustained TA response can be achieved also in solid media. Although the underlying physical mechanism exhibits interesting similarities with its counterpart in fluids, the theoretical framework highlights relevant differences that have important implications on the ability to trigger and sustain the TA response. This work shows both theoretically and numerically that TA instability can be achieved in solids in the form of both longitudinal standing and traveling waves, the most logical counterpart to pressure waves in gases. However, mechanical waves in solids are polarized, hence leading to multiple mode types unlike pressure waves in fluids. This research also reveals the existence of thermoacoustically excited flexural waves and presents theoretical and numerical analyses of flexural-mode thermoacoustic waves in a bilayer beam. Experimental investigations are

conducted to confirm the thermo-mechanical energy conversion associated with the flexural motion.

In contrast to conventional fluid-based thermoacoustics, SSTA systems offer the capability to leverage the tunable thermo-mechanical properties of engineered materials to improve thermoacoustic instabilities. Numerical evidence of using negative thermal expansion materials to intensify both axial-mode and flexural mode thermoacoustic intensities are shown in this work, which sheds light on the practical design and application of SSTA devices. This research opens a unique window on the use of solid materials as working substances to overcome the shortcomings of traditional thermoacoustic devices. Based on the fundamental theoretical and numerical explorations conducted in this research, it is believed that SSTA provides a promising path towards the development of more robust, more powerful, more cost-effective and more eco-friendly thermo-mechanical energy conversion devices, hence promoting practical applications and commercialization of thermoacoustic technologies.

1. INTRODUCTION

1.1 Introduction to Thermoacoustics

The existence of thermoacoustic (TA) oscillations in thermally driven gases has been known for centuries. When a pressure wave travels in a confined gas-filled cavity while being provided heat, the amplitude of the pressure oscillations can keep growing until it saturates due to nonlinear effects. This self-sustaining process builds upon the dynamic instabilities that are intrinsic in the TA process. The essence of TA phenomena is the two-way interaction between fluid motion and fluctuations in heat release rate, and ultimately, the resulting TA energy conversion processes. In this chapter, we will first provide an overview of TA energy conversion technology, briefly illustrating how it is applied in modern thermoacoustic devices. Followed by the initial introduction, we will explain the main characteristics of the two most common types of TA devices, namely the standing- and the traveling-wave TA devices. A literature review summarizing the development of TA technology from the historic explorations to the modern numerical and experimental studies will be conducted. Summarizing the key limitations of the development of fluid-based TA to date leads to the motivations and objectives of this study. This chapter is closed by an outline of this thesis.

1.1.1 Overview of Thermoacoustic Energy Conversion

Thermoacoustic devices, as the name suggests, rely on the heat exchange between sound waves in the working medium and the surrounding heat source to conduct energy-conversion process. The key components of thermoacoustic devices consist in a resonant tube, in which the sound field can be effectively excited. The heat-sound interaction takes place in a porous section that is inserted into the acoustic tube. The porous section can be as simple as a chunk of steel wool, a stack of metal gauze or foam, or a ceramic stack (Fig. 1.1). When sound waves pass through the small pores of such section, plane-wave assumption is no longer valid, due to the non-negligible thermoviscous effects, which are associated with the thermoacoustic energy exchange. When this porous section is sandwiched by a hot heat exchanger and a cold heat exchanger (Fig. 1.2), a spatial temperature gradient is established, with which

the diffusion in the small pores becomes beneficial to a thermoacoustic energy conversion process. The static temperature gradient that is imposed by the two heat exchangers with a temperature difference is the main driver of thermoacoustic instability, which accounts for the transient amplifying and the nonlinear steady-state acoustic oscillations. The solid porous material acts as a thermal reservoir with huge heat capacity, so it is usually modeled as an isothermal boundary condition with the specified temperature profile in numerical studies. From the perspective of wave propagation, when a sound wave progresses through a sufficiently thin passage from the cold to the hot end of the porous section, a Lagrangian gas parcel experiences a Stirling-like thermodynamic cycle [1], [2]. The proper phase difference between the heat release from the porous section and the deformation of the infinitesimal element is crucial to TA instability. If the temperature of a fluid parcel is higher than its mean state while it undergoes elastic expansion, the positive temperature fluctuation will further inflate the parcel on top of its elastic expansion. Same deformation amplification can happen when the parcel contracts. As a result, if heat is provided and extracted in a good 'timing', the motion of the infinitesimal parcel can grow, leading to TA instability in macroscopic scale.

Along with the heat exchangers, the porous section forms the essential component of a thermoacoustic device, known as the thermoacoustic core. In the thermoacoustic core, microscopic fluid parcels effectively go through a thermodynamic cycle and produce mechanical (acoustic) work by absorbing net heat input. In some studies, the name of this chunk of porous material is distinguished, i.e. stack for a standing wave engine (SWE) and regenerator for a traveling wave engine (TWE). See Fig. 1.2. In an SWE, the phase difference between pressure and particle velocity is close to 90°, while that for TWEs is practically in the range of $20° \sim 60°$, although ideally a zero-phase TWE operates at its optimal condition. Discussions on SWEs and TWEs will be expanded in Section 1.1.2.

Depending on the direction of energy conversion, TA devices are divided into prime movers (engines) and heat pumps (refrigerators). TA engines rely on the established temperature gradient to cyclically release heat to fluid parcels in the stack so that the energy is accumulated in the form of acoustic power in the absence of energy harvesting elements. The reverse effect, which relies on the input acoustic power to establish a temperature gradient

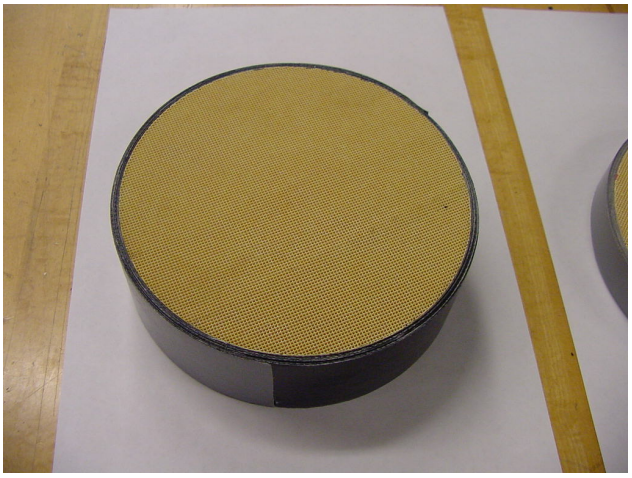

Figure 1.1. Ceramic stack [3].

from ambient temperature to a low temperature, is the principal mechanism of TA refrigeration [4]. Several prototypes of TA engines and heat pumps are built and can operate at power levels up to one megawatt [5].

1.1.2 Standing- and Traveling-wave Thermoacoustic Devices

Depending on the proportion of standing wave and traveling wave components in the acoustic field, TA devices are generally classified into standing-wave and traveling-wave devices. Fig. 1.2 shows a typical example of a standing-wave and a traveling-wave thermoacoustic engine with external loads. The difference between them lies in the phase difference between pressure and velocity oscillations. In a standing wave device, the phase difference is approximately (but not exactly equal to) $\pm 90°$ at all spatial locations. The slight phase drop from 90° is a result of imperfect thermal contact which allows heat flow to the acoustic load. It is worth-mentioning that a perfect thermal contact between stack and working medium is not thermoacoustically optimal in a standing-wave configuration. This aspect reflects in an optimal pore sizing of the stack, which is approximately two times the thermal penetration depth [6]. Under such condition, the imperfect thermal contact guarantees that heating follows compression and cooling follows expansion, thus creating the desired phase difference between pressure and velocity.

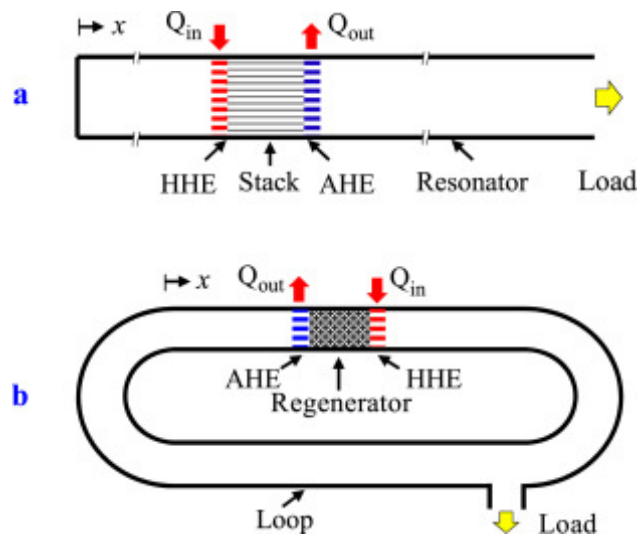

Figure 1.2. (a) A standing-wave and (b) a travelling-wave thermoacoustic engine with external loads. Note that the porous section where thermoacoustic energy conversion takes place is labeled as stack/regenerator in the standing-/traveling-wave configuration. In both configurations, the porous section is sandwiched by a hot heat exchanger (HHE) and a cold heat exchange (or ambient heat exchanger, AHE) [7].

However, in a traveling wave engine, the phase between pressure and velocity stays well below 90° depending on the specific design (e.g. between ±30° in the traveling wave TA engine built by Yazaki [8]). Generally in TWEs, a smaller pore size is always favorable because the intrinsic nature of synchronized pressure and velocity in pure traveling waves leads to the favorable compression-heating-expansion-cooling phasing under perfect thermal contact. As the pore size decreases, the delay between temperature rise and heat input becomes shorter. More quantitative explanations about the phasing in both configurations will be presented in Section 4.3.2.

To-date, the most researched and built TA devices are the traveling-wave types. Traveling-wave devices are generally easily triggered with low onset temperature. Traveling-wave TAEs are more efficient than their standing-wave counterparts because the fluid parcels in the regenerator of TWEs undergo a reversible thermodynamic cycle. The most efficient standing- and traveling-wave engines reported by researchers convert thermal energy to acoustic power at 18% and 30% (41% of Carnot efficiency), respectively [9].

1.1.3 Historical Notes on Thermoacoustics

The first laboratory TA experiment may be the one conducted by Higgins in 1777 when he inserted a hydrogen flame into an open pipe (Fig. 1.3) to produce a self-sustained standing wave [10]. This phenomenon was later dubbed a singing flame.

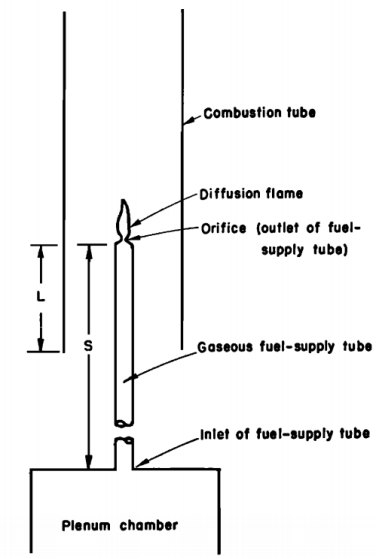

Figure 1.3. Higgins Tube [10].

It is 70 years later when Soundhauss prepared another experiment, which bears closer resemblance to the process of glassblowing. He attached a narrow tube to a closed bulb and put the flame near the junction, while left another end open (Fig. 1.4) . The flame raised the temperature of the closed end and resulted in an unstable standing sound wave [11]. The experimental apparatus was later dubbed Soundhass tube.

In 1859, Rijke used a hot metal gauze to replace the flame and observed similar phenomena (Fig. 1.5). He also pointed out that there existed an optimal location of such hot gauze. In a vertical open tube, the unstable sound wave reached its maximal power density when the gauze was placed one-fourth of its length from the lower end of the tube. More interestingly, either closing one end of the tube or reversing its direction suppressed the sound generation [13].

In 1896, the famous physicist and acoustician, Lord Rayleigh, proposed a qualitative explanation of the heat-induced sound phenomena [14]. He concluded that these heat-driven

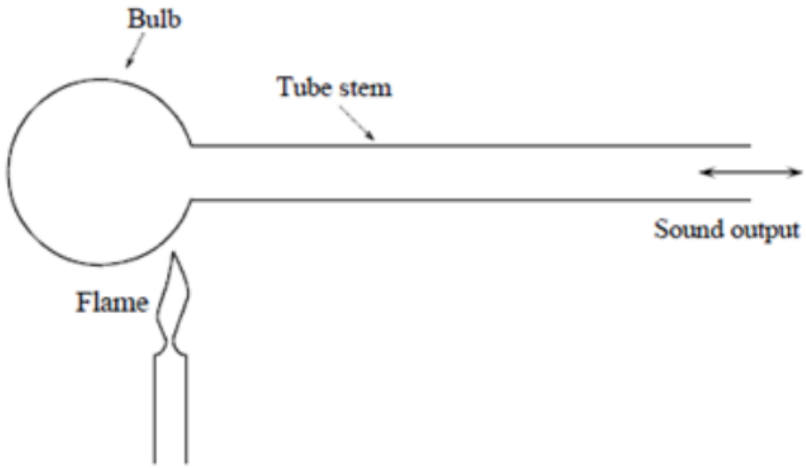

Figure 1.4. Soundhauss Tube [12].

sound would be generated if heat flowed into the gas when its density was high, and out of the gas when its density was low. Such qualitative explanation for the first time unveiled the essence of the coupling between pressure and temperature fluctuations and the dependence of TA instability on phasing.

In 1949, Kramers was the first to start the theoretical study of thermoacoustics by extending Kirchhoff's theory of the decay of sound waves at constant temperature to the case of attenuation in the presence of a temperature gradient [15]. However, his theory based on boundary-layer approximation did not present acceptable results compared to the experimental data.

Although a systematic and quantitative understanding of the phenomenon had not been built yet, Bell Telephone Laboratories proposed the idea of converting heat into electricity through a two-fold energy conversion strategy in 1950s [16], [17]. The concept consisted in the conversion from heat into sound energy with a thermoacoustic engine, followed by a sound-to-electricity conversion process. However, such device was not well accepted at that time due to the low efficiency of the TA energy conversion.

A plausible TA theory was finally established by Rott in 1970s, which marked the inception of quantitative understanding of TA phenomena [18]. Between 1969 and 1980. Rott published a series of papers, introducing a quasi-one-dimensional linear theory which was

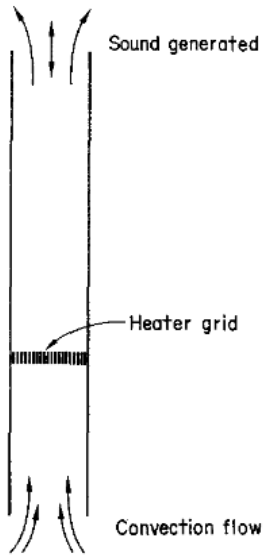

Figure 1.5. Rijke Tube [13].

based on linearized equations of conservation, i.e. conservation of mass, momentum and energy [18]–[24]. The transverse heat conduction and viscous loss were cross-sectionally averaged in the theory so that the fully 3D equations were collapsed to the dimension corresponding to the axis of wave propagation. This series of papers has been generally viewed as an important milestone for thermoacoustic research, which greatly stimulated the subsequent theoretical and numerical researches on thermoacoustics.

In 1979 and 1985, Ceperley pointed out that when a wave traveled through a regenerator with a temperature gradient, the fluid parcel experienced a Stirling-like thermodynamics cycle (Fig. 1.6) [2]. This heat-to-work cycle could thus amplify the traveling wave. It was further mentioned that the reversible nature of such thermodynamic cycle permitted a higher efficiency than the cycle that a standing wave went through. Based on this principle, a conceptual heat-driven refrigerator with torus topology was proposed to allow waves to travel in the loop without reflection.

Swift from Los Alamos National Laboratories (LANL) in 1988 published a reveiw article, which comprehensively summarized the historical progression, mathematical formulation for interaction between sound wave with both single plate and stack, components of TA engines, and some engine examples [1]. This review bridged the gap between TA theory and the

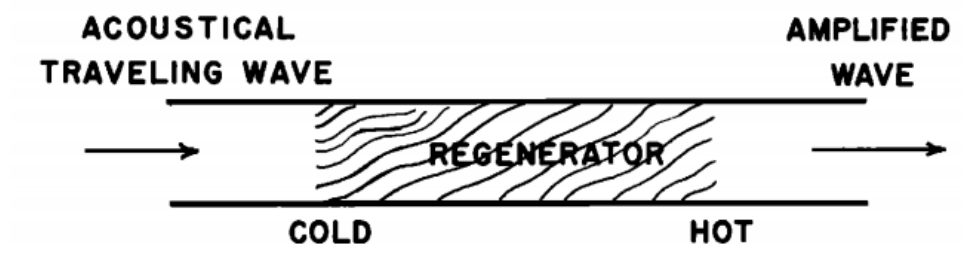

Figure 1.6. Sounds get amplified through a narrow channel with cold to hot temperature distribution [2].

buildups of real TA devices. Since then, extensive experimental rigs and even commercial prototypes have been built.

It is noteworthy that in 2008, a numerical simulation tool, DeltaEC (Design Environment for Low-Amplitude ThermoAcoustic Energy Conversion), was developed at LANL by Ward and Swift. DeltaEC is a well-integrated tool guiding the design of real TA devices based on Rott's linear theory. As a powerful tool, it is widely used in the process of designing TA devices and analyzing their performances. However, because the equations in DeltaEC describes the steady-state conditions, as Guedra and Penelet (2012) pointed out in [25], DeltaEC 'is not primarily devoted to the determination of the threshold condition itself'. It is in the same paper that they described the transient characteristics of TA engines using a complex frequency. The real part of this complex frequency represented the frequency of self-sustained acoustic oscillations, while its imaginary part characterized the amplification/attenuation of the wave due to the thermoacoustic coupling. This idea has been accepted by a number of researchers [26]–[29], including the author of this thesis, because it reveals the 'eigenvalue problem' nature of the transient process of thermoacoustic instability.

1.1.4 Experimental and Numerical Studies of Thermoacoustic Engines

With the mutual interaction between thermal and acoustic fields well understood, efforts have been dedicated to developing thermoacoustic devices with different configurations. This

section summarizes the most important leaps in the progression of thermoacoustic engine design, as well as several high fidelity numerical simulations of thermoaocoustic engines.

In 1998, Yazaki et al. for the first time presented a traveling wave thermoacoustic prototype engine (Fig. 1.7) [8], as an experimental realization of Ceperley's proposal. The phase difference between pressure and velocity in Yazaki's torus-shaped engine was brought down to ±30°, which guaranteed the traveling wave component being dominating. As predicted by Ceperley, the measurements showed that traveling wave device significantly outperformed a standing wave counterpart at the same operating frequency. However, the engine converted energy at a relatively low efficiency due to a low acoustic impedance within the thermoacoustic core, caused by the large velocity amplitude in the regenerator. This low impedance gave rise to a high acoustic loss, thus preventing the engine operating efficiently.

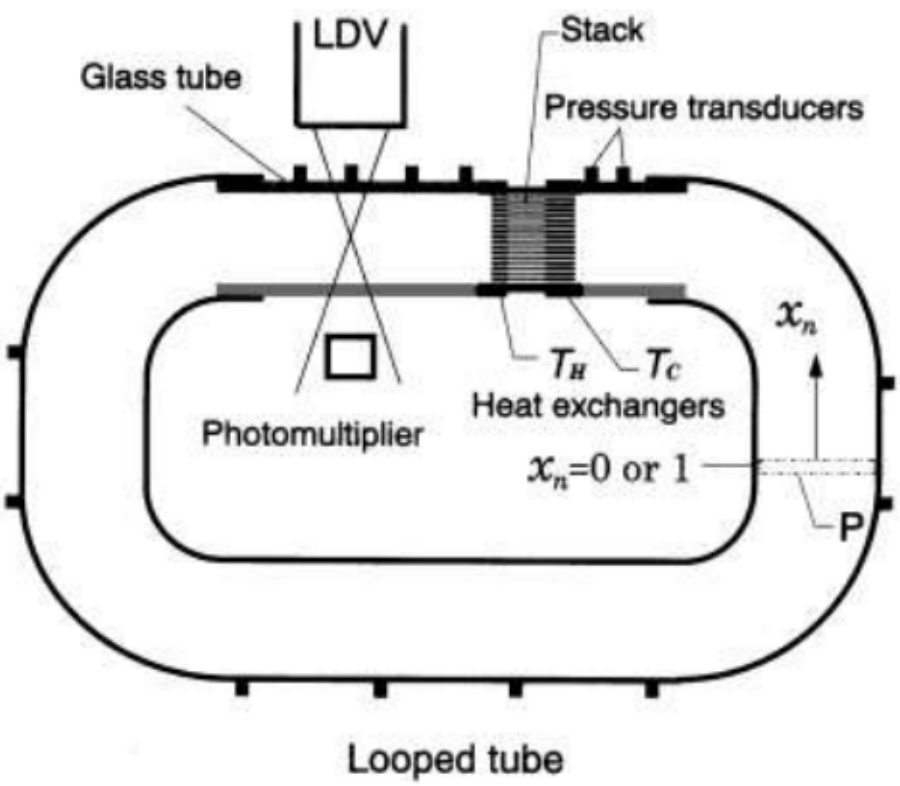

Figure 1.7. Yazaki et al.'s Engine [8].

This drawback was noticed by Backhaus and Swift, so they overcame the issue by proposing a new type of engine consisting of a loop tube attached by a long resonator pipe (Fig.

1.8) [9]. Three main modifications were made: (1) An inertance section was added to force a zero phase difference in the regenerator to achieve a local pure traveling wave; (2) To avoid the high viscous loss, they applied a compact acoustic network to decrease the particle velocity in the regenerator without using large resonator; (3) a jet pump and a tapered thermal buffer tube was designed to suppress the acoustic streaming due to nonlinearity. With all the aforementioned efforts made, their engine with 30 bar Helium as working gas reached 30% thermal efficiency (equivalently 41& Carnot efficiency), while operating at 80 Hz.

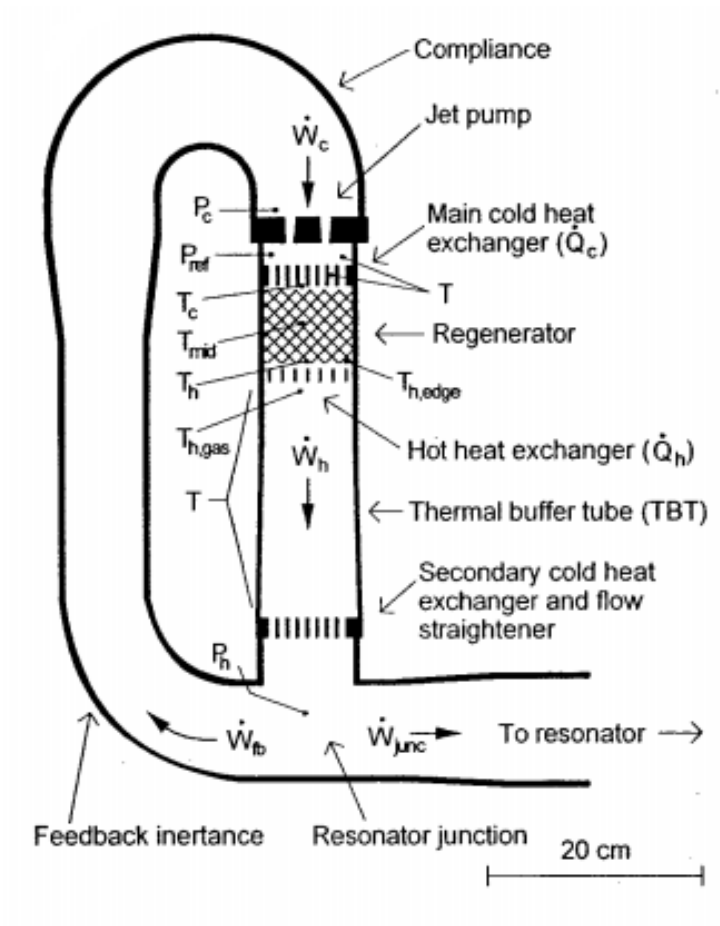

Figure 1.8. Backhauss and Swift's Engine [9].

Although with higher efficiency, Backhaus and Swift's engine operated at 725°C. The high operating temperature harmed its competitiveness especially when compared with traditional heat engines. As one of the solutions, De Blok (2008) developed a torus engine with a bypass

tube cascading two regenerators (Fig. 1.9), which was capable of utilizing low temperature differences from solar energy or industrial waste heat in the range of 70 − 200°C [30]. He

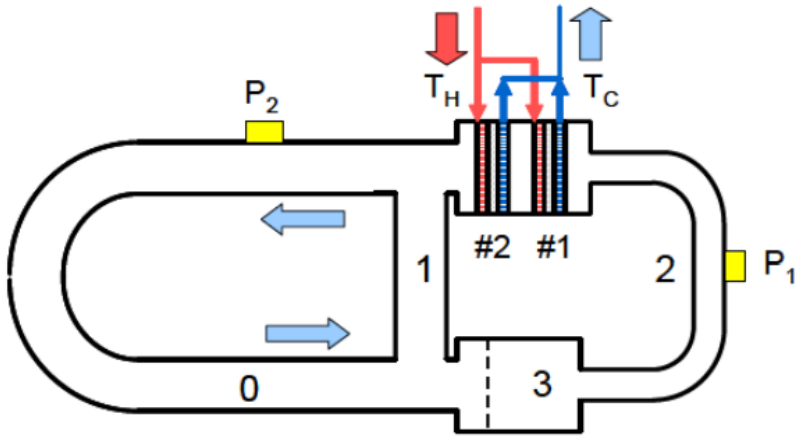

Figure 1.9. De Blok's Engine with bypass tube [30].

pointed out that a standing wave resonator should induce higher viscous loss because the two positively interfered waves results in higher amplitudes. His solution was to use a bypass tube as a traveling wave resonator. Also, he proposed to enlarge the cross section area of the regenrator to further reduce viscous losses. His engine utilized atmospheric air as working gas with an onset temperature as low as 65°C with two cascaded regenerators. He then improved his design by adding two more regenerators (Fig. 1.10) and achieved 40°C onset temperature in 2010 [31]. In the same year, Biwa et al. presented a multi-stack design with a standing wave resonator [32]. The engine with five stacks distributed along the torus achieved instability with the hot end temperature equal to 355K (Fig. 1.11).

In 2012, Yu et al. integrated the loop traveling wave engine with a commercially available loudspeaker as an alternator to study the serial thermal-acoustic-electric energy conversion (Fig. 1.12) [33]. Their prototype converted 800 W heat input eventually into 5.17 W electricity, achieving a thermal-to-electrical efficiency of 0.65%, showing the possibility of a low cost TA generator which could be used in developing areas rich of free solar energy. The full thermal-to-electrical energy conversion and harvesting was also theoretically and numerically studied by Smoker et al. [34] and Nouh et al. [35].

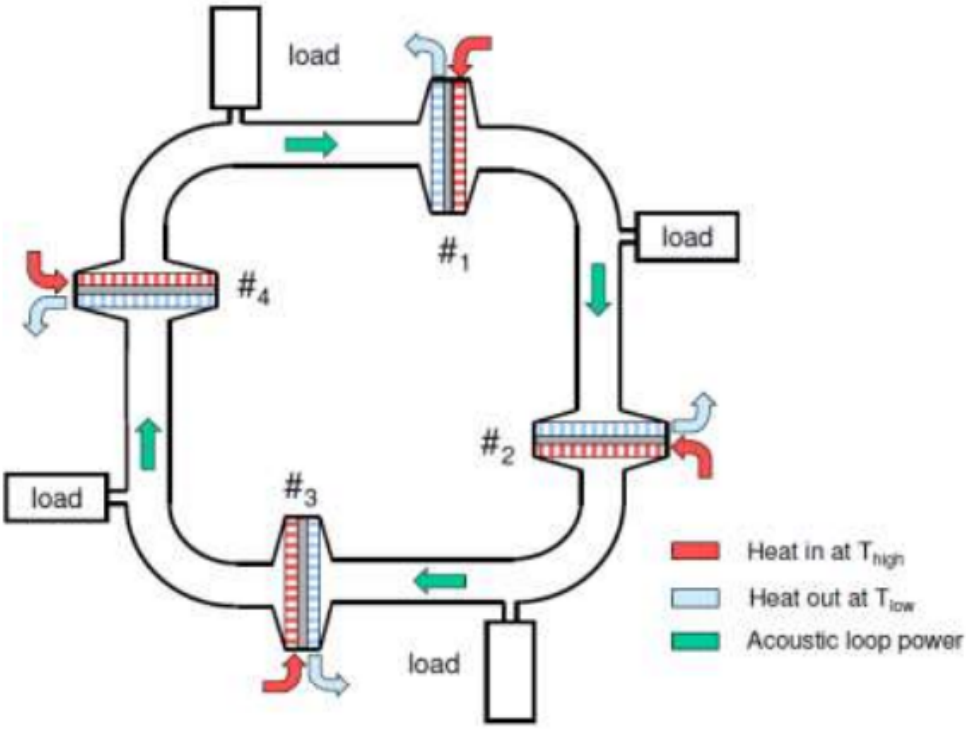

Figure 1.10. De Blok's Engine with four regenerators [31].

Other than the qualitative understanding gained from experimental studies of thermoacoustics, a few linear and nonlinear numerical simulations have been conducted to quantitatively understand the details of thermoacoustic energy conversion procedure.

Scalo et al. (2015) carried-out three-dimensional Navier-Stokes simulations, from quiescent conditions to the limit cycle, of a theoretical travelling-wave thermoacoustic heat engine (TAE) composed of a long variable-area resonator shrouding a smaller annular tube (Fig. 1.13) [26]. This simulation captured the process from transient exponential growth, consistent with the linear prediction based on Rott's theory, till the saturation to limit cycle governed by acoustic streaming. Fully compressible Navier–Stokes simulations of a standing wave thermoacoustic–piezoelectric engine were carried out by Lin et al. (2016) [27], providing accurate predictions of thermal-to-acoustic and acoustic-to-electrical energy conversion (Fig. 1.14). Gupta et al. (2017) investigated thermoacoustically amplified quasi-planar nonlinear waves driven through a hierarchical spectral broadening to the limit of shock-wave formation in a variable-area looped resonator (Fig. 1.15) [28]. The experimental observation

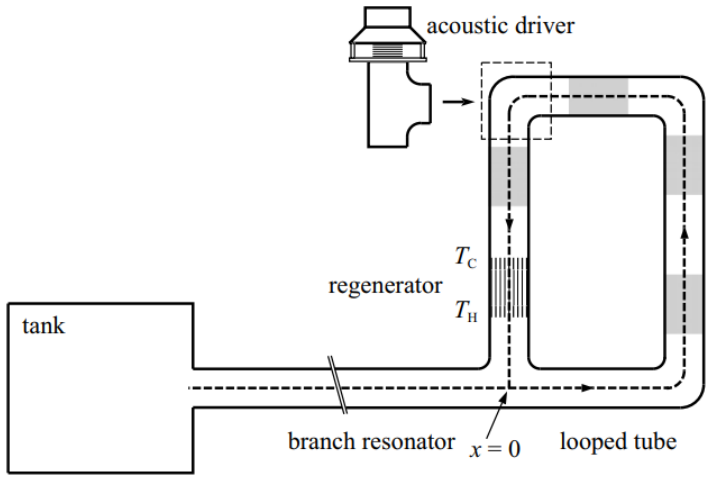

Figure 1.11. Biwa et al.'s Engine with five regenerators [32].

of thermoacoustic shock waves in a looped thermoacoustic tube were firstly reported by Biwa et al. in 2011 [36].

1.1.5 Benefits and Shortcomings of Thermoacoustic Devices

Through the theoretical, numerical, and experimental analyses of TA devices, it has been understood that TA devices bear advantages over conventional heat engines in various aspects. At the meantime, new challenges, accompanied with the shortcomings of TA devices, emerged for building efficient TA devices.

Among all the benefits of TA devices, we list the most significant advantages over conventional energy-conversion devices in the following:

1. TA devices do not require moving parts, translating into higher structural robustness. Little or no maintenance is required while the devices are in operation.

2. They are eco-friendly. The most studied and built TA devices generally use non-toxic gas like air, nitrogen or helium as working medium. With the environmental issues becoming challenging and more urgent globally, TA technology shows its special charm because it does not require the use of harmful working fluids.

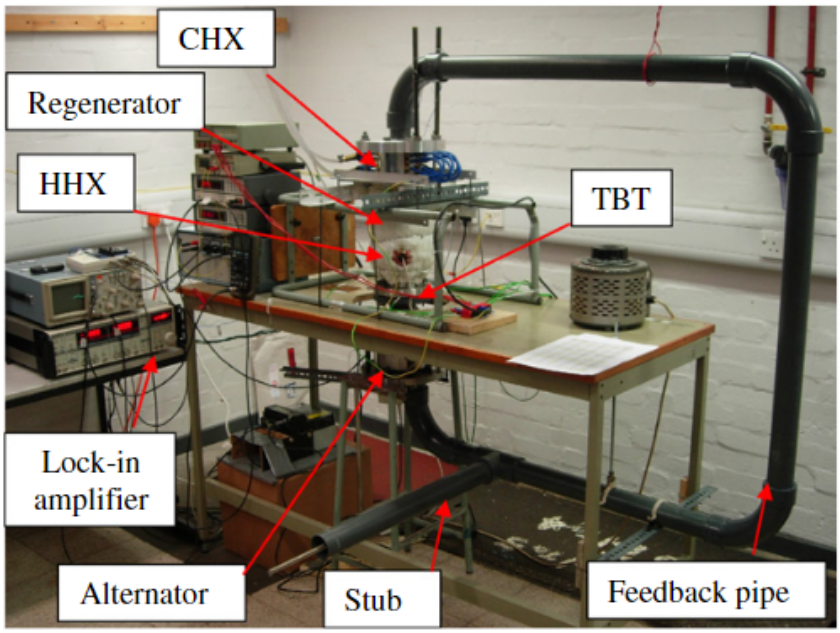

Figure 1.12. Yu et al.'s generator [33].

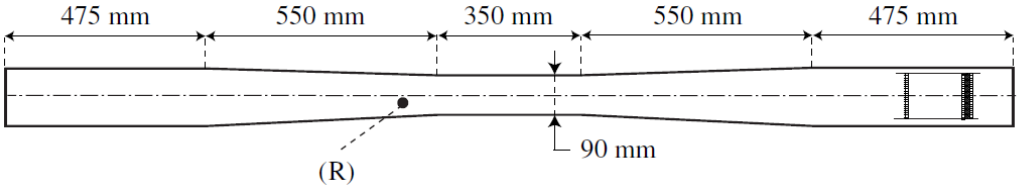

Figure 1.13. Scalo et al.'s Engine [26].

3. They can utilize low-grade heat as energy sources. Through a proper design, a TA engine only needs a temperature difference lower than 100°C to trigger instability. This makes the use of free solar energy and industrial waste heat to produce or harvest useful energy possible.

Despite the superiority of TA devices, their application is limited in the following aspects:

1. Due to the intrinsic nature of gaseous media, the power density produced by TA process is low, which limits the efficiency of TA devices.

2. Mass and thermal leakages require additional maintenance and complicate the design.

3. The nonlinearities involved in the TA process harms the device performance:

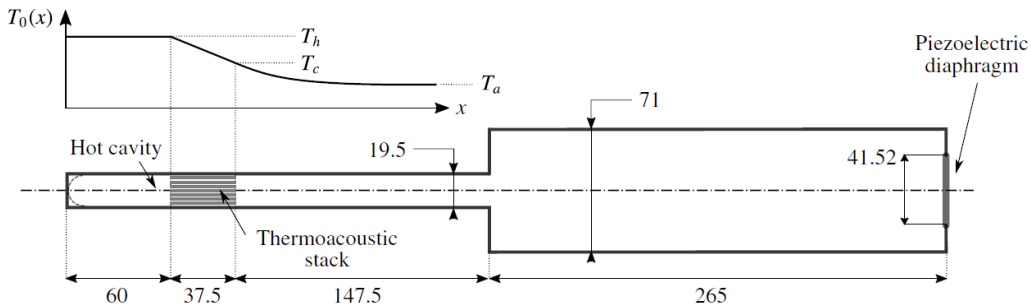

Figure 1.14. Lin et al.'s Engine [27].

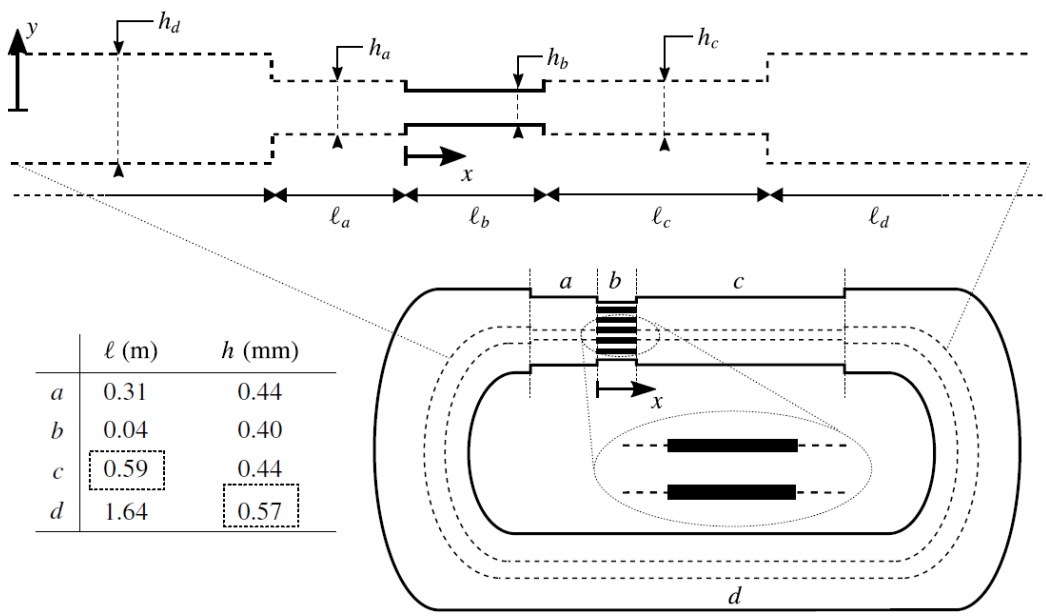

	ℓ (m)	h (mm)
a	0.31	0.44
b	0.04	0.40
c	0.59	0.44
d	1.64	0.57

Figure 1.15. Gupta et al.'s Engine [28].

(a) Acoustic streaming, generally found in traveling-wave engines, can lower the effective thermal gradient along the regenerator.

(b) Harmonic generation spreads energy over the spectrum, which harms the energy conversion at the main operating frequency.

(c) Turbulence aroused in the TA process dissipates acoustic energy.

Most of the limitations listed above are due to the intrinsic sound propagation characteristics in gaseous media. Considering the similarities between solids and fluids, in terms

of the nature of continua, it seems reasonable to wonder if TA phenomena can also exist in solid media. It is anticipated that some of the key bottlenecks for fluid-based TA devices, e.g., turbulence and acoustic streaming, are not problematic for solid-state thermoacoustic (SSTA) devices.

1.2 Motivations and Objectives of the Thesis

Thermoacoustics has been an active field of research for decades, leading to various types of practical devices. Yet, the TA phenomenon was explored only in fluids. The development of fluid-based TA devices is limited by different aspects, such as low power density, leakage and nonlinear losses. These aspects are mainly related to the nature of the working medium, which in the case of classical TA is a gas. When using solid medium to propagate sound instead, it is possible to envision larger power density and no leakage. The nonlinear effects, such as acoustic streaming and turbulence, which harm the engine efficiency significantly, do not take place in solids. These characteristics make solids a promising candidate medium for thermoacoustics. The main motivation of this research is to explore the existence of thermoacoustics in solids, its performance and possible limitations.

In addition, the development of engineered materials provides the opportunity to tailor the thermo-mechanical properties of solid materials in a way that could be beneficial for thermoacoustic devices. Other than the conventional treatments (e.g. phase adjustment) for performance enhancement of TAEs, the ease of control and tuning on certain thermal properties (e.g. thermal expansion coefficient) of solids opens another window to designing more efficient and more robust TA devices. One of the most common drawback of existing TA devices is their large size, needed to achieve low operating frequencies that are required for a more efficient heat transfer. Although efforts have been made by adding liquid pistons to bring down the operating frequency [37], this could lead to other issues associated with the instability of gas-liquid interface [38]. The length of a TA device, together with the sound speed of the working medium, determines the operating frequency of a TAE. To design a shorter engine with a low operating frequency, a medium in which sound travels slowly is preferred. Leveraging different dynamic mechanisms, such as local resonance, engineered

solid materials can exhibit tunable mass density and stiffness [39], [40], translating into tunable sound speed. This characteristic of solid materials provides the opportunity of designing more compact TA devices. Therefore, the potential application of engineered materials to more efficient and more compact thermoacoustic devices further motivates this research.

The detailed objectives of the present study are summarised in the following:

1. To extend the well-established theory of thermoacoustics to solid media. The theory of SSTA shall be established to present quantitative explanations of the following phenomena:

   (a) Axial-mode standing wave thermoacoustic instability in solids (Standing-wave A-SSTA).

   (b) Axial-mode traveling wave thermoacoustic instability in solids (Traveling-wave A-SSTA).

   (c) Flexural-mode thermoacoustic instability in solids (F-SSTA).

2. To develop simulation strategies and algorithms to perform stability and energy analyses of solid state devices.

3. To understand and analyze the thermo-mechanical principles of A-SSTA and F-SSTA.

4. To conduct experimental validations of the theory of SSTAs. The experiments shall show the evidence of thermo-mechanical energy conversion and self-sustained vibration when thermoacoustic instability is triggered.

5. To conduct parametric studies of SSTA systems in order to identify optimal designs of SSTA devices.

6. To explore configurations utilizing engineered materials to enhance or control the performance of both SSTA and conventional TA devices.

1.3 Thesis Outline

Following the introduction in this section, Chapter 2 reviews the conventional theory of thermoacoustics, theory of thermoelasticity. Both classical theories form a basic understanding of thermo-mechanical(acoustical) coupling in solid materials. They are the two essential building blocks of the proposed theory of solid-state thermoacoustics, which is derived in Chapter 3. The full mathematical derivations of the governing equations of these theories are presented in details.

Chapter 4 presents a numerical study of axial-mode SSTA instability. A quasi-1D linearized model, analogous to Rott's theory, is developed to perform stability analysis and characterize the effect of different design parameters. A 3D transient model is developed with commercial FEM software, COMSOL Multiphysics, to validate the proposed quasi-1D model. Numerical evidences are presented to show that the instability can be effectively triggered and sustained in an axially vibrating metal rod. A multi-stage configuration was proposed in order to overcome the effect of structural damping, which is one of the main differences with respect to the thermoacoustics of fluids. A looped solid configuration, investigating the existence of self-sustained thermoelastic oscillations associated with traveling wave modes in rod under the effect of a localized thermal gradient is then proposed. Configurations having different ratios of the rod radius R to the thermal penetration depth δ_k are explored and the traveling wave component (TWC) is found to become dominant as R approaches δ_k. The growth-rate-to-frequency ratio of the traveling TA wave is found to be significantly larger than that of the standing wave counterpart for the same wavelength. The perturbation energy budgets are analytically formulated and closed, shedding light onto the energy conversion processes of SSTA engines and highlighting differences with fluids. Efficiency is also quantified based on the thermoacoustic production and dissipation rates evaluated from the energy budgets. This Chapter lays the theoretical foundation of thermoacoustics of solids and provides key insights into the underlying mechanisms leading to self-sustained oscillations in thermally driven solid systems.

In Chapter 5, the governing equations of A-SSTAs are firstly recast into dimensionless form to develop an accurate analytical approaches to solve for the mode shapes and complex

frequencies for 1) a standing-wave fixed-mass SSTA rod, and 2) for a traveling-wave looped SSTA rod; then, it is found that the growth-rate-to-frequency ratio is governed by the dimensionless coefficient of thermal expansion (CTE), the Grüneisen parameter, the hot-to-cold temperature ratio, the normalized stage location and length, the dimensionless radius, the end mass ratio for the fixed-mass rod, and the thermal buffer segment (TBS) length for the looped rod. Based on these newly identified dimensionless parameters, a thorough numerical analysis is conducted in order to get a thorough understanding of the functional relationships controlling the complex dynamics in SSTAs. With the many mechanisms available in solids to tailor either their physical or effective properties, remarkable opportunities to enhance and tune the performance of SSTA devices can be potentially sought.

In Chapter 6, following the research on axial-mode solid-state thermoacoustics, the flexural-mode solid-state thermoacoustics (F-SSTAs), which is unique to solids, is theoretically and experimentally studied. More specifically, it is shown how flexural waves can grow unbounded when traveling in a bilayer beam subject to a spatial thermal gradient. A theoretical framework is developed to analyze the dynamics of the system and to establish the criterion controlling the onset of flexural thermoacoustic instability. Numerical calculations conducted in both the frequency and the time domains show the occurrence of two main effects due to the presence of thermal coupling: (1) the dynamic amplification of the flexural motion, and (2) the time-varying location of the neutral axis. An experimental investigation is also conducted in order to corroborate the existence of this thermal-to-mechanical energy conversion mechanism associated with flexural waves. Leveraging the tunable thermomechanical properties of architectured materials, the F-SSTA response of a hybrid bilayer beam that consists in both a continuous layer and an architectured layer having negative thermal expansion (NTE) properties is investigated. Numerical results confirm that the NTE layer significantly improves the F-SSTA instability, as predicted by the instability criterion. The energy conversion mechanism that takes place in the F-SSTA process is also explored by using the perturbation energy budget approach, developed based on a discrete order reduced model.

In Chapter 7, this thesis is concluded by briefly summarizing the key findings, followed by additional discussions of possible routes towards future developments of the study of solid-state thermoacoustics.

2. THERMOACOUSTICS AND THERMOELASTICITY: REVIEW OF FUNDAMENTAL THEORY

2.1 Introduction

The theory of solid-state thermoacoustics is developed based on two building blocks: (1) Rott's thermoacoustic theory and, (2) classical thermoelastic theory. Rott's thermoacoustic governing equations are a classical treatment of understanding and solving fluid-based thermoacoustics, which enlights the development of thermoacoustic theory of solids.

Mechanical waves in solid media, especially in audible range, are generally referred to elastic waves rather than acoustic waves. Therefore, to understand the coupling between heat and sound (mechanical waves) in solids, it is crucial to understand the fundamental of thermoelasticity. According to classical thermoelasticity [41]–[43], an elastic wave traveling through a solid medium is accompanied by a thermal wave, and vice versa. The thermal wave follows from the thermoelastic coupling which produces local temperature fluctuations (around an average constant temperature T_0) as a result of a propagating stress wave. When the elastic wave is not actively sustained by an external mechanical source, it attenuates and disappears over a few wavelengths due to the presence of dissipative mechanisms (such as material damping); in this case, the system has a positive decay rate (or, equivalently, a negative growth rate). When considering the thermoelastic coupling, even if the system is fully isolated from the environment (i.e. all adiabatic boundaries), the thermoelastic motion can still decay due to the well known thermoelastic damping aroused from the irreversible thermodynamics in the bulk of materials. The lost kinetic energy will then lead to a very slow rise of mean temperature, which is generally neglected.

Classical thermoelastic problem typically assumes the medium being at a uniform reference temperature T_0 under adiabatic condition. With the knowledge of thermoacoustic phenomena in fluids, we wonder what may happen if heat exchange is allowed at the boundary (known as wall heat transfer in thermoacoustic community), while the solid is subject to a non-uniform T_0 in the axial direction. Under such conditions, which are essential for TA instability in fluid-based devices, can we observe TA instability in solids as well?

The above question was aroused from the understanding of both Rott's thermoacoustic theory and classical theory of thermoelasticity, whose main elements are briefly reviewed in this chapter, to provide the foundation for the development of the SSTA theory and the associated analyses conducted in the following chapters.

2.2 Thermoacoustic theory: From Conservation Laws to Rott's Theory

In this section, we will review the derivations of Rott's thermoacoustic theory [18]–[24], [44]. The linear governing equations of thermoacoustics, which greatly facilitate the understanding of the thermoacoustic phenomena, thus beneficial to the development of the modern thermoacoustic research, will be rigorously derived based on the conservation laws of fluids.

2.2.1 Conservation Laws of Fluids

Conventional (fluid-based) thermoacoustics, like all the other phenomena in fluids, is governed by conservation laws of fluids. Other than the consideration of continuity and momentum conservation adopted in pressure acoustics, thermoacoustics also requires the entropy conservation to describe the heat transfer processes in the coupling mechanism. Before introducing Rott's linear thermoacoustic theory, which is the foundation of thermoacoustic engine design, the fully three dimensional conservation laws are discussed in this section. However, some of the results can be very tedious to derive, so rigorous step-by-step derivations are not provided here. They can easily be found in advanced fluid-mechanics textbooks [45], [46].

Conservation of Mass

Conservation of mass equation, also known as continuity equation, describes the conservation of mass for a microscopic control volume in a fluid. For a cubic fluid control volume

$dxdydz$, the mass can only be changed as a result of mass inflow and out flow through its boundary surfaces, i.e.:

$$-\frac{\partial \rho}{\partial t} dxdydz = \left(\frac{\partial(\rho u)}{\partial x} dx\right) dydz + \left(\frac{\partial(\rho v)}{\partial y} dy\right) dxdz + \left(\frac{\partial(\rho w)}{\partial z} dz\right) dxdy \tag{2.1}$$

where ρ is density, u, v and w are velocity in x, y and z directions. The left hand side indicates the mass decrease rate and the terms on the left hand size denote the mass outflow through the $dydz$, $dxdz$ and $dxdy$ surfaces. Factoring out $dxdydz$ and writing the result in a compact tensor form yields the well-known continuity equation:

$$\frac{\partial \rho}{\partial t} + \nabla \cdot (\rho \boldsymbol{v}) = 0 \tag{2.2}$$

Conservation of Momentum

The conservation of momentum in fluids, also known as the Navier-Stokes equation, is an expression of Newton's second law, i.e.: the summation of all the external forces applied to an object (fluid parcel) equals the mass of the object multiplied by its acceleration. In fluid mechanics, the acceleration typically includes the local acceleration and the convective acceleration, which describes how a fluid parcel is accelerated induced by different velocity of the location. The force equation is expressed as:

$$(\rho dxdydz)\left[\frac{\partial \boldsymbol{v}}{\partial t} + (\boldsymbol{v} \cdot \nabla)\boldsymbol{v}\right] = (\nabla \cdot \boldsymbol{\sigma}) dxdydz \tag{2.3}$$

where $\boldsymbol{\sigma}$ is total stress tensor including the pressure and visocous components:

$$\boldsymbol{\sigma} = (-p\boldsymbol{I} + \boldsymbol{\tau}) \tag{2.4}$$

where p is pressure, $\boldsymbol{I}$ is identity matrix and $\boldsymbol{\tau}$ is a third-order viscous stress tensor. Two of its elements are shown below as an example:

$$\boldsymbol{\tau}_{xx} = \mu\Big(2\frac{\partial u}{\partial x} - \frac{2}{3}\nabla \cdot \boldsymbol{v}\Big) + \zeta \nabla \cdot \boldsymbol{v} \tag{2.5}$$

$$\boldsymbol{\tau}_{xy} = \mu\Big(\frac{\partial u}{\partial y} + \frac{\partial v}{\partial x}\Big) \tag{2.6}$$

where μ and ζ are the dynamic and bulk viscosity, respectively. Divided by $dxdydz$, Eqn (2.3) is reduced to:

$$\rho\Big[\frac{\partial \boldsymbol{v}}{\partial t} + (\boldsymbol{v} \cdot \nabla)\boldsymbol{v}\Big] = (\nabla \cdot \boldsymbol{\sigma}) \tag{2.7}$$

Inserting the constitutive equation (2.4) yields:

$$\rho\Big[\frac{\partial \boldsymbol{v}}{\partial t} + (\boldsymbol{v} \cdot \nabla)\boldsymbol{v}\Big] = (-\nabla p + \mu \nabla^2 \boldsymbol{v}) \tag{2.8}$$

The result is reached with the assumptions that the effects of viscosity gradient and compressibility of fluids are neglected. Such assumptions were also adopted by Rott, whose linear theory can provide a fairly good prediction of the exponential growth regime of thermoacoustic oscillations.

Conservation of Entropy

The infinitesimal change of entropy of a microscopic fluid parcel is expressed as the following:

$$d(\rho s)dxdydz = \Sigma \frac{dQ}{T} + \Sigma s dM + \rho (ds)_{\text{irrev}} dxdydz \tag{2.9}$$

where the three terms on the right hand side denote respectively: reversible entropy change due to the addition of heat dQ at temperature T, entropy change due to mass exchange, irreversible entropy increase due to effects like viscous loss. The third term, according to thermodynamic second law, shall be positive.

Divided by $dxdydzdt$ and with Green's theorem applied, Eqn. (2.9) becomes:

$$\frac{\partial(\rho s)}{\partial t} = \nabla \cdot \left(\frac{k\nabla T}{T}\right) - \nabla \cdot (\rho \boldsymbol{v} s) + \rho \frac{\partial s_{\text{irrev}}}{\partial t} \tag{2.10}$$

Recasting yields,

$$\rho T\left(\frac{\partial s}{\partial t} + \boldsymbol{v} \cdot \nabla s\right) = \nabla \cdot k\nabla T - k\frac{|\nabla T|^2}{T} + \rho T \frac{\partial s_{\text{irrev}}}{\partial t} \tag{2.11}$$

Through combining other conservation equations [45], the above equation can be converted to the well-known general heat transfer equation, i.e.:

$$\rho T\left(\frac{\partial s}{\partial t} + \boldsymbol{v}\nabla \cdot s\right) = \nabla \cdot k\nabla T + (\boldsymbol{\tau} \cdot \nabla) \cdot \boldsymbol{v} \tag{2.12}$$

2.2.2 Thermodynamics of Ideal Gas

The fluid-based TA devices typically use gases (air, helium, argon, etc.) as working medium and these gases can be modeled as ideal gas for simplicity while achieving satisfactory results.

Ideal gases are fluids which are governed by the following two fundamental thermodynamic relations:

$$p = \rho R_{\text{gas}} T \tag{2.13}$$

$$\epsilon = \frac{R_{\text{gas}} T}{\gamma - 1} \tag{2.14}$$

where ϵ is the internal energy per unit mass, R_{gas} is gas constant which varies for different gases but related to the universal gas constant $R_{\text{univ}} = 8.314\text{J/mol} \cdot \text{K}$ by molar mass $\mathcal{M}$ via the following relation:

$$R_{\text{gas}} = R_{\text{univ}}/\mathcal{M} \tag{2.15}$$

The constant γ is the ratio of specific heat, which is 1.667 and 1.4 for monoatomic and diatomic gases at ambient temperature. The values of γ and $\mathcal{M}$ are tabulated in Table (2.1). All other quantities related to the thermodynamic process can be independently expressed in terms of R_{gas} (or $\mathcal{M}$) and γ.

Equations (2.13) and (2.14) yield the expressions of the following quantities and relations:

Thermal expansion coefficient:

$$\beta \equiv -\frac{1}{\rho}\left(\frac{\partial \rho}{\partial T}\right)_p = \frac{1}{T} \tag{2.16}$$

Isothermal bulk modulus:

$$B_T = \rho\left(\frac{\partial p}{\partial \rho}\right)_T = p \tag{2.17}$$

The changes of p, T and ρ

$$dp = \rho R_{\text{gas}} dT + R_{\text{gas}} T d\rho \tag{2.18}$$

The changes of internal energy and temperature

$$d\epsilon = \frac{R_{\text{gas}}}{\gamma - 1} dT \tag{2.19}$$

First law of thermodynamics tells that of a unit mass, the increase in internal energy shall equal the heat absorbed distracted by the work done, i.e.:

$$d\epsilon = dq - dw \tag{2.20}$$

For an isentropic (reversible and adiabatic) process, $dq = 0$, so

$$(d\epsilon)_s = -dw \tag{2.21}$$

where the work done is the product of pressure and the volume of the unit mass, i.e.:

$$dw = pd\left(\frac{1}{\rho}\right) \tag{2.22}$$

As a result, in an isentropic process, $\frac{R_{\text{gas}}}{\gamma-1}dT + pd(\frac{1}{\rho}) = 0$, yielding:

$$dT = \frac{(\gamma-1)p}{R_{\text{gas}}\rho^2}d\rho \tag{2.23}$$

Plugging in Eqn.(2.18) yields:

$$dp = \gamma p d\rho \tag{2.24}$$

Hence, the isentropic bulk modulus is written as:

$$B_s = \rho\left(\frac{\partial p}{\partial \rho}\right)_s = \gamma p \tag{2.25}$$

The sound speed under isentropic conditions is:

$$a \equiv \sqrt{(\frac{\partial p}{\partial \rho})_s} = \sqrt{\gamma R_{\text{gas}} T} \tag{2.26}$$

The specific heat at constant volume and pressure are expressed as:

$$c_p = \gamma c_v = \frac{\gamma}{\gamma-1}R_{\text{gas}} \tag{2.27}$$

The change of entropy $ds = dq/T$ can be expressed according to first law of thermodynamics Eqn. (2.20) as:

$$ds = \frac{d\epsilon}{T} + \frac{dw}{T} = \frac{R_{\text{gas}}}{\gamma-1}\frac{dT}{T} - R_{\text{gas}}\frac{d\rho}{\rho} \tag{2.28}$$

Table 2.1. Gas constants and indices used in power law for $T_0 = 300K$ [6]

	m(kg/mol)	γ	μ_0(g/m·s)	k_0(W/m·K)	s_μ	s_k
air	0.02896	1.4	0.0185	0.026	0.76	0.89
nitrogen	0.02801	1.4	0.0182	0.026	0.69	0.75
helium	0.00400	1.667	0.0199	0.0152	0.68	0.72
neon	0.02018	1.667	0.0320	0.049	0.66	0.66
argon	0.03995	1.667	0.0230	0.018	0.85	0.84
xenon	0.1313	1.667	0.0240	0.0058	0.85	0.84

2.2.3 Material Properties

Unlike solids, fluid materials' properties are more sensitive to temperature variation. However, for a large range of temperature, both the viscosity and thermal conductivity of gases satisfy the power laws:

$$\mu = \mu_0 (T/T_0)^{s_\mu} \tag{2.29}$$

$$k = k_0 (T/T_0)^{s_k} \tag{2.30}$$

The constants are tabulated in Table (2.1) for common gases.

Other than the power law, other relations are also used to describe the dependence of material properties on temperature. For example, in the matieral library of the commercial FEM software, COMSOL Multyphysics, the fourth order polynomials are used and produce fairly close approximation compared to Eqns. (2.29-2.30) in a certain temperature range (Figs. (2.1)& (2.2)).

2.2.4 Assumptions of Linear Thermoacoustic Theory

In this section, the conservation laws presented in Section 2.2.1 are simplified with proper assumptions adapt to thermoacoustic calculations.

In low-amplitude pressure acoustics, the well-accepted harmonic assumption is expressed as $\mathcal{X}_1(\boldsymbol{r}, t) = \mathcal{X}_1(\boldsymbol{r})\mathrm{e}^{\mathrm{i}\omega t}$, where $\mathcal{X}_1(\boldsymbol{r}, t)$ is a dummy fluctuating variable at location $\boldsymbol{r}$. This

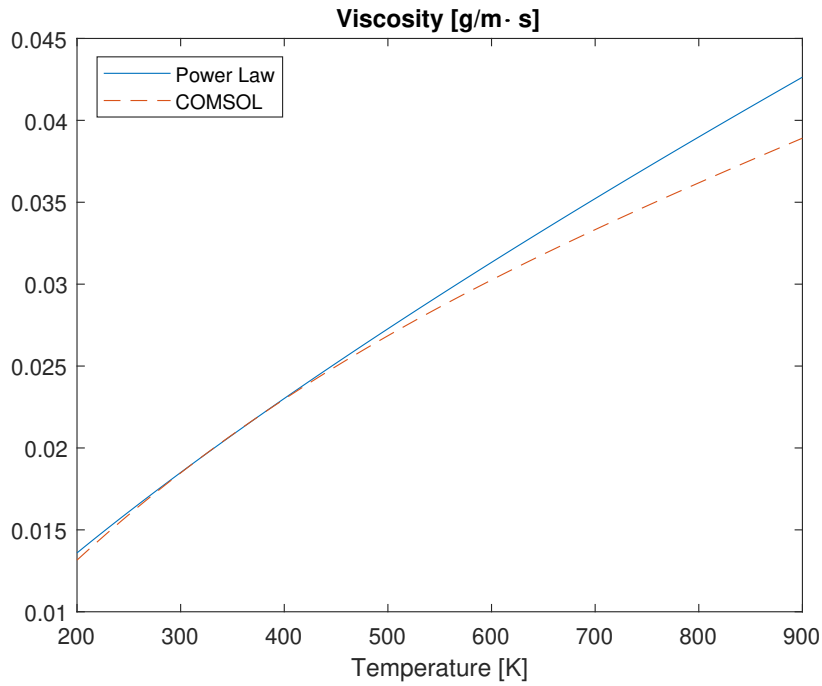

Figure 2.1. Viscosity vs. temperature for air

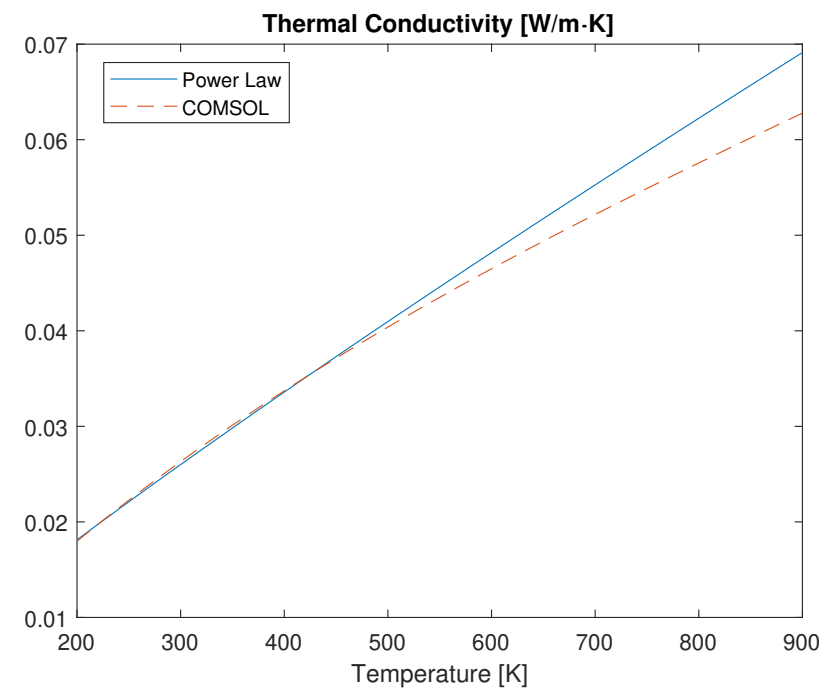

Figure 2.2. Thermal conductivity vs. temperature for air

assumption is also adopted in thermoacoustics, but some researchers prefer to use a complex frequency $\omega = \omega_r + \mathrm{i}\omega_\mathrm{i}$ to capture the transient exponential growth.

Linear assumptions are adopted as well, which allows to drop all terms higher than order one, e.g. the convective derivative in the momentum conservation, $(\boldsymbol{v} \cdot \nabla)\boldsymbol{v}$. It is emphasized that the convective derivatives are not always totally dropped because if there exist a mean temperature for instance, the convective derivative of entropy, $\boldsymbol{v} \cdot \nabla s$ still contains a linear component, which is essential for thermacoustic instability. The fact that the convective derivative of velocity can always be neglected (under linear assumption) is that velocity is assumed to have a zero mean, so the total quantity per se is a first order term.

Considering the large axial-to-transverse aspect ratio of thermoacoustic systems, the (zero-order) mean state component of variables are assumed to be functions of only axial coordinate, x. However, the zero-order components of pressure and velocity are assumed to be constants, i.e. P_0 and 0, respectively. Besides, the fluctuating pressure is assumed to be varying only in x direction, which is justified with an argument in the same way Prandtl used in his historic analysis of steady-flow boundary layers, which can be easily found in most fluid-mechanics textbooks [45], [47], [48]. Thus, the relevant variables are expressed as:

$$\rho(\boldsymbol{r}, t) = \rho_0(x) + \rho_1(\boldsymbol{r})\mathrm{e}^{\mathrm{i}\omega t} \tag{2.31}$$

$$T(\boldsymbol{r}, t) = T_0(x) + T_1(\boldsymbol{r})\mathrm{e}^{\mathrm{i}\omega t} \tag{2.32}$$

$$s(\boldsymbol{r}, t) = s_0(x) + s_1(\boldsymbol{r})\mathrm{e}^{\mathrm{i}\omega t} \tag{2.33}$$

$$p(\boldsymbol{r}, t) = P_0 + p_1(x)\mathrm{e}^{\mathrm{i}\omega t} \tag{2.34}$$

$$\boldsymbol{v}(\boldsymbol{r}, t) = \boldsymbol{v}_1(\boldsymbol{r})\mathrm{e}^{\mathrm{i}\omega t} \tag{2.35}$$

All the first order terms are assumed to be much smaller than the zero-order mean states, while the particle velocities are assumed to be much smaller than sound speed. It is also due to the geometric properties of thermoacoustic devices, the axial component of the velocity tensor is generally much greater than the other two components in y and z directions. This fact leads to the fluctuating pressure gradient in y and z much smaller than it in x, which can serve as another justification of keeping only the x dependence of p_1.

Additional simplifications can be justified solely in the case of narrow channels that, the derivatives of first-order quantities with respective to x can be neglected. That is due to the fact that in narrow tubes, $\partial/\partial x$ is of the order of $1/\lambda_w$, where λ_w is the wavelength, while the other two derivatives with respective to the transverse directions are of the order of the boundary layer thickness δ_k or δ_v. In practice, the conditions $\lambda_w \gg \delta_k$ and $\lambda_w \gg \delta_v$ can be easily achieved in thermoacoustic systems.

With the above assumptions explained, the conservation laws derived in the previous seciton can be easily recast into simpler forms. The continuity equation (Eqn. (2.53)) is converted into:

$$\mathrm{i}\omega\rho_1 + \frac{d\rho_m}{dx}u_1 + \rho_m \nabla \cdot \boldsymbol{v}_1 = 0 \tag{2.36}$$

The ideal gas law (Eqn. (2.13)) can be decomposed into zero-order and first-order expressions:

$$P_0 = \rho_0 R_{\text{gas}} T_0 \tag{2.37}$$

$$p_1 = \rho_0 R_{\text{gas}} T_1 + R_{\text{gas}} T_0 \rho_1 \tag{2.38}$$

where the first-order equation is more often written in the form of:

$$\frac{p_1}{P_0} = \frac{T_1}{T_0} + \frac{\rho_1}{\rho_0} \tag{2.39}$$

The entropy is then:

$$s_1 = -\frac{p_1}{\rho_0 T_0} + \frac{c_p T_1}{T_0} \tag{2.40}$$

Similarly, the axial component of the momentum conservation is recast into:

$$\mathrm{i}\omega\rho_0 u_1 = -\frac{dp}{dx} + \mu\left(\frac{\partial^2 u_1}{\partial^2 y} + \frac{\partial^2 u_1}{\partial^2 z}\right) \tag{2.41}$$

with the axial viscous diffusion and bulk viscosity ζ neglected.

The heat-transfer equation (Eqn. 2.2.1) is re-written as:

$$\rho_0 c_p \left(\mathrm{i}\omega T_1 + \frac{dT_0}{dx} u_1 \right) = \mathrm{i}\omega p_1 + k \left(\frac{\partial^2 T_1}{\partial^2 y} + \frac{\partial^2 T_1}{\partial^2 z} \right) \tag{2.42}$$

The relation in Eqn. (2.40) is used to get the above equation. The axial heat conduction is also neglected.

It is stressed that unlike conventional understanding of acoustics that acoustic waves are sinulsoidal both in time and in space, under the approximations adopted in this section, thermoacoustic waves can be harmonic in time, but not necessarily in space, mainly due to the existence of the convective derivatives as a result of a non-zero mean temperature gradient dT_0/dx.

2.2.5 Rott's Linear Theory

The conservation laws under thermoacoustic assumptions, i.e., Eqns. (2.36, 2.41 & 2.42) are further simplified by operating cross-sectional averaging to get rid of variables' transverse-direction dependency. Thus, the equations eventually become a set of quasi-one-dimensional (quasi-1D) equations. The derivations are shown in this section.

Considering the momentum equation (Eqn. (2.41)) as an ordinary differential equation (ODE) for $u_1(y, z)$, one can solve it with the non-slip ($u_1 = 0$) boundary conditions resolved. The solution is thus written as:

$$u_1 = \frac{\mathrm{i}}{\omega \rho_0} [1 - h_v(y, z)] \frac{dp_1}{dx} \tag{2.43}$$

where $h_v(y, z)$ is a complex function, which varies for channels of different geometry.

Applying cross-sectional averaging on Eqn. (2.43) yields the important thermoacoustic momentum equation:

$$\text{Thermoacoustic Momentum Equation}: \quad \mathrm{i}\omega (U_1/A) = -\frac{1 - f_v}{\rho_0} \frac{dp_1}{dx} \tag{2.44}$$

where U_1 is the flow rate, i.e. $U_1 = \int_A u_1 dA$ and A is cross-sectional area.

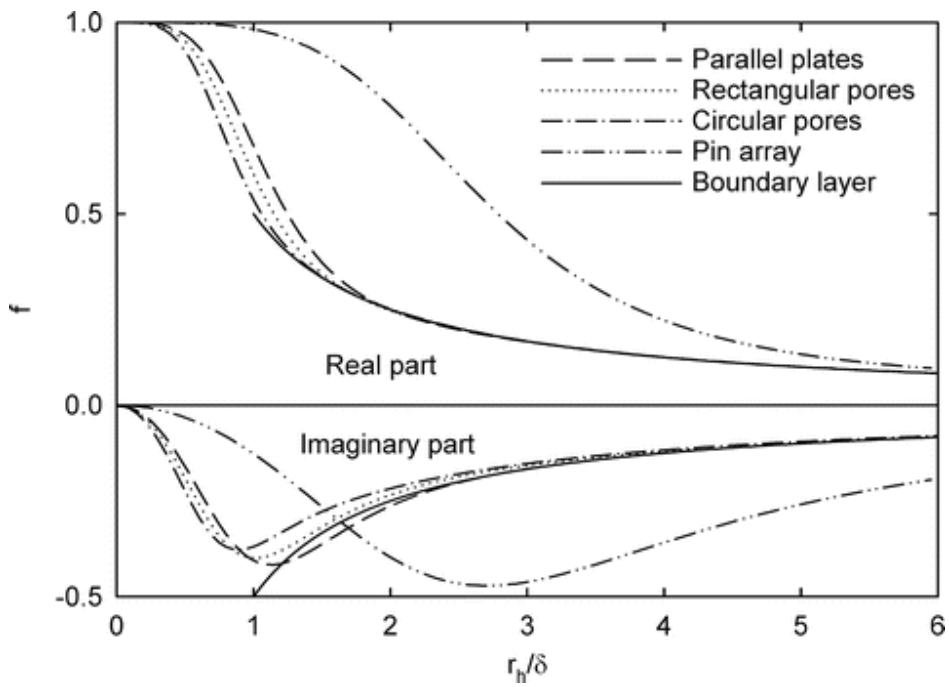

Figure 2.3. Cross-sectional-average function f for different geometries[6].

f_v in Eqn. (2.44) is the cross sectional integration of h_v, which is also a complex function. The one-dimensional Euler's equation in linear form can be recovered if $f_v = 0$. It can be also noticed that if f_v is purely real, the pressure gradient is totally inertial, which leads to no loss. However, if the imaginary part of f_v appears due to the existence of sound hard wall and gas viscosity, the pressure gradient includes a resistive component, which contributes to the change of velocity as well.

Same as h_v, f_v also varies with channel's cross-sectional geometry, Fig. 2.3 shows the thermo-viscos function f vs. dimensionless channel size for different pore geometry[6]. The viscous function f_v is yielded if r_h/δ_v is used for the horizontal axis, where r_h is the hydraulic radius. Alternatively, using r_h/δ_k for the horizontal axis yields f_k, which will be introduced

below. The complex functions for two commonly modeled geometry, parallel plates (2D model) and circular pore (2.5D model) are expressed as:

$$h = \frac{\cosh[(1+\mathrm{i})y/\delta]}{\cosh[(1+\mathrm{i})h/\delta]} \tag{2.45}$$

$$f = \frac{\tanh[(1+\mathrm{i})h/\delta]}{(1+\mathrm{i})h/\delta} \tag{2.46}$$

for parallel plates with spacing $2h$, and

$$h = \frac{J_0[(\mathrm{i}-1)r/\delta]}{J_0[(\mathrm{i}-1)R/\delta]} \tag{2.47}$$

$$f = \frac{2J_1[(\mathrm{i}-1)R/\delta]}{J_0[(\mathrm{i}-1)R/\delta](\mathrm{i}-1)R/\delta} \tag{2.48}$$

for circular pores with radius R, where J_n are Bessel's functions of the nth kind.

Note that the subscript v is neglected in the above expressions because such expressions also hold for thermal complex functions f_k of thermal boundary layer δ_k, which will be introduced in the next paragraph. And the two boundary layers are related by Prandtl number, Pr:

$$\delta_v = \sqrt{\mathrm{Pr}}\delta_k \tag{2.49}$$

Similarly, the heat equation (Eqn. (2.42)) can also be cross-sectionally averaged and gives:

$$\langle T_1 \rangle = \frac{1}{\rho_0 c_p}\frac{1-f_k}{p_1} - \frac{1}{\mathrm{i}\omega}\frac{dT_0}{dx}\frac{(1-f_k)-\mathrm{Pr}(1-f_v)}{(1-f_v)(1-\mathrm{Pr})}\left(\frac{U_1}{A}\right) \tag{2.50}$$

where the angle brackets denote cross-sectionally averaged quantities.

Now we have two equations (2.44) and (2.50) and three unknown variables T_1, p_1 and U_1, so the continuity equation (Eqn. (2.36)) shall be included. Averaging Eqn. (2.36) yields:

$$\mathrm{i}\omega\langle\rho_1\rangle + \frac{d}{dx}[\rho_0(U_1/A)] \tag{2.51}$$

The ideal gas law for first-order quantities, Eqn. (2.39) is used here to link $\langle\rho_1\rangle$ and $\langle T_1\rangle$. Averaging Eqn. (2.39) and eliminating $\langle\rho_1\rangle$ yields:

$$\mathrm{i}\omega\rho_0[\frac{p_1}{P_0} - \frac{\langle T_1\rangle}{T_0}] + \frac{d}{dx}[\rho_0(U_1/A)] = 0 \tag{2.52}$$

Combining Eqns. (2.50) and (2.52) to eliminate $\langle T_1\rangle$ yields the thermoacoustic version continuity equation:

$$\text{Thermoacoustic Continuity Equation:} \quad \mathrm{i}\omega p_1 = \frac{\gamma P_0}{1+(\gamma-1)f_k}\Big[-\frac{d}{dx}+g\Big]\Big(\frac{U_1}{A}\Big) \tag{2.53}$$

where g is a complex proportional constant for flow rate U_1 representing the gain or attenuation of the temperature gradient dT_0/dx, which is expressed as:

$$g = \frac{(f_k - f_v)}{(1-f_v)(1-\mathrm{Pr})}\frac{1}{T_0}\frac{dT_0}{dx} \tag{2.54}$$

Physical interpretations can be made by carefully examining Eqn. (2.53). The pressure rate is composed of two componetns, one proportional to dU_1/dx and the other proportional to dT_0/dxU_1. The first dependence is relatively easier to interpret with the understanding of adiabatic pressure acoustics. An adiabatic and lossless pressure wave equation can be recovered if both $f_k = 0$ and $f_v = 0$ hold, in which case the bulk modulus is the one defined in Eqn. (2.25). However, if the heat transfer is perfect, i.e. $f_k = 1$, the compressibility becomes P_0, which is the reciprocal of the isothermal bulk modulus expressed in Eqn. (2.17). To understand the second term on the right hand side, we isolate the effect of viscosity for now ($f_v = 0, \mathrm{Pr} = 0$), so it becomes $(f_k/T_0)(dT_0/dx)(U_1/A)$. This term vanishes in the following two cases. (1) $f_k = 0$. That means no wall heat transfer, so the temperature difference (if there is any) doesn't induce any energy exchange, but only affects the material properties instead. (2) $dT_0/dx = 0$. The zero axial temperature difference lead to zero net energy exchange per cycle. Instead, the instantaneous heat exchange (if there is any) can only happen in the progress of gas compression and dilatation. Pushing towards another limit when the gas is always at the local temperature ($f_k = 1$), leads to the second term proportional to $(dT_0/dx)U_1$. As a result, when a fluid parcel flow from cold to hot, it is

expanded. Otherwise, it is extracted. Thus, if the heat-transfer-induced deformation and the elastic deformation are well 'coordinated' so that they happen at 'right timing', the desired thermoacoustic instability can be potentially achieved. Although the limit cases described above help understanding the thermoaoucstic process, in practice, the situation always lies in the intermidiate regime.

Finally, by combining Eqns. (2.44) and (2.53) we arrive the complete expression of Rott's thermoacoutic wave equation:

$$\frac{\gamma P_0}{\omega^2}\frac{d}{dx}\left[\frac{1-f_v}{\rho_0}\frac{dp_1}{dx}\right]-\frac{a^2}{\omega^2}g\frac{dp_1}{dx}+[1+(\gamma-1)f_k]p_1=0 \tag{2.55}$$

It is a second-order ODE in pressure fluctuation. Swift considered it as a Rott's version of Helmholtz equation and 'a milstone in the devepoment of thermoacoustics'. Equantion (2.55) indeed marks a giant leap of the development of thermoacoustic theory, however for numerical calculations, the easiest way is to solve Eqns. (2.44) and (2.53) separately.

It is also notable that by carefully inspecting Eqns. (2.44) and (2.53), they can be viewed as an eigenvalue problem with the eigenvalue iω and eigenfunction $[p_1, U_1]^{\mathrm{T}}$, if the parameters are all knowns. The dependence of thermo-viscous functions f_k and f_v of ω can be iteratively resolved in the eigenvalue solving process. Therefore, under linear assumption, the steady state (reflected by a purely real ω) considered in the simulation software DeltaEC is not always achievable with arbitrary temperature gradient dT_0/dx. For a given dT_0/dx, there shall be a set of eigenvalues corresponding to different modes, and they are generally complex. The real part of the eigenvalue is the exponential growth/decay rate and the imaginary part is the angular natural frequency. The dT_0/dx corresponding to a purely imaginary eigenvalue is often called the onset temperature associated with that mode. An exponential growth predicted by the linear theory does not guarantee that a realistic unstable thermoacoustic wave can grow unbounded. The 'steady-state' oscillations seen in thermoacoustic devices or combustion systems are a nonlinear saturation effect which is not captured in linear theory. In reality, after the onset of thermoacoustic oscillations, the pressure reaches very high level rapidly and makes the nonlinear terms (e.g. the convective derivatives) become vital. In that

regime, the linear theory is no longer valid. Nonlinear thermoacoustic waves were formulated and numerically simulated in a different fashion, which are out of the scope of this thesis.

2.3 Basic Concepts of Thermoelasticity

Considering that the motivation of this thesis is to study the thermoacoustic behavior in solid media, it's necessary to revisit a few key concepts of the conventional thermoelastic theory to understand the coupling between elastic and thermal stress waves. This section derives the thermoelastic governing equations from conservation laws and paves the way to solid-state thermoacoustic theory.

When studying fluid mechanics, the velocity field is more often used as the basic variables, while in solid mechanics, equations are generally formulated in terms of particle displacements. This could induce certain notational confusions, although by carefully inspecting the equations, one can easily tell if a symbol u indicates displacement or velocity. To keep consistency, hereinafter, when discussing the fluid-based thermoacoustics, u, u_1, U_1, etc. are used for total particle, first-order particle and first-order volumetric velocity in axial direction. However when it's in the context of thermoelasticity or axial-mode solid-state thermoacoustics, u denotes particle displacement in the axial direction, and v particle velocity in the axial direction. Note that the bold $\boldsymbol{v}$ still denotes the velocity tensor.

The conservation laws written in the most general forms are adapt to any continuum, regardless that it's a fluid or a solid. These equations already derived in previous section are Eqns. (2.2), (2.7) &(2.11). To simplify them, assumptions adapt to solid dynamics are made through rewriting the equations.

2.3.1 Continuity Equation

In solids, the density variation over a large temperature range is quite small, compared to its static value. As a result, for a homogeneous and isotropic solid, the mean density ρ_0 is with zero spatial gradient. Equation (2.2) is then simplified as:

$$\frac{\partial \rho_1}{\partial t} + \rho_0 \nabla \cdot \boldsymbol{v} = 0 \tag{2.56}$$

Note that the nonlinear term $\rho_1 \nabla \cdot \boldsymbol{v}$ is neglected in the above equation. Unlike fluids, the constitutive relation of solids does not require the coupling between continuity and other two conservation equations, so the continuity equation is not often solved in solid mechanics. However, once the displacement (velocity) field is known, one can still use Eqn. (2.56) to recover the density variation.

2.3.2 Momentum Equation

To simplify the momentum equation (Eqn. (2.7)), the constitutive equation for solids is considered. The constitutive stress-strain relation for an isotropic solid considering the thermal expansion effect is written as:

$$\sigma_{\mathrm{ij}} = \lambda_L \delta_{\mathrm{ij}} \varepsilon_{kk} + \mu_L (\varepsilon_{\mathrm{ij}} + \varepsilon_{\mathrm{ji}}) - (3\lambda_L + 2\mu_L)\delta_{\mathrm{ij}} \alpha_l \Delta T \tag{2.57}$$

where $\mathrm{i}, \mathrm{j}, k = 1, 2, 3$, δ_{ij} is Kronecker delta, λ_L and μ_L are the Lamé constants, α_l is the linear thermal expansion coefficient. ΔT is the temperature difference deviated from a reference temperature, usually taken as the ambient temperature.

The normal stress in the axial direction x is the $\mathrm{ij} = 11$ component of Eqn. (2.57), written as:

$$\sigma_{11} = 2\mu_L \varepsilon_{11} + \lambda_L \mathrm{e} - (3\lambda_L + 2\mu_L)\delta_{\mathrm{ij}} \alpha_l \Delta T \tag{2.58}$$

where e is the volumetric strain, expressed as $\mathrm{e} = \varepsilon_{\mathrm{ii}}$. Considering the axial vibration of a slender rod, the normal stresses in transverse direction y and z are zero. Adding the $\mathrm{ij} = 22$ and $\mathrm{ij} = 33$ components of Eqn. (2.57) yields,

$$\mathrm{e} = \frac{\mu_L}{\lambda_L + \mu_L} \varepsilon_{11} + \frac{3\lambda_L + 2\mu_L}{\lambda_L + \mu_L} \alpha_l \Delta T \tag{2.59}$$

Plugging in Eqn.(2.58) yield,

$$\sigma_{11} = \mu_L \frac{3\lambda_L + 2\mu_L}{\lambda_L + \mu_L} (\varepsilon_{11} - \alpha_l \Delta T) \tag{2.60}$$

The proportional constant can be replaced by Young's modulus, i.e. $E = \mu\frac{3\omega+2\mu}{\omega+\mu}$, so the one dimensional thermoelastic consititutive relation, with the subscript dropped, is written as:

$$\sigma = E(\varepsilon - \alpha_l \Delta T) \tag{2.61}$$

Equation (2.61) can be inserted into Eqn. (2.7) to reach the ii = 11 component of momentum equations for solids:

$$\rho_0 \frac{\partial v}{\partial t} = E[\frac{\partial \varepsilon}{\partial x} - \alpha_l \frac{\partial(\Delta T)}{\partial x}] \tag{2.62}$$

Note that the nonlinear convective derivative is neglected agian with the same argument. Considering the total temperature $T(\boldsymbol{r}, t) = T_0 + T_1(\boldsymbol{r}, t)$, Eqn. (2.62) becomes:

$$\rho_0 \frac{\partial v}{\partial t} = E[\frac{\partial \varepsilon}{\partial x} - \alpha_l \frac{\partial T_1}{\partial x}] \tag{2.63}$$

2.3.3 Heat Transfer Equation

Same as the heat transfer equation for fluids, the counterpart for solids is also derived from first law of thermodynamics and entropy conservation. However the derivations are also tedious, as the case in fluids. Therefore, in this section, only a few key steps are provided as a hand-waving proof. The rigorous derivations can be found in classical thermoelasticity textbooks [41]–[43] or seminal paper in thermodynamics of thermoelasticity like Biot (1956) [49].

According to Biot, the entropy variation per unit mass is defined as:

$$s_1 = c_\varepsilon \frac{T_1}{T} + \frac{3\lambda_L + 2\mu_L}{\rho} \alpha_l \mathrm{e} \tag{2.64}$$

where c_ε is the specific heat at constant strain per unit mass.

In classical thermoelasticity, the convective derivative of entropy is not considered because in most of problems where thermoelasticity is involved, (1) a uniform mean temperature distribution is generally considered and (2) the heat transfer across the solid boundaries affects

the system very little, which is analogous to the configuration of $f_k = 0$ in thermoacoustics. With the convective derivative neglected, Eqn. (2.11) is rewritten as:

$$\rho T \frac{\partial s}{\partial t} = \nabla \cdot k \nabla T - k \frac{|\nabla T|^2}{T} + \rho T \frac{\partial s_{\text{irrev}}}{\partial t} \tag{2.65}$$

The last two terms are treated in the same fashion as in thermoacoustics; and the heat equation with coupling term is eventually expressed as:

$$\rho c_\varepsilon \frac{\partial T}{\partial t} + T(3\lambda_L + 2\mu_L)\alpha_l \frac{\partial \mathrm{e}}{\partial t} = \nabla \cdot k \nabla T \tag{2.66}$$

Applying Eqn. (2.59), the second term of Eqn. (2.66) becomes

$$T(3\lambda_L + 2\mu_L)\frac{\partial \mathrm{e}}{\partial t} = \alpha_l E T \Big(\frac{\partial \varepsilon}{\partial t} + \frac{3\lambda_L + 2\mu_L}{\mu_L} \alpha_l \frac{\partial \Delta T}{\partial t} \Big) \tag{2.67}$$

Considering the total temperature $T(t) = T_0 + T_1(t)$, Eqn. (2.66) becomes:

$$\Big[\rho c_\varepsilon + \alpha_l^2 E \frac{3\lambda_L + 2\mu_L}{\mu_L} T \Big] \frac{\partial T}{\partial t} + \alpha_l E T \frac{\partial \varepsilon}{\partial t} = \nabla \cdot k \nabla T \tag{2.68}$$

For most of solid materials, especially metallic materials analyzed in this thesis, the second term in the bracket ($\sim 10^3$[J/m^3 K]) is much smaller than the first term ($\sim 10^6$[J/m^3 K]). With that term neglected and linearizing the equation yields:

$$\rho_0 c_\varepsilon \frac{\partial T_1}{\partial t} + \alpha_l E T_0 \frac{\partial \varepsilon}{\partial t} = \nabla \cdot k \nabla T_1 \tag{2.69}$$

Equations (2.63) and (2.69) are the two fundamental coupled equations governing the longitudinal dynamics of a slender rod.

2.4 Concluding Remarks

This chapter reviews the derivation of Rott's linear thermoacoustic theory from conservation laws and the thermodynamics of ideal gas. The assumptions adopted by Rott are

revisited to justify the associated simplifications. Rott's linear governing equations are revealed, which not only improve the qualitative understanding of thermoacoustic processes, but also enable the quantitative calculations, especially if the equations are recast in the form of an eigenvalue problem. Theory of thermoelasticity is also revisited because the main structure of SSTA theory is born out of thermoelastic theory.

In short, the review of fundamental theories conducted in this chapter lays the foundation for the development of SSTA theory and all the analyses throughout this thesis.

3. SOLID-STATE THERMOACOUSTICS THEORY

3.1 Introduction

The fundamental understanding of Rott's thermoacoustic theory and thermoelasticity theory provides the foundation for the development of the theory of solid-state thermoacoustics. This theory allows quantitatively predicting the unstable motion in solid media as a result of thermo-elastic/acoustic coupling.

Different from thermoacoustic waves in fluids, the thermoacoustic waves in solids can sustain multiple modes. This is a characterisitc inhereted by the well-known wave polarization of solids. For slender structures, the main emphasis of this thesis, attention is taken to the axial-mode and flexural-mode thermoacoustic waves. In particular, the axial-mode TA waves in solid rods resemble the TA waves in fluids, in that the direction of wave propagation is parallel to the direction of particle oscillation. However, the flexural-mode TA wave is unique to solids, where the direction of particle displacement is perpendicular to the direction of wave propagation.

In this chapter, the theory of axial-mode solid-state thermoacoustics is derived based on the conservation laws of solids, where as the derivation for flexural-mode solid-state thermoacoustics originates from Euler-Bernoulli beam assumptions.

3.2 Axial-Mode Solid-State Thermoacoustics (A-SSTA)

Inspired by Rott's theory, the linear theory of axial-mode solid-state thermoacoustics is established in this section, which serves as the theoretical foundation for all relevant results and analyses that will be demonstrated in Chapters 4 and 5 .

3.2.1 Assumptions

Other than the general assumptions adopted by thermoelasticity, which are mentioned above, the following assumptions are also important to achieve the final governing equations of A-SSTAs:

1. Linear approximation: Terms higher than or equal to second order are neglected.

2. The structure should have a large axial-to-transverse aspect ratio so that the 1D approximation is acceptable.

3. The wavelength is much greater than the boundary layer size. This condition is easily met in 1D systems, but it allows to drop the axial diffusion term in heat equation, which greatly simplifies the modeling.

4. The mean temperature T_0 is only a function of axial coordinate, i.e. $T_0 = T_0(x)$.

5. The displacement and velocity are assumed to be constant across the transverse direction, while the temperature fluctuation T_1 does have full dependence on 3D coordinates. i.e. $u = u(x), v = v(x)$ and $T_1 = T_1(x, y, z)$. Note that in fluid-based thermoacoustics, the velocity varies in the cross-section, due to the wall shear effects. However, in solids, it's the Poisson effect that happens in the transverse direction which does not deform the cross-sectional distribution of axial displacement. However, no viscosity in solids does not mean zero dissipation. The dissipative mechanism in solids are more complex. Its effects are discussed in the following chapters.

With the above approximations, the governing equations of 1D A-SSTA are derived based on thermoelasticiy equations.

3.2.2 Momentum and Heat Equations

The momentum equation (Eqn. (2.63)) is re-written in terms of displacement:

$$\rho_0 \frac{\partial^2 u}{\partial^2 t} = E\left[\frac{\partial^2 u}{\partial^2 x} - \alpha_l \frac{\partial T_1}{\partial x}\right] \tag{3.1}$$

To capture the heat transport due to the mutual effect of wall heat transfer and axial motion, the convective derivatives are included in the temperature derivative. The axial thermal conduction is neglected, which is justified by Assumption 3. Equation (2.69) then becomes:

$$\rho_0 c_\varepsilon \left(\frac{\partial T_1}{\partial t} + v\frac{dT_0}{dx}\right) + \alpha_l E T_0 \frac{\partial \varepsilon}{\partial t} = k\left(\frac{\partial^2 T_1}{\partial^2 y} + \frac{\partial^2 T_1}{\partial^2 z}\right) \tag{3.2}$$

3.2.3 A-SSTA Equations: An Eigenvalue Problem

Under harmonic assumptions $\mathcal{Y}_1(\boldsymbol{r},t) = \hat{\mathcal{Y}}(\boldsymbol{r})\mathrm{e}^{\mathrm{i}\omega t}$, where $\mathcal{Y}_1$ and $\hat{\mathcal{Y}}$ are a dummy fluctuating variable in time and Fourier domain, Eqns. (3.1) and (3.2) can be converted into:

$$-\omega^2\rho_0\hat{u} = E\left[\frac{\partial^2\hat{u}}{\partial^2 x} - \alpha_l\frac{\partial\hat{T}}{\partial x}\right] \tag{3.3}$$

$$\rho_0 c_\varepsilon\left(\mathrm{i}\omega\hat{T} + \hat{v}\frac{dT_0}{dx}\right) + \alpha_l E T_0\frac{\partial\hat{v}}{\partial x} = k\left(\frac{\partial^2\hat{T}}{\partial^2 y} + \frac{\partial^2\hat{T}}{\partial^2 z}\right) \tag{3.4}$$

The relation $\partial\varepsilon/\partial t = \partial v/\partial x$ is used. Note that as the case in fluid-based thermoacoustics, the frequency ω can be complex valued. To transform the above equations into an eigenvalue problem, an intermediate relation $v = \partial u/\partial t$ is used, which yields:

$$\mathrm{i}\omega\hat{u} = \hat{v} \tag{3.5}$$

$$\mathrm{i}\omega\hat{v} = \frac{E}{\rho_0}\left(\frac{d^2\hat{u}}{dx^2} - \alpha_l\frac{d\hat{T}}{dx}\right) \tag{3.6}$$

$$\mathrm{i}\omega\hat{T} = -\frac{dT_0}{dx}\hat{v} - \gamma_G T_0\frac{d\hat{v}}{dx} + \kappa\left(\frac{\partial^2\hat{T}}{\partial^2 y} + \frac{\partial^2\hat{T}}{\partial^2 z}\right) \tag{3.7}$$

where $\gamma_G = (\alpha_l E)/(\rho_0 c_\varepsilon)$ is Grüneisen constant, $\kappa = k/(\rho_0 c_\varepsilon)$ is thermal diffusivity.

Inspired by Rott's theory, cross-sectional averaging is applied to Eqns. (3.6) and (3.7), yielding

$$\mathrm{i}\omega\hat{v} = \frac{E}{\rho_0}\left(\frac{d^2\hat{u}}{dx^2} - \alpha_l\frac{d\langle\hat{T}\rangle}{dx}\right) \tag{3.8}$$

$$\mathrm{i}\omega\langle\hat{T}\rangle = -\frac{dT_0}{dx}\hat{v} - \gamma_G T_0\frac{d\hat{v}}{dx} + \mathrm{i}\omega g_k\langle\hat{T}\rangle \tag{3.9}$$

Similarly, g_k is also a complex function denoting the strength of transverse heat transfer. It varies with different rod cross-sectional geometry. Through this thesis, the rod is assumed to be a cylindrical one. The expression of the corresponding g_k is derived in the following.

For a circular cross-section rod, Eqn. 3.7 becomes:

$$\mathrm{i}\omega\hat{T} = -\frac{dT_0}{dx}\hat{v} - \gamma_G T_0 \frac{d\hat{v}}{dx} + \kappa \frac{1}{r}\frac{\partial}{\partial r}\left(r\frac{\partial \hat{T}}{\partial r}\right) \tag{3.10}$$

where r is the radial coordinate.

In order to find a solution to the energy equation, a coordinate transformation is performed:

$$\xi = \sqrt{-2\mathrm{i}}\frac{r}{\delta_k} \tag{3.11}$$

where the thermal penetration thickness δ_k is defined as:

$$\delta_k = \sqrt{\frac{2\kappa}{\omega}}. \tag{3.12}$$

The energy equation in the transformed coordinate becomes:

$$\xi^2\frac{\partial^2\tilde{T}}{\partial\xi^2} + \xi\frac{\partial\tilde{T}}{\partial\xi} + \xi^2\tilde{T} = 0 \tag{3.13}$$

where

$$\tilde{T} = -\frac{\hat{T}}{[\hat{u}(dT_0/dx) + \gamma_G T_0(d\hat{u}/dx)]} - 1 \tag{3.14}$$

The general solution to Eqn. (3.13) is:

$$\tilde{T}(\xi) = \mathcal{A}J_0(\xi) + \mathcal{B}Y_0(\xi) \tag{3.15}$$

where $\mathcal{A}$ and $\mathcal{B}$ are constants of integration determined by imposing the boundary conditions, $J_0(\cdot)$ and $Y_0(\cdot)$ are Bessel functions of the first and second kind, respectively. On the axis of the rod, the temperature fluctuation is bounded, and considering that $Y_0(0) = \infty$ then it must be $\mathcal{B} = 0$. At the boundaries, the isothermal boundary condition enforces $\hat{T}(R) = 0$,

so $\tilde{T}(\xi_{\text{top}}) = -1$, where $\xi_{\text{top}} = \sqrt{-2\text{i}}(R/\delta_k)$. Substituting the constants in Eqn. (3.15), we find $\tilde{T} = -J_0(\xi)/J_0(\xi_{\text{top}})$. It follows that:

$$\hat{T} = -\left(\hat{u}\frac{dT_0}{dx} + \gamma_G T_0 \frac{d\hat{u}}{dx}\right)\left(1 - \frac{J_0(\xi)}{J_0(\xi_{\text{top}})}\right) \tag{3.16}$$

By averaging Eqns. (3.16) over the cross section and substituting into Eqn. (3.10) and comparing to Eqn. (3.9), the complex thermo-conductive function g_k is expressed as

$$g_k = \left[1 - \frac{1}{2}\xi_{\text{top}}\frac{J_0(\xi_{\text{top}})}{J_1(\xi_{\text{top}})}\right]^{-1} \tag{3.17}$$

g_k for other cross-section geometry can also be derived following the similar fashion. With the g_k function well defined, Eqns. (3.5), (3.6) and (3.9) form a complete eigenvalue problem with eigenvalue iω and eigenfunctions $[\hat{u}, \hat{v}, \langle\hat{T}\rangle]^{\text{T}}$. These three equations can be further combined to arrive a second-order ODE with respect to $\hat{u}$ by canceling other two variables. The A-SSTA wave equation is written as:

$$\left[1 + \frac{\alpha_l \gamma_G}{1 - g_k} T_0\right]\frac{d^2\hat{u}}{dx^2} + \frac{\alpha_l(1+\gamma_G)}{1-g_k}\frac{dT_0}{dx}\frac{d\hat{u}}{dx} + \omega^2\hat{u} = 0 \tag{3.18}$$

In practice, Eqns. (3.5), (3.8) and (3.9) are solved separately in numerical calculations. However, Eqn. (3.18) is also analytically solvable under certain circumstances, thanks to the insensitivity of solid material properties to temperature, which allows all the coefficients to be extracted from the spatial derivatives. A nondimensional form of Eqn. (3.18) is proposed in Chapter 5. The variable $\hat{u}$ can be written as an analytical infinite series. The solutions, although not amenable to closed form, provide valuable information on the form of mode shapes, and lay the foundation for the dimensionless parametric study.

3.3 Flexural-Mode Solid-State Thermoacoustics (F-SSTA)

The unstable flexural motion considered in this study is subject to a thin layer Euler-Bernoulli beam. The slender beam's transverse oscillation is within long wavelength limit, so the displacement over the cross section is assumed to be uniform.

An infinitesimal element in the beam of arbitrary cross section geometry satisfies force balance in the transverse direction, i.e.:

$$\rho A \frac{\partial^2 v}{\partial t^2} = \frac{\partial Q}{\partial x} \tag{3.19}$$

where A is total area of beam cross section, v is transverse displacement, ρ is effective density, expressed as:

$$\rho = \frac{\int_A \rho_l dA}{\int_A dA} \tag{3.20}$$

ρ_l is the local density at an arbitrary point on the cross section. Q is shear force:

$$Q = \frac{\partial M}{\partial x} \tag{3.21}$$

which is related to moment M by:

$$M = \int \sigma y dA \tag{3.22}$$

where σ is axial stress defined as:

$$\sigma = E(\varepsilon - \alpha_l T) \tag{3.23}$$

The strain in thin beams is expressed as:

$$\varepsilon = -y \frac{\partial^2 v}{\partial x^2} \tag{3.24}$$

Hence, the stress-strain relation and the heat transfer equation in this case are written as:

$$\sigma = E\Big(- y \frac{\partial^2 v}{\partial x^2} - \alpha_l T \Big) \tag{3.25}$$

$$\rho_0 c_\varepsilon \Big(\frac{\partial T}{\partial t} \Big) - \alpha_l E T_0 y \frac{\partial^3 v}{\partial x^2 \partial t} = k \Big(\frac{\partial^2 T}{\partial^2 x} + \frac{\partial^2 T}{\partial^2 y} + \frac{\partial^2 T}{\partial^2 z} \Big) \tag{3.26}$$

Equations (3.20) and (3.26) are the simplest form for an Euler-Bernoulli beam without specification of the cross-section geometry. In Chapter 6, a bimetallic beam is considered, where further simplification of equations is conducted. With proper application of thermal coupling, the bimetallic beam can become unstable. This thermally-induced flexural-mode instability of a bilayer beam is called flexural-mode solid-state thermoacoustics in this study.

3.4 Concluding Remarks

Based on Rott's thermoacoustic theory and theory of thermal elasticity, the mathematical formulation of both axial-mode and flexural-mode thermoacoustics is proposed. In axial-mode solid-state thermoacoustics, the convective derivative of temperature in heat equation is retained to capture the transverse heat transfer happening in the region with temperature gradient. The governing equations can be formulated either as an eigenvalue problem for easier numerical calculation or as a second-order ODE with respect to particle displacement to pursue analytical solutions. Governing equations of flexural-mode solid-state thermoacoustics are also derived in the last part of this chapter.

In short, the derivation of theories conducted in this chapter lays the theoretical foundation for all the analyses throughout this thesis.

4. NUMERICAL STUDY OF A-SSTA

4.1 Introduction

With the theory of A-SSTA established in Chapter 3, numerical evidence of the existence of this phenomenon in solid media is provided in this chapter. In particular, we show that a solid metal rod, with finitely straight or infinitely looped topology, subject to a prescribed temperature gradient on its outer boundary can undergo self-sustained vibrations driven by a thermoacoustic instability phenomenon. Besides, it is anticipated that, although the fundamental physical mechanism resembles the thermoacoustic of fluids, the different nature of sound and heat propagation in solids produces noticeable differences in the theoretical formulations and in the practical implementations of the phenomenon.

4.2 A-SSTA in a Fixed-Mass Rod Device

The fundamental system under investigation consists of a slender solid metal rod with circular cross section (Fig. 4.1). The rod is subject to a temperature (spatial) gradient applied on its outer surface at a prescribed location, while the remaining sections have adiabatic boundary conditions. We investigate the coupled thermoacoustic response that ensues as a result of an externally applied thermal gradient and of an initial mechanical perturbation of the rod.

We anticipate that the fundamental dynamic response of the rod is governed by the laws of thermoelasticity. According to classical thermoelasticity [41]–[43], an elastic wave traveling through a solid medium is accompanied by a thermal wave, and viceversa. The thermal wave follows from the thermoelastic coupling which produces local temperature fluctuations (around an average constant temperature T_0) as a result of a propagating stress wave. When the elastic wave is not actively sustained by an external mechanical source, it attenuates and disappears over a few wavelengths due to the presence of dissipative mechanisms (such as, material damping); in this case the system has a positive decay rate (or, equivalently, a negative growth rate). In the ideal case of an undamped thermoelastic system, the mechanical wave does not attenuate but, nevertheless, it maintains bounded amplitude. In such

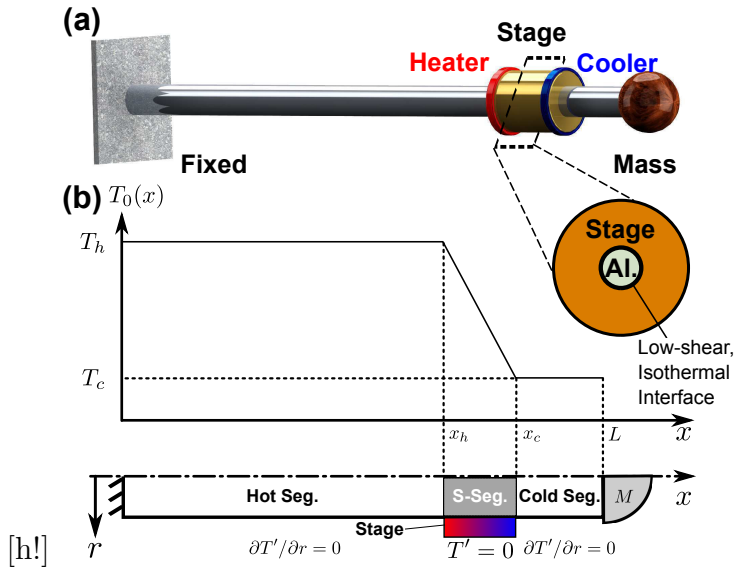

[h!]

Figure 4.1. (a) Notional schematic of the system exhibiting thermoacoustic response. An aluminum rod with circular cross-section under fixed-free boundary conditions. The free end carries a concentrated mass used to tune the frequency of the longitudinal resonance and the corresponding wavelength. A section of the rod is surrounded by a large thermal inertia (represented by a highly-thermally-conductive solid) on which a heater and a cooler are connected in order to create a predefined thermal gradient; this component is referred to as a stage. The stage is the equivalent of the stack in classical thermoacoustic setups. The ideal interface between the stage and the rod should be isothermal and capable of negligible shear force (see inset). Heat insulating material (not showed) is assumed to be placed around the rod to reduce radiative heat losses and therefore approximate adiabatic boundary conditions. (b) (top) idealized reference temperature profile $T_0(x)$ produced along the rod, and (bottom) schematic of an axi-symmetric cross section of the rod showing the characteristic geometric parameters and the correspondence to the temperature profile. Three relevant segments are identified: 1) S-segment, 2) hot segment, 3) cold segment. These three segments correspond to the isothermal and the two adiabatic boundary conditions, respectively.

situation, the total energy of the system is conserved (energy is continuously exchanged between the thermal and mechanical waves) and the stress wave exhibits a zero decay rate (or, equivalently, a zero growth rate).

Contrarily to the classical thermoelastic problem where the medium is at a uniform reference temperature T_0 with an adiabatic outer boundary, when the rod is subject to heat transfer through its boundary (i.e. non-adiabatic conditions) the thermoelastic response can

become unstable. In particular, when a proper temperature spatial gradient is enforced on the outer boundary of the rod then the initial mechanical perturbation can grow unbounded due to the coupling between the mechanical and the thermal response. This last case is the exact counterpart that leads to thermoacoustic response in fluids, and it is the specific condition analyzed in this study. For the sake of clarity, we will refer to this case, which admits unstable solutions, as the thermoacoustic response of the solid (in order to differentiate it from the classical thermoelastic response).

4.2.1 Linear Stability Analysis

Equations (3.5), (3.6) and (3.7) form an eigenvalue problem. However, to perform linear stability analysis, we assume the eigenvalue as a complex-valued quantity, $\mathrm{i}\Lambda = \beta + \mathrm{i}\omega$ to capture both the real angular frequency and the growth rate, while the frequency-dependent coefficient $\mathrm{i}\omega g_k(x)$ is kept as a function of only the real part of the complex frequency, considering the fact that $\beta/\omega \ll 1$. In this regard, Equations (3.5), (3.6) and (3.7) are rewritten as:

$$\mathrm{i}\Lambda\hat{u} = \hat{v} \tag{4.1}$$

$$\mathrm{i}\Lambda\hat{v} = \frac{E}{\rho}\left(\frac{d^2\hat{u}}{dx^2} - \alpha_l\frac{d\langle\hat{T}\rangle}{dx}\right) \tag{4.2}$$

$$\mathrm{i}\Lambda\langle\hat{T}\rangle = -\frac{dT_0}{dx}\hat{v} - \gamma_G T_0\frac{d\hat{v}}{dx} + \mathrm{i}\omega g_k(x)\langle\hat{T}\rangle \tag{4.3}$$

Note that the complex function $g_k(x)$ is only non-zero, expressed in Eqn. (3.17), in the S-segment where the transverse heat transfer happens. It is zero elsewhere.

The one-dimensional model was used to perform a stability eigenvalue analysis. The eigenvalue problem is given by $(\mathrm{i}\Lambda\mathbf{I} - \mathbf{A})\mathbf{y} = \mathbf{0}$ where $\mathbf{I}$ is the identity matrix, $\mathbf{A}$ is a matrix of coefficients, 0 is the null vector, and $\mathbf{y} = [\hat{\mathbf{u}}; \hat{\mathbf{v}}; \langle\hat{\mathbf{T}}\rangle]$ is the vector of state variables where $\hat{\mathbf{u}}, \hat{\mathbf{v}}$, and $\langle\hat{\mathbf{T}}\rangle$ are the particle displacement, particle velocity, and cross-sectionally averaged temperature fluctuation eigenfunctions.

The eigenvalue problem was solved numerically for the case of an aluminum rod having a length of $L = 1.8$m and a radius $R = 2.38$mm. The following material parameters

were used: density $\rho = 2700\text{kg/m}^3$, Young's modulus $E = 70\text{GPa}$, thermal conductivity $\kappa = 238\text{W/(m}\cdot\text{ K)}$, specific heat at constant strain $c_\epsilon = 900\text{J/(kg}\cdot\text{ K)}$, and thermal expansion coefficient $\alpha = 23 \times 10^{(-6)}\text{K}^{-1}$. The strength of the instability in classical thermoacoustics (often quantified in terms of the ratio β/ω) depends, among the many parameters, on the location of the thermal gradient. This location is also function of the wavelength of the acoustic mode that triggers the instability, and therefore of the specific (mechanical) boundary conditions. We studied two different cases: 1) fixed-free and 2) fixed-mass. In the fixed-free boundary condition case, the optimal location of the stage was approximately around 1/2 of the total length of the rod, which is consistent with the design guidelines from classical thermoacoustics. Considerations on the optimal design and location of the stage/stack will be addressed in the following section; at this point we assumed a stage located at $x = 0.5L$ with a total length of $0.05L$.

Assuming a mean temperature profile equal to $T_h = 493.15\text{K}$ in the hot part and to $T_c = 293.15\text{K}$ in the cold part, the 1D theory returned the fundamental eigenvalue to be $\text{i}\Lambda = 0.404 + \text{i}4478(\text{rad/s})$. The existence of a positive real component of the eigenvalue revealed that the system was unstable and self-amplifying, that is it could undergo growing oscillations as a result of the positive growth rate β. The growth ratio was found to be $\beta/\omega = 9.0 \times 10{-}5$.

Equivalently, we analyzed the second case with fixed-mass boundary conditions. In this case, a $2kg$ tip mass was attached to the free end with the intent of tuning the resonance frequency of the rod and increasing the growth ratio β/ω which controls the rate of amplification of the system oscillations. An additional advantage of this configuration is that the operating wavelength increases. To analyze this specific boundary condition configuration, we chose $x_h = 0.9L$ and $x_c - x_h = 0.05L$. The stability analysis returned the first eigenvalue as $\text{i}\Lambda = 0.210 + \text{i}585.5(\text{rad/s})$ resulting in a growth ratio $\beta/\omega = 3.6 \times 10^{-4}$, larger than the fixed-free case.

The above results from the quasi-1D thermoacoustic theory provided a first important conclusion of this chapter, that is confirming the existence of thermoacoustic instabilities in solids as well as their conceptual affinity with the analogous phenomenon in fluids.

To get a deeper physical insight into this phenomenon, we studied the themodynamic cycle of a particle located in the S-region. The mechanical work transfer rate or, equivalently, the volume-change work per unit volume may be defined as $\dot{w} = -\sigma\frac{\partial\varepsilon}{\partial t}$ [50], where σ and ε are the total axial stress (i.e. including both mechanical and thermal components) and strain, respectively. During one acoustic/elastic cycle, the time averaged work transfer rate per unit volume is $\langle\dot{w}\rangle = \frac{1}{\tau}\int_0^\tau(-\sigma)\frac{\partial\varepsilon}{\partial t}dt = \frac{1}{\tau}\int_0^\tau(-\sigma)d\varepsilon = \frac{1}{\tau}\int_0^\tau\bar{\sigma}d\varepsilon$, where τ is the period of a cycle, and $\bar{\sigma} = (-\sigma)$. Figure 4.2a shows the $\bar{\sigma}$-ε diagram where the area enclosed in the curve represents the work per unit volume done by the infinitesimal volume element in one cycle. All the particles located in the regions outside the S-segment do not do net work because the temperature fluctuation T' is in phase with the strain ε, which ultimately keeps the stress and strain in phase (thus, the area enclosed is zero). Figure 4.2b shows the time-averaged work $\langle\dot{w}\rangle = \frac{1}{2}Re[\hat{\bar{\sigma}}(\mathrm{i}\omega\hat{\varepsilon})^*]$ along the rod, where $()^*$ denotes the complex conjugate. Note that the rate of work $\langle\dot{w}\rangle$ was evaluated based on modal stresses and strains, therefore its value must be interpreted on an arbitrary scale. The large increase of $\langle\dot{w}\rangle$ at the stage location indicates that a non-zero net work is only done in the section where the temperature gradient is applied (and therefore where heat transfer through the boundary takes place).

Figure 4.2c shows a schematic representation of the thermo-mechanical process taking place over an entire vibration cycle. When the infinitesimal volume element is compressed, it is displaced along the x direction while its temperature increases (step 1). As the element reaches a new location, heat transfer takes place between the element and its environment. Assuming that in this new position the element temperature is lower than the surrounding temperature, then the environment provides heat to the element causing its expansion. In this case, the element does net work dW (step 2) due to volume change. Similarly, when the element expands (step 3), the process repeats analogously with the element moving backwards towards the opposite extreme where it encounters surrounding areas at lower temperature so that heat is now extracted from the particle (and provided to the stage). In this case, work dW' is done on the element due to its contraction (step 4). The net work generated during one cycle is $dW - dW'$.

4.2.2 Time-Dependent Analysis

In order to validate the quasi-1D theory and to estimate the possible impact of three-dimensional and nonlinear effects, we solved the full set of thermoelasticity governing equations in the time domain. The equations were solved by finite element method on a three-dimensional geometry using the commercial software COMSOL Multiphysics. We highlight that with respect to the momentume equation, we drop the nonlinear convective derivative $v_{\mathrm{i}}\frac{\partial v_{\mathrm{i}}}{\partial x_{\mathrm{i}}}$ which effectively results in the linearization of the momentum equation. Full nonlinear terms are instead retained in the energy equation.

To facilitate the COMSOL analysis, given the largely disparate time scales involved in the wave propagation and heat diffusion processes, we first solved a static problem to calculate the elastic deformation induced by the thermal boundary conditions and to achieve the steady state mean temperature distribution inside the rod. These elastic and thermal equilibrium states where imposed as initial conditions when solving the time-dependent response. In order to reduce the effect of the initial transient we also included in the initial conditions the particle displacement field associated with the eigenfunction at the given excitation frequency (and obtained from the quasi-1D eigenvalue analysis). The linear temperature profile T_0 was imposed as an isothermal boundary condition on the outer surface of the rod.

Figure 4.2d shows the time history of the axial displacement fluctuation u at the free end of the rod. The dominant frequency of the oscillation is found, by Fourier transform, to be equal to $\omega = 583.1(\mathrm{rad/s})$, which is within 0.4% from the prediction of the 1D theory. The time response is evidently growing in time therefore showing clear signs of instability. The growth rate was estimated by either a logarithmic increment approach or an exponential fit on the envelope of the response. The logarithmic increment approach returns β as:

$$\beta = \frac{1}{N-1}\sum_{\mathrm{i}=2}^{N} \ln\frac{A_{\mathrm{i}}}{A_1}/(t_{\mathrm{i}} - t_1) \tag{4.4}$$

where A_1 and A_{i} are the amplitudes of the response at the time instant t_1 and t_{i}, and where t_1 and t_{i} are the start time and the time after $(\mathrm{i}-1)$ periods. Both approaches return $\beta = 0.212(\mathrm{rad/s})$. This value is found to be within 1% accuracy from the value obtained via

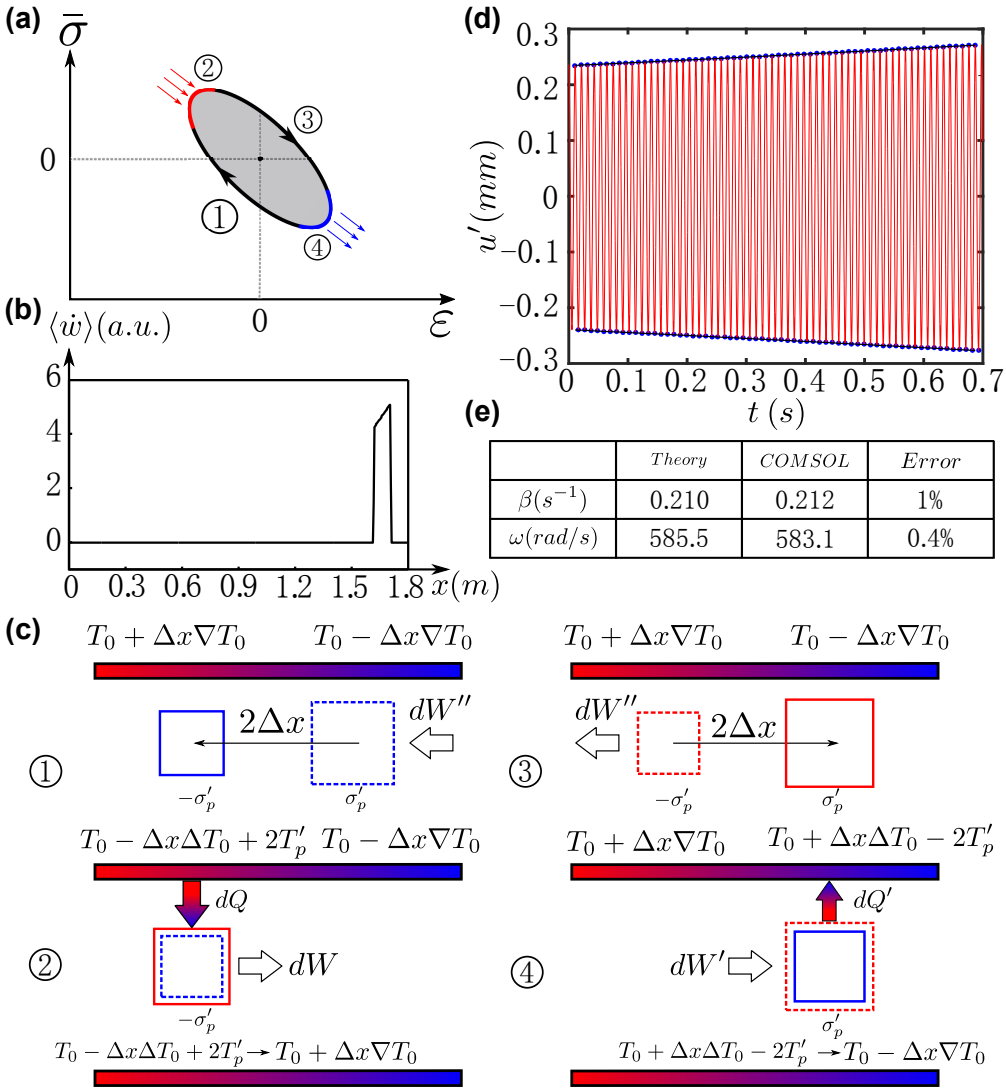

	Theory	*COMSOL*	*Error*
$\beta(s^{-1})$	0.210	0.212	1%
$\omega(rad/s)$	585.5	583.1	0.4%

Figure 4.2. (a) Schematic of the thermodynamic cycle of a Lagrangian particle in the S-segment during an acoustic/elastic cycle (see also the supplementary material of [51]). (b) The time averaged volume-change work $\langle \dot{w} \rangle$ (presented in arbitrary scale and units) along the length of the rod showing that the net work is generated in the stage. (c) Schematic view showing the evolution of an infinitesimal volume element during the different phases of the thermodynamic cycle (a). For simplicity, the cycle is divided in two reversible adiabatic steps and two irreversible constant-stress steps. $()'_p$ indicates the peak value of the corresponding fluctuating variables. (d) Time history of the axial displacement fluctuation at the end of the rod for the fixed-mass configuration. 'Red –': Response, 'Blue •': Peak values, 'Black –': Exponential fit. (e) Table presenting a comparison of the results between the quasi-1D theory and the numerical FE 3D model.

the quasi-1D stability analysis, therefore confirming the validity of the 1D theory and of the corresponding simplifying assumptions.

4.2.3 Considerations on Structural Damping

An important factor for the thermoacoustic amplification in solids is the energy dissipation of the system. This is probably the element that differentiates more clearly the thermoacoustic process in the two media.

The mechanism of energy dissipation in solids, typically referred to as damping, is quite different from that occurring in fluids. Although in both media damping is a macroscopic manifestation of non-conservative particle interactions, in solids their effect can dominate the dynamic response. Considering that the thermoacoustic instability is driven by the first axial mode of vibration, some insight in the effect of damping in solids can be obtained by mapping the response of the rod to a classical viscously damped oscillator. The harmonic response of an underdamped oscillator is of the general form $x(t) = A\mathrm{e}^{\mathrm{i}\Lambda_D t}$, where $\mathrm{i}\Lambda_D$ is the system eigenvalue given by $\mathrm{i}\Lambda_D = -\zeta\omega_0 + \mathrm{i}\sqrt{1-\zeta^2}\omega_0$, where ω_0 is the undamped angular frequency, and ζ is the damping ratio. The damping contributes to the negative real part of the system eigenvalue, therefore effectively counteracting the thermoacoustic growth rate (which, as shown above, requires a positive real part). In order to obtain a net growth rate, the thermally induced growth (i.e. the thermoacoustic effect) must always exceed the decay produced by the material damping. Mathematically, this condition translates into the ratio $\frac{\beta}{\omega} > \zeta$.

For metals, the damping ratio ζ is generally very small (on the order of 1% for aluminum [52]). By accounting for the damping term in the above simulations, we observe that the undamped growth ratio $\frac{\beta}{\omega}$ becomes one or two orders of magnitude lower than the damping ratio ζ. Therefore, despite the relatively low intrinsic damping of the material the growth is effectively impeded.

Considering that dissipative forces exist also in fluids, then a logical question is why their effect is so relevant in solids to be able to prevent the thermoacoustic growth? Our analyses have highlighted two main contributing factors:

1. In fluids, the dissipation is dominated by viscous losses localized near the boundaries. This means that while particles located close to the boundaries experience energy dissipation, those in the bulk can be practically considered loss-free. Under these conditions, even weak pressure oscillations in the bulk can be sustained and amplified. In solids, structural damping is independent of the spatial location of the particles (in fact it depends on the local strain). Therefore, the bulk can still experience large dissipation. In other terms, even considering an equivalent dissipation coefficient between the two media, the solid would always produce a higher energy dissipation per unit volume.

2. The net work during a thermodynamic cycle in fluids is done by thermal expansion at high pressure (or stress, in the case of solids) and compression at low pressure [1]. Thermal deformation in fluids and solids can occur on largely disparate spatial scales. This behavior mostly reflects the difference in the material parameters involved in the constitutive laws with particular regard to the Young's modulus and the thermal expansion coefficient. In general terms, a solid exhibits a lower sensitivity to thermal-induced deformations which ultimately limits the net work produced during each cycle, therefore directly affecting the growth rate of the system.

In principle, we could act on both the above mentioned factors in order to get a strong thermoacoustic instability in solids. Nevertheless, damping is an inherent attribute of materials and it is more difficult to control. Therefore, unless we considered engineered materials able to offer highly controllable material properties, pursuing approaches targeted to reducing damping appears less promising. On the other hand, we choose to explore an approach that targets directly the net work produced during the cycle.

4.2.4 Multi-stage Configuration

In the previous section, we indicated that thermoacoustics in solids is more sensitive to dissipative mechanisms because of the lower net work produced in one cycle.

In order to address directly this aspect, we conceived a multiple stage (here below referred to as multi-stage) configuration targeted to increase the total work per cycle. As the

name itself suggests, this approach simply uses a series of stages uniformly distributed along the rod. The separation distance between two consecutive stages must be small enough, compared to the fundamental wavelength of the standing mode, in order to not alter the phase lag between the temperature and velocity fields.

We tested this design by numerical simulations using thirty stage elements located on the rod section [0.1 $\sim$ 0.9]L, with $T_h = 543.15$K and $T_c = 293.15$K (Fig. 4.3a). The resulting mean temperature distribution $T_0(x)$ was a periodic sawtooth-like profile with a total temperature difference per stage $\Delta T = 250$K. Note that, in the quasi-1D theory, in order to account for the finite length of each stage and for the corresponding axial heat transfer between the stage and the rod we tailored the gradient according to an exponential decay. In the full 3D numerical model, the exact heat transfer problem is taken into account with no assumptions on the form of the gradient. We anticipate that this gradient has no practical effect on the instability, therefore the assumption made in the quasi-1D theory has a minor relevance. A tip mass $M = 0.353$kg was used to reduce the resonance frequency and increase the wavelength so to minimize the effect of the discontinuities between the stages.

The stability analysis performed according to the quasi-1D theory returned the fundamental eigenvalue as $\mathrm{i}\Lambda_u = 8.15 + \mathrm{i}598.6$(rad/s) without considering damping, and $\mathrm{i}\Lambda_d = 2.27 + \mathrm{i}598.7$(rad/s) with 1% damping. Figure 4.3(a.2) shows the time averaged mechanical work $\langle \dot{w} \rangle$ along the rod. The elements in each stage do net work in each cycle. Although the segments between stages are reactive (because the non-uniform T_0 still perturbs the phase), their small size does not alter the overall trend. The positive growth rate obtained on the damped system shows that thermoacoustic oscillations can be successfully obtained in a damped solid if a multi-stage configuration is used.

Full 3D simulations were also performed to validate the multi-stage response. In the damped model, Rayleigh damping $\zeta = 0.5(\frac{\alpha_R}{\omega} + \beta_R \omega)$ was used, where α_R and β_R are Rayleign parameters, ζ and ω are the damping ratio and angular frequency respectively. The parameters were determined by matching $\zeta = 0.01$ at the natural frequency (i.e. $\alpha_R = 3.3344 \times 10^{-5}(rad/s), \beta_R = 3.3344 \times 10^{-5}(s/rad)$ for $\omega = 598(rad/s)$). Figures 4.3b and 4.3c show the time response of the axial displacement fluctuation at the mass-end for both the undamped and the damped rods. The growth rates for the two cases are $\beta_u = 6.87$(rad/s)

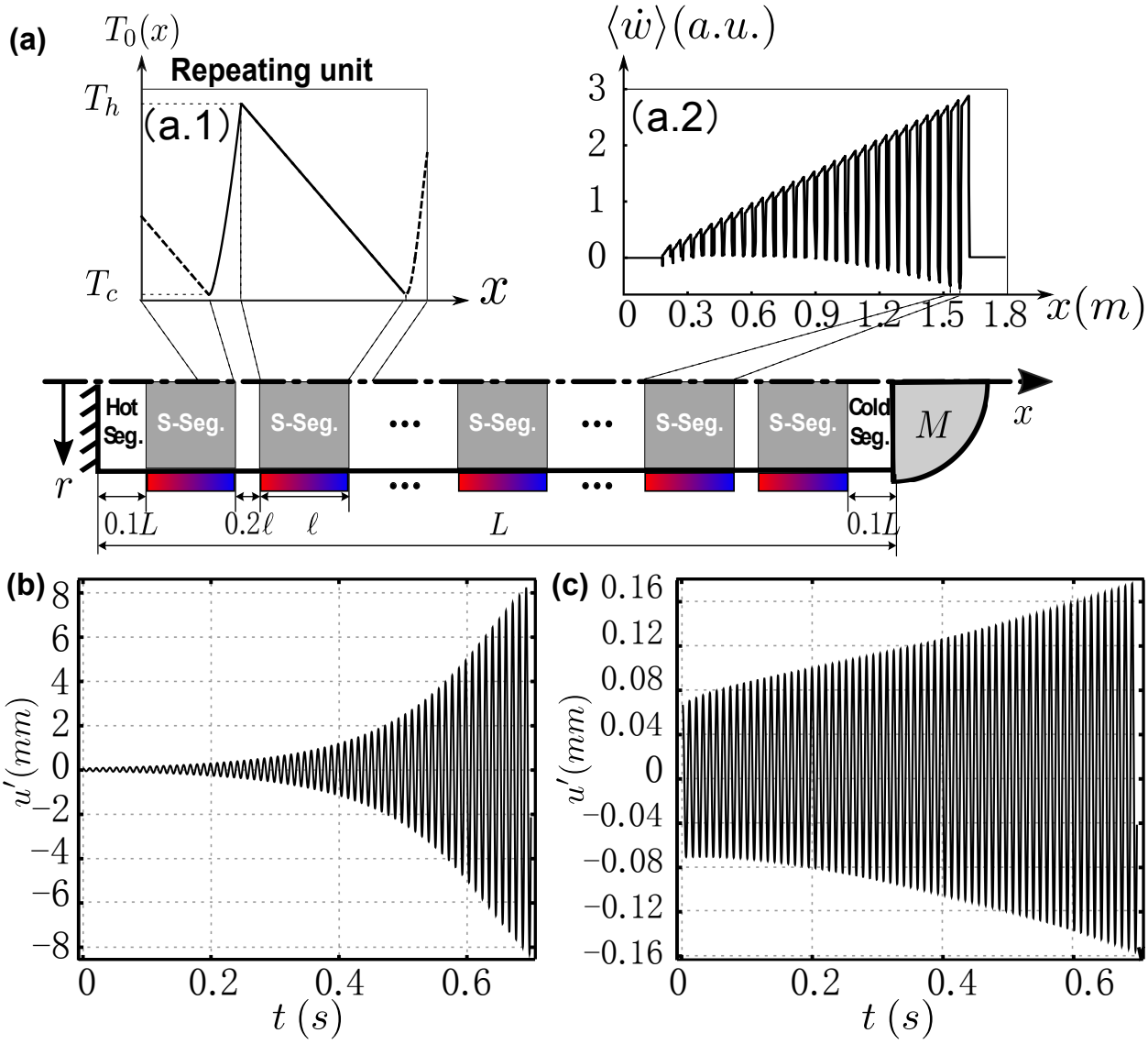

Figure 4.3. (a) Schematic diagram of the multi-stage configuration. The two insets show the mean temperature T_0 profile along the axial direction x and the time averaged volume-change work $\langle \dot{w} \rangle$ (arbitrary scale and unit) along the rod. Time response at the moving end of a fixed-mass rod for the (b) undamped and (c) 1% damped configurations.

(undamped) and $\beta_d = 1.28$(rad/s) (damped). Contrarily to the single stage case, these results are in larger error with respect to those provided by the 1D solver. In the multi-stage configuration, the quasi-1D theory is still predictive but not as accurate. The reason for this discrepancy can be attributed to the effect of axial heat conduction. For the single stage configuration, the net axial heat flux $\kappa \frac{\partial^2 \hat{T}}{\partial x^2}$ is mostly negligible other than at the

edges of the stage (see Fig. S4a). Neglecting this term in the 1D model does not result in an appreciable error. On the contrary, in a multi-stage configuration the existence of repeated interfaces where this term is non-negligible adds up to an appreciable effect (see Fig. S4b). This consideration can be further substantiated by comparing the numerical results for an undamped multi-stage rod produced by the 1D model and by the 3D model in which axial conductivity is artificially impeded. These two models return a growth ratio equal to $\beta_{1D} = 6.38$(rad/s) and $\beta_{3D}^{\kappa_x=0} = 6.60$(rad/s).

4.2.5 General Considerations on the Design of SSTA Devices and Applications

The present chapter confirmed from a theoretical and numerical standpoint the possibility of inducing thermoacoustic response in solids. The next logical step in the development of this new branch of thermoacoustics consists in the design of an experiment capable of validating the SS-TA effect and of quantifying the performance. The most significant challenge that the authors envision consists in the ability to fabricate an efficient interface (stage-medium) capable of high thermal conductivity and negligible shear force. In conventional thermoacoustic systems, it is relatively simple to create a fluid/solid interface with high heat capacity ratio which is a condition conducive to a strong TA response. In solids, the absolute difference between the heat capacities of the constitutive elements (i.e. the stage and the operating medium) is lower but still sufficient to support the TA response. To this regard, we highlight two important factors in the design of an SS-TA device. First, the selection of constitutive materials having large heat capacity ratio is an important design criterion to facilitate the TA response. Second, the stage should have a sufficiently large volume compared to the SS-TA operating medium (in the present case the aluminum rod) in order to behave as an efficient thermal reservoir.

High thermal conductivity at the interface is also needed to approximate an effective isothermal boundary condition while a zero-shear-force contact would be necessary to allow the free vibration of the solid medium with respect to the stage. Such an interface could be approximated by fabricating the stage out of a highly conductive medium (e.g. copper) and using a thermally conductive silver paste as coupler between the stage and the solid rod.

Unfortunately, this design tends to reduce the thermal transfer at the interface (compared to the conductivity of copper) and therefore it would either reduce the efficiency or require larger temperature gradients to drive the TA engine. Nonetheless, we believe that optimal interface conditions could be achieved by engineering the material properties of the solid so to obtain tailored thermo-mechanical characteristics.

Concerning the methodologies for energy extraction, the solid state design is particularly well suited for piezoelectric energy conversion. Either ceramics or flexible piezoelectric elements can be easily bonded on the solid element in order to perform energy extraction and conversion. Compared to fluid-based TA systems, the SS-TA presents an important advantage. In SS-TA the acoustic energy is already generated in the form of elastic energy within the solid medium and it can be converted directly via the piezoelectric effect. On the contrary, fluid-based systems require an additional intermediate conversion from acoustic to mechanical energy that further limits the efficiency. It is also worth noting that, with the advent of additive manufacturing, the SS-TA can enable an alternative energy extraction approach if the host medium could be built by combining both active and passive materials fully integrated in a single medium.

The author expect SS-TA to provide a viable technology for the design, as an example, of engines and refrigerators for space applications[53], [54] (satellites, probes, orbiting stations, etc.), energy extraction or cooling systems driven by hydro-geological sources, and autonomous TA machines (e.g. the ARMY fridge[55]). Although this is a similar range of application compared to fluid-based systems, it is envisioned that solid state thermoacoustics would provide superior robustness and reliability while enabling ultra-compact devices. In fact, solid materials will not be subject to mass or thermal losses that are instead important sources of failure in classical thermoacoustic systems. In addition, the solid medium allows a largely increased design space where structural and material properties can be engineered for optimal performance and reduced dimensions.

4.3 A-SSTA in Looped and Resonance Rods

Section 4.2 has theoretically demonstrated that the unstable thermo-mechanical energy conversion process can occur with elastic waves in solid media.

This section provides two key contributions: 1) it extends the concept of solid-state thermoacoustics to traveling wave configurations, and 2) offers an in-depth analysis of the wave energy budgets of SSTAs. In this section, we prove the existence of traveling thermoacoustic waves in solid media based on the theoretical framework developed in the previous section. We also show that the growth-rate-to-frequency ratio (shorten as growth ratio hereinafter) of the traveling wave oscillations is considerably larger than that of a standing wave oscillation of the same wavelength. Heat flux, mechanical power, and work source for theoretical solid-state thermoacoustic (SSTA) engines are defined heuristically in light of their definitions in fluids. The acoustic energy budgets are analyzed in detail to interpret the energy conversion process in SSTA engines and to define the efficiencies of SSTA engines. Through the detailed study and comparison of traveling and standing wave thermoacoustics, this paper expands the theory of thermoacoustics of solids and may lead to implementations of new generations of ultra-compact and robust SSTA devices capable of direct thermal-to-mechanical energy conversion.

4.3.1 Looped and Resonance Rods: Traveling- and Standing-Wave A-SSTA

In this section, we consider two configurations (Fig. 4.4) in which a ring-shaped slender metal rod with circular cross section is under investigation. Specifically, they are called the looped rod (Fig. 4.4(a) and (c)) and the resonance rod (Fig. 4.4(b) and (d)). The rod experiences an externally imposed axial thermal gradient applied via isothermal conditions on its outer surface at a certain location, while the remaining exposed surfaces are adiabatic. The difference between the two configurations lies in the imposition of a displacement/velocity node (Fig. 4.4(d)), which is used in the resonance rod to suppress the traveling wave mode. Practically, the displacement node could be realized by constraining the rod with a clamp at a proper location (Fig. 4.4(b)). The coupled thermoacoustic response induced by the external thermal gradient and the initial mechanical excitation is investigated.

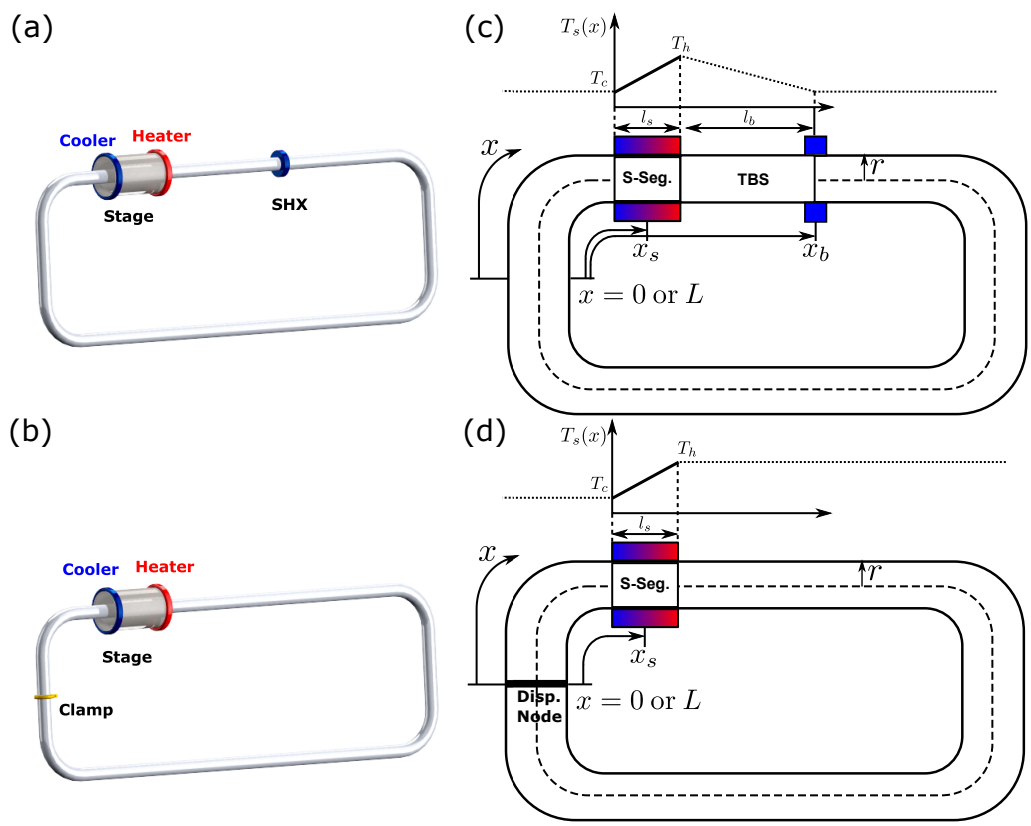

Figure 4.4. Notional schematics of (a) the looped rod and (b) the resonance rod. A component with a large thermal inertia, stage, connected to a heater and a cooler on opposite ends, is mounted on the outer surface of the rod to sustain a linear thermal gradient. In (a), a secondary cold heat exchanger (SHX) is attached to the rod creating the Thermal Buffer Segment (TBS, shown in (c)). In (b), a clamp is used to apply the displacement node (abbreviated as Disp. Node in (d)), which is necessary to suppress the traveling wave mode. (c) and (d) show the temperature profile $T_0(x)$ in the S-seg. (solid line, $T_s(x)$), and in the remaining sections (dashed line), and the characteristic geometric parameters. T_h and T_c are the hot and cold temperatures respectively. The stage is $l_s = 0.05L$ long centered about $x = x_s$ (irrelevant for the looped design). The SHX is mounted at x_b ($l_b = 0.45L$ away from the stage). The optimal location of the stage's midpoint x_s for the full-wavelength standing wave is $x_s = 0.845L$.

The initial mechanical excitation could grow with time as a result of the coupling between the mechanical and thermal response provided a sufficient temperature gradient is imposed on the outer boundary of a solid rod at a proper location. This phenomenon is identified as the thermoacoustic response of solids in [51].

By analogy with fluid-based traveling wave thermoacoustic engines [1], [8], a stage element is used to impose a thermal gradient on the surface of the looped rod (Fig. 4.4(a)). The specific location of the stage element in this case is irrelevant due to the periodicity of the system. The segment surrounded by the stage is named S-segment, which experiences a spatial temperature gradient (from T_c to T_h) due to the externally enforced temperature distribution. The interface between the stage and the S-segment is ideally assumed to have a high thermal conductivity, which assures the isothermal boundary conditions along with a zero shear stiffness. One can anticipate the compromise between these two seemingly contradictory conditions in an experimental validation. The stage is considered as a thermal reservoir so that the temperature fluctuation on the surface of S-segment is assumed to be zero (isothermal). A Thermal Buffer Segment (TBS) next to the thermal gradient provides a thermal buffer between T_h and room temperature T_c. The temperature drop in the TBS is caused by the secondary cold heat exchanger (SHX, Fig. 4.4(a)) located at x_b. A linear temperature profile in the TBS from T_h to T_c is adopted to account for the natural axial thermal conduction along the looped rod.

To show the superiority of traveling wave thermoacoustics, a fair comparison was conducted with a resonance rod. The resonance rod, as Fig. 4.4(d) shows, was constructed by enforcing a displacement/velocity node at an arbitrary position labeled $x = 0$. This node is equivalent to a fixed and adiabatic boundary condition. If only plane wave propagation is considered, this resonance rod has no difference with a straight rod with both ends clamped. The TBS is not necessary in the resonance rod since the temperature can be discontinuous at the displacement node. To make a comparison, we calculated the growth ratio of a standing wave mode in the resonance rod with the same wavelength ($\lambda = L$) and frequency ($\approx$ 2830Hz) as the traveling wave mode in the looped rod without the displacement node. We highlight the essential difference of the mode numbering in Fig. 4.5 and propose a naming convention for the modes for brevity. The modes in comparison in this section are $Loop - I$ and $Res - II$ (the shaded blocks).

With the boundary conditions well defined, the governing equations, i.e.: Eqns. (4.1), (4.2) and (4.3) can be solved to show the transient thermoacoustical response of the system.

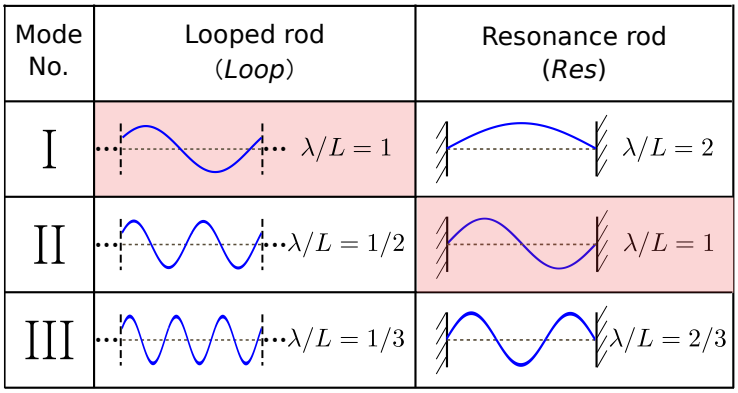

Figure 4.5. The mode shapes of the looped and the resonance rod and the naming convention for modes. Note that same mode numbers correspond to different wavelengths. Especially, the looped rod starts with a full-wavelength mode as its first mode while a resonance rod starts with a half-wavelength one. To make a comparison based on the same wavelength, $Loop - I$ and $Res - II$ represent our contrast group (the shaded blocks).

4.3.2 Stability Analysis and Mode Shifting

We solved the eigenvalue problem numerically for both cases of a $L = 1.8$m long aluminum rod, being the looped or the resonance rod, under a 200K temperature difference ($T_h = 493.15$K and $T_c = 293.15$K) with a $0.05L$ long stage to investigate the thermoacoustic response of the system. The material properties of aluminum are chosen as: Young's modulus $E = 70$GPa, density $\rho = 2700\text{kg/m}^3$, thermal expansion coefficient $\alpha = 23 \times 10^{(-6)}\text{K}^{-1}$, thermal conductivity $\kappa = 238\text{W/(m·K)}$ and specific heat at constant strain $c_\epsilon = 900\text{J/(kg·K)}$.

The first traveling wave mode in the looped rod, with a full wavelength ($\lambda = L$) is considered, and will be referred to as $Loop - I$, following the naming convention of modes shown in Fig. 4.5. The dimensionless growth ratio β/ω is used as a metric of the SSTA engine's ability to convert heat into mechanical energy; such normalization accounts for the fact that thermoacoustic engines operating at high frequencies naturally exhibit high growth rates [27] and vice versa. Besides, in solids the inherent structural damping is commonly expressed as a fraction of the frequency of the oscillations, i.e. the damping ratio; the latter is widely used to quantify the frequency-dependent loss/dissipative effect in solids. The optimal growth ratio was found by gradually varying the radius R of the looped rod. We

used the dimensionless radius R/δ_k to represent the effect of geometry, where δ_k was assumed to be constant at the operating frequency $f = \frac{c}{\lambda} \approx \frac{\sqrt{E/\rho}}{L} = 2830$Hz. The '$Loop - I$' curve in Fig. 4.6 shows the growth ratio β/ω vs. the dimensionless radius R/δ_k of a full-wavelength traveling wave mode. The frequency variation with radius is neglected. Positive growth ratios are obtained in the absence of losses, and the losses in solids are mainly induced by intrinsic structural damping. The positive growth ratio suggests that the undamped system is capable of sustaining and amplifying the propagation of a traveling wave. It is noteworthy that in fluid-based thermoacoustic devices, the thermal buffer tube (TBT), whose companion component in solids is the TBS (Fig. 4.4), acts as a wave scatterer due to the temperature dependence of sound speed of the fluid media. [56] The speed of sound in solids is expressed as $c = \sqrt{E/\rho}$ for longitudinal waves, and has a negligible dependency on temperatures; as such, the TBS is not expected to yield wave scattering effect. However, the length of the TBS l_s does affect the growth ratio of the traveling wave mode in solid-state thermoacoustic devices; in particular, $l_s = 0.45L$ achieves the optimal growth ratio for the setup analyzed herein. A plot of growth ratio β/ω vs. nondimensional TBS length l_s/L can be found in Fig. 5.7.

On the other hand, for the resonance rod configuration, only standing-wave thermoacoustic waves can exist since the traveling wave mode is suppressed by the displacement node. In this case, the second mode (also ($\lambda = L$)) is considered, and denoted as $Res - II$ (Fig. 4.5) The presence of a displacement node also decreases the rod's degree of symmetry. Thus, the stage location, while being irrelevant in the looped rod configuration, crucially affects the growth ratio in the standing wave resonance rod. An improper placement of the stage on a resonance rod can lead to a negative growth rate, physically attenuating the oscillations. As Fig. 4.7 shows, only a proper location falling into the shaded region leads to a positive growth ratio. Other than the stage location, the radius of the rod is also another important factor, which can affect the growth ratio for the resonance rod configuration. In Fig. 4.6, we show the β/ω vs. R/δ_k relations of a resonance rod for different stage locations as well. The maximum thermoacoustic response is obtained for a stage location $x_s = 0.845L$ ($Res - II$,case A).

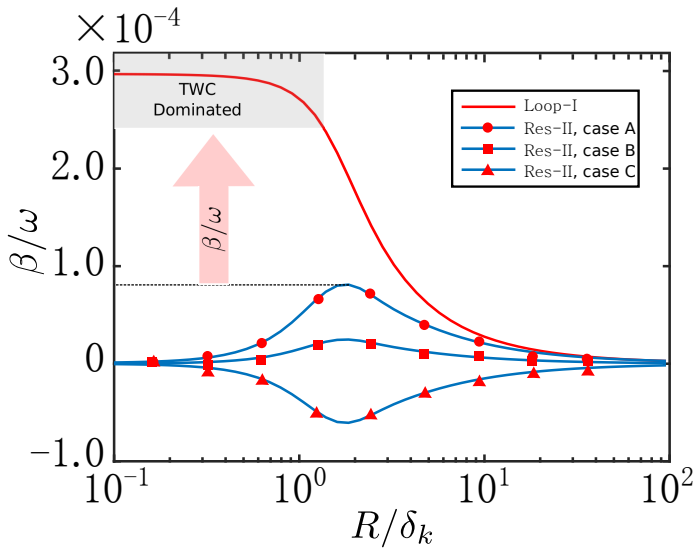

Figure 4.6. A semilog plot of the growth ratio versus the nondimensional radius for the $Loop - I$ mode in the looped rod and the $Res - II$ mode in the resonance rod. Case A, B, C correspond to $Res - II$ mode with the stage placed at different locations. The growth ratios of these three cases at optimal R/δ_k are plotted in Fig. 4.7

Figure 4.6 shows that as $R \gg \delta_k$, all the curves, whether the looped or the resonance rod, reach zero due to the weakened thermal contact between the solid medium and the stage. However, as R/δ_k reaches zero (shaded grey region), the stage is very strongly thermally coupled with the elastic wave. As a result, the traveling wave mode dominates. The reason for mode switching will be discussed later in this section. The stability curves also tell that the traveling wave engine has about 4 times higher growth ratio in the limit $R/\delta_k \to 0$, compared to the standing wave resonance rod ($Res - II$,case A) in which maximal growth ratio is obtained (at $R/\delta_k \approx 2$). The noteworthy improvement on growth ratio is essential to the design of more robust solid state thermoacoustics devices.

Hereafter, the modes or results from $Loop - I$ and $Res - II$ will be taken for values of R of 0.1mm and 0.184mm, i.e. R/δ_k of 1.0 and 1.8 respectively.

In classical thermoacoustics, the phase delay between pressure and cross-sectional averaged velocity is an essential controlling parameter of thermoacoustic energy conversion[2], [8]. Ceperley [2] stated that the energy conversion process of a traveling wave TA machine resembles that of a Stirling engine with the piston being an air column, while the standing wave

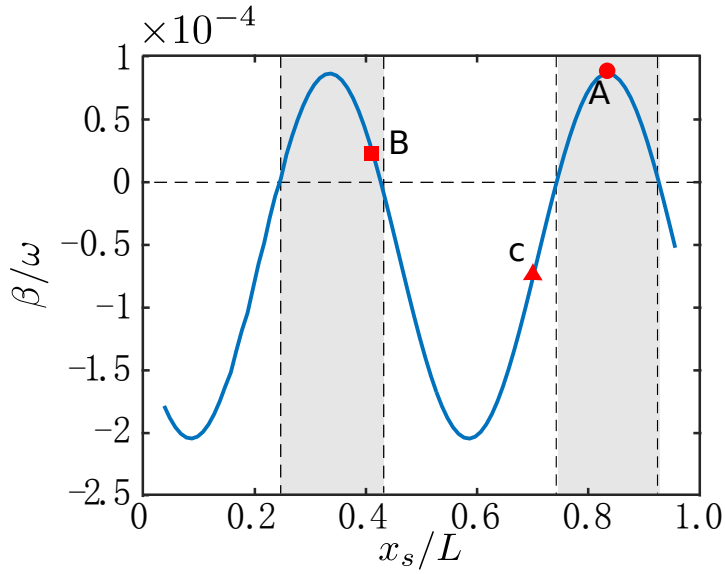

	Case A	Case B	Case C
x_s/L	0.845	0.415	0.715

Figure 4.7. Plot of the growth ratio versus the normalized stage location for the resonance rod $Res - II$ at optimal $R/\delta_k(= 1.8)$. Three specific cases are labeled A, B and C corresponding to the stability curves in Fig. 4.6. Only the location of the stage falling into the shaded region gives a positive growth ratio.

engines need a thermal delay to effectively convert energy. In analogy with thermoacoustics in fluids, we use the phase difference Φ between negative stress $\bar{\sigma} = -\sigma = |\hat{\bar{\sigma}}|\mathrm{Re}[\mathrm{e}^{\mathrm{i}(\omega t+\phi_{\bar{\sigma}})}]$ and particle velocity $v = |\hat{v}|\mathrm{Re}[\mathrm{e}^{\mathrm{i}(\omega t+\phi_v)}]$, where $\phi_{\bar{\sigma}}$ and ϕ_v denote the phases of $\bar{\sigma}$ and v respectively, $\Phi = \phi_v - \phi_{\bar{\sigma}}$. Note that a negative stress in solids indicates compression which is equivalent to a positive pressure in fluids. The standing wave component (SWC) and traveling wave component (TWC) of velocity are quantified as $v_S = |\hat{v}|\mathrm{Re}[\mathrm{e}^{\mathrm{i}(\omega t+\phi_{\bar{\sigma}}+\pi/2)}]\sin\Phi$ and $v_T = |\hat{v}|\mathrm{Re}[\mathrm{e}^{\mathrm{i}(\omega t+\phi_{\bar{\sigma}})}]\cos\Phi$, which are 90° out-of-phase and in-phase with $\bar{\sigma}$, respectively. In a resonance rod, TWC is negligible because the wave propagation at the extremities is impeded by the clamped boundary condition, the displacement node. However, the non-zero growth rate β will cause a small phase shift, which makes the phase difference Φ close to but not exactly 90°. The blue solid line in Fig. 4.8 shows the phase difference of a $R = 0.184$mm resonance rod ($Res - II$). In the case of a thick looped rod ($R \gg \delta_k$) with a poor degree of

thermal contact, the mode shape is much similar to that of a resonance rod because SWC is still dominant and the phase difference is close to 90°. Supplementary Movie 1 shows that the displacement nodes may exist intrinsically in the system without clamped points. However, when the looped rod is sufficiently thin ($R \sim \delta_k$) the traveling wave component plays a dominant role. Thus, the phase delay decreases to 30° at most. The orange dashed line in Fig. 4.8 shows the phase difference of a $R = 0.1$mm looped rod ($Loop - I$). The time history of the displacement along the looped rod in Supplementary Movie 2 shows that, as $R \leq \delta_k$ (small phase difference), the wave mode is dominated by TWC. Figure 4.8 also presents an intermediate case ($Loop - M$, the orange solid line) in which the phase difference of a looped rod whose radius is equal to that of $Res - II$ is shown. The phase difference is 50° at most, indicating that neither TWC nor SWC plays a dominating role so the wave mode is highly mixed.

In the looped rod, the TWC of the thermoacoustically unstable waves increases with respect to the SWC as the degree of thermal contact in the thermoacoustic core, expressed as the ratio of the thermal penetration depth δ_k to the radius R, is increased. This is consistent with Ceperley's classical statement [2]: excellent thermal contact between the stage and the medium is favorable to traveling waves, while standing waves prefer imperfect thermal contact. This can be understood by considering an infinitesimal solid element in the S-seg. shown in Fig. 4.4, where positive velocity leads to the element moving into a hotter region and, hence, being heated. In a traveling wave, velocity and negative (compressive) stress $\hat{\bar{\sigma}}$ are in phase, so the solid element undergoes a cycle with compression, heating, expansion and cooling phases distinct from each other, resembling a Stirling cycle. In a standing wave, however, negative stress and velocity have a 90° phase difference, so a thermal delay is necessary to avoid simultaneous compression and heating, and simultaneous expansion and cooling, which would lead to no thermal-to-elastic energy conversion. The thermal delay, or poor thermal contact, is in fact achieved by increasing the radius of the rod. The inward radial heat transfer can be expressed as $\hat{q} = R\rho c_\varepsilon(\mathrm{i}\omega g_k)\hat{T}$. (See Eqn. (22) in Supplementary Material). Figure 4.9 (a) shows that as the radius decreases, the real part of g_k becomes negligible compared to the large imaginary part, so an element at a temperature lower than the base temperature will instantly absorb heat from the boundary, indicating an excellent

thermal contact. Contrarily, as $R/\delta_k \gg 1$, the real and imaginary parts of g_k become comparable (See the inset), leading to a phase/thermal delay, which favors a standing-wave phasing. The change of Φ_m, referring to the maximal phase difference between $\hat{v}$ and $\hat{\tilde{\sigma}}$, with R/δ_k is plotted in Fig. 4.9 (b); and it is shown that as the thermal contact/rod radius becomes stronger/smaller, the mode in the rod switches from SWC dominated ($\Phi_m \approx 90°$) to TWC dominated ($\Phi_m \approx 30°$). The blue curves for $Res - II$ in Fig. 4.6 provide another evidence that perfect thermal contact (low R/δ_k) does not promote standing-wave phasing. In the resonance rod, traveling wave is suppressed by the clamped boundaries; and as $R/\delta_k \ll 1$, β/ω tends to zero, which proves the limited amplification of the standing wave under high degrees of thermal contact.

It is noteworthy that in either the resonance rod or the looped rod, neither a pure standing wave nor traveling wave is ever achieved due to the presence of the base temperature gradient and thermoacoustic production of power. Therefore, when referring to a standing-wave or traveling-wave mode, the latter are intended as the dominating contributions to the instability. The $Res - II$ mode in the resonance rod is dominated by the SWC with a phase difference close to, but never exactly equal, to 90° and the $Loop - I$ mode in the looped rod is dominated by the TWC, with the phase difference at most 30° at a few locations in the domain (Fig. 4.8).

4.3.3 Energy Conversions in SSTA Engines

In this section, we explore the energy conversion process in the resonance and the looped rods. The resonance rod, '*Res*', has a length of 1.8m, radius of $R = 0.184$mm and the stage location $x_s = 0.805L$. The looped rod, '*Loop*', has the same total length, but the radius $R = 0.1$mm is selected to allow the TWC to dominate. The location of the stage in looped rods does not influence the thermoacoustic response, thus only for illustrative purposes, it is located at $x_s = 0.205L$ so that the TBS does not cross the point where periodicity is applied.

We firstly present definitions of heat flux, work flux (mechanical power) and work source for the SSTA system. The latter are then discussed within the context of acoustic energy budgets rigorously derived from the governing equations, naturally yielding the consistent

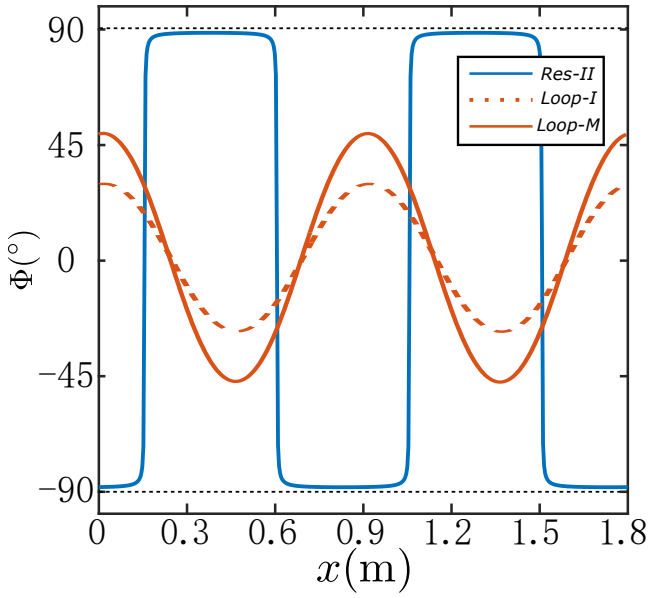

Figure 4.8. Plot of the phase difference between negative stress $\bar{\sigma}$ and particle velocity v for an $R = 0.184$mm resonance rod '$Res - II$', an $R = 0.1$mm looped rod '$Loop - I$', and an $R = 0.184$mm looped rod '$Loop - M$'.

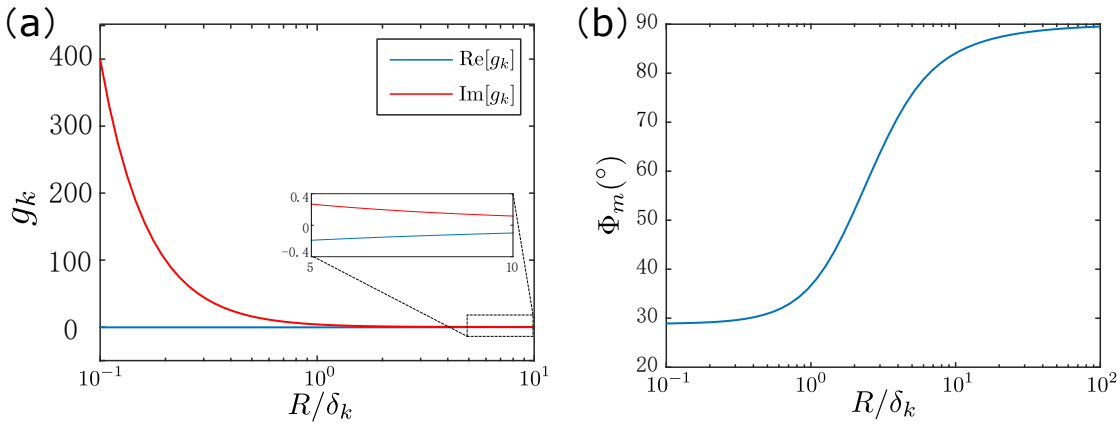

Figure 4.9. (a) The real and imaginary parts of the dimensionless complex function g_k vs. the dimensionless radius R/δ_k. g_k is a geometry-dependent function accounting for the radial heat conduction in the S-segment. The high imaginary part of g_k on the left indicates an excellent thermal contact between the medium and the boundary. (b) The maximal value of the phase difference between $\hat{\bar{\sigma}}$ and $\hat{v}$ vs. the dimensionless radius R/δ_k, showing as the looped rod becomes thinner, the phase difference decreases and eventually TWC dominates.

expressions of the second order energy norm, energy redistribution term, and the thermoacoustic production and dissipation. The thermal-to-acoustic (or thermodynamic) efficiency,

defined as the ratio of the net acoustic energy gain per cycle to the total heat absorbed by the medium, is analyzed for SSTA devices where it is found that the first mode of the traveling wave engine ('$Loop - I$') is more efficient than the second standing wave mode ('$Res - II$').

Heat Flux, Mechanical Energy and Work Source

A cycle-averaged heat flux in the axial direction is generated in the S-segment due to its heat exchange with the stage. Neglecting the axial thermal conductivity, the transport of entropy fluctuations due to the fluctuating velocity v_1 (subscript 1 for a first order fluctuating term in time) is the only way heat can be transported along the axial direction [57]. The instantaneous heat flux is expressed in the time domain as

$$\dot{q_2} = T_0 \rho_0 (s_1 v_1) \text{ [W/m}^2\text{]} \tag{4.5}$$

where the subscript 2 denotes a second-order quantity. Entropy fluctuations in solids are related to temperature and strain rate fluctuations via the following relation from thermoelasticity theory [49]:

$$s_1 = \frac{c_\epsilon}{T_0} T_1 + \alpha E \varepsilon_1. \tag{4.6}$$

Substituting Eqn. (4.6) into Eqn. (4.5), $\dot{q_2}$ can be expressed in terms of T_1, v_1 and ε_1. Note that the quantities with subscript 1 are instantaneous and dependent on both radial and axial coordinates, while the hatted quantities $\hat{T}$, $\hat{v}$ and $\hat{\varepsilon}$ are the Fourier amplitudes of the cross-sectional averaged first order fluctuations. The latter can be extracted from the eigenfunctions of the eigenvalue problem (Eqns. (4.1), (4.2) and (4.3)). Under the assumptions: (1) $\beta/\omega \ll 1$, and (2) v_1 is uniform through the cross section, the cycle average of the second order cross-sectionally-averaged products, $\langle a_1 v_1 \rangle_r$, can be evaluated as $\langle \langle a_1 v_1 \rangle_r \rangle = \langle \langle a_1 \rangle_r \langle v_1 \rangle_r \rangle = \frac{1}{2}\text{Re}[\hat{a}\hat{v}^*]\text{e}^{2\beta t}$ (e.g. $\langle \langle s_1 v_1 \rangle_r \rangle = \frac{1}{2}\text{Re}[\hat{s}\hat{v}^*]\text{e}^{2\beta t}$), where a is a dummy harmonic variable following the $\text{e}^{\text{i}\Lambda t}$ convention, the superscript $*$ denotes the complex conjugate, and $\langle\rangle$ and $\langle\rangle_r$ are the cycle averaging and cross-sectional averaging, respectively. Note that since hatted quantities already denote cross-sectional averaged quantities in the

frequency domain, angular brackets are omitted for quantities such as $\hat{T}$, $\hat{v}$ and $\hat{\varepsilon}$. We want to stress that the uniformity of v_1 through the cross section is necessary for the above evaluation to hold because the cross-sectional average of the product of two first-order terms ($\langle a_1 v_1 \rangle_r$) can be equal to the product of two cross-sectionally averaged terms ($\langle a_1 \rangle_r \langle v_1 \rangle_r$) only if one of the two terms is uniform in the cross section. Contrary to the fluids case, where viscous effects cause a non-uniform distribution of velocity along radial direction, in the case of longitudinal waves in solids, it is correct to assume a uniform radial velocity distribution.

We obtain $\langle \dot{q}_2 \rangle = \tilde{Q} \mathrm{e}^{2\beta t}$, where

$$\tilde{Q} = \frac{1}{2}\rho_0 c_\epsilon \mathrm{Re}[\hat{T}\hat{v}^*] + \frac{1}{2}T_0 \alpha E \mathrm{Re}[\hat{\varepsilon}\hat{v}^*] \qquad [\mathrm{W/m^2}]. \tag{4.7}$$

The total heat flux through the cross section of the rod is

$$\dot{Q} = \int_A \langle \dot{q}_2 \rangle dS = A \langle \dot{q}_2 \rangle \qquad [\mathrm{W}]. \tag{4.8}$$

The second equality holds because the eigenfunctions are all cross-section-averaged quantities. We note that $\dot{Q}$ is a function of the axial position x.

The instantaneous mechanical power carried by the wave is defined as

$$I_2 = (-\sigma_1) v_1 = \bar{\sigma}_1 v_1. \qquad [\mathrm{W/m^2}] \tag{4.9}$$

This quantity physically represents the rate per unit area at which work is done by an element onto its neighbor. It can be also called 'work flux' because it shows the work flow in the medium as well. When an element is compressed ($\bar{\sigma} > 0$), it 'pushes' its neighbor so that a positive work is done on the adjacent element. A notable fact is that there is a directionality to I_2, which depends on the direction of v_1.

Similarly, the cycle-average mechanical power $\langle I_2 \rangle$ can be expressed as $\langle I_2 \rangle = \tilde{I} \mathrm{e}^{2\beta t}$, where

$$\tilde{I} = \frac{1}{2}\mathrm{Re}[\hat{\bar{\sigma}}\hat{v}^*] \qquad [\mathrm{W/m^2}]. \tag{4.10}$$

The total mechanical power through the cross section I of the rod is given by

$$I = \int_A \langle I_2 \rangle dS = A\langle I_2 \rangle \qquad [\mathrm{W}]. \tag{4.11}$$

The work source can be further defined as the gradient of the mechanical power as

$$w_2 = \frac{\partial I_2}{\partial x} \qquad [\mathrm{W/m^3}]. \tag{4.12}$$

By expanding Eqn. (4.12), w_2 can be further expressed as

$$w_2 = \frac{\partial \bar{\sigma}_1}{\partial x} v_1 + \frac{\partial v_1}{\partial x} \bar{\sigma}_1 \tag{4.13}$$

The first term of w_2 vanishes after applying cycle-averaging, because according to the momentum conservation (Eqn. (4.2)), $\partial \sigma_1 / \partial x$ and v_1 are 90° out of phase under the assumption that the small phase difference caused by the non-zero β can be neglected due to: $\beta/\omega \ll 1$. The remaining term is equivalent to $\bar{\sigma}_1 \frac{\partial \epsilon_1}{\partial t}$, i.e.

$$\frac{\partial v_1}{\partial x} \bar{\sigma}_1 = \bar{\sigma}_1 \frac{\partial \epsilon_1}{\partial t}, \tag{4.14}$$

whose cycle average is consistent with the cycle-averaged volume change work defined in [51].

The cross sectional integral of the work source is given by

$$W = \int_A \langle w_2 \rangle dS = A\langle w_2 \rangle \qquad [\mathrm{W/m}]. \tag{4.15}$$

Figure 4.10 shows the cycle-averaged quantities: heat flux $\tilde{Q}$ and mechanical power $\tilde{I}$ of a traveling wave engine ('*Loop*') and a standing wave one ('*Res*'). Note that the quantities indicated with $\tilde{()}$ satisfy the assumption of cycle averaging: $\langle ()_2 \rangle = \tilde{()} e^{2\beta t}$. Figure 4.10(a) and (c) illustrate that heat flux only exists in the S-segment and that wave-induced transport of heat occurs from the hot to the cold heat exchanger. The negative values in the S-segment in (a) and (c) are due to the fact that the hot exchanger is on the right side of the cold

one, so heat flows to the negative x direction in that case. The non-zero spatial gradient in $\tilde{Q}$ in the S-segment proves that there is heat exchange happening on the boundary of this segment because the heat flux in the axial direction is not balanced on its own.

Fig. 4.10(d) shows the mechanical power in the standing wave engine. The positive slope of $\tilde{I}$ in the S-segment elucidates the fact that the work generated in this region is positive, as discussed in detail in Section 4.3.3. This amount of work drops along the axial direction in the remaining segments at the spatial rate of $\mathrm{d}\tilde{I}/\mathrm{d}x$. The work drop in the hot and cold segments balances the accumulation of energy because there is no radial energy exchange in these sections. Clearly, if there is no energy growth, the slope of $\tilde{I}$ should be zero in these sections, as also discussed in Section 4.3.3.

The work flow in the traveling wave engine, as Fig. 4.10(b) shows, has a very large value, which is due to the fact that negative stress $\bar{\sigma}$ and particle velocity v have a phase difference much smaller than 90° (Fig. 4.8). This means that a nearly uniform work flow is circulating the '*Loop*' carried by the wave dominated by TWC. Contrarily to the standing wave case, the slope of $\tilde{I}$ is negative in the S-segment, because it is balancing the positive work created by $\tilde{I}$ against the temperature gradient in the TBS. The volumetric integration of the work source w, i.e. the spatial integration of W along the rod, should be zero because, globally, their is no energy output in the system. All the energy converted from the heat in the S-segment should eventually lead to a uniformly distributed perturbation energy growth. More discussions will be addressed in the following section.

Acoustic Energy Budgets

The acoustic energy budgets are derived from the governing equations

$$\frac{\partial v_1}{\partial t} = \frac{1}{\rho}\frac{\partial \sigma_1}{\partial x}, \tag{4.16}$$

$$\frac{\partial T_1}{\partial t} = -\frac{\mathrm{d}T_0}{\mathrm{d}x}v_1 - \gamma_G T_0 \frac{\partial v_1}{\partial x} + \frac{\kappa}{\rho c_\varepsilon}\frac{1}{r}\frac{\partial}{\partial r}\left(r\frac{\partial T_1}{\partial r}\right). \tag{4.17}$$

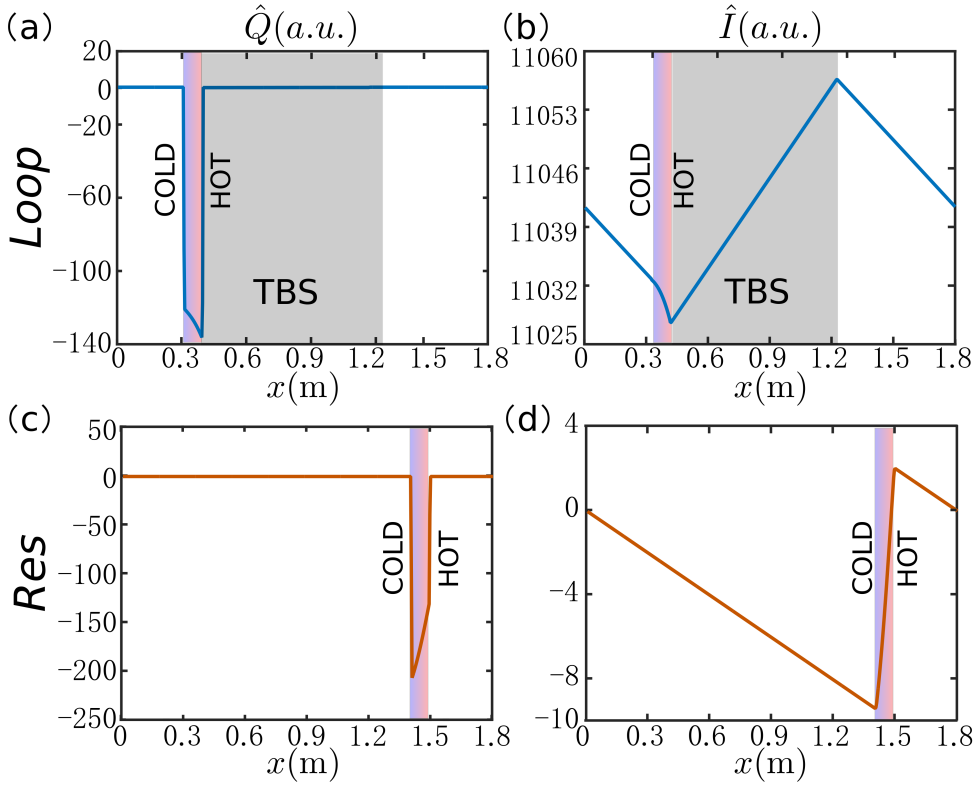

Figure 4.10. Cycle-averaged heat flux $\tilde{Q}$ and mechanical power $\tilde{I}$ in the frequency domain (arbitrary units) for the looped rod '*Loop*' and the resonance rod '*Res*', respectively. These components are evaluated from eigenfunctions from the stability analysis (Eqns. (4.1), (4.2) and (4.3)). The color gradient strips indicate the location of S-segment, and the shaded grey strips indicate the location of the TBS in '*Loop*'.

Define $\bar{\sigma}_1 = -\sigma_1$. The constitutive relation is written as

$$T_1 = \frac{1}{\alpha}(\varepsilon_1 + \frac{\bar{\sigma}_1}{E}). \tag{4.18}$$

Combined with Eqn. (4.18), the cross-sectional averages of Eqns. (4.16) and (4.17) are expressed as

$$\frac{\partial \langle v_1 \rangle_r}{\partial t} = -\frac{1}{\rho}\frac{\partial \langle \bar{\sigma}_1 \rangle_r}{\partial x}, \tag{4.19}$$

$$\frac{\partial \langle \bar{\sigma}_1 \rangle_r}{\partial t} = -E(1+\alpha\gamma_G T_0)\frac{\partial \langle v_1 \rangle_r}{\partial x} - \alpha E \frac{\mathrm{d}T_0}{\mathrm{d}x}\langle v_1 \rangle_r + \frac{\alpha E}{R\rho c_\varepsilon}\langle q_1 \rangle_r, \tag{4.20}$$

where $\langle\rangle_r$ indicates cross-sectional averaging and $\langle q_1 \rangle_r = 2\kappa \frac{\partial T_1}{\partial r}\mid_{r=R}$ indicates the heat conduction at the medium-stage interface. The relation $\frac{\partial \varepsilon_1}{\partial t} = \frac{\partial v_1}{\partial x}$ is used in the transformation above.

Multiplying Eqn. (4.19) by $\rho\langle v_1 \rangle_r$ and Eqn. (4.20) by $\frac{\langle \bar{\sigma}_1 \rangle_r}{E(1+\alpha\gamma_G T_0)}$, and adding them gives

$$\frac{\partial \mathscr{E}_2}{\partial t} + \frac{\partial I_2}{\partial x} + \mathscr{R}_2 = \mathscr{P}_2 - \mathscr{D}_2, \tag{4.21}$$

where

$$\mathscr{E}_2 = \frac{1}{2}\rho\langle v_1 \rangle_r^2 + \frac{1}{2}\frac{1}{E(1+\alpha\gamma_G T_0)}\langle \bar{\sigma}_1 \rangle_r^2, \tag{4.22}$$

$$I_2 = \langle \bar{\sigma}_1 \rangle_r \langle v_1 \rangle_r, \tag{4.23}$$

$$\mathscr{R}_2 = \frac{\alpha}{1+\alpha\gamma_G T_0}\frac{\mathrm{d}T_0}{\mathrm{d}x} I_2, \tag{4.24}$$

$$\mathscr{P}_2 - \mathscr{D}_2 = \frac{\alpha}{1+\alpha\gamma_G T_0}\frac{1}{R\rho c_\varepsilon}\langle q_1 \rangle_r \langle \bar{\sigma}_1 \rangle_r. \tag{4.25}$$

$\mathscr{E}_2, I_2, \mathscr{R}_2, \mathscr{P}_2$ and $\mathscr{D}_2$ are the second order energy norm, work flux, energy redistribution term, thermoacoustic production and dissipation, respectively. Note that the work flux shown in Eqn. (4.23) is consistent with the heuristic definition adopted in the previous section (Eqn. (4.9)). If two first order quantities $\langle a_1 \rangle_r$ and $\langle b_1 \rangle_r$ are in the form of $()_1 = \hat{()}\mathrm{e}^{(\beta+\mathrm{i}\omega)t}$

with $\beta/\omega \ll 1$, we adopt the assumption $\langle\langle a_1\rangle_r\langle b_1\rangle_r\rangle = \frac{1}{2}\mathrm{Re}[\hat{a}\hat{b}^*]\mathrm{e}^{2\beta t}$, where $\langle\rangle$ indicates cycle averaging and the superscript * indicates the complex conjugate. This is because

$$\langle\langle a_1\rangle_r\langle b_1\rangle_r\rangle = \mathrm{Re}[\int_{t-\mathscr{T}>/2}^{t+\mathscr{T}>/2} \hat{a}\mathrm{e}^{(\beta+\mathrm{i}\omega)t}\cdot\hat{b}\mathrm{e}^{(\beta+\mathrm{i}\omega)t}dt] \tag{4.26}$$

$$\approx \mathrm{e}^{2\beta t}\mathrm{Re}[\int_{t-\mathscr{T}>/2}^{t+\mathscr{T}>/2} \hat{a}\mathrm{e}^{\mathrm{i}\omega t}\cdot\hat{b}\mathrm{e}^{\mathrm{i}\omega t}dt] \tag{4.27}$$

$$= \mathrm{e}^{2\beta t}(\frac{1}{2}\mathrm{Re}[\hat{a}\hat{b}^*]) \tag{4.28}$$

$$= \frac{1}{2}\mathrm{Re}[\hat{a}\hat{b}^*]\mathrm{e}^{2\beta t}, \tag{4.29}$$

where $\mathscr{T} = (2\pi)/\omega$ is the period of the harmonic oscillation. Note that we use the hat to denote the cross sectional averaging of quantities in the frequency domain for brevity, so angular brackets are neglected. A notable fact is that in an instable system, the second order cycle averages are no longer constant numbers. Instead they grow with time, but at twice the first oder terms' growth rate.

Taking the cycle average of Eqn. (4.21) we get

$$2\beta\tilde{\mathscr{E}} + \frac{\mathrm{d}\tilde{I}}{\mathrm{d}x} + \tilde{\mathscr{R}} = \tilde{\mathscr{P}} - \tilde{\mathscr{D}}, \tag{4.30}$$

where $\tilde{\mathscr{E}}, \tilde{\mathscr{R}}, \tilde{I}, \tilde{\mathscr{P}}$, and $\tilde{\mathscr{D}}$are transformed from the cycle averages of the cross-sectionally-averaged second order terms in Eqns. (4.22-4.25), following the assumption of cycle averaging: $\langle()_2\rangle = \tilde{()}\mathrm{e}^{2\beta t}$. Note that a common factor $\mathrm{e}^{2\beta t}$ is canceled in each term.

It's clear that $\tilde{\mathscr{E}}, \tilde{\mathscr{R}}$ and $\tilde{I}$ are expressed as

$$\tilde{\mathscr{E}} = \frac{1}{2}\rho|\hat{v}|^2 + \frac{1}{2}\frac{1}{E(1+\alpha\gamma_G T_0)}|\hat{\bar{\sigma}}|^2 \qquad [\mathrm{W/m^3}], \tag{4.31}$$

$$\tilde{I} = \frac{1}{2}\mathrm{Re}[\hat{\bar{\sigma}}\hat{v}^*] \qquad [\mathrm{W/m^2}], \tag{4.32}$$

$$\tilde{\mathscr{R}} = \frac{1}{2}\frac{\alpha}{1+\alpha\gamma_G T_0}\frac{\mathrm{d}T_0}{\mathrm{d}x}\mathrm{Re}[\hat{\bar{\sigma}}\hat{v}^*] \qquad [\mathrm{W/m^3}] \tag{4.33}$$

Now we are to find the separate expressions of $\tilde{\mathscr{P}}$ and $\tilde{\mathscr{D}}$. With the definition of the dimensionless function g_k, we transform $\langle q_1 \rangle_r$ to the frequency domain. The cross sectional average of the third term on the right hand side of Eqn. (4.17) can be written as

$$\langle \frac{\kappa}{\rho c_\varepsilon} \frac{1}{r} \frac{\partial}{\partial r} (r \frac{\partial T_1}{\partial r}) \rangle_r = \frac{2\kappa}{R\rho c_\varepsilon} \frac{\partial T_1}{\partial r} \mid_{r=R} = \frac{\langle q_1 \rangle_r}{R\rho c_\varepsilon} \tag{4.34}$$

Transforming $\langle q_1 \rangle_r$ to the frequency domain, the above term is written as $\frac{\hat{q}}{R\rho c_\varepsilon}$ in frequency. Comparing $\frac{\hat{q}}{R\rho c_\varepsilon}$ to the third term on the RHS of Eqn. (6) in the main text, $\hat{q}$ can be written as

$$\hat{q} = R\rho c_\varepsilon (\mathrm{i}\omega g_k) \hat{T} = \frac{R\rho c_\varepsilon}{\alpha} (\mathrm{i}\omega g_k)(\hat{\varepsilon} + \frac{\hat{\bar{\sigma}}}{E}). \tag{4.35}$$

Expanding the right hand side of Eqn. (4.30), we get the clear expressions of $\tilde{\mathscr{P}}$ and $\tilde{\mathscr{D}}$ separately,

$$\tilde{\mathscr{P}} = \frac{1}{2} \frac{1}{1 + \alpha\gamma_G T_0} \{\mathrm{Re}[g_k]\mathrm{Re}[\hat{\bar{\sigma}}(\mathrm{i}\omega\hat{\varepsilon})^*] + \mathrm{Im}[g_k]\mathrm{Im}[\hat{\bar{\sigma}}(\mathrm{i}\omega\hat{\varepsilon})^*]\} \qquad [\mathrm{W/m^3}], \tag{4.36}$$

$$\tilde{\mathscr{D}} = \frac{\omega}{2} \frac{1}{E(1 + \alpha\gamma_G T_0)} |\hat{\bar{\sigma}}|^2 \mathrm{Im}[g_k] \qquad [\mathrm{W/m^3}]. \tag{4.37}$$

which indicate the thermoacoustic production and dissipation in each cycle. Note that the thermoacoustic dissipation $\tilde{\mathscr{D}}$ comes from the wall heat transfer. It's a pure conductive loss, nothing to do with mechanical dissipations.

The growth rate can be recovered via

$$\beta_{\mathrm{EB}} = \frac{\tilde{\mathscr{P}} - \tilde{\mathscr{D}} - (\frac{\partial \tilde{I}}{\partial x} + \tilde{\mathscr{R}})}{2\tilde{\mathscr{E}}}. \tag{4.38}$$

As Fig. 4.11 shows, the growth rates β_{EB} calculated from Eqn. (4.38) are within 0.4% from the direct output of the eigenvalue problem (Eqns. (4.1), (4.2) and (4.3)) in both the standing wave and the traveling wave configurations, which validates the consistency of the derivations in this section.

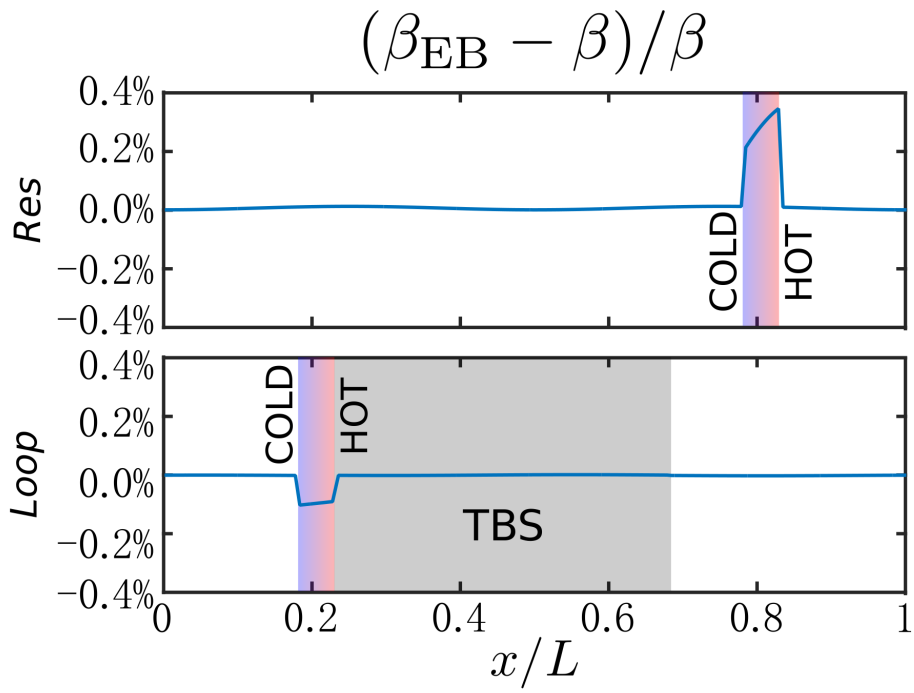

Figure 4.11. The relative difference of the growth rates estimated from the energy budgets β_{EB} and directly retrieved from the eigenvalue problem in Eqns. (4.1), (4.2) and (4.3) for the standing wave configuration ('*Res*') and the traveling wave configuration ('*Loop*').

From the physical point of view, the significance of the terms in Eqn. (4.30) are illustrated as following. $2\beta\tilde{\mathscr{E}}$ quantifies the rate of energy accumulation, $\mathrm{d}\tilde{I}/\mathrm{d}x$ is the work source defined in the previous section, $\tilde{\mathscr{R}}$ is an energy redistribution term. $\tilde{\mathscr{P}}$ and $\tilde{\mathscr{D}}$ are the thermoacoustic production and dissipation, respectively. The energy redistribution term in the acoustic energy budgets of solid thermoacoustics cannot be found in the fluid counterpart of the same equations [28]. This term is absent in fluids because it is canceled in the algebraic derivations by expressing the variation of mean density according to the ideal gas law, as a function of the mean temperature gradient. On the other hand, in solid-state thermoacoustics, the heat-induced density variation is neglected and the impact of the temperature gradient is manifest in the stress-strain constitutive relation. It is proved numerically that the spatial integration of this term is zero (see Supplementary Material), so it does not produce or dissipate energy, but just redistributes it. In summary, it represents the work created by the acoustic flux acting against the temperature gradient. Figure 4.12

plots every term in the acoustic energy budgets (Eqn. (4.30)) in the standing wave and traveling wave configurations, respectively.

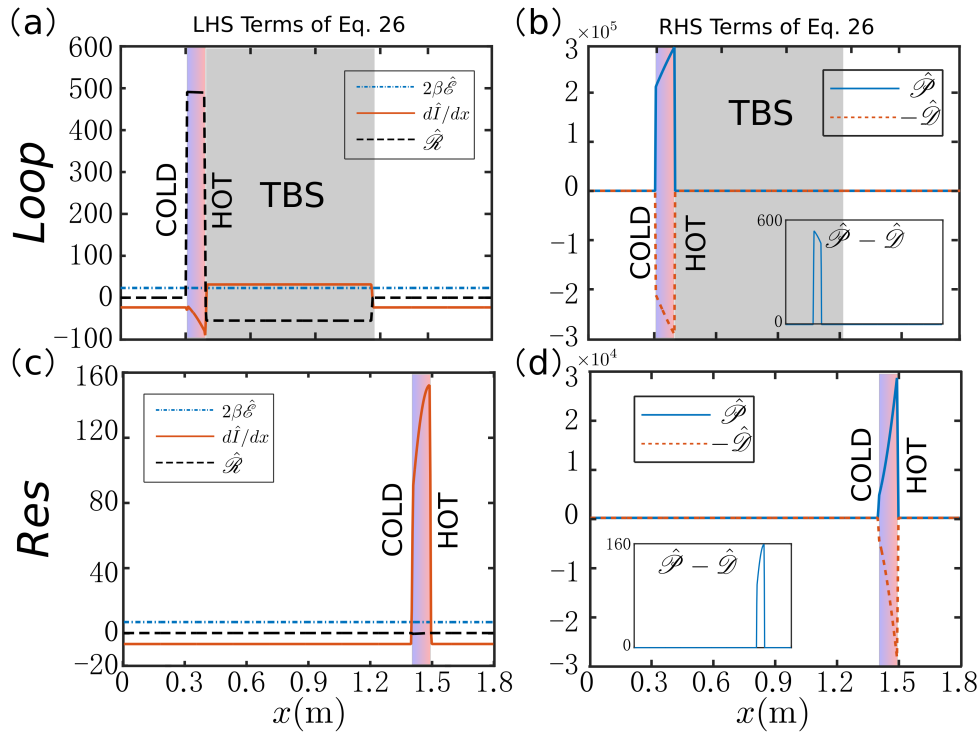

Figure 4.12. The terms in the acoustic energy budgets (Eqn. (4.30)) for (a) and (b) the traveling wave configuration ('*Loop*') and, (c) and (d) the standing wave configuration ('*Res*'). The insets in (b) and (d) plot the difference of the thermoacoustic production $\tilde{\mathscr{P}}$ and dissipation $\tilde{\mathscr{D}}$ in both configurations. The spatial integration of $\tilde{\mathscr{P}} - \tilde{\mathscr{D}}$ yields the total energy accumulation rate (see Eqn. (4.39)).

The values of $\tilde{\mathscr{P}}$ and $\tilde{\mathscr{D}}$ are non-zero only in the S-segment. The dissipation $\tilde{\mathscr{D}}$ is due to wall heat transfer, which is a conductive loss. Although they are very similar in the S-segment, there exists a small difference between them. Thus, from a thermal standpoint, as a given amount of heat is transported through this section, a small portion of it (proportional to $\tilde{\mathscr{P}} - \tilde{\mathscr{D}}$) is converted into wave energy which accumulates in the rod, hence sustaining growth. Regarding $\tilde{\mathscr{P}}$, a remarkable difference with thermoacoustic waves in fluids is present. In the latter case [28], $\tilde{\mathscr{P}}$ can be explicitly expressed as the weighted combination of a standing wave ($\mathrm{Im}[\hat{p}^*\hat{U}]$) and traveling wave ($\mathrm{Re}[\hat{p}^*\hat{U}]$) (Eqn. (4.13a) in [28]), where p and U are

the pressure and flow rates, respectively, so the traveling-/standing-wave contribution of the thermoacoustic production $\tilde{\mathscr{P}}$ is zero when the mode is purely standing/traveling. However in solids, the two terms on the right hand side of Eqn. (4.36) do not depend on the wave phasing, since whether they are zero or not only depends on if there is thermal coupling (if $\hat{T}$ is zero). So these two terms can not be considered as the TWC and SWC contributions of the thermoacoustic energy production $\tilde{\mathscr{P}}$.

As can be seen, $2\beta\tilde{\mathscr{E}}$ is flat, meaning that the rate of the energy accumulation along the rod is uniform and exponential in time, consistent with the eigenvalue ansatz.

In the standing wave configuration, the work flux gradient $\mathrm{d}\tilde{I}/\mathrm{d}x$ peaks in the S-segment, and has a constant negative value out of the S-segment. As foreshadowed by the discussions in the previous section, this distribution means that $\mathrm{d}\tilde{I}/\mathrm{d}x$ adjusts itself so that β is uniform. In other words, energy is accumulated everywhere at the same rate.

Neglecting the small phase shift caused by β, the energy redistribution $\tilde{\mathscr{R}}$ does not exist in the standing wave configuration because of the 90° phase difference between $\hat{\bar{\sigma}}$ and $\hat{v}$. Locally, the produced work in the S-segment, is converted from the most of the net production $\tilde{\mathscr{P}} - \tilde{\mathscr{D}}$. The remaining of $\tilde{\mathscr{P}} - \tilde{\mathscr{D}}$ transforms to the accumulated energy in this small segment. Outside the S-segment, the negative value of $\mathrm{d}\tilde{I}/\mathrm{d}x$ is exactly the same as the rate of the energy accumulation to keep the condition of zero local net production.

In the traveling wave configuration, the energy conversion becomes different because of the existence of the TBS. The TBS creates a temperature drop, which makes the energy redistribution term non zero in this section. To balance the negative value in the TBS, it peaks up in the S-segment so that the spatial integration is zero. In the TBS, the shape of the work flux gradient is the mirror image of that of the energy redistribution term because the addition of these two terms should be the negative of the spatially uniform energy accumulation rate. For the work flux gradient itself, a negative distribution in the S-segment is necessary to balance the positive redistributed work in the TBS so that the spatial integration is zero. The above supplements the explanations in the previous section on why the work source is negative in the S-segment.

Globally, in both configurations, given that both the spatial integrations of the work flux gradient and the energy redistribution terms are zero, the total net production $\int_0^L (\tilde{\mathscr{P}} - \tilde{\mathscr{D}})dx$ only leads to the accumulation of energy

$$\int_0^L 2\beta\tilde{\mathscr{E}}dx = \int_0^L (\tilde{\mathscr{P}} - \tilde{\mathscr{D}})dx. \tag{4.39}$$

Efficiency

Generally, efficiency is defined as the ratio of work done to thermal energy consumed. However, since there is no energy harvesting element in the system, the rod has no work output. Thus, we take the accumulated energy, which could be potentially converted to energy output, as the numerator of the ratio. For the denominator, limited to the 1D assumption, the thermal energy consumed is not available directly from the quasi-1D model because the evaluation of the radial heat conduction at the boundary is lacking. Swift [57] suggested that the heat flux $\dot{Q}$ could be considered as uniform for a short stack, which is approximately equal to the consumed thermal energy. Thus, we use the averaged $\dot{Q}$ over the S-segment, an estimate of the consumed thermal energy, as the denominator of the efficiency. As a result, the efficiency η is expressed as

$$\eta = \frac{A\int_0^L \frac{\partial \mathscr{E}_2}{\partial t}dx}{\frac{1}{l_s}\int_{x_s-\frac{l_s}{2}}^{x_s+\frac{l_s}{2}} \dot{Q}dx} \tag{4.40}$$

$$= \frac{\int_0^L 2\beta\tilde{\mathscr{E}}dx}{\frac{1}{l_s}\int_{x_s-\frac{l_s}{2}}^{x_s+\frac{l_s}{2}} \tilde{Q}dx}. \tag{4.41}$$

Although this definition is the best estimate we could make based on the quasi-1D model, we highlight that fully nonlinear 3D simulations are capable of providing more accurate estimates of the efficiency.

Figure 4.13 shows the efficiencies of '*Loop*' and '*Res*' at different temperature difference $\Delta T = T_h - Tc$. It can be seen from this plot that (1) the efficiency of the traveling wave configuration '*Loop*' is much higher than that of the standing wave configuration *Res*, which

is consistent with the conclusions drawn in fluids, and (2) for the traveling wave configuration, the efficiency goes up with ΔT increasing, while for the standing wave one, the efficiency is insensitive to the change of ΔT. For the cases studied in the previous sections ($\Delta T = 493.15\text{K} - 293.15\text{K} = 200\text{K}$), the efficiencies η are 37% and 7% for '*Loop*' and '*Res*', respectively, as the red dots show in Fig. 4.13.

Considering that the material properties of solids are much more tailorable than fluids, the authors expect that the efficiency of SSTA can be improved by designing an inhomogeneous medium having optimized mechanical and thermal thermoacoustic properties.

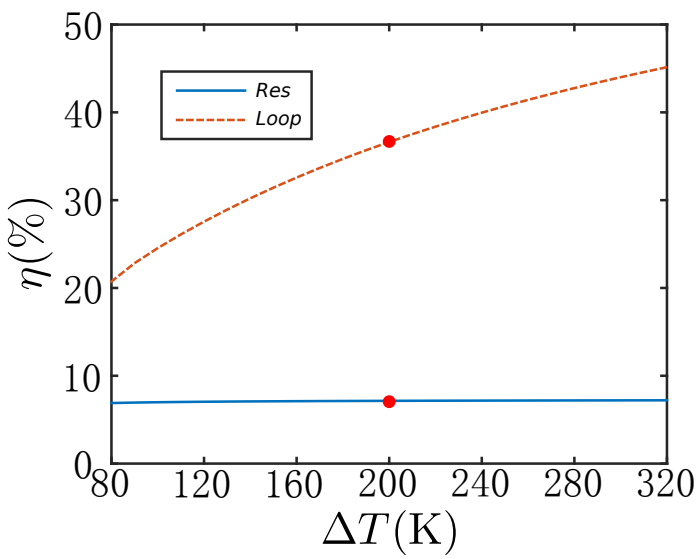

Figure 4.13. The efficiencies of the traveling wave configuration ('*Loop*') and the standing wave configuration ('*Res*') at different temperature difference ΔT. The efficiencies are 37% and 7%, respectively at $\Delta T = 200K$ (The red dots).

4.4 Concluding Remarks

In this chapter, we firstly show the numerical evidence of existence of thermoacoustic oscillations in a sample system consisting of a fixed-mass metal rod. The theory served as a starting point to develop a quasi-1D linearized model to perform stability analysis. A multi-stage configuration was proposed in order to overcome the effect of structural damping, which is one of the main differences with respect to the thermoacoustics of fluids.

In the second part of the chapter, we have shown numerical evidence of the existence of traveling wave thermoacoustic oscillations in a looped solid rod. The growth ratio of a full wavelength traveling wave in a looped rod is found to be significantly larger than that of a full wavelength standing wave in a resonance rod. The phase delay in the looped rod between negative stress and particle velocity, which controls the value of TWC, is at most 30° under the situation that the stage is $5\%L$ long and $\Delta T_0 = 200K$. Heat flux, mechanical power and work source are derived in analogous ways to their counterparts in fluids. The perturbation acoustic energy budgets are performed to interpret the energy conversion process of SSTA engines. The efficiency of SSTA engines is defined based on the rigorously derived energy budgets. The traveling wave SSTA engine is found to be more efficient than its standing wave counterpart.

This chapter laid the theoretical foundation of thermoacoustics of solids and provided key insights into the underlying mechanisms leading to self-sustained oscillations in thermally-driven solid systems. It is envisioned that the physical phenomenon explored in this study could serve as the fundamental principle to develop a new generation of solid state thermoacoustic engines and refrigerators.

5. PARAMETRIC ANALYSIS OF A-SSTA

5.1 Introduction

Chapter 4 showed the existence of unstable thermoacoustic waves in solids in both standing and traveling modes. Contrary to fluids, solids exhibit unique opportunities to tailor both physical and effective dynamic properties that can ultimately greatly benefit the thermoacoustic response of SSTA. The many recent efforts in the development of engineered materials and structures have highlighted the remarkable design space offered by these man-made materials.[58], [59] In order to take full advantage of this capability of tailoring the dynamic response of solids for the design of SSTA devices methodologies for the systematic performance and parametric analysis of SSTA systems are necessary.

In this Chapter, an analytical approach is proposed to solve the governing equations of axial-mode standing and traveling SSTA waves in a fixed-mass rod [51] and a looped rod [60] configuration, respectively [61]. The governing equations are recast into dimensionless form facilitating the identification of a set of seven dimensionless parameters that directly impact the growth-rate-to-frequency ratio (growth ratio) [25]. In the present thesis, this ratio is considered as the fundamental metric to compare the performance of different designs. The seven dimensionless parameters are: the dimensionless coefficient of thermal expansion (CTE), the Grüneisen parameter, the hot-to-cold temperature ratio, the normalized stage location and length, the dimensionless radius, the end mass ratio for the fxed-mass rod, and the dimensionless thermal buffer segment (TBS) length for the looped rod. The above parameters will be analyzed in detail particularly from a perspective of growth ratio optimization. This parametric analysis allows shedding light on the effect of different material and structural parameters on the design of SSTA devices.

5.2 Dimensionless Quasi-1D model

The two configurations being considered in this chapter are: 1) the fixed-mass axial SSTA [51], and 2) the looped rod in [60]. The axial thermoacoustic modes for both systems can

be obtained using the governing equations defined in Chapter 4, i.e.: Eqns. (4.1), (4.2) and (4.3).

The two SSTA configurations differ in terms of the distribution of the reference mean temperature $T_0(x)$, function $G_k(x)$ and of the boundary conditions (BCs). The specific conditions for the two cases are given here below:

Case 1: Fixed-mass rod - Standing mode SSTA

$$T_0(x) = \begin{cases} T_h & 0 < x < x_h \\ T_h + \frac{T_c - T_h}{x_c - x_h}(x - x_h) & x_h < x < x_c \\ T_c & x_c < x < L \end{cases} \tag{5.1}$$

$$G_k(x) = \begin{cases} g_k = \dfrac{1}{1 - \frac{1}{2}\zeta_{top}\dfrac{J_0(\zeta_{top})}{J_1(\zeta_{top})}} & x_h < x < x_c \\ 0 & \text{elsewhere} \end{cases}, \tag{5.2}$$

where x_h and x_c are the axial locations of the two ends of the stage, T_h and T_c are temperatures of segment 1 ($0 < x < x_h$) and segment 3 ($x_c < x < L$), corresponding to the hot and cold temperatures.

The dimensional boundary conditions are:

$$\hat{u}|_{x=0} = 0 \tag{5.3}$$

$$\hat{\sigma}|_{x=L}\mathcal{A} = -\mathrm{i}\Lambda(\hat{v}|_{x=L})M \tag{5.4}$$

where $\mathcal{A}$ is the rod cross-sectional area, and M is the end mass.

Case 2: Looped rod - Traveling mode SSTA

$$T_0(x) = \begin{cases} T_c & 0 < x < x_c,\ x_b < x < L \\ T_c + \frac{T_h - T_c}{x_h - x_c}(x - x_c) & x_c < x < x_h \\ T_h + \frac{T_b - T_h}{x_b - x_h}(x - x_h) & x_h < x < x_b \end{cases} \tag{5.5}$$

$$G_K(x) = \begin{cases} g_k & x_c < x < x_h \\ 0 & \text{elsewhere} \end{cases}, \tag{5.6}$$

where x_b is the end position of the thermal buffer segment (TBS).

The dimensional BCs are:

$$\hat{u}|_{x=0} = \hat{u}|_{x=L} \tag{5.7}$$

$$\hat{\sigma}|_{x=0} = \hat{\sigma}|_{x=L} \tag{5.8}$$

Considering Table 5.1, we can recast both the governing equations (Eqns. (4.1), (4.2) and (4.3)) and the boundary conditions (Eqns. 5.3-5.8) into a dimensionless form:

$$\mathrm{i}\lambda\tilde{u} = \tilde{v} \tag{5.9}$$

$$\mathrm{i}\lambda\tilde{v} = \frac{\mathrm{d}^2\tilde{u}}{\mathrm{d}\xi^2} - A\frac{\mathrm{d}\tilde{T}}{\mathrm{d}\xi} \tag{5.10}$$

$$\mathrm{i}\lambda\tilde{T} = -\frac{\mathrm{d}\theta_0(\xi)}{\mathrm{d}\xi}\tilde{v} - \gamma_G\theta_0(\xi)\frac{\mathrm{d}\tilde{v}}{\mathrm{d}\xi} + \mathrm{i}\lambda G_k(\xi)\tilde{T} \tag{5.11}$$

Fixed-mass:

$$\tilde{u}|_{\xi=0} = 0 \tag{5.12}$$

$$\tilde{\sigma}|_{\xi=1} = m\lambda^2\tilde{u}|_{\xi=1} \tag{5.13}$$

Table 5.1. Dimensionless variables, parameters, and auxiliary dimensional quantities

Dimensionless variables

$\xi = x/L$	Dimensionless axial coordinate
$\tilde{u} = \hat{u}/L$	Dimensionless particle displacement
$\tilde{v} = \hat{v}/a_0$	Dimensionless particle velocity
$\tilde{T} = \langle\hat{T}\rangle/Tc$	Dimensionless temperature fluctuation
$\tilde{\sigma} = \hat{\sigma}/E = du/d\xi - A\tilde{T}$	Dimensionless stress
$\mathrm{i}\lambda = \mathrm{i}\Lambda/\omega_0$	Dimensionless eigenvalue
$\beta = \mathrm{Re}[\mathrm{i}\lambda]$	Dimensionless growth rate
$\omega = \mathrm{Im}[\mathrm{i}\lambda]$	Dimensionless frequency

Dimensionless parameters

$A = \alpha T_c$	Dimensionless coefficient of thermal expansion (CTE)
$\gamma_G = \alpha E/(\rho c_\varepsilon)$	Grüneisen constant
$\Theta = T_h/Tc$	Temperature ratio
$r = R/\delta_k$	Dimensionless radius (frequency dependent)
$\xi_h = x_h/L$	Dimensionless stage hot end position
$\xi_c = x_c/L$	Dimensionless stage cold end position
$\xi_b = x_b/L$	Dimensionless TBS end position (looped rod only)
$m = M/(\rho L\mathcal{A})$	Mass ratio (fixed-mass rod only)

Auxiliary dimensional quantities

$a_0 = \sqrt{E/\rho}$ [m/s]	Sound speed
$\omega_0 = a_0/L$ [1/s]	Characteristic frequency
$\delta_k = \sqrt{2\kappa/(\omega\rho c_\varepsilon)}$ [m]	Thermal penetration depth (frequency-dependent)

Looped:

$$\tilde{u}|_{\xi=0} = \tilde{u}|_{\xi=L} \tag{5.14}$$

$$\tilde{\sigma}|_{\xi=0} = \tilde{\sigma}|_{\xi=L} \tag{5.15}$$

Figure 5.1 shows the distribution of the dimensionless mean temperature $\theta_0(\xi)$ and of the wall-heat-transfer function $G_k(\xi)$.

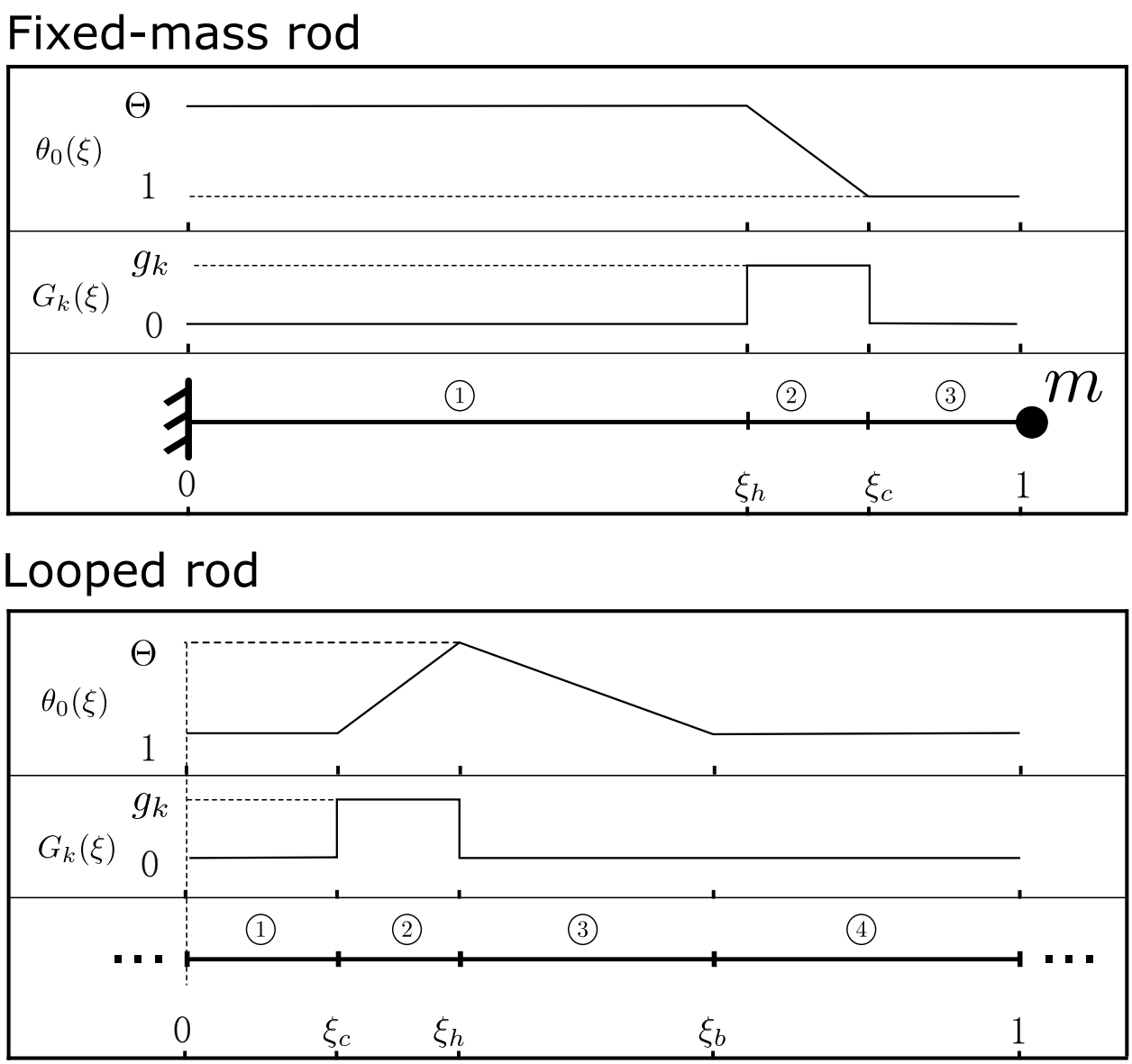

Figure 5.1. Distribution of $\theta_0(\xi)$ and $G_k(\xi)$ for the fixed-mass rod and the looped rod. Circled numbers indicate the segmentation of the rods.

5.3 Analytical Solution: Derivation and Validation

From Eqns. (5.9-5.15), the dimensionless parameters which determine the value of λ are the material parameters A and γ_G, the dimensionless temperature profile $\theta_0(\xi)$, specifically Θ, ξ_h and ξ_c, the frequency-dependent dimensionless radius r, which determines g_k, and (only for the fixed-mass case) the mass ratio m.

Rearranging Eqn. (5.11), a local solution of T is obtained:

$$\tilde{T} = \frac{[\mathrm{d}\theta_0(\xi)/\mathrm{d}\xi]\tilde{u} + \gamma_G\theta_0(\xi)[\mathrm{d}\tilde{u}/\mathrm{d}\xi]}{G_k(\xi) - 1} \tag{5.16}$$

Thus:

$$\frac{\mathrm{d}\tilde{T}}{\mathrm{d}\xi} = (G_k(\xi) - 1)^{-1}[(1 + \gamma_G)\frac{\mathrm{d}\theta_0}{\mathrm{d}\xi}\frac{\mathrm{d}\tilde{u}}{\mathrm{d}\xi} + \gamma_G\theta_0(\xi)\frac{\mathrm{d}^2\tilde{u}}{\mathrm{d}\xi^2}] \tag{5.17}$$

Note that $\mathrm{d}^2\theta_0/\mathrm{d}\xi^2 = 0$ is assumed due to the piece-wise linearity of $\theta_0(\xi)$.

Substituting Eqns. (5.9) and (5.17) into Eqn. (5.10) and rearranging, a second order ODE is obtained:

$$a(\xi)\frac{\mathrm{d}^2\tilde{u}}{\mathrm{d}\xi^2} + b(\xi)\frac{\mathrm{d}\tilde{u}}{\mathrm{d}\xi} + c\tilde{u} = 0 \tag{5.18}$$

where:

$$a(\xi) = 1 + \frac{A\gamma_G}{1 - G(x)}\theta_0(\xi) \tag{5.19}$$

$$b(\xi) = \frac{A(1 + \gamma_G)}{1 - G(x)}\frac{\mathrm{d}\theta_0(\xi)}{\mathrm{d}\xi} \tag{5.20}$$

$$c = \lambda^2 \tag{5.21}$$

From this point on, the procedure for the two cases requires a different treatment.

Case 1: Fixed-mass rod (Standing mode):

For the three segments shown in Fig. 5.1 (1: $0 < \xi < \xi_h$, 2: $\xi_h < \xi < \xi_c$, 3: $\xi_c < \xi < 1$), the expressions for $a(\xi)$, $b(\xi)$, and c are given in Table 5.2.

Table 5.2. Coefficients $a(\xi)$, $b(\xi)$, and c for segments of the fixed-mass rod

<u>Segment 1</u> $(0 < \xi < \xi_h)$: $\begin{cases} a_1 &= 1 + A\gamma_G\Theta \\ b_1 &= 0 \\ c_1 &= \lambda^2 \end{cases}$

<u>Segment 2</u> $(\xi_h < \xi < \xi_c)$: $\begin{cases} a_2(\xi) &= 1 + \frac{A\gamma_G}{1-g_k}(\Theta + \frac{1-\Theta}{\xi_c-\xi_h}(\xi - \xi_h)) \\ b_2 &= \frac{A(1+\gamma_G)}{1-g_k}\frac{1-\Theta}{\xi_c-\xi_h} \\ c_2 &= \lambda^2 \end{cases}$

<u>Segment 3</u> $(\xi_c < \xi < 1)$: $\begin{cases} a_3 &= 1 + A\gamma_G \\ b_3 &= 0 \\ c_3 &= \lambda^2 \end{cases}$

So for Segment 1 and 3, Eqn. (5.18) degenerates to two constant-coefficient second order ODEs. Their general solution is given by:

$$\tilde{u}_1 = A_1 \mathrm{e}^{\mathrm{i}\lambda R_1 \xi} + B_1 \mathrm{e}^{-\mathrm{i}\lambda R_1 \xi} \tag{5.22}$$

$$\tilde{u}_3 = A_3 \mathrm{e}^{\mathrm{i}\lambda R_3 \xi} + B_3 \mathrm{e}^{-\mathrm{i}\lambda R_3 \xi} \tag{5.23}$$

where A_1, B_1, A_3, and B_3 are coefficients to be determined, while R_1 and R_3 are given by:

$$R_1 = \frac{1}{\sqrt{1 + A\gamma_G\Theta}} \tag{5.24}$$

$$R_3 = \frac{1}{\sqrt{1 + A\gamma_G}} \tag{5.25}$$

For Segment 2, $a(\xi)$ becomes a linear function $a_2(\xi) = a_{21} + a_{22}\xi$ where:

$$a_{21} = 1 + \frac{A\gamma_G}{1 - g_k}(\Theta - \frac{1-\Theta}{\xi_c - \xi_h}\xi_h) \tag{5.26}$$

$$a_{22} = \frac{A\gamma_G}{1 - g_k}(\frac{1-\Theta}{\xi_c - \xi_h}) \tag{5.27}$$

and $b(\xi)$ becomes a constant b_2 (Table 5.2). Thus Eqn. (5.18) for this segment becomes:

$$(a_{21} + a_{22}\xi)\frac{\mathrm{d}^2\tilde{u}_2}{\mathrm{d}\xi^2} + b_2\frac{\mathrm{d}\tilde{u}_2}{\mathrm{d}\xi} + c_2\tilde{u}_2 = 0 \tag{5.28}$$

Assume that the solution u_2 can be expanded via a Taylor series that converges on the interval ($\xi_h < \xi < \xi_c$). Specifically:

$$\tilde{u}_2 = \sum_{n=0}^{\infty} \beta_n \xi^n \tag{5.29}$$

Substituting the expansion back into Eqn. (5.28) yields:

$$\sum_{n=1}^{\infty} [a_{21}(n+2)(n+1)\beta_{n+2} + [b_2 + a_{22}n](n+1)\beta_{n+1} + c_2\beta_n]\xi^n \\ +[2a_{21}\beta_2 + b_2\beta_1 + c_2\beta_0] = 0 \tag{5.30}$$

Considering that ξ^{j} is independent of ξ^k for $\mathrm{j} \neq k$, for any $n \geqslant 0$, the above equation gives:

$$a_{21}(n+2)(n+1)\beta_{n+2} + [b_2 + a_{22}n](n+1)\beta_{n+1} + c_2\beta_n = 0 \tag{5.31}$$

From Eqn. (5.31), all β_n for $n \geqslant 2$ could be determined from assigned values of β_0 and β_1. β_n can be expressed as a linear combination of β_0 and β_1, namely:

$$\beta_n = c_{\beta 0}(n)\beta_0 + c_{\beta 1}(n)\beta_1 \qquad n \geqslant 2 \tag{5.32}$$

where, the coefficients $c_{\beta 0}(n)$ and $c_{\beta 1}(n)$ can be found recursively by:

$$c_{\beta 0}(n+2) = -\frac{c_2}{a_{21}(n+2)(n+1)}c_{\beta 0}(n) - \frac{b_2 + a_{22}n}{a_{21}(n+2)}c_{\beta 0}(n+1) \tag{5.33}$$

$$c_{\beta 1}(n+2) = -\frac{c_2}{a_{21}(n+2)(n+1)}c_{\beta 1}(n) - \frac{b_2 + a_{22}n}{a_{21}(n+2)}c_{\beta 1}(n+1), \qquad n \geqslant 0 \tag{5.34}$$

$$c_{\beta 0}(0) = 1, \quad c_{\beta 0}(1) = 0, \quad c_{\beta 1}(0) = 0, \quad c_{\beta 1}(1) = 1 \tag{5.35}$$

Consider the fact that Eqns. (5.9-5.13) are linear equations; and $\tilde{u}, \tilde{v}$, and $\tilde{T}$ denote the corresponding mode shapes, A_1 is arbitrarily taken as $A_1 = 1$. Therefore, the six independent

unknowns β_0, β_1, B_1, B_2, B_3 and λ should be evaluated. The boundary conditions of each segment (a total of six BCs) are expressed as:

$$\xi = 0: \quad \tilde{u}_1|_{\xi=0} = 0 \tag{5.36}$$

$$\xi = \xi_h: \quad \tilde{u}_1|_{\xi=\xi_h} = \tilde{u}_2|_{\xi=\xi_h} \tag{5.37}$$

$$\xi = \xi_h: \quad \tilde{\sigma}_1|_{\xi=\xi_h} = \tilde{\sigma}_2|_{\xi=\xi_h} \tag{5.38}$$

$$\xi = \xi_c: \quad \tilde{u}_2|_{\xi=\xi_c} = \tilde{u}_3|_{\xi=\xi_c} \tag{5.39}$$

$$\xi = \xi_c: \quad \tilde{\sigma}_2|_{\xi=\xi_c} = \tilde{\sigma}_3|_{\xi=\xi_c} \tag{5.40}$$

$$\xi = 1: \quad \tilde{\sigma}_3|_{\xi=1} = m\lambda^2(\tilde{u}_3|_{\xi=1}) \tag{5.41}$$

This set of equations could be solved iteratively by initializing the calculation with an initial guess $\lambda^{(0)}$. The steps of one iteration are as follows:

Step 1: By Eqn. (5.36):

$$B_1 = -1 \tag{5.42}$$

$$\tilde{u}_1 = 2\mathrm{i}\sin(\lambda R_1 \xi) \tag{5.43}$$

Step 2: Eqns. (5.37) and (5.38) give:

$$\underline{\mathrm{F}}_2 = \underline{\mathrm{C}}_2\, \underline{\mathrm{b}}_2 \tag{5.44}$$

where:

$$\underline{\mathrm{F}}_2 = 2\mathrm{i} \begin{bmatrix} 1 & 0 \\ -\frac{A}{1-g_k}\frac{1-\Theta}{\xi_h-\xi_c} & (1+A\gamma_G\Theta)(\lambda R1) \end{bmatrix} \begin{bmatrix} \sin(\lambda R_1 \xi_h) \\ \cos(\lambda R_1 \xi_h) \end{bmatrix} \tag{5.45}$$

$$\underline{\mathrm{C}}_2 = \begin{bmatrix} 1 + \sum_{n=2}^{\infty} \xi_h^n c_{\beta 0}(n) & \xi_h + \sum_{n=2}^{\infty} \xi_h^n c_{\beta 1}(n) \\ (1+\frac{A\gamma_G\Theta}{1-g_k}) \sum_{n=2}^{\infty} n\xi_h^{n-1} c_{\beta 0}(n) & (1+\frac{A\gamma_G\Theta}{1-g_k})(1+\sum_{n=2}^{\infty} n\xi_h^{n-1} c_{\beta 1}(n)) \end{bmatrix} \tag{5.46}$$

$$\underline{\mathrm{b}}_2 = \begin{bmatrix} \beta_0 \\ \beta_1 \end{bmatrix} \tag{5.47}$$

Rename β_0 and β_1 as A_2 and B_2. They are therefore given by:

$$\begin{bmatrix} A_2 \\ B_2 \end{bmatrix} = \underline{\mathrm{b}}_2 = \underline{\mathrm{C}}_2{}^{-1}\underline{\mathrm{F}}_2 \tag{5.48}$$

Step 3: Eqns. (5.39) and (5.40) give:

$$\underline{\mathrm{F}}_3 = \underline{\mathrm{C}}_3\,\underline{\mathrm{b}}_3 \tag{5.49}$$

where:

$$\underline{\mathrm{F}}_3 = \begin{bmatrix} 0 & 1 \\ 1 + \frac{A\gamma_G}{1-g_k} & \frac{A}{1-g_k}\frac{1-\Theta}{\xi_c-\xi_h} \end{bmatrix} \begin{bmatrix} \sum_{n=1}^{\infty} \beta_n n \xi_c^{n-1} \\ \sum_{n=0}^{\infty} \beta_n \xi_c^{n} \end{bmatrix} \tag{5.50}$$

$$\underline{\mathrm{C}}_3 = \begin{bmatrix} \exp(\mathrm{i}\lambda R_3 \xi_c) & \exp(-\mathrm{i}\lambda R_3 \xi_c) \\ [1 + A\gamma_G(2\mathrm{i}\lambda R_3)]\exp(\mathrm{i}\lambda R_3 \xi_c) & -[1 + A\gamma_G(2\mathrm{i}\lambda R_3)]\exp(\mathrm{i}\lambda R_3 \xi_c) \end{bmatrix} \tag{5.51}$$

$$\underline{\mathrm{b}}_3 = \begin{bmatrix} A_3 \\ B_3 \end{bmatrix} \tag{5.52}$$

Therefore, A_3 and B_3 are given by:

$$\begin{bmatrix} A_3 \\ B_3 \end{bmatrix} = \underline{\mathrm{b}}_3 = \underline{\mathrm{C}}_3{}^{-1}\underline{\mathrm{F}}_3 \tag{5.53}$$

Step 4: By Eqn. (5.41), λ can be solved iteratively through:

$$\lambda^{(p+1)} = \mathrm{i}\frac{(1 + A\gamma_G)R_3}{m}\frac{A_3\exp(\mathrm{i}\lambda^{(p)}R_3) - B_3\exp(-\mathrm{i}\lambda^{(p)}R_3)}{A_3\exp(\mathrm{i}\lambda^{(p)}R_3) + B_3\exp(-\mathrm{i}\lambda^{(p)}R_3)} \tag{5.54}$$

where (p) is the index for iterative step.

Step 5: Average $\lambda^{(p+1)}$ and $\lambda^{(p)}$, and perform a new iteration until the difference between λ's from two consecutive iterations is satisfied.

The coefficients A_{j} and $B_{\mathrm{j}}, (\mathrm{j} = 1, 2, 3)$ are expressed by Eqns. (5.42), (5.48) and (5.53) once λ reaches its convergence value. Thus, the displacement mode shape $\tilde{u}_{\mathrm{j}}$, the strain

$\tilde{\varepsilon}_{\mathrm{j}} = \mathrm{d}\tilde{u}_{\mathrm{j}}/\mathrm{d}\xi$, and the temperature $\tilde{T}_{\mathrm{j}}$ (see Eqn. (5.16)) for the three segments can be written in terms of $A_{\mathrm{j}}, B_{\mathrm{j}}$, and λ.

Case 2: Looped rod (Traveling mode)

The looped rod is virtually divided into four segments (Fig. 5.1), while continuity conditions (continuous $\tilde{u}$ and $\tilde{\sigma}$) hold at ξ_h ξ_c and ξ_b. In this case, The quantities $a(\xi)$, $b(\xi)$, and c are given in Table 5.3

Table 5.3. Coefficients $a(\xi)$, $b(\xi)$, and c for segments of the looped rod

Segment 1 & 4 ($0 < \xi < \xi_c$, $\xi_b\xi < 1$):	$\begin{cases} a_{1,4} &= 1 + A\gamma_G \\ b_{1,4} &= 0 \\ c_{1,4} &= \lambda^2 \end{cases}$
Segment 2 ($\xi_h < \xi < \xi_c$):	$\begin{cases} a_2(\xi) &= 1 + \frac{A\gamma_G}{1-g_k}(1 + \frac{1-\Theta}{\xi_c-\xi_h}(\xi - \xi_c)) \\ b_2 &= \frac{A(1+\gamma_G)}{1-g_k}\frac{1-\Theta}{\xi_c-\xi_h} \\ c_2 &= \lambda^2 \end{cases}$
Segment 3 ($\xi_c < \xi < 1$):	$\begin{cases} a_2(\xi) &= 1 + (A\gamma_G)(\Theta + \frac{1-\Theta}{\xi_b-\xi_h}(\xi - \xi_h)) \\ b_2 &= A(1+\gamma_G)\frac{1-\Theta}{\xi_b-\xi_h} \\ c_2 &= \lambda^2 \end{cases}$

By the periodicity condition at $\xi = 0$ and $\xi = 1$, the displacement $\tilde{u}$ of Segment 1 and 4 are:

$$\tilde{u}_1 = A_1 \mathrm{e}^{\mathrm{i}\lambda R_3 \xi} + B_1 \mathrm{e}^{-\mathrm{i}\lambda R_3 \xi} \tag{5.55}$$

$$\tilde{u}_4 = A_1 \mathrm{e}^{\mathrm{i}\lambda R_3 (\xi-1)} + B_1 \mathrm{e}^{-\mathrm{i}\lambda R_3 (\xi-1)} \tag{5.56}$$

Assuming that the displacement of Segment 2 and 3, (i.e. $\tilde{u}_2$ and $\tilde{u}_3$) have converging Taylor series on their own intervals:

$$\tilde{u}_2 = \sum_{n=0}^{\infty} \phi_n \xi^n \tag{5.57}$$

$$\tilde{u}_3 = \sum_{n=0}^{\infty} \psi_n \xi^n \tag{5.58}$$

Similar to Case 1, ϕ_n and ψ_n are linear combinations of ϕ_0 and ϕ_1, and ψ_0 and ψ_1, respectively:

$$\phi_n = d_{\phi 0}(n)\phi_0 + d_{\phi 1}(n)\phi_1 \qquad n \geqslant 2 \tag{5.59}$$

$$\psi_n = d_{\psi 0}(n)\psi_0 + d_{\psi 1}(n)\psi_1 \qquad n \geqslant 2 \tag{5.60}$$

where the coefficients $d_{\phi 0}(n)$, $d_{\phi 1}(n)$, $d_{\psi 0}(n)$, and $d_{\psi 1}(n)$ can be found recursively in the same fashion described in Case 1 (see Eqns. (5.33, 5.34)). By applying the continuity conditions at ξ_c, ξ_h, and ξ_b the following equation holds:

$$\underline{\mathrm{C}}\,\underline{\mathrm{b}} = 0 \tag{5.61}$$

where $\underline{\mathrm{C}}$ is a 6×6 matrix whose elements are expressed as:

$$\underline{\mathrm{C}}(1,1) = \mathrm{e}^{\mathrm{i}\lambda R_3 \xi_c}, \quad \underline{\mathrm{C}}(1,2) = \mathrm{e}^{-\mathrm{i}\lambda R_3 \xi_c}$$

$$\underline{\mathrm{C}}(1,3) = 1 + \sum_{n=2}^{\infty} \xi_c^n d_{\phi 0}(n), \quad \underline{\mathrm{C}}(1,4) = \xi_c + \sum_{n=2}^{\infty} \xi_c^n d_{\phi 1}(n)$$

$$\underline{\mathrm{C}}(2,1) = [(1 + A\gamma_G)(\mathrm{i}\lambda R_3) - \frac{A}{1-g_k}\frac{\Theta - 1}{\xi_h - \xi_c}]\mathrm{e}^{\mathrm{i}\lambda R_3 \xi_c}$$

$$\underline{\mathrm{C}}(2,2) = -[(1 + A\gamma_G)(\mathrm{i}\lambda R_3) + \frac{A}{1-g_k}\frac{\Theta - 1}{\xi_h - \xi_c}]\mathrm{e}^{-\mathrm{i}\lambda R_3 \xi_c}$$

$$\underline{\mathrm{C}}(2,3) = -(1 + \frac{A\gamma_G}{1-g_k}) \sum_{n=2}^{\infty} n \xi_c^{n-1} d_{\phi 0}(n)$$

$$\underline{\mathrm{C}}(2,4) = -(1 + \frac{A\gamma_G}{1-g_k}) \sum_{n=2}^{\infty} n \xi_c^{n-1} d_{\phi 1}(n)$$

$$\underline{\mathrm{C}}(3,3) = 1 + \sum_{n=2}^{\infty} \xi_h^n d_{\phi 0}(n), \quad \underline{\mathrm{C}}(3,4) = \xi_h + \sum_{n=2}^{\infty} \xi_h^n d_{\phi 1}(n)$$

$$\underline{\mathrm{C}}(3,5) = 1 + \sum_{n=2}^{\infty} \xi_h^n d_{\psi 0}(n), \quad \underline{\mathrm{C}}(3,6) = \xi_h + \sum_{n=2}^{\infty} \xi_h^n d_{\psi 1}(n)$$

$$\underline{\mathrm{C}}(4,3) = (1 + \frac{A\gamma_G\Theta}{1-g_k}) \sum_{n=2}^{\infty} n \xi_h^{n-1} d_{\phi 0}(n) + \frac{A}{1-g_k}\frac{\Theta - 1}{\xi_h - \xi_c}(1 + \sum_{n=2}^{\infty} \xi_h^n d_{\phi 0}(n))$$

$$\underline{\mathrm{C}}(4,4) = (1 + \frac{A\gamma_G\Theta}{1-g_k}) \sum_{n=2}^{\infty} n \xi_h^{n-1} d_{\phi 1}(n) + \frac{A}{1-g_k}\frac{\Theta - 1}{\xi_h - \xi_c}(1 + \sum_{n=2}^{\infty} \xi_h^n d_{\phi 1}(n))$$

$$\underline{\mathrm{C}}(4,5) = -(1 + A\gamma_G\Theta) \sum_{n=2}^{\infty} n \xi_h^{n-1} d_{\psi 0}(n) - A\frac{\Theta - 1}{\xi_h - \xi_b}(1 + \sum_{n=2}^{\infty} \xi_h^n d_{\psi 0}(n))$$

$$\underline{\mathrm{C}}(4,6) = -(1 + A\gamma_G\Theta) \sum_{n=2}^{\infty} n \xi_h^{n-1} d_{\psi 1}(n) - A\frac{\Theta - 1}{\xi_h - \xi_b}(1 + \sum_{n=2}^{\infty} \xi_h^n d_{\psi 1}(n))$$

$$\underline{\mathrm{C}}(5,1) = -\mathrm{e}^{\mathrm{i}\lambda R_3 (\xi_b - 1)}, \quad \underline{\mathrm{C}}(5,2) = -\mathrm{e}^{-\mathrm{i}\lambda R_3 (\xi_b - 1)}$$

$$\underline{\mathrm{C}}(5,5) = 1 + \sum_{n=2}^{\infty} \xi_b^n d_{\psi 0}(n), \quad \underline{\mathrm{C}}(5,6) = \xi_b + \sum_{n=2}^{\infty} \xi_b^n d_{\psi 1}(n)$$

$$\underline{\mathrm{C}}(6,1) = [A\frac{\Theta - 1}{\xi_h - \xi_b} - (1 + A\gamma_G)(1\mathrm{i}\lambda R_3)]\mathrm{e}^{\mathrm{i}\lambda R_3 (\xi_b - 1)}$$

$$\underline{\mathrm{C}}(6,2) = [A\frac{\Theta - 1}{\xi_h - \xi_b} + (1 + A\gamma_G)(1\mathrm{i}\lambda R_3)]\mathrm{e}^{-\mathrm{i}\lambda R_3 (\xi_b - 1)}$$

$$\underline{\mathrm{C}}(6,5) = (1 + A\gamma_G) \sum_{n=2}^{\infty} n \xi_b^{n-1} d_{\psi 0}(n) \quad \underline{\mathrm{C}}(6,6) = (1 + A\gamma_G) \sum_{n=2}^{\infty} n \xi_b^{n-1} d_{\psi 1}(n)$$

The elements in $\underline{\mathrm{C}}$ that were not defined above are implicitly assumed equal to zero. The vector $\underline{\mathrm{b}}$ is:

$$\underline{\mathrm{b}} = \begin{bmatrix} A_1 & B_1 & \phi_0 & \phi_1 & \psi_1 & \psi_1 \end{bmatrix}^{\mathrm{T}} \tag{5.62}$$

From Eqn. 5.61, the complex frequency λ is the root of:

$$\det[\underline{\mathrm{C}}(\lambda)] = 0 \tag{5.63}$$

which can be solved by a nonlinear numerical root finding approach. By arbitrarily choosing $A_1 = 1$, the remaining elements in the vector $\underline{\mathrm{b}}$ can be calculated. These coefficients enable recovering the mode shapes of displacement, strain and temperature.

To validate the analytical approach, we performed numerical simulations using the dimensional parameters tabulated in Table 5.4.

Table 5.4. Dimensional parameters used in numerical simulations

General:			
$\alpha = 23 \times 10^{-6}$ [1/K]	$E = 70$ [GPa]	$\rho = 2700$ [kg/m^3]	$\kappa = 238$ [W/mK]
$c_\varepsilon = 900$ [J/kgK]	$T_h = 493.15$ [K]	$T_c = 293.15$ [K]	$L = 1.8$ [m]
Fixed-mass rod:			
$x_h = 0.9L$	$x_c = 0.95L$	$r = 1$ [mm]	$M = 0.3527$ [kg]
Looped rod:			
$x_c = 0.18L$	$x_h = 0.23L$	$x_b = 0.68L$	$r = 0.1$ [mm]

The dimensional parameters were used in the numerical solver adopted by [51]. The spatial domain was discretized uniformly into 500 cells using a central Euler scheme on a staggered grid. The output eigenvalue and mode shape will be reported later in comparison to the analytical results.

The dimensional parameters can be grouped and recast into dimensionless parameters (Table 5.5).

Note that r is a frequency dependent quantity, which can be determined in either the iterative process or the nonlinear root finder.

λ is then solved differently for the two cases:

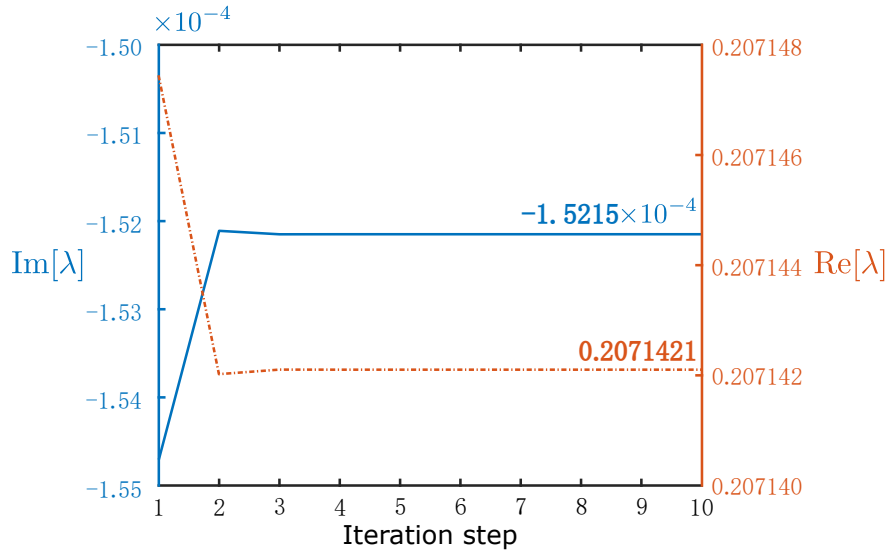

Figure 5.2. Iteration of real and imaginary part of the dimensionless λ.

Table 5.5. Dimensionless parameters used in analytical approach

General:	$A = 6.74 \times 10^{-3}$	$\gamma_G = 0.6626$	$\Theta = 1.682$	
Fixed-mass rod:	$r = 3.80\sqrt{1/\omega}$	$\xi_h = 0.9$	$\xi_c = 0.95$	$m = 23.101$
Looped rod:	$r = 0.38\sqrt{1/\omega}$	$\xi_c = 0.18$	$\xi_h = 0.23$	$\xi_b = 0.68$

Fixed-mass rod: To solve for λ, Eqn. (5.29) was truncated to six terms. By Eqn. (5.54), the value of λ at convergence was calculated as $0.20714 - (1.5215 \times 10^{-4})\mathrm{i}$. The iteration of the real and imaginary parts of λ are shown in Fig. 5.2. It is seen that the iterative process is very efficient for the calculation of λ. The dimensional eigenvalue $\mathrm{i}\Lambda$ can be recovered as $0.430 + 585.95\mathrm{i}$, the error is within 0.5% from $0.429 + 584.68\mathrm{i}$, the result calculated by the numerical solver with $N = 500$ cells.

Looped rod: Equation (5.63) is divided into real and imaginary parts and numerically solved for $\mathrm{Re}[\lambda]$ and $\mathrm{Im}[\lambda]$. λ is returned as $6.2984 - 1.7598\mathrm{i}$. The dimensional eigenvalue $\mathrm{i}\Lambda$ can be recovered as $4.9781 + 17816.51\mathrm{i}$ which has an error within 1% from the numerical solution $4.9209 + 17816.32\mathrm{i}$ obtained using $N = 500$ cells.

The amplitude normalized mode shapes for displacement $\bar{u}$, strain $\bar{\varepsilon}$, and temperature fluctuation $\bar{T}$ are shown in Fig. 5.3, where $\bar{z} = |z|/\max(|z|)$, and $z = \tilde{u}, \tilde{\varepsilon}$ or $\tilde{T}$. The

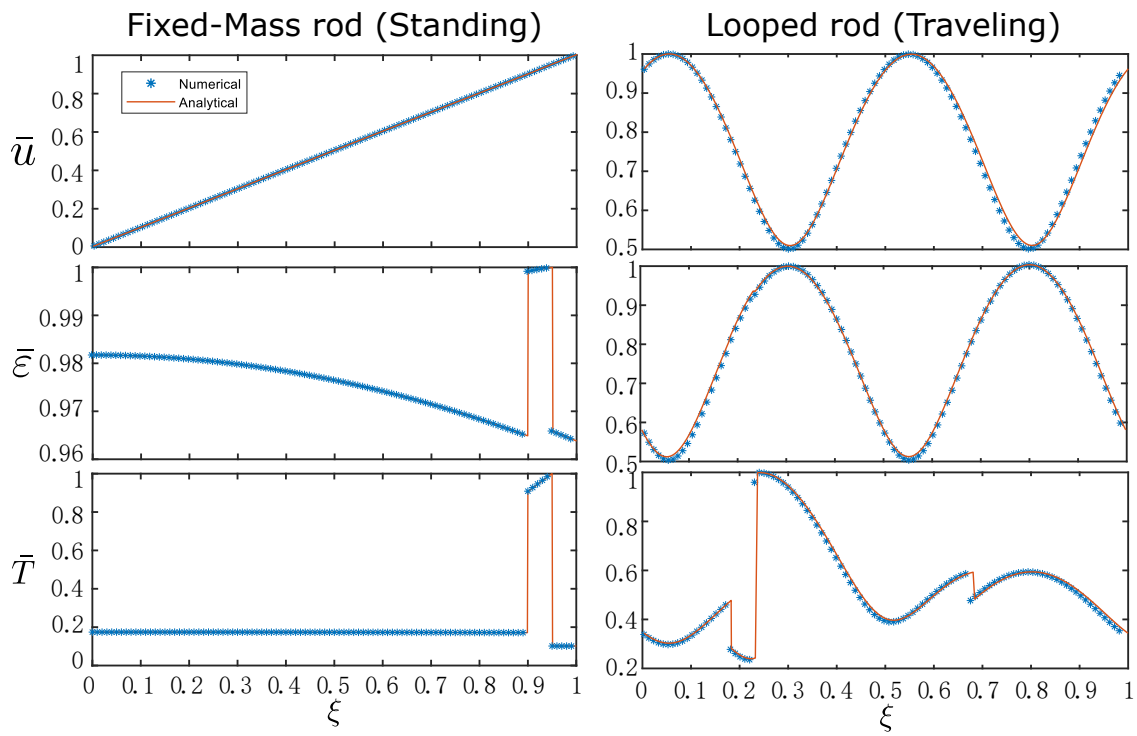

Figure 5.3. Mode shapes of displacement, strain, and temperature (normalized by their own maximum value) obtained from both the numerical solver and the analytical approach.

good agreement between the results provide good confidence in the validity of the analytical approaches.

5.4 Dimensionless Parametric Analysis

By deriving the dimensionless expressions for the governing equations and boundary conditions (see Eqns. (5.9-5.15)), it is understood that the growth-to-frequency ratio β/ω is determined by the following dimensionless parameters (divided into four groups):

1. Stage parameters: Temperature ratio, Θ and dimensionless stage location parameter, ξ_h and ξ_c
2. Material parameters: Dimensionless CTE, A and Grüneisen parameter, γ_G
3. Heat-transfer parameter: Dimensionless radius, r

4. Unique parameters

   (a) Fixed-mass rod: Mass ratio, m

   (b) Looped rod: Thermal buffer segment (TBS) end position ξ_b

This section focuses on the analysis regarding the above four groups of parameters and on their effects with regard to the optimization of the growth ratio β/ω. The parameters tabulated in Table 5.6 are chosen as references for Fixed-mass rod and Looped rod configurations.

Table 5.6. Reference cases of parametric analysis

General:	$A = 6.74 \times 10^{-3}$	$\gamma_G = 0.6626$	$\Theta = 1.682$	
Fixed-mass rod:	$r = 3.80\sqrt{1/\omega}$	$\xi_h = 0.9$	$\xi_c = 0.95$	$m = 23.101$
Looped rod:	$r = 0.38\sqrt{1/\omega}$	$\xi_c = 0.02$	$\xi_h = 0.07$	$\xi_b = 0.52$

Note that during the parametric analysis, when one group of parameters is varied the remaining are kept constant. This approach helps isolating the effect of a specific set of parameters on β/ω.

5.4.1 The Effect of Stage Parameters

It is well known that the temperature difference is the key element to determine the onset of TA instability. In the field of fluid thermoacoustics, the stack design is crucial to the efficiency of TAEs [4], [62]. For an ideal SSTA engine, the stage (equivalent to a one-pore stack in fluids) has infinite heat capacity, hence it is capable of both suppressing the temperature fluctuation on the surface of the stage segment (Segment 2 for both configurations) and sustaining the spatial temperature gradient. It is intuitive that a larger temperature difference causes a higher growth rate. A quantitative analysis conducted in this section is in line with the intuition. The three parameters in the first group determine the strength of the temperature difference, by Θ, and the location and length of the stage, by ξ_h and ξ_c. In a previous study, Hao et al. [51] pointed out that for a standing wave configuration, the optimal stage location $\xi_s = (\xi_c + \xi_h)/2$ is at 1/8 wavelength from the hot fixed end.

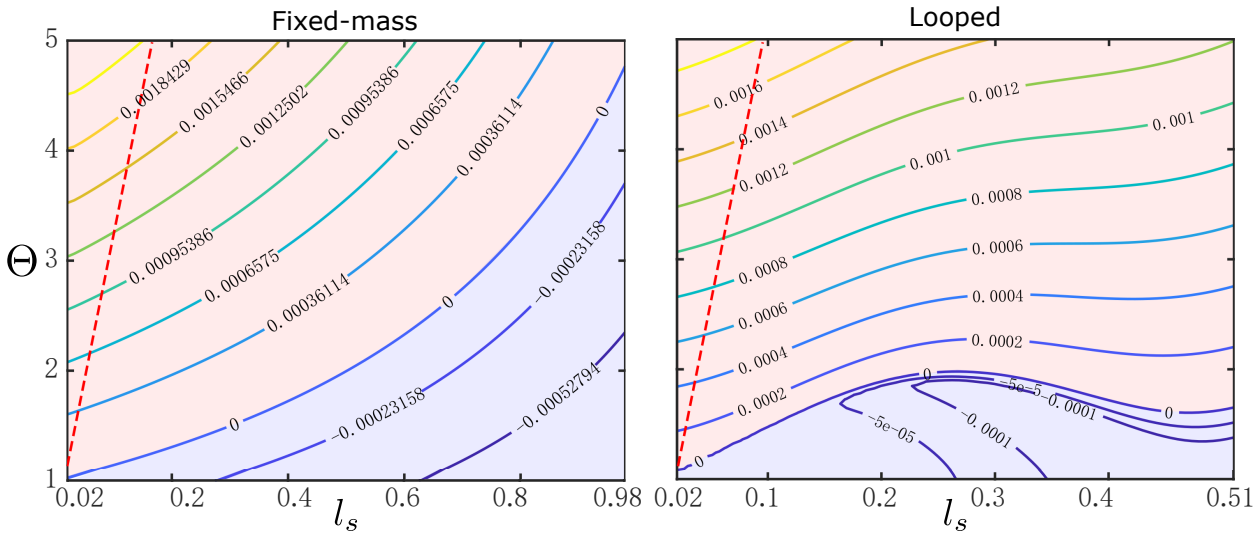

Figure 5.4. Contour plots of the growth ratio β/ω on the $\Theta - l_s$ plane. The whole plane is divided into the stable (blue) and unstable (pink) regions by the $\beta/\omega = 0$ level, indicating the onset of TA instability. The red dashed line represents an isoline of the stage temperature gradient, illustrating the difference of β/ω on the same level of temperature gradient.

This observation was consistent with the conclusions drawn in fluid TA devices [25][1]. For a fixed-mass rod with heavy end mass, the rod length is smaller than 1/8 wavelength, so the optimal location for the stage is at the rod's extremity $\xi = 1 - l_s/2$, where $l_s = |\xi_c - \xi_h|$ is the dimensionless stage length. However, in order to focus on the effect of the stage length l_s and the temperature ratio Θ on growth ratio, the stage location was fixed at the midpoint of the rod $\xi_s = 0.5$ (although not the optimal location).

Differently from the standing wave configuration, the stage location is irrelevant for the looped rod due to its periodicity. Therefore, ξ_c is fixed at 0.02 (close to the left boundary) so to get a larger span of l_s by varying ξ_h. Note that ξ_h cannot exceed $(1 - l_b + \xi_c)$, where $l_b = \xi_b - \xi_h$ is the length of TBS; $l_b = 0.45$ is taken. Fig. 5.4 shows the growth ratio contours for different temperature ratios Θ and stage lengths l_s. The transition from stable (blue) to unstable (pink) regions is very evident. For a fixed stage length, a stronger temperature difference gives rise to a higher growth ratio, which is consistent with the phenomena observed in fluid TAEs. The red dashed line represents an isoline of temperature

[1]↑In Ref. [25], the optimal stage location for the first mode of a closed-closed tube is 1/4 length away from the hot end. 1/4 tube length for a half-wavelength tube is 1/8 wavelength.

gradient $[(\Theta - 1)/l_s]$. It reveals that for stages with same temperature gradient, those providing higher temperature difference, although longer, generate higher growth ratios. This results illustrate that increasing the temperature difference is generally more effective than shortening the stage. From Fig. 5.4, another noteworthy observation is that for a short stage (small l_s), the SSTA engine becomes unstable as long as it has a non-zero temperature difference. This result is explained by the fact that the ideal SSTA engine analyzed in this chapter has zero structural damping, which is the main mechanism of dissipation in solids. In the presence of damping, the critical temperature shall be larger. For a practical design in which damping is present, the multi-stage configuration proposed in [51] is capable of lowering the onset temperature.

5.4.2 The Effect of Material Parameters

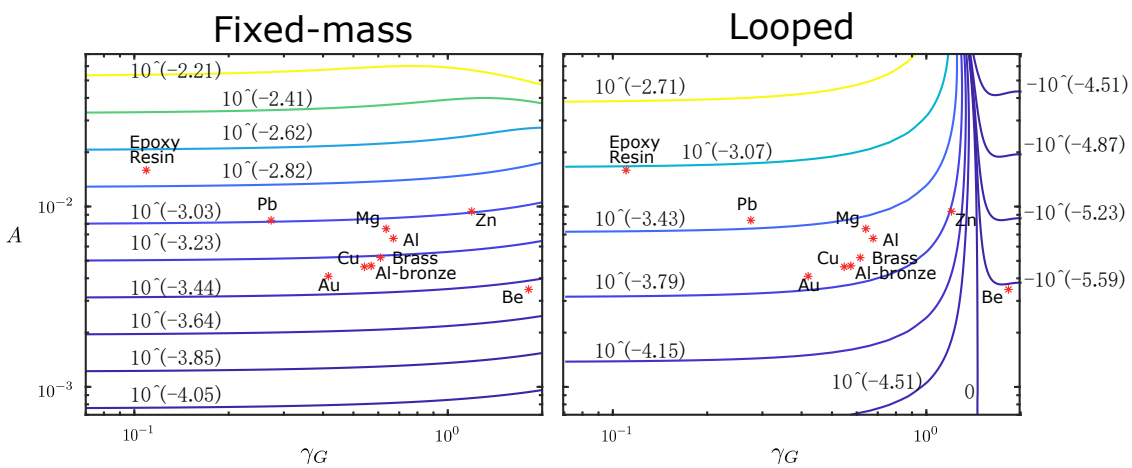

Figure 5.5. Contour plots of β/ω on $A - \gamma_G$ plane. The scatters denote the corresponding metals on the plane.

Compared to fluids, properties of solids can be more easily engineered. Many areas of research including composites, smart materials, and metamaterials have explored several avenues to achieve material properties not readily available in natural materials. Examples include, to name a few, negative density [63], negative stiffness [64], and negative, zero, or colossal CTE [65]. Realistically, one can envision these properties to play a key role in the development of SSTA engines characterized by ultra high efficiency and more versatility in

the application spectrum. Therefore, understanding the effect of material properties on TA performance is a crucial step for their development.

From the dimensionless governing equations (Eqns. 5.9-5.11), the two material-related parameters left in the equations are the dimensionless CTE $A = \alpha T_c$, and the Grüneisen parameter $\gamma_G = \alpha E/(\rho c_\varepsilon)$. Figure 5.5 presents the contour plots of the growth ratio β/ω on $A - \gamma_G$ plane. The markers indicate where some typical solid materials would fall on this plane. The reference case ($A = 6.74 \times 10^{-3}, \gamma_G = 0.6626$) corresponds to Aluminum. The contour plots reveal that for the fixed-mass rod, the growth ratio is always positive and weakly dependent on γ_G (at least, in the chosen range). The growth ratio increases with A. On the contrary, for the looped rod, this same behavior occurs only when $\gamma_G < 1.5$, although most of the showcased materials are located in this region. Beyond $\gamma_G \approx 1.5$, for a given A, the growth ratio decreases rapidly with γ_G increasing and eventually becomes negative. Note that γ_G is the coefficient in front of the thermoelastic coupling term in Eqn. (5.11). This term acts in the energy equation as a source caused by the irreversible entropy increase due to stress inhomogeneity. The same term acts, in the momentum equation, as a dissipating term that is well-known as thermoelastic damping [49], [66].[2] As a result, the increase of γ_G can amplify thermoelastic damping which eventually makes the overall growth rate null or, even, negative. To enhance the TA performance, those materials with high CTE and low γ_G are preferred. Generally, a high CTE is accompanied with low Young's modulus. This behavior is due to the fact that high CTE is due to loose chemical bonds that ultimately prevent high modulus. As a result, a material with high CTE usually has low or moderate γ_G (e.g. epoxy resin). More discussions regarding material properties are presented in Section 5.5.

5.4.3 The effect of Heat-Transfer Parameter

The onset of TA instability is a result of energy conversion from heat to mechanical oscillations. The transverse heat transfer taking place underneath the stage plays a crucial role for the performance of TAEs. The ratio of the rod radius R to the thermal penetration

[2]↑From an energy perspective, the decrease in kinetic energy leads to a very slow rise in mean temperature T_0. However, in this study, temperature fluctuation is the variable and the slow variation in T_0 is neglected.

depth δ_k is a metric for thermal coupling that has significant effects on the growth ratio. It has been shown in earlier work that $r = R/\delta_k \approx 2$ is an optimal value for standing wave SSTA systems (Fig. 3(b) in [51] and Fig. 3 in [60]). For traveling wave configurations, as $r < 1$, the growth ratio β/ω converges to a value where the traveling wave mode dominates the motion (Fig. 3 in [60]). In general, a rod with very low radius-to-length aspect ratio is avoided so to prevent the rod being dominated by flexural mode. Therefore, to pursue a larger R while keeping the optimal value of r, a larger δ_k is required as well. The thermal penetration depth is expressed as $\delta_k = \sqrt{2k/\omega}$, where k is thermal diffusivity. Thus, a material with higher thermal diffusivity is preferred in practical sense. δ_k is a frequency-dependent parameter as well, so for structures with different fundamental frequency, which is affected by rod length and end mass, the radius R should be adjusted accordingly in order to achieve optimal performance.

5.4.4 The Effect of Unique Parameters

This subsection focuses on the discussion of parameters that are unique to each configuration. They are the mass ratio m for the fixed-mass rod and the TBS end location ξ_b for the looped rod.

Fixed-Mass Rod: Mass ratio

For the dimensionless representation of the fixed-mass rod, the mass ratio m is the only parameter which controls the fundamental frequency, given the negligible effect of thermal coupling and structural damping on frequency. To study the effect of the tip mass, the impact of the heat transfer coefficient is isolated by choosing $r = 2$ (corresponding to the optimal radius value for performance). Fig. 5.6 (a) shows the relation between the mass ratio m and the dimensionless frequency ω. Fig. 5.6 (b) exhibits the change of growth ratio β/ω with frequency ω. In the range of $\omega \in [0.1, \pi/4]$, the value of β/ω varies within $\pm 3\%$ compared to the average in the frequency range. Therefore, we conclude that the dependency of growth ratio on frequency is weak when both the radius and the stage location are selected at their

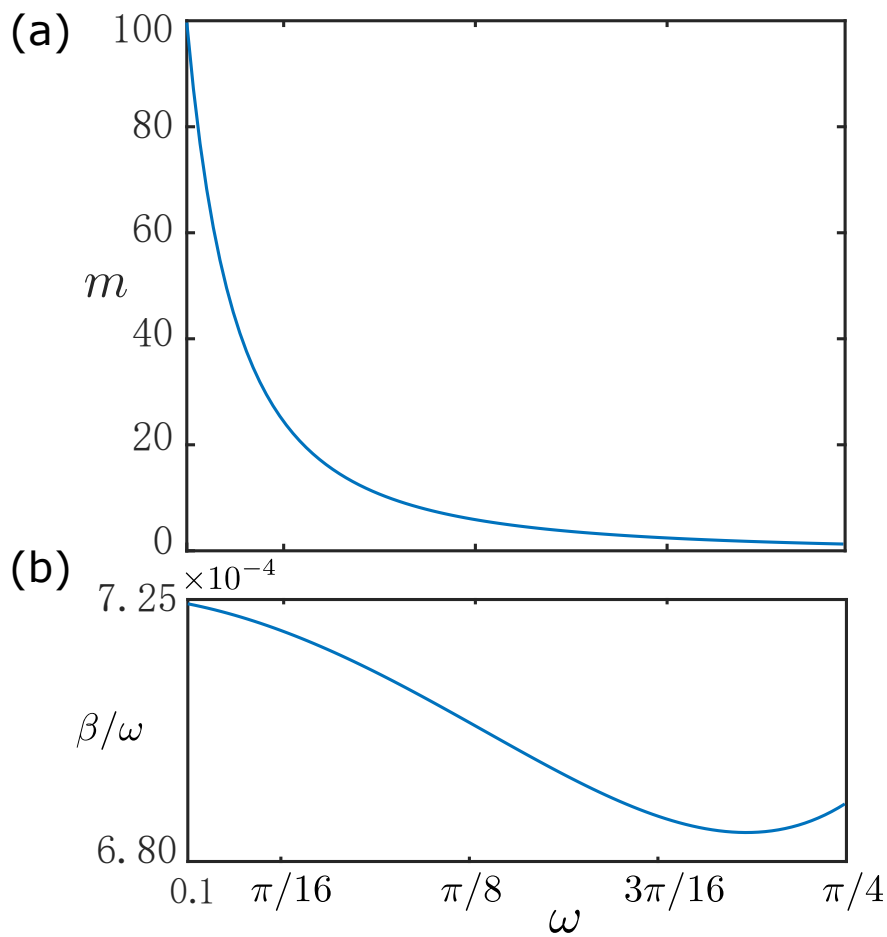

Figure 5.6. (a) The relation between mass ratio and dimensionless frequency. (b) Plot of growth ratio for different frequencies induced by variation of mass ratio.

optimal values. It is noteworthy that, in practical designs, a low frequency is still preferable in order to avoid small values of both $\delta_k \propto 1/\sqrt{\omega}$ and R for optimal performance.

The lower limit of ω is chosen as 0.1, since the corresponding mass ratio $m = 100$ is high enough for practical designs. The upper limit $\pi/4$ is to keep the mass end as the optimal stage location for all the values of ω within the range. The frequency is related to the (dimensionless) wavelength λ_w of the rod by $\lambda_w = 2\pi/\omega$. The wavelength determines the optimal location of the stage by $\min[1, \lambda_w/8]$, which has impacts on β/ω, as seen in [51]. In order to perform a meaningful comparison with the reference, the maximum value of ω was chosen as $\pi/4$, corresponding to $\lambda_w = 8$, the shortest wavelength which makes the mass end the optimal location for stage. To adapt to the 3-segment division of the rod developed for

the analytical approach, we set the stage at [0.90 0.95], same as the reference case, which is not the exact optimal location (extremity) but sufficiently close. For all the values of ω under consideration, this location is regarded the optimal. Hence, in the frequency range $\omega \in [0.1, \pi/4]$, fixing the stage at [0.90 0.95] excludes the effect of stage location on β/ω. The variation of β/ω is shown in Fig. 5.6(b) and it is exclusively due to the effect of the frequency.

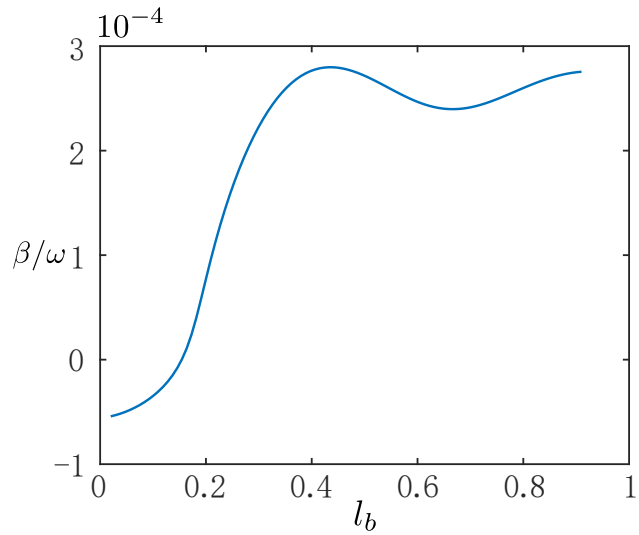

Figure 5.7. The plot of β/ω vs. l_b

Looped Rod: TBS Length

Figure 5.7 plots the growth ratio β/ω versus the TBS length l_s of the looped rod. It is seen that the optimal TBS length is $l_b = 0.45$. This is consistent with the conclusion drawn in Ref. [60], Fig. S1.

5.5 Instability Enhancement with Tunable-CTE Metamaterials

Section 5.4.2 revealed that in the "γ_G-independent" region, a larger CTE is preferable for both standing- and traveling-wave configurations. Polymers generally have one-order-of-magnitude larger CTE compared to metals. The epoxy resin (see Fig. 5.5), as an example, causes higher growth ratio according to the prediction of the lossless linear SSTA theory.

However, the high viscous loss in polymers is unfavorable for SSTA devices. Besides, the applicability of the linear theory for polymers is reduced very quickly due to their nonlinear viscoelastic behavior enhanced by large amplitude oscillations. So, unless considering engineered polymers, it is not likely that polymers could provide better performance for SSTA devices.

Another promising type of cellular solid is made of curved bimetallic ribs with void spaces. This two-dimensional material, first proposed by Lakes [65], can exhibit tunable and colossal CTE. A three-dimensional lattice was also envisioned in a follow-up work [67] by Lakes. Experiments on 3D fabricated prototypes of highly tunable CTE structures have been conducted by Xu and Pasini [68]. The CTE of such a structure is given by:

$$\alpha = \frac{l_{arc}}{t}(\alpha_1 - \alpha_2)\frac{\phi}{12} \tag{5.64}$$

where l_{arc}, t, and ϕ are the arc length, thickness, and angle of the bimetallic rib, while α_1 and α_2 are the CTE for the two layers. By making the ribs more slender (a smaller aspect ratio $t/_{arc}$), the magnitude of α can become unbounded. While exhibiting high CTE, the dissipation of such structure shall be in the same order of bulk metals. In addition, the voids inside the structure reduce the density ρ and the specific heat c_ε, although they cause lower thermal conductivity κ as well. Lower ρ and c_ε might lead to higher thermal penetration depth δ_k, which is favorable for practical designs.

According to Eqn. (5.64), the effective CTE can be made negative if $\alpha_1 < \alpha_2$, which physically means that the layer with higher CTE is on the convex side. The negative CTE is a unique property for solids. Negative-CTE materials can be potentially applied in SSTA engines.

We first numerically prove that a negative-CTE material accompanied with an inverse temperature gradient can produce SSTA instability as well. Figure 5.8 shows the comparison between a regular SSTA configuration (reference) and one with inverse temperature gradient and negative CTE of the same magnitude. The growth ratio for the latter configuration is also postive and quite close to the reference case.

	Positive CTE (Ref.)	Negative CTE
$T_0(x)[K]$	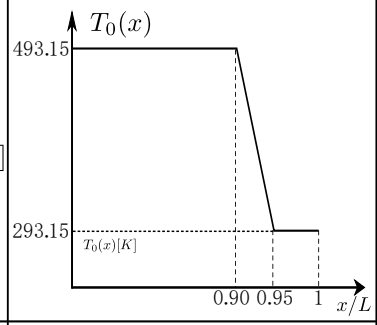	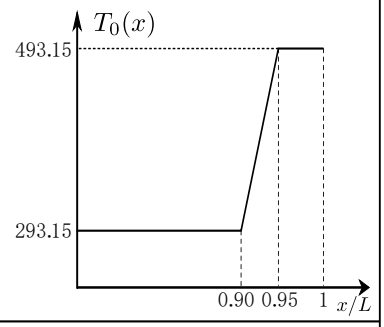
CTE	$\alpha = 23 \times 10^{-6}$[1/K]	$\boldsymbol{\alpha = -23 \times 10^{-6}}$**[1/K]**
Growth ratio	$\beta/\omega = 7.345 \times 10^{-4}$	$\beta/\omega = 7.347 \times 10^{-4}$

Figure 5.8. Comparison between the reference case (left column) and its counterpart with negative CTE of same magnitude and inverse temperature gradient (right column). Both induce TA instability with an approximately equivalent growth ratio. To keep the notation consistent with the analytical approach, in the "Negative CTE" case, T_c and T_h still correspond to the temperature for Segment 1 and Segment 3, respectively, although in this case T_c is higher than T_h.

The negative-CTE material accompanied by the inverse temperature gradient can be applied to the multi-stage configuration proposed in [51]. As the distance between adjacent stages is reduced, the natural conduction between them might become problematic leading to the reduction of the temperature difference in each stage (see red line in Fig. 5.9 (a)). As an alternative, a new configuration with staggered stages (see Fig. 5.9(b)) could be envisioned. The direction of the temperature gradient of adjacent stages (being opposite to each other) avoids the natural conduction between stages. However, in this configuration, the segment underneath the inverse temperature gradient needs to have negative CTE to make positive contributions to the TA process.In order to explore the performance of these concepts, the two configurations were numerically simulated using a commercial finite element software (COMSOL Multiphysics). Thirty stages with 250K temperature difference were distributed along an aluminum rod with 1.8m length and 1mm radius. One end of the rod was fixed, while a 0.3527kg mass was attached to the other end. The negative CTE was chosen to be -23×10^{-6} [1/K] for case (b). Figure 5.9 (c) and (d) show the displacement at the mass end

in configuration (a) and (b). The non-zero mean is due to the static thermal expansion of the rod. In case (b), the contraction effects due to the negative-CTE segments cancel part of the expansion from other segments. As a result, the mean thermal deformation is smaller than that in case (a). Note that in case (b), while the CTE was chosen to be a negative value, the other parameters were kept consistent with those of aluminum. In reality, a hollow structure has lower effective density, specific heat, and Young's modulus, so more elaborate modeling considerations should be employed to properly account for effective properties of materials. Nevertheless, Fig. 5.9(b) shows that a staggered multi-stage configuration by use of negative-CTE materials is plausible and could yield more robust SSTA devices.

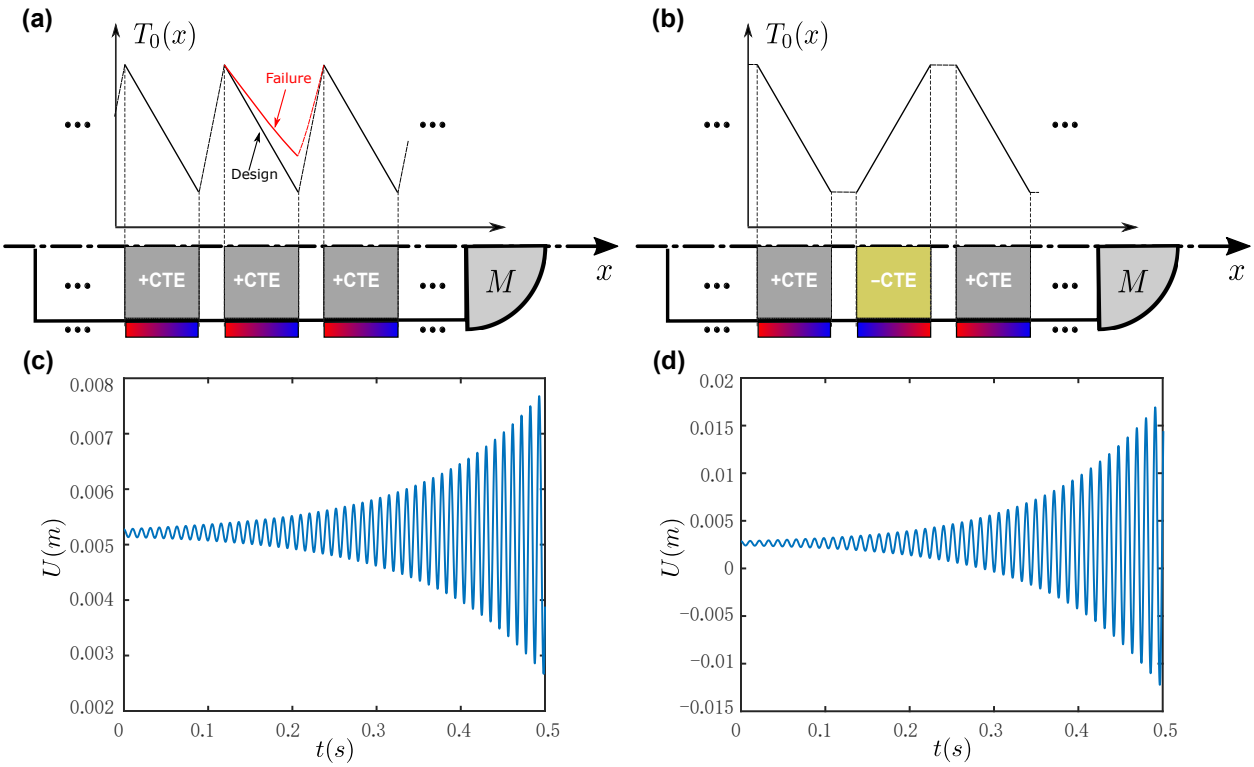

Figure 5.9. (a) Multi-stage configuration proposed in [51]. Natural conduction in between stages might be detrimental to performance if the separation is small. (b) Staggered multi-stage design with segments alternating positive and negative CTE as well as the temperature gradient profile. In this configuration, the temperature at the two ends of adjacent stages is identical, hence no natural conduction takes place. (c) Displacement at the mass end in case (a). (d) Displacement at the mass end in case (b).

5.6 Concluding Remarks

In this Chapter, we have presented contributions that impact the science of SSTA at three different levels

(1) A dimensionless form of the governing equations for SSTA responses of a fixed-mass rod and a looped rod is derived and analytical approaches to solve them are proposed. Although the analytical solutions are not amenable to closed form, they provide valuable information on the form of mode shapes, and lay the foundation for the dimensionless parametric study. (2) The analysis regarding the dimensionless parameters reveals the dependence of the growth ratio on the stage design, the rod radius (wall heat transfer), the material properties, and the parameters unique to each configuration. (3) Possible design configurations enlightened by the parametric study are envisioned, and some preliminary results are provided. More specific conclusions for the enhancement of SSTA performance are summarized in the following:

1. The ratio of rod radius R to thermal penetration depth δ_k, which is dependent on frequency, is a metric for thermal coupling. For a standing wave configuration, $R/\delta_k \approx 2$ is optimal [51], [60].

2. For a given stage length, there exists a critical temperature difference which triggers the onset of TA instability. The higher the temperature difference, the stronger the TA response. For a same level of temperature gradient, higher temperature difference is favorable.

3. For fixed-mass rods, the mass ratio m affects the operating frequency ω. In the range $\omega \in [0.1, \pi/4]$, where the mass end is kept at the optimal location, the growth ratio β/ω only varies 3% with frequency ω.

4. Unlike the thermal buffer tube in fluid-based thermoacoustic devices, the TBS in SSTA engines is not expected to yield wave-scattering effect, due to the negligible temperature dependency of sound speed [60]. However, for looped rods, there does exist an optional length of the TBS. For the configuration studied in this paper (an aluminum looped

rod under 200 K temperature difference over a 5%L stage), the optimal TBS length is $0.45L$.

5. Large CTE materials are favorable for SSTA instability. However, polymers, having CTE one order of magnitude larger than metals, are highly dissipative due to their nonlinear viscoelastic nature. More comprehensive analyses leveraging a nonlinear formulation would be needed in order to determine the feasibility of the use of polymers for SSTA devices.

6. Engineering structures involving curved bimetallic ribs with voids can exhibit positive or negative CTE with unbounded magnitude. Hollow micro-scale structures with high CTE could be a good choice for SSTA devices due to their low dissipation and low density and specific heat. Negative-CTE segments allow the application of inverse temperature gradient, which can be used in multi-stage configurations. A staggered multi-stage SSTA design is proposed in this chapter. By elaborating the staggered distribution of positive- and negative-CTE segments (Fig. 5.8(b)), the detrimental effect due to the natural conduction between adjacent stages can be eliminated.

The parametric analyses conducted in this work provide new insights on the selection and design of materials for the optimization of SSTA devices. The authors envision that with the unique properties of solid-based engineered materials, robust SSTA devices can provide a wider range of applications than their fluid counterparts.

6. NUMERICAL AND EXPERIMENTAL STUDY OF F-SSTA

6.1 Introduction

In Chapter 4, the theory of axial-mode thermoacoustic oscillations in solids was established. By numerical means, the existence of self-sustained longitudinal TA oscillations in solids is shown, hence providing a direct counterpart to the well-known thermoacoustic response of fluids. Both standing and traveling axial-mode wave configurations were explored. The latter configuration shows a higher efficiency of the energy conversion mechanism, an observation consistent with fluid-based TA systems.

Unlike in fluids, waves in solids are polarized which means that, beyond the primary (also known as longitudinal or axial) waves, two shear-type waves are also admissible states of motion. The shear-type waves, which are not present in gases, produce particle motion in a direction perpendicular to the direction of propagation. In finite elastic waveguides, shear waves give rise to flexural type of motion. In the first part of this Chapter, we will establish the theoretical framework of flexural solid-state thermoacoustics and discuss the existence of unstable flexural thermoacoustic waves in a continuous bilayer beam. More specifically, Section 6.2 focuses on a bilayer slender beam subject to two types of spatial thermal gradients. The Type I gradient is linear and, although less practical for an experimental implementation, it allows a fully analytical treatment of the dynamical problem hence facilitating the detailed understanding and the physical interpretation of the phenomenon. In the Type II gradient, the inward heat flux is a sign function of the transverse displacement. This type of gradient is instead more amenable to an experimental implementation, but it does not allow an analytical solution of the governing equations. Theoretical analyses of the flexural motion of the continuous bilayer beam under these two types of heating reveal the criterion to determine the occurrence of flexural instability. Also, the dynamics of the neutral axis location and the mechanism behind the self-amplifying flexural solid-state thermoacoustic (F-SSTA) oscillations will be explored in detail. The results of an experimental investigation of the thermoacoustic response of a continuous bilayer beam will also be presented. Although a fully self-sustained flexural motion was not observed due to the limited heating and cooling

capacity, a visibly reduced effective damping rate was achieved, demonstrating that the thermal-to-mechanical energy conversion process does exist in an F-SSTA system.

Interestingly, revisiting the (in)stability criterion suggests the possibility of utilizing a layer of negative-thermal-expansion (NTE) material to significantly enhance the F-SSTA instability. Recall that NTE materials contract upon heating, and expand upon cooling. Despite a limited number of natural materials (e.g. ZrW_2O_8) possesses NTE properties [69], it is the rapidly growing field of architectured materials that is offering remarkable opportunities to achieve a broad range of coefficient of thermal expansion (CTE) spanning all the way from positive to negative values.

In Section 6.3, we first presented the motivation to explore NTE materials as a way to significantly enhance F-SSTA instability, provided by the instability criterion. Then, we perform a numerical study of the F-SSTA response of a hybrid bilayer beam in cantilever configuration. The term hybrid refers to the particular structure of the bilayer beam that employs both a fully solid and homogeneous layer and an architectured material layer. The selection of an architectured material design is motivated by the need to tune the thermo-mechanical properties and achieve NTE behavior. NTE properties are obtained by exploiting a bi-material octet truss design. Overall, the design of the truss structure gives rise to an effective axial NTE of the entire architectured layer. Upon heating, the effective NTE produces an axial contraction of the architectured layer as opposed to the axial extension of the homogeneous layer. The contrast between the behavior of the two layers results in a pronounced thermal bending, which is beneficial for the F-SSTA instability. Numerical results indicate that the NTE-aided F-SSTA instability is enhanced with respect to a more traditional bilayer homogeneous design.

In Section 6.4, a simplified one degree-of-freedom (1DOF) model is presented in order to quantify the thermal energy budget and to better understand the thermo-mechanical process leading to the instability. Despite its simplicity, the 1DOF model qualitatively describes the flexural motion of a bilayer beam under the heat flux gradient, modeled as a sign function of the transverse displacement. It is found that the motion of the 1DOF system, in the absence of structural damping, grows linearly to infinity in a similar manner as the bilayer beam. However, when structural damping is taken into account, the motion converges to

a limit-cycle oscillation. The perturbation energy budgets of the 1DOF system reveals the dependence of variation of energy accumulation on the thermoacoustic power production and structural-damping-induced dissipation.

Before concluding this Chapter, we will discuss several topics relevant to F-SSTA systems, including a conceptual comparison between F-SSTA systems with the thermal flutter previously observed in space applications [70], [71]. The advantages of using architectured NTE structures compared to natural NTE materials will also be discussed. We also provided some thoughts on manufacturing the architectured NTE materials for a successful experimental validation of such system.

6.2 F-SSTA in a Bilayer Beam

Consider the small amplitude dynamic response of a slender beam. Under Euler-Bernoulli assumptions, the force balance of an infinitesimal beam element of arbitrary cross section in the transverse direction is given by:

$$\rho\mathcal{A}\frac{\partial^2 v}{\partial t^2} = \frac{\partial \mathcal{Q}}{\partial x} \tag{6.1}$$

where $\mathcal{A}$ is the total area of the beam cross section, v is the transverse displacement, $\rho = (\int_{\mathcal{A}} \varrho d\mathcal{A})/\mathcal{A}$ is the effective density, ϱ is the density distribution over the across section, $\mathcal{Q} = \partial\mathcal{M}/\partial x$ is the shear force, $\mathcal{M} = \int_{\mathcal{A}} \sigma y d\mathcal{A}$ is the bending moment and σ is the axial stress defined as:

$$\begin{aligned}\sigma &= E(\varepsilon - \alpha T)\\ &= E\Big(-y\frac{\partial^2 v}{\partial x^2} - \alpha T\Big)\end{aligned} \tag{6.2}$$

where E and α are the Young's modulus and the linear thermal expansion coefficient, $\varepsilon = -y(\partial^2 v)/(\partial x^2)$ is the axial strain and T is the temperature fluctuation. y is the transverse coordinate defined from the neutral axis of the cross section.

In this study, we consider the case of a beam having a rectangular cross section formed by two adjoined layers of different material having the same width b and height $h/2$ (Fig.

6.1(b)). We assume an ideal interface between the two layers hence discard the possibility of relative slip.

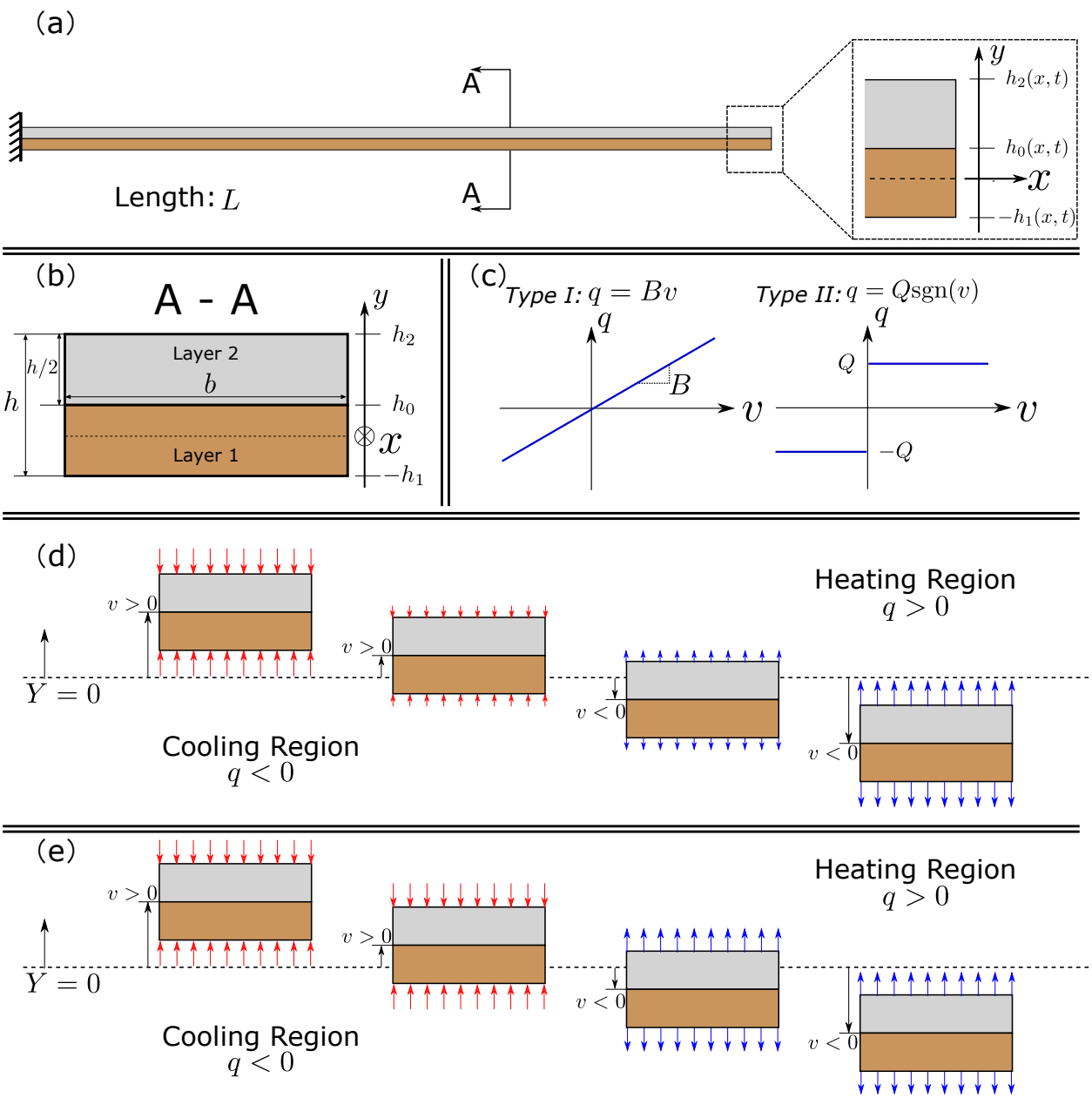

Figure 6.1. (a) and (b) Basic notation and local coordinate frame for the bilayer beam. (c) Top and bottom surfaces of the cross section experience heat flux (positive if inward). Two types of thermal loads are investigated, namely $q = Bv$ and $q = Q\mathrm{sgn}(v)$. (d) and (e) The beam moving from heating region to cooling region under (d) Type I: $q = Bv$ and (e) Type II: $q = Q\mathrm{sgn}(v)$ thermal loads. The red and blue arrows indicate surface heating and cooling, respectively.

The flexural motion of the beam is governed by:

$$\rho h \frac{\partial^2 v}{\partial t^2} = \frac{\partial^2 m}{\partial x^2} \tag{6.3}$$

where the effective density $\rho = (\rho_1 + \rho_2)/2$, m is the moment per unit width expressed as:

$$m = \int_{-h_1}^{h_0} \sigma_1 y dy + \int_{h_0}^{h_2} \sigma_2 y dy \tag{6.4}$$

where σ is the axial stress defined in Eqn. (6.2). For the $\mathrm{i} - th$ layer (with i=1,2), the axial stress is given by:

$$\sigma_{\mathrm{i}} = E_{\mathrm{i}} \Big(- y \frac{\partial^2 v}{\partial x^2} - \alpha_{\mathrm{i}} T_{\mathrm{i}} \Big), \qquad (\mathrm{i} = 1, 2) \tag{6.5}$$

Note again that y is a local coordinate defined at the neutral axis (Fig. 6.1(a) and (b)) which, as clarified in the following, can change its position due to the effect of the thermoelastic coupling. In Eqn. (6.5), the first term on the right hand side represents the mechanical stress while the second term represents the thermoelastic stress. h_0 in Eqn. (6.4) indicates the location of the neutral axis on the local coordinate system y (Fig. 6.1(a) and (b)). The magnitude of h_0 denotes the distance between the neutral axis and the interface between the two layers. h_1 and h_2 are related to h_0 by:

$$h_1 + h_0 = \frac{h}{2} \tag{6.6}$$

$$h_2 - h_0 = \frac{h}{2} \tag{6.7}$$

The neutral axis location h_0 is determined by imposing a vanishing total axial force:

$$\int_{-h_1}^{h_0} \sigma_1 dy + \int_{h_0}^{h_2} \sigma_2 dy = 0 \tag{6.8}$$

which yields:

$$h_0 = h_{\mathrm{e}} - \frac{A I_T}{h/2 v_{xx}(n+1)} \tag{6.9}$$

where $h_{\mathrm{e}} = h(n-1)/4(n+1)$ denotes the neutral axis location in a purely elastic bilayer beam with no thermoelastic coupling, $n = E_1/E_2$, and v_{xx} is a compact notation for $\partial^2 v/\partial x^2$. The second term in Eqn. (6.9) shows the effect of thermoelastic coupling. AI_T is given by:

$$AI_T = n\alpha_1 \int_{-h_1}^{h_0} T_1 dy + \alpha_2 \int_{h_0}^{h_2} T_2 dy \tag{6.10}$$

Equation (6.9) shows that, unlike its elastic counterpart, the location of the neutral axis of a beam in presence of thermoelastic coupling depends on the temperature fluctuations in the cross section. Consequently, the location of the neutral axis is a function of both time t and spatial x coordinates.

The fluctuating temperature field in the 2D beam is governed by:

$$\rho_{\mathrm{i}} c_{\varepsilon_{\mathrm{i}}} \frac{\partial T_{\mathrm{i}}}{\partial t} + E_{\mathrm{i}} \alpha_{\mathrm{i}} T_0 \frac{\partial \varepsilon}{\partial t} = k_{\mathrm{i}} \left(\frac{\partial^2 T_{\mathrm{i}}}{\partial x^2} + \frac{\partial^2 T_{\mathrm{i}}}{\partial y^2} \right) \tag{6.11}$$

where k_{i} and $c_{\varepsilon_{\mathrm{i}}}$ are thermal conductivity and specific heat at constant strain. The mean temperature T_0 is assumed as the ambient temperature set at $293.15[K]$. The second term on the left-hand side is the heat source induced by the thermoelastic coupling, as a result of the local heat flux caused by the stress inhomogeneity [66]. According to thermodynamic laws, this local heat flux leads to an entropy increase, reflected in a (very slow) rise of the mean temperature T_0. However, in this study, only the fluctuating temperature is considered and the slow variation of T_0 is neglected. From a dynamic perspective, this irreversible process dissipates kinetic energy and induces a slow decay of the response that is well known as thermoelastic damping (TED) [49]. Note that although coupling the thermal and elastic fields induces the existence of TED, this quantity differs from the structural damping which is an intrinsically dissipative mechanism in solids. Without loss of generality, structural damping is not included in the theoretical analyses conducted in this study because its effect on the dynamics is well-known. However, its effect is observed in the experiments. A more detailed discussion can be found in Section 6.2.3.

The thermoacoustic response of a cantilever bilayer beam subject to two different types of surface heating will be considered (Fig. 6.1(c)). Type I is $q = Bv$, where q is the inward heat

flux on the top ($y = h_2$) and bottom ($y = -h_1$) surfaces, and B is a constant. This type of heating represents a linear thermal gradient anchored in space (with a transverse coordinate Y in spatial frame, see Fig. 6.1(d)). We assume that the equilibrium position of the beam, $v = 0$, is aligned with the $Y = 0$ location in the absolute spatial frame. As a result, the beam experiences a linearly varying rate of heating (cooling) as it vibrates in the positive (negative) Y domain. Type II is $q = Q\text{sgn}(v)$, where Q is a constant value and sgn() is the sign function. This type of surface heating represents an abrupt change of heat flux in space as the beam moves through the upper half plane towards the lower half plane. Note that the Euler-Bernoulli theory assumes that the flexural displacement v is homogeneous across the cross section, while the stress and the temperature in presence of thermoelastic coupling are not. It follows that, when taking these two types of heating into consideration, once the geometric center of the cross section is positively (negatively) displaced, i.e. $v > 0$ ($v < 0$), the whole cross section experiences surface heating (cooling), as shown in Fig. 6.1(d) and (e). The analysis for Type I is based on a modal approach which allows developing useful analytical expressions to understand the physical mechanisms governing the coupled dynamic response of the system. Type II is analyzed instead by using time-domain numerical integration. It confirms the existence of the self-amplifying mechanism due to F-SSTAs. The time evolution of neutral axis location h_0 associated with the flexural instability is observed and analyzed.

Under the two types of thermal loads, we adopted different assumptions for (1) the neutral axis location, (2) the interfacial thermal resistance, and (3) the thermoelastic damping. The basis for these assumptions will be articulated in details in the following. The assumptions corresponding to the two thermal loads are listed below:

1. Type I thermal load
   (a) Time-invariant neutral axis location:
      i. Both infinite and zero interfacial thermal resistance are considered. These two cases are referred to Case 1 and Case 2 respectively in Sections 6.2.1 and 6.2.2.
      ii. Both cases with and without thermoelastic damping (w/. and wo/. TED) are considered.

(b) Time-varying neutral axis location:

i. Both infinite and zero interfacial thermal resistance (Case 1 and Case 2) are considered.

ii. Negligible thermoelastic damping (wo/. TED).

2. Type II thermal load

(a) Time-varying neutral axis location:

i. Zero interfacial thermal resistance (Case 2).

ii. Negligible thermoelastic damping (wo/. TED).

6.2.1 Type I: $q = Bv$ Heating

This thermal load case is selected to obtain analytical solutions capable of describing the dynamics of the F-SSTA bilayer beam while revealing the role of the design parameters on both the dynamic response and the occurrence of the instability. We will first assume a time-invariant neutral axis location h_0 in section 6.2.1, which allows a relatively compact and quantitatively accurate estimate of the growth rate and natural frequency. Then in section 3, we will remove the constant h_0 assumption and explore the dynamics of the neutral axis under thermoelastic coupling. The latter assumption, despite its modeling and computational complexity, provides a more accurate representation of the underlying physics.

Time-Invariant Neutral Axis Location (Constant h_0)

In this section, we assume $h_0 = h_\mathrm{e}$ where h_e is a constant value denoting the location of the neutral axis in a bilayer beam with no thermoelastic coupling. This is a common assumption in most studies on thermal induced vibrations [70], [72]–[74] and implies that the second term in the right-hand side of Eqn. (6.9) is neglected.

Under this assumption, equation (6.3) becomes:

$$\rho h \frac{\partial^2 v}{\partial t^2} + D \frac{\partial^4 v}{\partial x^4} + \frac{\partial^2 m_T}{\partial x^2} = 0 \tag{6.12}$$

where D is flexural rigidity expressed as:

$$D = \frac{1}{3}E_2\left[n\left(h_0^3 - \left(h_0 - \frac{h}{2}\right)^3\right) + \left(h_0 + \frac{h}{2}\right)^3 - h_0^3\right] \tag{6.13}$$

The thermal moment per unit width m_T is expressed as:

$$m_T = E_2\left(n\alpha_1 \int_{-h_1}^{h_0} yT dy + \alpha_2 \int_{h_0}^{h_2} yT dy\right) \tag{6.14}$$

The assumed $q = Bv$ heating implies the following boundary conditions for the temperature on the free surfaces:

$$-k_2 \left.\frac{\partial T_2}{\partial y}\right|_{y=h_2} = -Bv \tag{6.15}$$

$$-k_1 \left.\frac{\partial T_1}{\partial y}\right|_{y=-h_1} = Bv \tag{6.16}$$

Assume the variables are harmonic in time so that $() = \hat{()}\mathrm{e}^{\mathrm{i}\lambda t}$, where the complex frequency $\lambda = \omega - \mathrm{i}\beta$, i is the imaginary unit, β is the growth/decay rate, and ω is the angular frequency. $\hat{()}$ denotes quantities in modal space. By neglecting the heat conduction in x (since the heat flows mainly in the transverse direction), Eqn. (6.11) becomes:

$$(\mathrm{i}\lambda)\hat{T}_\mathrm{i} = \frac{k_\mathrm{i}}{\rho_\mathrm{i} c_{\varepsilon_\mathrm{i}}}\left(\frac{\partial^2 \hat{T}_\mathrm{i}}{\partial y^2}\right) + \gamma_\mathrm{i} T_0 y(\mathrm{i}\lambda)\frac{\partial^2 \hat{v}}{\partial x^2} \tag{6.17}$$

where $\gamma_\mathrm{i} = E_\mathrm{i}\alpha_\mathrm{i}/(\rho_\mathrm{i} c_{\varepsilon_\mathrm{i}})$ is the Grüneisen parameter. Note that neglecting the axial diffusion term is a very common simplification used in thermoacoustics [70] because the axial derivative is on the order of $1/\lambda_w$, much smaller than the transverse derivative which is on the order of $1/\delta_k$. λ_w and δ_k are the wavelength and the thermal penetration depth, respectively. This assumption is due to the large difference in scale between $1/\lambda_w$ and $1/\delta_k$, so it is reasonable for solids as well.

Equation. (6.17) can be solved for $\hat{T}$, yielding:

$$\hat{T}_\mathrm{i} = C\cos\left(\frac{\sqrt{-2\mathrm{i}}}{\delta_{k_\mathrm{i}}}y\right) + S\sin\left(\frac{\sqrt{-2\mathrm{i}}}{\delta_{k_\mathrm{i}}}y\right) + \gamma_\mathrm{i} T_0 y\frac{\partial^2 \hat{v}}{\partial x^2} \tag{6.18}$$

where C and S are coefficients to be determined based on the boundary conditions. Converting Eqn. (6.14) into modal space and substituting $\hat{T}_{\mathrm{i}}$ from Eqn. (6.18) yields:

$$\hat{m}_T = c_A \hat{v} + c_E \hat{v}_{xx} \tag{6.19}$$

where c_A and c_E are complex coefficients and their real and imaginary parts are determined by the constants C and S.

In the following, the two cases of different interfacial thermal conditions: Case 1 (infinite thermal resistance) and Case 2 (zero thermal resistance) are analyzed separately. Note that a realistic interface has finite thermal resistance, so the two cases represent the upper and lower bounds of a realistic case.

<u>Case 1:</u> Infinite interfacial thermal resistance

Assuming that the thermal resistance at the interface is infinitely large, no heat flux is allowed at the interface, therefore:

$$\left.\frac{\partial T_2}{\partial y}\right|_{y=h_0} = \left.\frac{\partial T_1}{\partial y}\right|_{y=h_0} = 0 \tag{6.20}$$

By applying the counterpart of Eqns. (6.15), (6.16) and (6.20) in modal space, the temperature field in each layer is found as:

$$\hat{T}_{\mathrm{i}} = -\frac{B}{k_{\mathrm{i}}} \frac{\delta_{k_{\mathrm{i}}}}{\sqrt{-2\mathrm{i}}} \frac{\cos\left[\frac{\sqrt{-2\mathrm{i}}}{\delta_{k_{\mathrm{i}}}}(h_0 - y)\right]}{\sin\left[\frac{\sqrt{-2\mathrm{i}}}{\delta_{k_{\mathrm{i}}}}\frac{h}{2}\right]} \hat{v} + \gamma_{\mathrm{i}} T_0 \left\{ y - \frac{\delta_{k_{\mathrm{i}}}}{\sqrt{-2\mathrm{i}}} \frac{\sin\left[\frac{\sqrt{-2\mathrm{i}}}{\delta_{k_{\mathrm{i}}}}(y - h_0 \pm \frac{h}{4})\right]}{\cos\left[\frac{\sqrt{-2\mathrm{i}}}{\delta_{k_{\mathrm{i}}}}\frac{h}{4}\right]} \right\} \hat{v}_{xx} \tag{6.21}$$

where the $\pm$ sign is replaced by a plus sign for layer 1 (i = 1) and a minus sign for layer 2 (i = 2). The real and imaginary parts of c_A and c_E in Eqn. (6.19) for this case are expressed as:

$$\mathrm{Re}[c_A] = \left[E_1\alpha_1\frac{\delta_{k1}^3}{4k_1}f_-(\eta_1) - E_2\alpha_2\frac{\delta_{k2}^3}{4k_2}f_-(\eta_2)\right]B \tag{6.22}$$

$$\mathrm{Im}[c_A] = \left[E_1\alpha_1\frac{\delta_{k1}^3}{4k_1}\left(\frac{2h_1}{\delta_{k1}} - f_+(\eta_1)\right) - E_2\alpha_2\frac{\delta_{k2}^3}{4k_2}\left(\frac{2h_2}{\delta_{k2}} - f_+(\eta_2)\right)\right]B \tag{6.23}$$

$$\mathrm{Re}[c_E] = E_1\alpha_1\gamma_1T_0\left[\frac{1}{3}(h_0^3 + h_1^3) + \frac{\delta_{k1}^3}{2}f_-(\eta_1)\right] + E_2\alpha_2\gamma_2T_0\left[\frac{1}{3}(h_2^3 - h_0^3) + \frac{\delta_{k2}^3}{2}f_-(\eta_2)\right] \tag{6.24}$$

$$\mathrm{Im}[c_E] = E_1\alpha_1\gamma_1T_0\frac{\delta_{k1}^3}{2}\left(\eta_1 - f_+(\eta_1)\right) + E_2\alpha_2\gamma_2T_0\frac{\delta_{k2}^3}{2}\left(\eta_2 - f_+(\eta_2)\right) \tag{6.25}$$

where

$$\eta_{\mathrm{i}} = \frac{h}{2\delta_{k_{\mathrm{i}}}} \tag{6.26}$$

$$f_+(z) = \frac{\sin(z) + \sinh(z)}{\cos(z) + \cosh(z)} \tag{6.27}$$

$$f_-(z) = \frac{\sin(z) - \sinh(z)}{\cos(z) + \cosh(z)} \tag{6.28}$$

where z is a dummy variable.

<u>Case 2:</u> Zero interfacial thermal resistance

Assuming that the thermal resistance at the interface is zero, heat is perfectly conducted and temperature is continuous at the interface, therefore:

$$k_2\left.\frac{\partial T_2}{\partial y}\right|_{y=h_0^+} = k_1\left.\frac{\partial T_1}{\partial y}\right|_{y=h_0^-} \tag{6.29}$$

$$T_2|_{y=h_0^+} = T_1|_{y=h_0^-} \tag{6.30}$$

By applying the counterpart of Eqns. (6.15), (6.16) and (6.30) in modal space, the coefficients C_{i} and S_{i} are found as:

$$[C_1, S_1, C_2, S_2]^{\mathrm{T}} = M_c^{-1}(M_0\hat{v} + M_2\hat{v}_{xx}) \tag{6.31}$$

where the superscript T denotes matrix transpose and:

$$
\begin{aligned}
M_c &= \begin{bmatrix} 0 & 0 & -\sin\left(\frac{\sqrt{-2\mathrm{i}}}{\delta_{k2}}h_2\right) & \cos\left(\frac{\sqrt{-2\mathrm{i}}}{\delta_{k2}}h_2\right) \\ \sin\left(\frac{\sqrt{-2\mathrm{i}}}{\delta_{k1}}h_1\right) & \cos\left(\frac{\sqrt{-2\mathrm{i}}}{\delta_{k1}}h_1\right) & 0 & 0 \\ \cos\left(\frac{\sqrt{-2\mathrm{i}}}{\delta_{k1}}h_0\right) & \sin\left(\frac{\sqrt{-2\mathrm{i}}}{\delta_{k1}}h_0\right) & -\cos\left(\frac{\sqrt{-2\mathrm{i}}}{\delta_{k1}}h_0\right) & -\sin\left(\frac{\sqrt{-2\mathrm{i}}}{\delta_{k1}}h_0\right) \\ -k_1\frac{\sqrt{-2\mathrm{i}}}{\delta_{k1}}\sin\left(\frac{\sqrt{-2\mathrm{i}}}{\delta_{k1}}h_0\right) & k_1\frac{\sqrt{-2\mathrm{i}}}{\delta_{k1}}\cos\left(\frac{\sqrt{-2\mathrm{i}}}{\delta_{k1}}h_0\right) & k_2\frac{\sqrt{-2\mathrm{i}}}{\delta_{k2}}\sin\left(\frac{\sqrt{-2\mathrm{i}}}{\delta_{k2}}h_0\right) & -k_2\frac{\sqrt{-2\mathrm{i}}}{\delta_{k2}}\cos\left(\frac{\sqrt{-2\mathrm{i}}}{\delta_{k2}}h_0\right) \end{bmatrix} \\
M_0^{\mathrm{T}} &= \begin{bmatrix} \frac{\delta_{k2}}{\sqrt{-2\mathrm{i}}}\frac{B}{k_2} & -\frac{\delta_{k1}}{\sqrt{-2\mathrm{i}}}\frac{B}{k_1} & 0 & 0 \end{bmatrix} \\
M_2^{\mathrm{T}} &= \begin{bmatrix} -\frac{-\delta_{k2}}{\sqrt{-2\mathrm{i}}}\gamma_2 T_0 & -\frac{-\delta_{k1}}{\sqrt{-2\mathrm{i}}}\gamma_1 T_0 & (\gamma_2-\gamma_1)T_0 h_0 & (k_2\gamma_2 - k_1\gamma_1)T_0 \end{bmatrix}
\end{aligned}
\tag{6.32}
$$

Thus, c_A and c_E can be obtained by performing the integrals in Eqn. (6.14).

Once converted to modal space, the momentum equation (Eqn. (6.12)) is expressed as:

$$
-\rho h \lambda^2 \hat{v} = \frac{\partial^2 \hat{m}}{\partial x^2} \tag{6.33}
$$

Knowing c_A and c_E, Eqn. (6.33) becomes:

$$
-\rho h \lambda^2 \hat{v} + (D + c_E)\frac{\partial^4 \hat{v}}{\partial x^4} + c_A \frac{\partial^2 \hat{v}}{\partial x^2} = 0 \tag{6.34}
$$

A possible solution to the fourth order ODE in Eqn. (6.34) has the form $\hat{v} = \mathrm{e}^{\mathrm{i}\kappa_{\mathrm{j}} x}$, where κ_{j} (with $\mathrm{j} = 1, 2, 3, 4$) is the wavenumber obtained from the roots of the characteristic equation:

$$
(D + c_E)\kappa^4 - c_A \kappa^2 - \rho h \lambda^2 = 0 \tag{6.35}
$$

The complete solution of $\hat{v}$ to Eqn. (6.34) is:

$$
\hat{v} = \sum_{\mathrm{j}=1}^{4} C_{\mathrm{j}} \mathrm{e}^{\mathrm{i}\kappa_{\mathrm{j}} x} \tag{6.36}
$$

The mode shape $\hat{v}$ satisfies cantilever beam boundary conditions:

$$\hat{v}(0) = 0 \tag{6.37}$$

$$\frac{\partial \hat{v}}{\partial x}(0) = 0 \tag{6.38}$$

$$\hat{Q}(L) = -(D + c_E)\frac{\partial^3 \hat{v}}{\partial x^3}(L) - c_A \frac{\partial \hat{v}}{\partial x}(L) = 0 \tag{6.39}$$

$$\hat{M}(L) = -(D + c_E)\frac{\partial^2 \hat{v}}{\partial x^2}(L) - c_A \hat{v}(L) = 0 \tag{6.40}$$

Substituting Eqn. (6.36) into the above boundary condition equations, they can be rewritten in a more compact form as:

$$\det[M_\kappa] = 0 \tag{6.41}$$

where the (i, j)th element in the 4x4 matrix M_κ is given by:

$$M(1, \mathrm{j}) = 1 \tag{6.42}$$

$$M(2, \mathrm{j}) = \kappa_\mathrm{j} \tag{6.43}$$

$$M(3, \mathrm{j}) = \kappa_\mathrm{j}[-(D + c_E)\kappa_\mathrm{j}^2 + c_A]\mathrm{e}^{\mathrm{i}k_\mathrm{j}L} \tag{6.44}$$

$$M(4, \mathrm{j}) = [-(D + c_E)\kappa_\mathrm{j}^2 + c_A]\mathrm{e}^{\mathrm{i}k_\mathrm{j}L} \tag{6.45}$$

Equation (6.41) can then be solved for the complex frequency $\lambda = \omega - \mathrm{i}\beta$.[1]

Numerical results

Consider a cantilever beam where layer 1 is made out of copper and layer 2 is made out of aluminum. The beam is subject to an inward heat flux $q = Bv$ applied at both the top and bottom surfaces. The relevant coefficients and parameters are listed in Table 6.1.

The application of the method described above yields the complex frequency λ for both Case 1 and Case 2. The corresponding results are 1)$\lambda_{\mathrm{c1w}} = 6.6147 - 0.0868\mathrm{i}$[rad/s] and 2) $\lambda_{\mathrm{c2w}} = 6.6104 - 0.0388\mathrm{i}$[rad/s]. Note that the c in the subscripts indicates "constant h_0"; the 1 and 2 correspond to Case 1 and Case 2 respectively; and the w denotes "with TED".

[1]↑An alternative approach to find λ is to discretize Eqn. (6.34) in x and then solving the corresponding eigenvalue problem.

Table 6.1. Material properties and relevant parameters.

Layer 1		Layer 2	
$E_1 = 110$[GPa]	$\rho_1 = 8960$ [kg/m^3]	$E_2 = 70$[GPa]	$\rho_2 = 2700$ [kg/m^3]
$\alpha_1 = 17 \times 10^{-6}$[K^{-1}]	$k_1 = 400$ [W/(mK)]	$\alpha_2 = 23 \times 10^{-6}$[K^{-1}]	$k_2 = 238$ [W/(mK)]
$c_{\varepsilon_1} = 385$ [J/(kgK)]		$c_{\varepsilon_2} = 900$ [J/(kgK)]	
Dimensions		**Heating parameter**	
$h = 1/8$[inch]$= 3.175$[mm]	$L = 4.5$[ft]$= 1.37$[m]	$B = 10^6$[(W/m^3)]	

According to the $\lambda = \omega - \mathrm{i}\beta$ notation, in both cases we get positive growth rates β, which indicates that the motion is being amplified exponentially. Remember that the structural damping, which counteracts the exponential growth, is not accounted for in this analyses. Damping ratio of metals is generally on the order of 10^{-3} [75].

The coefficient c_E can be viewed as a modification to the flexural rigidity due to the adiabatic thermoelastic coupling. The imaginary part of c_E, expressed as Eqn. (6.25), is positive regardless of the value of η_{i}, because the inequality $\eta - f_+(\eta) > 0$ always holds for $\eta > 0$. This result indicates that the modified flexural rigidity $(D + c_E)$ is complex with a small positive imaginary part, which leads to a slowly decaying response in time. This is the well-known thermoelastic damping effect, caused by stress inhomogeneities in the vibrating beam [66]. We can neglect the thermoelastic damping in order to evaluate its effect on the growth rate by setting $\gamma_{\mathrm{i}} = 0$ in the energy equation (Eqn. (6.17)). The resulting eigenvalues λ for both cases are 1) $\lambda_{c1wo} = 6.6054 - 0.0871\mathrm{i}$ [rad/s] and 2) $\lambda_{c2wo} = 6.6102 - 0.0396\mathrm{i}$ [rad/s]. Note that the wo denotes "without TED". Comparing these results with those obtained when keeping the thermoelastic coupling term in the energy equation, it is observed that β is slightly larger when the thermoelastic damping is neglected. Therefore it can be concluded that the thermoelastic coupling term in the energy equation has a small effect on the mechanical damping. In addition, if the heat flux (B) is large enough, the thermoelastic damping becomes negligible compared to the strong exponential growth caused by thermoacoustic instability.

The additional term associated with c_A accounts for the effects of the external heating by the coefficient B. Similar to the thermoelastic damping coefficient c_E, c_A is also complex, hence it is capable of inducing either a decaying or a growing response depending on the sign of $\mathrm{Im}[c_A]$. A negative $\mathrm{Im}[c_A]$ produces motion amplification. It is seen by Eqn. (6.23) that the sign of $\mathrm{Im}[c_A]$ depends on the material properties of the two layers and on the sign of the coefficient B. To achieve a more intense thermoacoustic growth, a negative $\mathrm{Im}[c_A]$ with

a larger absolute value is preferred. If the beam is thin compared to the thermal penetration thickness, that is $\eta_{\mathrm{i}} \ll 1$, $f_+(\eta_{\mathrm{i}}) \approx \eta_{\mathrm{i}}$, hence $\mathrm{Im}[c_A]$ is approximately equal to:

$$\begin{aligned}\mathrm{Im}[c_A] &\approx \left[E_1\alpha_1\frac{\delta_{k1}^3}{4k_1}\left(\frac{2h_1}{\delta_{k1}}-\eta_1\right)-E_2\alpha_2\frac{\delta_{k2}^3}{4k_2}\left(\frac{2h_2}{\delta_{k2}}-\eta_2\right)\right]B\\ &= \left[E_1\alpha_1\frac{\delta_{k1}^2}{4k_1}\left(\frac{h}{2}-2h_0\right)-E_2\alpha_2\frac{\delta_{k2}^2}{4k_2}\left(\frac{h}{2}+2h_0\right)\right]B\\ &= \frac{\alpha_1}{2\omega(\rho_1 c_{\varepsilon_1})}\frac{E_1E_2}{E_1+E_2}h\left[1-\left(\frac{\alpha_2}{\alpha_1}\right)\left(\frac{\rho_1 c_{\varepsilon_1}}{\rho_2 c_{\varepsilon_2}}\right)\right]B \end{aligned} \tag{6.46}$$

Therefore, the following inequality is necessary to achieve flexural thermoacoustic instability:

$$H_1\frac{E_1E_2}{E_1+E_2}\left[1-\frac{H_2}{H_1}\right]B<0 \tag{6.47}$$

where the ratio

$$H_{\mathrm{i}}=\frac{\alpha_{\mathrm{i}}}{(\rho_{\mathrm{i}}c_{\varepsilon_{\mathrm{i}}})} \tag{6.48}$$

is a measure of the rate of linear expansion of a thin material layer in response to a certain amount of heat being provided.

Equation (6.47) shows that for conventional materials whose thermal and mechanical properties are positive ($H_{\mathrm{i}} > 0$ and $E_{\mathrm{i}} > 0$), the layer with higher ratio H should coincide with the hot region ($[1 - H_2/H_1]B < 0$), so that both the thermal bending and the phase lag between heating/cooling and deformation work together to amplify the motion.

As depicted in Fig. 6.1(d) and (e), we consider the hot region being in the upper half plane ($B > 0$, i.e. $q > 0$ when $v > 0$), then the top layer (layer 2) requires larger thermal expansion coefficient α and lower heat capacity ρc_ε compared to the bottom layer. A lower heat capacity causes faster temperature changes when heated/cooled and a larger thermal expansion coefficient causes larger deformations induced by a given temperature fluctuation. A more detailed discussion on these aspects can be found in Section 6.2.2. Clearly, if the two layers are made out of the same material, $\mathrm{Im}[c_A]$ becomes zero by Eqns. (6.22-6.23). Thus, a single layer beam being heated at the same rate on both sides cannot sustain thermoacoustically induced motion.

Table 6.2. Values of λ calculated from Eqns. (6.34) and (6.51) with constant and varying h_0, respectively. Case 1 and 2 indicate bilayer beams having either infinite or zero interfacial thermal resistance, respectively. For the case of constant h_0, the eigenvalues λ calculated either with (w) or without (wo) thermoelastic damping (TED) are tabulated in the second row. Results show that the effect of TED is essentially negligible. The last row shows the eigenvalues λ for the case including both varying h_0 and negligible TED. These results are very close to those calculated from constant h_0.

λ	Case 1	Case 2
Constant h_0 w/. Eqn. (6.34)	λ_{c1w} =6.6147-0.0868i λ_{c1wo} =6.6054-0.0871i	λ_{c2w} =6.6104-0.0388i λ_{c2wo} =6.6102-0.0396i
Varying h_0 w/. Eqn. (6.51)	λ_{v1wo} =6.6053-0.0870i	λ_{v2wo} =6.6100-0.0396i

In summary, an asymmetric temperature distribution achieved via the use of an heterogeneous cross section can induce a non-zero thermal moment m_T capable of producing either a growing or a decaying response. This observation is consistent with the conclusions drawn in other studies on thermally induced vibrations [70], [72]–[74].

By comparing the growth rate β of the two cases studied in previous sections, one can conclude that the heat transfer at the interface between the two layers is actually detrimental to the onset of the instability. This is due to the fact that the interfacial heat transfer tends to smear out some of the temperature asymmetry.

Time-Varying Neutral Axis Location (Varying h_0)

In this section, we remove the previous assumption of stationary neutral axis and we consider a more physically accurate condition where the location of the neutral axis can vary according to Eqn. (6.9). Note this case, also the flexural rigidity D is no longer a constant but it depends on x. The procedure to solve the equation is conceptually equivalent to that described in Section 6.2.1. Remembering that the thermoelastic damping effect is small when B is large (see first row of Table 6.2), we can neglect the thermoelastic coupling term by setting $\gamma_{\mathrm{i}} = 0$ in order to simplify the analytical derivation.

The temperature fluctuation $\hat{T}$ and the integral quantity $\hat{A}I_T$ are determined by Eqn. (6.17) with $\gamma_{\mathrm{i}} = 0$. Since the heat flux $\hat{q}$ is proportional to $\hat{v}$, $\hat{A}I_T$ can be expressed as $\hat{A}I_T = c_T\hat{v}$. Thus:

$$h_0 = h_{\mathrm{e}} - \frac{c_T}{h/2(n+1)}\frac{\hat{v}}{\hat{v}_{xx}} \tag{6.49}$$

By Eqn. (6.5), σ_{i} is a linear combination of $\hat{v}$ and $\hat{v}_{xx}$. From Eqn. (6.4):

$$m = \int_{-h_1}^{h_0} \sigma_1 y dy + \int_{h_0}^{h_2} \sigma_2 y dy = -\left(\phi_1\hat{v} + \phi_2\hat{v}_{xx} + \phi_3\frac{\hat{v}^2}{\hat{v}_{xx}}\right) \tag{6.50}$$

where ϕ_{j} (with $\mathrm{j} = 1, 2, 3$) are constants determined by h_0 and the integral in Eqn. (6.50). Substituting Eqn. (6.50) into Eqn. (6.33) yields:

$$-\rho h\lambda^2\hat{v} + \phi_1\frac{\partial^2\hat{v}}{\partial x^2} + \phi_2\frac{\partial^4\hat{v}}{\partial x^4} + \phi_3\frac{\partial^2(\hat{v}^2/\hat{v}_{xx})}{\partial x^2} = 0 \tag{6.51}$$

Since $h_0 = h_0(x)$ is x-dependent, Eqn. (6.51) is a nonlinear equation homogeneous in terms of $\hat{v}$ and its derivatives. This indicates that the mode shapes $\hat{v}$ in modal space are scale-independent, because linearity is sufficient but not necessary for homogeneity.

Equation (6.51) can be discretized on x and solved by using a nonlinear algorithm for root extraction. The spatial derivatives are approximated by a second order central difference scheme. At each boundary, two ghost points are assumed, whose displacements are extrapolated according to a fourth order polynomial in order to ensure the boundary conditions. The eigenvalues λ and the mode shapes $\hat{v}$ are obtained for the same two cases considered in Section 6.2.1. The calculated values of λ for the two cases are 1) $\lambda_{\mathrm{v1wo}} = 6.6053 - 0.0870\mathrm{i}$ and 2) $\lambda_{\mathrm{v2wo}} = 6.6100 - 0.0396\mathrm{i}$, both are very close to the results in Section 6.2.1. The v in the subscripts denotes "varying h_0" Table 6.2 summarizes the results calculated through Eqn. (6.34) and (6.51). Figure 6.2 shows the mode shape $\hat{v}$, the neutral axis location h_0, and the effective flexural rigidity $D_{\mathrm{eff}} = -\hat{m}/\hat{v}_{xx}$. The black solid lines in the mid and right columns in Fig. 6.2 indicate the reference values of the neutral axis location h_{e} and the flexural rigidity D_{e} for an elastic beam without thermoelastic coupling. Results show that both h_0 and D_{eff} resemble their elastic counterparts near the fixed end of the beam, while they

deviate considerably near the free end. The imaginary part of D_{eff} being negative, similar to a negative $\text{Im}[c_A]$ described in Section 6.2.1, is another driver to achieve positive β, that is a growing motion.

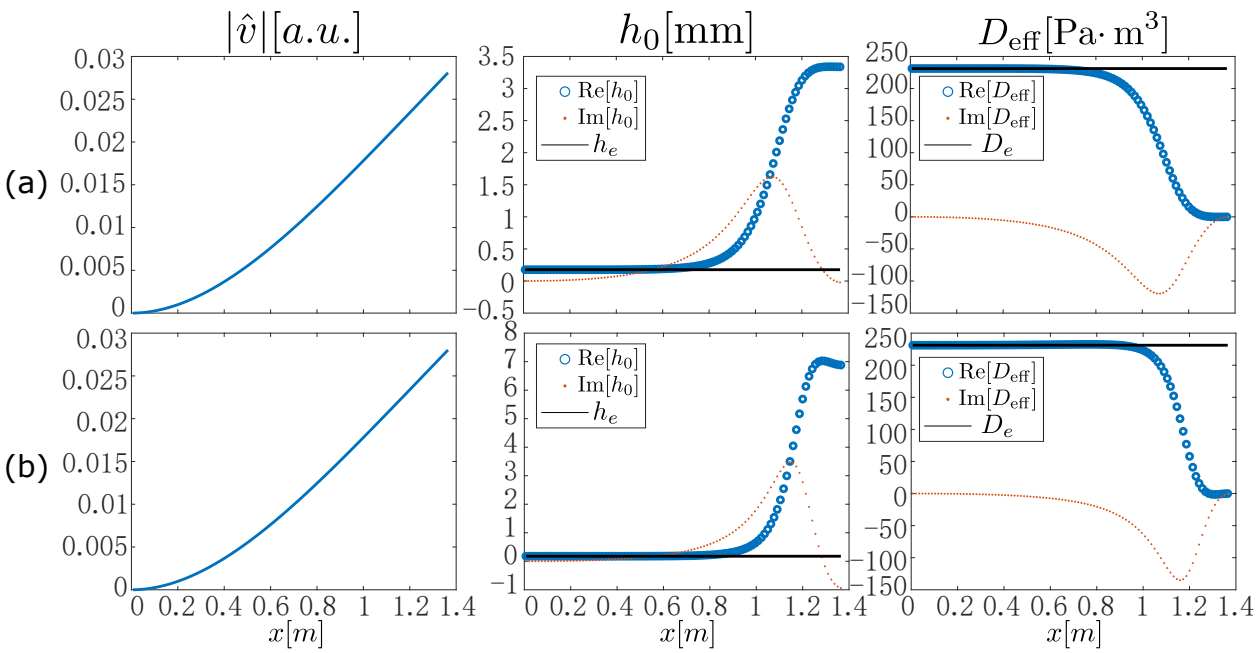

Figure 6.2. Mode shape $|\hat{v}|$, real (blue circles) and imaginary (orange dots) parts of neutral axis location h_0 and effective flexural rigidity D_{eff} for (a) Case 1. Infinite interfacial thermal resistance, and (b) Case 2. Zero interfacial thermal resistance. The black solid lines in h_0 and D_{eff} plots are the neutral axis location and flexural rigidity of a pure elastic beam as references.

6.2.2 Type II: $q = Q\text{sgn}(v)$ Heating

In this section, we consider a heating configuration which is more practical from an experimental standpoint. As depicted in Fig. 6.1, we consider a hot region in the upper half plane ($q = +Q$ when $v > 0$), and a cold region in the lower half plane ($q = -Q$ when $v < 0$). As soon as the geometrical center of the cross section is positively (negatively) displaced, the whole cross section experiences uniform surface heating (cooling) rate Q. This configuration, shown in Fig. 6.1(e), results in a non-harmonic heat flux so that the modal approach cannot be applied. Therefore, Eqn. (6.3) was solved by direct time integration with a forward-time-central-space (FTCS) scheme. The space was discretized in the same

fashion as described in Section 3. A fourth order Runge-Kutta scheme with adaptive time step was adopted for the time integration. Note that according to Eqn. (6.9), h_0 might become singular in correspondence to a zero local curvature value, that is $v_{xx} = 0$. While this scenario is physically possible, as it indicates a local change of concavity, it is numerically challenging. Hence, in order to overcome this numerical issue, a continuous filter g is imposed on $(h_0 - h_\mathrm{e})/h$. The filter is given by:

$$g\left(\frac{h_0 - h_\mathrm{e}}{h}\right) = \psi \tanh\left(\frac{1}{\psi}\frac{h_0 - h_\mathrm{e}}{h}\right) \tag{6.52}$$

Note that $g(z) \approx z$ when z is small and $g(z) \approx \psi$ when z is large. z is a dummy variable. Figure 6.3 shows the trend of this function for different values of the parameter ψ. In order to avoid the numerical instability in our study, we choose $\psi = 10000$ to approximate the case of zero curvature when h_0 approaches the singularity ($h_0 = \infty$).

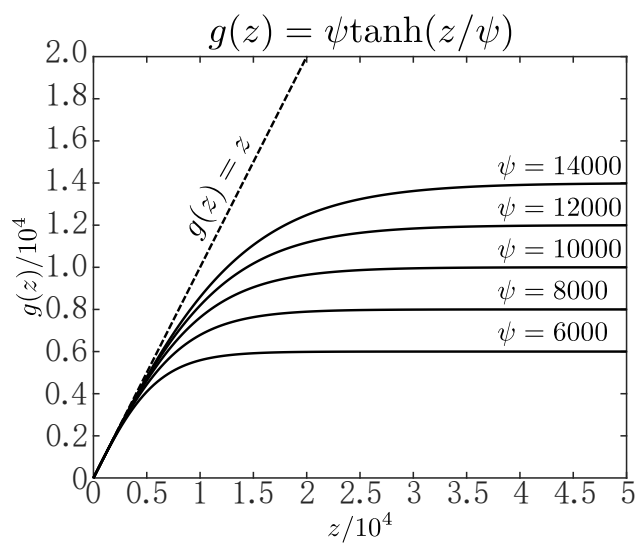

Figure 6.3. The trend of the function $g(z)$ parameterized in ψ. The dashed line shows that $g(z) \approx z$ when z is small.

By solving Eqn. (6.3), we can evaluate the time evolution of h_0, v_{xx}, v, m and of the cross-sectional averaged thermal strain $\varepsilon_T = \alpha\langle T\rangle$ over each layer. In the latter expression, the angle brackets indicate layer-cross-sectional averaging (see also online supplementary material). Results show that 1) the motion of the beam is self-amplifying, and 2) a singularity

in h_0 (i.e. a zero-curvature point) exists and propagates towards the fixed end. These two points are closely related to each other and are the result of two factors: 1) the existence of a phase lag between the thermal-induced deformation and the thermal perturbation, and 2) the differential expansion and contraction of each layer. The time evolution of ε_T (see supplementary video) shows that the thermal strain of the top layer increases (decreases) faster than the bottom layer when the beam is heated (cooled), thus insuring that the thermal strain of the top layer is larger (smaller) when the beam is moving downward (upward). This situation occurs because the top layer (here assumed to be aluminum) has a larger thermal expansion coefficient and a lower heat capacity so it reacts faster to the heat stimulus than the bottom one (here assumed to be copper). This observed behavior is consistent with the discussion on Eqn. (6.47) in Section 6.2.1.

Figure 6.4 shows the time history of the transverse displacement of the beam's midpoint numerically calculated via time integration. Differently from the $q = Bv$ type heating, the motion grows linearly instead of exponentially. This is a clear evidence of a growing motion under spatial thermal gradient.

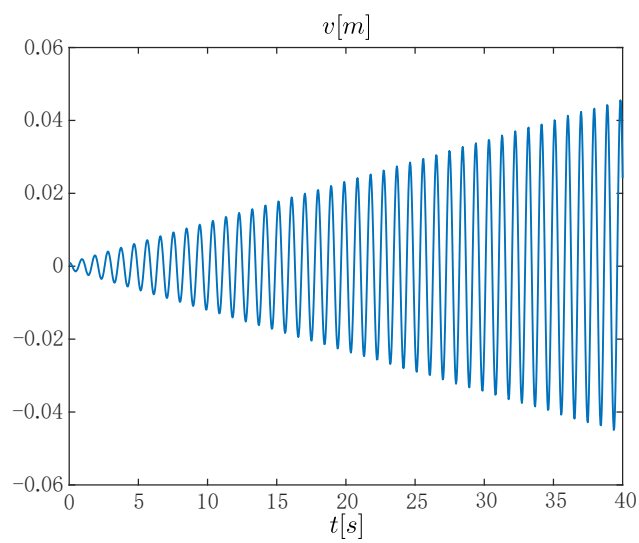

Figure 6.4. Time history of the transverse displacement at the midpoint of the beam under $q = Q\text{sgn}(v)$ type heating.

Figures 6.5 (I-IV) show the four fundamental states occurring over each selected quarter of a period, that qualitatively explain the mechanism of flexural thermoacoustic response

in the bilayer beam. In the first quarter of period (Fig. 6.5 (I)), the beam is warping upward while moving downward. The thermal strain ε_T of the top layer is larger than that of the bottom one, which makes the free end of the beam deflect downwards as a result of thermal bending. This effect changes the concavity of the beam, inducing a sign change of curvature and a singularity of h_0 at the same location. When the beam is in the upper half plane, the heating increases the difference between the elongation of the two layers, thus further increasing the bending of the beam downward. This mechanism explains why the singularity of h_0 propagates towards the fixed end (as visible in the supplementary material video). The downward thermal bending accelerates the downward elastic motion (compare the two rows in Fig. 6.5(I)), hence amplifying the motion. In the second quarter of period (Fig. 6.5 (II)), the beam is warping downward and moving downward as well. Although the beam is cooled since it is in the lower half plane, the temperature fluctuation, as well as ε_T, is still positive due to the phase delay with respect to heating. Therefore, there is still a thermally-induced downward bending which accelerates the original downward motion. However, in this quarter, the beam is elastically warping downward as well, so the additional thermally-induced downward bending does not change the sign of the curvature, but rather increases its absolute value. As a result, in this period, there is no singularity on h_0. The motion in the third and fourth quarters are analogous to the first and second, but the two layers contract instead of expanding.

An interesting observation can be drawn concerning the opportunities opened by SSTA devices. For all the configurations discussed above, the materials used for the two layers were assumed to have positive properties, i.e. $H_\mathrm{i} > 0$ & $E_\mathrm{i} > 0$, and satisfy Eqn. (6.47) by ensuring $[1-H_2/H_1]B < 0$. In recent decades, the engineering community has made much progress in the discovery and development of engineered materials capable of unusual effective dynamic properties such as, for example, negative density [63], negative modulus [64], and negative thermal expansion coefficient (CTE) [65], [67], [68]. Assuming the availability of materials having such unusual properties, we could conceive a bilayer beam capable of satisfying $H_1 < 0$ or $E_1E_2/(E_1 + E_2) < 0$. For example, assuming the top layer still made of aluminum while replacing the bottom layer with a material exhibiting negative CTE (i.e. $\alpha_1 < 0$), Eqn. (6.47) could still be satisfied. With this combination of materials, the thermally-induced

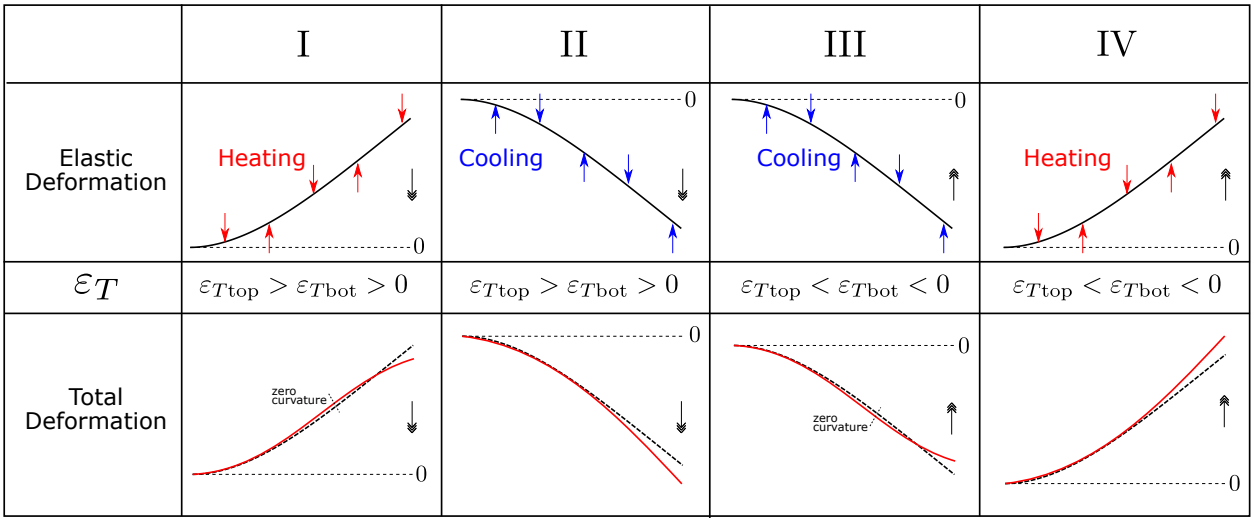

Figure 6.5. Conceptual schematic summarizing the flexural SSTA mechanism. In a given period of oscillation, the beam motion can be divided into four phases. (I, III) In the first (third) phase, the beam moves down (up), warps up (down) and is heated (cooled). The top layer expands (contracts) more than the bottom one does. Thus the beam under the effect of heat, bends down (up) starting from the free end, which (1) causes a sign change of the curvature, and (2) accelerates the downward (upward) motion. (II, IV) In the second (fourth) period, the beam moves and warps down (up), and is cooled (heated). In this phase, the temperature fluctuation, hence the thermal strain, is still positive (negative) due to the phase delay between temperature and heat flux. The top layer expands (contracts) more than the bottom one does. Thus, the beam under the effect of heat, bends down (up) further from the free end, which does not change the concavity along the beam but accelerates the downward (upward) motion. This schematic explains the self-amplifying mechanism of flexural SSTAs.

bending would be increased because the degree of thermal bending depends on the difference between the thermally-induced axial deformation of the two layers. Obviously, this difference increases if, during heating, one layer is expanded while the other is contracted. We merely note here that the use of a solid state medium as a basis for TA devices provides an excellent opportunity for tailoring the dynamic behavior and the resulting performance by leveraging engineered materials.

6.2.3 Experimental Validation

In order to validate the concept of F-SSTAs as well as the corresponding modeling framework, we performed an experimental investigation. The experimental sample consisted in a bilayer beam made of a layer of Aluminum 6061 and a layer of Copper 110. The dimensions of each strip were 1/2 inch wide, 1/16 inch thick and 4.5 feet long (Fig. 6.6). The two metallic strips were combined in a bilayer beam by means of riveted joints spaced 2 inches along the axial direction (Fig. 6.6). Two rivets were used in the width direction. The beam was oriented in a vertical position, clamped at one end, and with a 2 lbs mass attached to the free end. The mass was applied in order to lower the fundamental frequency ω of the beam so to increase the time the beam is exposed to either heating or cooling. Note that a larger thermal penetration depth $\delta_k \propto \sqrt{1/\omega}$ is in favor of the cross-sectional temperature variation subject to surface heating. The weight of the mass also limits the static thermal deformation of the beam which results from the differential expansion of the two layers. Two infrared (IR) lamps having a nominal power output of 1500 Watts were used as heat source. The lamps were located on the same side of the aluminum strip, for the argument following Eqn. (6.47). The dynamic response was measured via a Laser Doppler Vibrometer (LDV) at a point located 20 inches from the end mass.

The perturbation needed to initiate the oscillatory response was provided by displacing the free end of the beam by approximately 10 inches. When the beam enters the heating region, it absorbs heat radiated by the IR lamps; when it leaves the heating region, it cools down by natural convection. Therefore, the combination of the heating region and the natural convection cooling form a spatial thermal gradient. Although less effective in creating strong thermal gradients, natural convection was preferred to forced convection because the latter might induce aerodynamic loading possibly alter the TA response of the beam.

A few considerations should be made comparing the experimental setup with the numerical model. The transition through the hot-cold region at the interface is not as sharp as considered in the numerical simulations. This is due to heat escaping the heating region through the opening realized to allow the oscillatory motion of the beam. Also, note that the heat source is fixed in space, so only when the equilibrium position of the beam is exactly

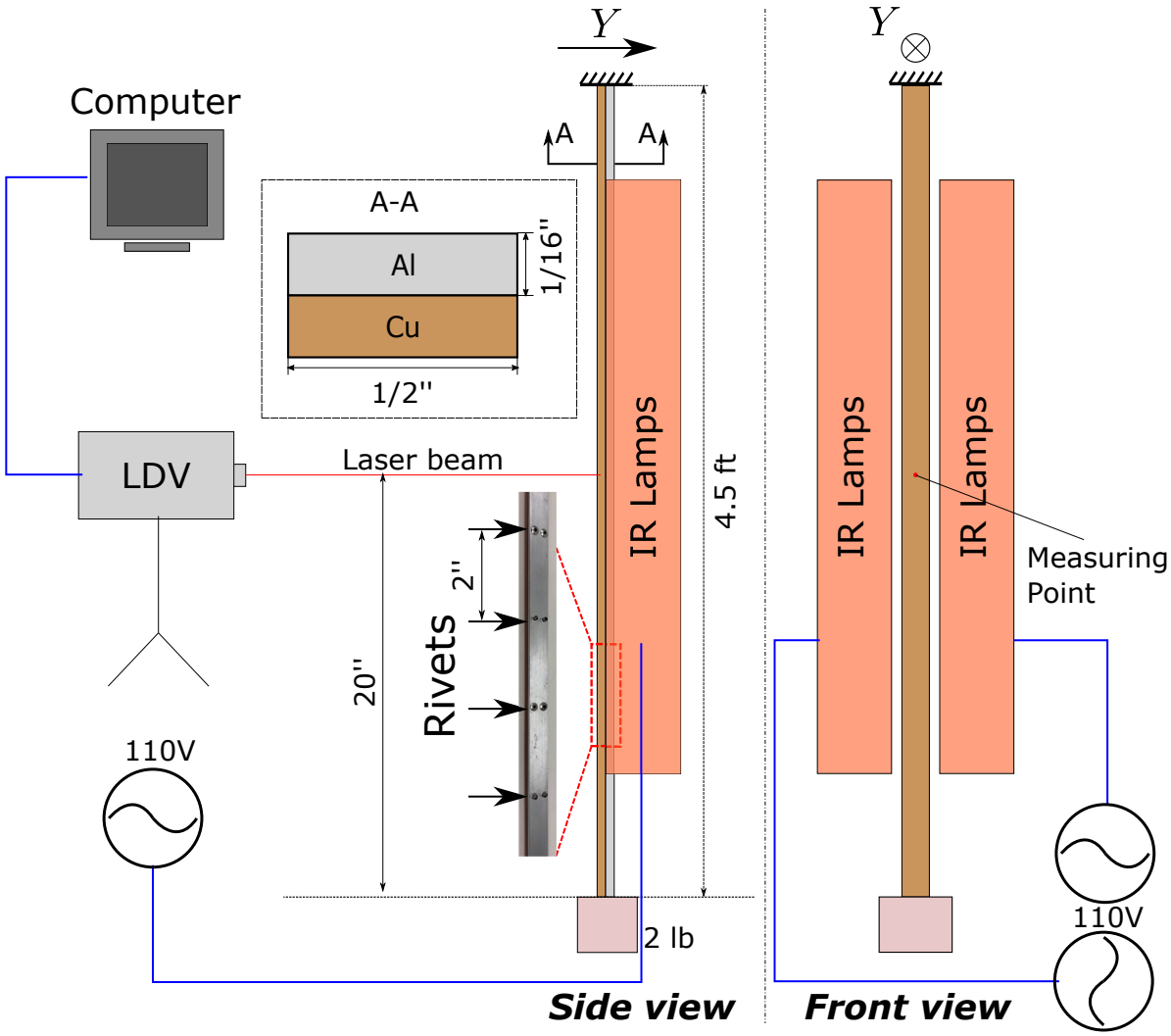

Figure 6.6. A notional schematic of the experimental setup. The cantilever beam is made of one layer of Aluminum and one of Copper joined together by an array of rivets spaced 2 inches in the axial direction (inset photo). Two 1500 watts infrared (IR) lamps were used as heat source. A mass was applied at the free end to lower the fundamental resonance frequency of the beam and to counteract its static thermoelastic deformation. The response of the beam was measured in terms of the transverse displacement of the point located 20 inches from the free end. The dynamic response is measured by an LDV.

aligned with the interface between the heating and the cooling regions, the physical thermal gradient would match the theoretical gradient of Type II thermal load. If equal amount of heating and cooling could be provided during one cycle, as assumed in the theory derived in Section 6.2, the equilibrium position of the beam would always coincide with the straight

configuration. However, in practice, the cooling does not balance exactly the heat absorbed, hence producing an increase of the average temperature of the beam. The most direct result of this average temperature increase is a static deformation of the beam due to the differential thermal expansion of the two layers. The end mass partially helps counteracting this static thermal deformation.

The experimental data were acquired under three different conditions: (1) lamps off, (2) lamps on with the beam moving only within the hot region, and (3) lamps on with the beam moving across the thermal gradient. Case (1) captures the response of the beam at room temperature and in presence of structural damping. Case (2) corresponds to the oscillatory motion of the beam occurring always in a hot environment, which leads to stronger thermoelastic damping effect. The decay in this case should be larger than Case (1). Recall that, as discussed in Sections 6.2.1 and 6.2.2, the decay induced by thermoelastic damping is negligible compared to the large growth due to strong F-SSTA effect. However, in Case (2), the F-SSTA effect is absent, so the thermoelastic effect must be noticeable. Case (3) correspond to the beam operating under actual F-SSTA conditions. Figure 6.7 (a) presents the measured transverse displacement history in these three cases. Five measurements for each case were taken. The solid lines displayed in Fig. 6.7 show the algebraic mean of these five data sets. The shaded area represents the 3σ standard deviations from the mean. The expected decay of the oscillatory motion due to either the structural or the thermoelastic dissipative mechanisms can be observed in Case (1) and (2). The response in Case (2) decays faster because both dissipative mechanisms (i.e. structural and thermoelastic) are active. In Case (3), that is the F-SSTA case, a self-sustaining motion could not be observed due to an insufficient thermal gradient. A few aspect contributed to this low grade thermal gradient: (1) the low directivity of the IR lamps which disperse part of the heat away from the beam; (2) the cooling capacity of natural convection is limited; (3) part of the heat from the hot region leaks into the cold region via the opening left for the motion of the beam, hence decreasing the strength of the thermal gradient (compared to numerical case). Nonetheless, this data set still provides useful information to characterize the dynamics of the system. By visual comparison, it appears that in Case (3) the amplitude of the displacement is the largest and the decay rate is the lowest. More quantitatively, the displacement level in Case

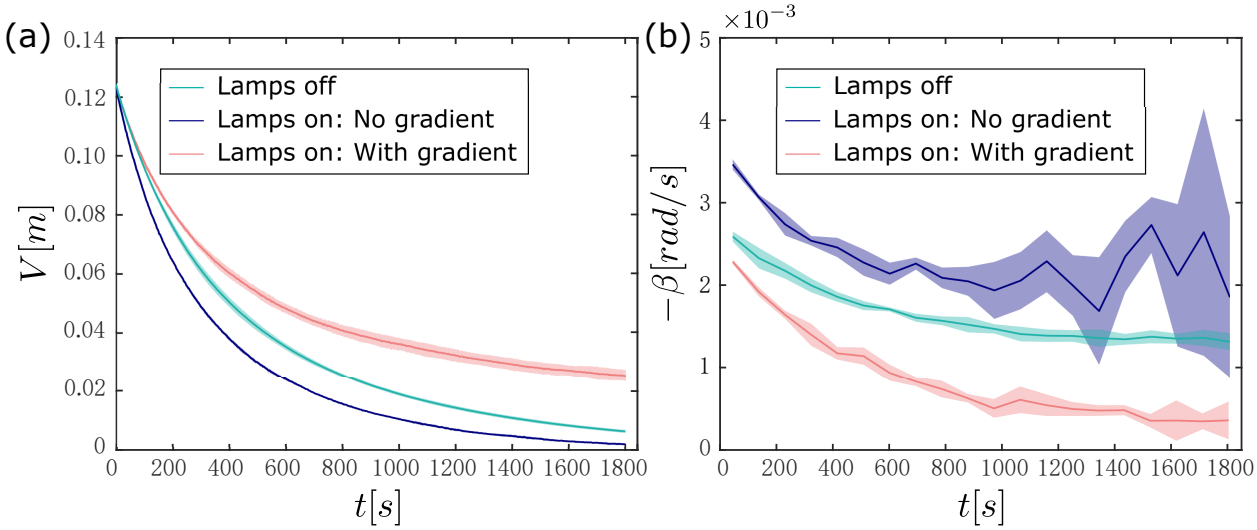

Figure 6.7. (a) Amplitude of the measured displacement for the three heating cases. Case (1), "Lamps off" shows that the damping ratio of the bilayer beam is $\sim 1.3 \times 10^{-3}$, consistent with observed values typical of metals. Case (2), "Lamps on: No gradient" decays the fastest due to the additional thermoelastic damping at high temperature. Case (3), "Lamps on: With gradient" corresponds to the F-SSTA conditions. Although no self-sustained oscillations could be observed in this case, an evident and strong reduction of the decay rate highlights the amplifying effect of the TA response. (b) Calculated decay rates (i.e. the inverse of the growth rate β) with time. The large deviations from the mean value observed towards the end of the time window in the case "Lamps on: No gradient" case are due to the signal decaying quickly below the noise floor level. Solid lines: mean value of five measurements in each case. Shaded region: 3σ error deviation from the mean.

(3) is 13.5 dB and 25.2 dB higher than that of Case (1) and Case (2), respectively. The decay rate (Fig. 6.7 (b)) is calculated by using a logarithmic decrement approach combined with a sliding window having length of 93 s ($\sim$ 20 cycles). In all cases, the decay rate is large during the initial part of the transient, while it decreases as the amplitude of the oscillation reduces. This trend can be explained as losses due to both structural and aerodynamic damping are directly related to the amplitude of the transverse displacement. Other effects affecting the global decay rate can include friction forces at the riveted interface between the two layers. As the motion reaches lower amplitudes, the decay rate stabilizes around a constant value. The decay rates of the three cases are extracted and compared in this range. In Case (1), the decay rate induced by structural damping is around 1.3×10^{-3},

which is consistent with the average value of the damping ratio for metals [75]. The higher dissipation in Case (2), due to the additional thermoelastic damping, induces a fast decay of the response that falls quickly below the noise floor level. Therefore, the measured signal is actually dominated by the ambient noise which explains the larger fluctuations towards the end of the time window. In Case (3), the decay rate nearly reaches zero towards the end of the time window, hence showing an evident delay of damping under the effect of the spatial thermal gradient. This reduction in decay rate (or, equivalently, enhancement in growth rate) is due to the thermo-mechanical energy conversion occurring in the F-SSTA process. By subtracting the time signal in Case (1) from that in Case (3), the amplified motion induced by the thermoacoustic instability can be obtained. In summary, even if a self-sustained thermoacoustic response could not be obtained in the current setup, the hallmarks of thermoacoustic growth are clearly present in the experimental data.

6.3 F-SSTA in a Hybrid Beam

Section 6.2 established the theory of flexural solid-state thermoacoustics. According to this theory, the flexural motion of slender beams (a vibration mode unique to solids) can become unstable when subject to a spatial heat flux gradient. While the experiments conducted in Section 6.2.3 could not trigger a self-sustained flexural motion, the reduction of the effective damping was a clear indicator of the thermal-to-mechanical energy conversion taking place in the flexural solid-state thermoacoustic (F-SSTA) process. In this section we will first revisit the (in)stability criterion proposed in Section 6.2, thus analyzing the possibility of utilizing a layer of negative-thermal-expansion (NTE) material to significantly enhance the F-SSTA instability. Then, we perform a numerical study of the F-SSTA response of a hybrid bilayer beam in cantilever configuration. The term hybrid refers to the particular structure of the bilayer beam that employs both a fully solid and homogeneous layer and an architectured material layer. The selection of an architectured material design is motivated by the need to tune the thermo-mechanical properties and achieve NTE behavior. NTE properties are obtained by exploiting a bi-material octet truss design. Overall, the design of the truss structure gives rise to an effective axial NTE of the entire architectured layer.

Upon heating, the effective NTE produces an axial contraction of the architectured layer as opposed to the axial extension of the homogeneous layer. The contrast between the behavior of the two layers results in a pronounced thermal bending, which is beneficial for the F-SSTA instability. Numerical results indicate that the NTE-aided F-SSTA instability is enhanced with respect to a more traditional bilayer homogeneous design.

6.3.1 Revisiting the Instability Criterion

Considering the continuous bilayer beam (Fig. 6.1(a) under a $q = Bv$ type thermal load (Fig. 6.1(c)), the transverse motion v in the frequency domain, relabeled as $\hat{v}$, is governed by:

$$-\rho h \lambda^2 \hat{v} + (D + c_E)\frac{\partial^4 \hat{v}}{\partial x^4} + c_A \frac{\partial^2 \hat{v}}{\partial x^2} = 0 \tag{6.53}$$

where h is the total height of the two layers, λ is the complex frequency, whose imaginary part is indicative of either the amplifying or the attenuating motion, depending on its sign. D is flexural rigidity, and c_E and c_A are complex coefficients due to the thermoelastic coupling and the inward heat flux q, respectively (see also Eqn. 6.34). The use of the $q = Bv$ type thermal load is convenient because it is amenable to analytical treatment. Following a $q = Bv$ type thermal load, the thermal bending term $\partial^2 m_T/\partial x^2$ in Eqn. (6.12) can be recast into $[c_E \partial^4 \hat{v}/\partial x^4 + c_A \partial^2 \hat{v}/\partial x^2]$, as shown in Eqn. (6.53). This manipulation of the thermal bending term facilitates a more detailed interpretation of the coupled response (See also Section 6.2). In fact, the motion can grow exponentially in time if $\mathrm{Im}[\lambda] < 0$, because $v \sim \exp[(-\mathrm{Im}[\lambda] + \mathrm{i}\mathrm{Re}[\lambda])t]$. The symbols Re[ ] and Im[ ] denote the real and imaginary parts of a complex-valued quantity.

To facilitate the understanding of the F-SSTA instability, we isolate the thermoelastic effect (c_E in Eqn. (6.53)) and the thermoacoustic coupling (c_A). If the thermoacoustic coupling is neglected, that is $c_A = 0$, Eqn. (6.53) becomes

$$-\rho h \lambda^2 \hat{v} + (D + \mathrm{Re}[c_E] + \mathrm{i}\mathrm{Im}[c_E])\frac{\partial^4 \hat{v}}{\partial x^4} = 0 \tag{6.54}$$

It was proven in Section 6.2 that $\mathrm{Re}[c_E] \ll D$ and $\mathrm{Im}[c_E] > 0$. Therefore, the effective flexural rigidity $D_{\mathrm{eff}} = D + \mathrm{Re}[c_E] + \mathrm{i}\mathrm{Im}[c_E] \approx D + \mathrm{i}|\mathrm{Im}[c_E]|$ is complex-valued with a positive imaginary part, which eventually leads to a decaying motion. Considering $\mathrm{Im}[c_E] \ll D$, the exponential decay rate induced by the thermoelastic damping should be proportional to $\mathrm{Im}[c_E]/D$, or, equivalently $(\mathrm{Im}[\lambda]/\mathrm{Re}[\lambda]) \sim (\mathrm{Im}[c_E]/D)$.A short proof is developed below.

Considering $\partial/\partial x \sim 1/\Lambda$, where Λ denotes the wavelength, Eqn. (6.54) is rewritten as:

$$-\rho h \lambda^2 + \frac{D + \mathrm{i}\mathrm{Im}[c_E]}{\Lambda^4} \sim 0 \tag{6.55}$$

Note that $\mathrm{Re}[c_E]$ is neglected due to $\mathrm{Re}[c_E] \ll D$. Equation (6.55) can be further manipulated to yield:

$$\lambda \sim \sqrt{\frac{D + \mathrm{i}\mathrm{Im}[c_E]}{\Lambda^4 \rho h}} = \sqrt{\frac{D}{\Lambda^4 \rho h}} \sqrt{1 + \mathrm{i}\frac{\mathrm{Im}[c_E]}{D}} \sim \sqrt{\frac{D}{\Lambda^4 \rho h}} \left[1 + \mathrm{i}\left(\frac{\mathrm{Im}[c_E]}{2D}\right)\right] \tag{6.56}$$

Note that the relation $\sqrt{1 + \mathrm{i}(\mathrm{Im}[c_E]/D)} \approx 1 + \mathrm{i}(2\mathrm{Im}[c_E]/D)$ is used thanks to $\mathrm{Im}[c_E]/D \ll 0$. Therefore, the exponential decay rate $(\mathrm{Im}[\lambda]/\mathrm{Re}[\lambda])$ is expressed as:

$$\frac{\mathrm{Im}[\lambda]}{\mathrm{Re}[\lambda]} \sim \frac{\mathrm{Im}[c_E]}{2D} \sim \frac{\mathrm{Im}[c_E]}{D} \tag{6.57}$$

Analogously, the thermoacoustic coupling can also lead to a decaying motion if $\mathrm{Im}[c_A] > 0$, or an amplifying motion if $\mathrm{Im}[c_A] < 0$ (See also Section 6.2). The third term (thermoacoustic coupling term) in Eqn. (6.53) is on the order of $\Lambda^2 c_A(\partial^4 \hat{v}/\partial x^4)$, considering $(\partial^2/\partial x^2) \sim \Lambda^2(\partial^4/\partial x^4)$. Following the same procedure of the previous proof, the growth-rate-to-frequency ratio β/ω of this bilayer beam is approximately proportional to:

$$\beta/\omega = -\frac{\mathrm{Im}[\lambda]}{\mathrm{Re}[\lambda]} \sim \frac{|\mathrm{Im}[c_A]|\Lambda^2}{D} \sim -\frac{\mathrm{Im}[c_A]}{D} \tag{6.58}$$

Therefore, to achieve an unstable F-SSTA response, we require $\beta/\omega > 0$, or equivalently, $\mathrm{Im}[c_A] < 0$. The latter is the instability criterion proposed in Section 6.2, which is recast into:

$$\mathrm{Im}[c_A] = \frac{1}{2\omega} hB(H_1 - H_2)E_2 \frac{n}{n+1} < 0 \tag{6.59}$$

where $n = E_1/E_2$ is the Young's modulus ratio of the two layers, which indicates the relative stiffness. The ratio $H = \alpha/(\rho c_\varepsilon)$, where ρ is density, and c_ε is the specific heat at constant strain. It is seen that H is a measure of the rate of linear expansion of a thin material layer in response to a certain amount of heat being provided.

To achieve a negative $\mathrm{Im}[c_A]$, our previous study exploited two layers consisting of different materials so that the ratio $H_h = H_2$ associated with the properties of the material on the heated side must be larger than the ratio $H_c = H_1$ provided by the material on the cooled side. Qualitatively speaking, in a continuous bilayer beam composed of two positive CTE materials, both layers expand upon heating. However, the layer with higher CTE undergoes a more pronounced expansion than the layer with lower CTE. The result of this differential behavior is a thermal moment that causes the beam to bend towards the side of the lower-CTE layer (See also Eqn. (6.12)). This thermally-induced bending occurs periodically (i.e. at every cycle of oscillation) and it is the main cause of the ensuing unstable flexural motion. The instability criterion (Eqn. (6.59)) also suggested that, by selecting a material with negative H_c, or H_1, the F-SSTA response could be enhanced. Given the functional dependencies of H, it appears that one way to get a negative ratio is to use materials with negative CTE. In the system with a negative-CTE layer, upon provided heat, the positive-CTE layer expands in the axial direction while the negative-CTE layer contracts. This mechanism further enhances the thermal bending by enlarging the difference between the axial thermal deformation of the two layers.

From the above discussion, it appears that to achieve high performance F-SSTA systems and to facilitate an experimental implementation (See alsoSection 6.2), a design capable of negative CTE components could be particularly efficient. In this study, we present a novel design that consists of a hybrid bilayer beam where one layer is engineered to exhibit axial negative thermal expansion. It is anticipated that such hybrid bilayer beam could outperform

a continuous bilayer beam in terms of their F-SSTA instability, according to the instability criterion of F-SSTA systems (Eqn. 6.59).

6.3.2 Description of the Hybrid Bilayer Beam

The benchmark system under consideration consists in a hybrid beam made of two layers (Fig. 6.8). One layer has a continuous solid design (i.e. a slender beam having rectangular cross section) and it is made of a homogeneous and isotropic material. The second layer is conceived as an architectured periodic material whose building block is an octet truss composed of eight bi-material tetrahedrons, proposed by Xu and Pasini [68]. The effective CTE of the tetrahedron in the z_1 direction (See Fig. 6.8 (a.2)) can be adjusted by properly selecting the two constituent materials (on the basis of their respective CTEs) as well as the skew angle θ. For a material pair such as aluminum and titanium alloy Ti-6Al-4V, the anisotropic CTE in the z_1 direction varies between -60×10^{-6}[1/K] to 10×10^{-6}[1/K] as θ is varied [68]. As explained in Section 6.3.1, the F-SSTA motion relies on the beam's thermal moment induced by the distinct axial deformations of the two layers upon heating (See also Section 6.2). Therefore, the octet truss is oriented in a way that its z_1 axis (Fig. 6.8 (a.2)), that is the axis along which the value of CTE can be tuned to negative values, is parallel to the axial direction (z-direction) of the hybrid bilayer beam. The hybrid beam is mounted in a cantilever configuration as shown in Fig. 6.8 (b). The beam is subject to an inward heat flux $q = Q\text{sgn}(v)$ that is a sign function of the beam's transverse displacement v. We stress that the heat flux is applied to all surfaces of the hybrid beam that are exposed to air. As shown in Section 6.2, this type of thermal gradient gives rise to a linearly growing flexural motion of a continuous bilayer beam (under assumptions of negligible structural damping). In practice, this type of thermal load can be realized by utilizing uniform and vertically aligned heat sources (e.g. infrared lamps in Section 6.2.3) and placed on the same side of the aluminum layer, hence creating an effective hot region characterized by $q = Q$ when $v > 0$. The other half space can be subject to either forced or natural convection which enforces the cold region (approximately modeled as $q = -Q$ when $v < 0$, see Fig. 6.8(b)). More details

related to the practical implementation of this type of heat source can be found in Section 6.2.3.

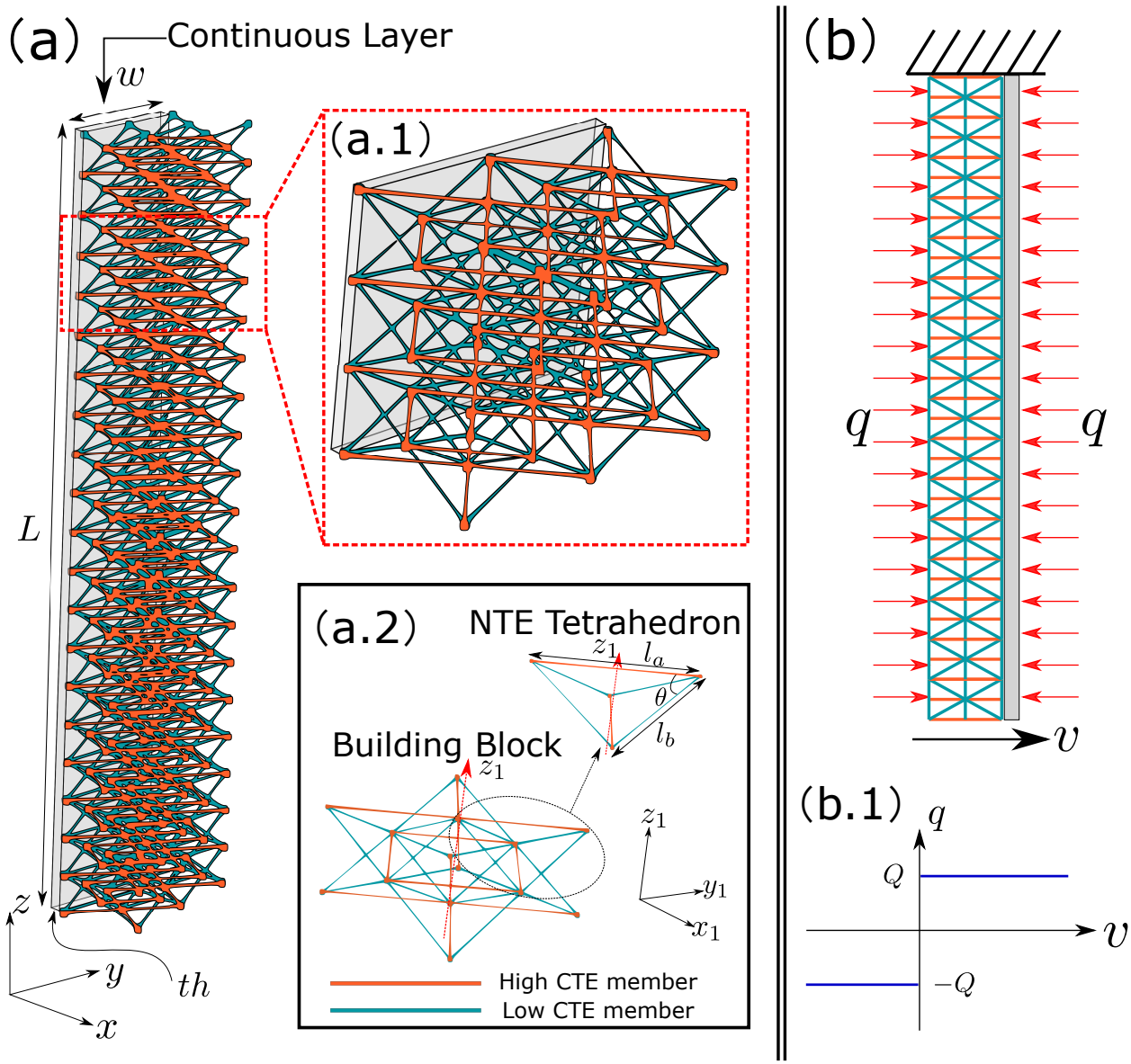

Figure 6.8. (a) Schematic of the hybrid beam composed of two layers, one being continuous and the other being a periodic truss structure. For illustration, we show a truss layer that consists of 40 units ($N_z \times N_y = 20 \times 2$), while the geometrical details of 6 repeating units ($N_z \times N_y = 3{\times}2$) are shown in (a.1). (a.2) The building block of the truss structure is an octet composed of eight tetrahedrons having negative CTE in the z_1 direction. (b) The hybrid beam is under an inward heat flux, which is a sign function of its transverse displacement, shown in (b.1)

Table 6.3. Geometrical parameters. Refer to Fig. 6.8 for labels. $h_{a/b}$ and $d_{a/b}$, which are not shown in Fig. 6.8, indicate the width and the thickness of the rectangular cross section of the individual truss member. The high CTE and low CTE truss members are represented by the orange and blue lines in Fig. 6.8(a.2).

Continuous layer (Aluminum)		
$w = 40$ [mm]	$th = 1.59$ [mm]	$L = 733$ [mm]
High CTE truss members (Aluminum)		
$h_a = 0.283$ [mm]	$d_a = 0.141$ [mm]	$l_a = 14.1$ [mm]
Low CTE truss members (Titanium)		
$h_b = 0.0826$ [mm]	$d_b = 0.141$ [mm]	$l_b = 11.0$ [mm]
Skewness angle $\theta = 50°$		

Table 6.4. Material properties.

	Aluminum	Titanium
E [Gpa]	70	113.8
ρ [kg/m^3]	2700	4430
c_ε [J/(kgK)]	900	526.3
CTE [10^{-6} 1/K]	23	11.5

Consider the hybrid beam in Fig. 6.8 where the continuous layer is made out of aluminum. The architectured periodic layer is made out of two constituent materials, namely aluminum and titanium alloy Ti-6Al-4V. In the following, this architectured layer will be referred to as the truss layer. The relevant geometrical and material parameters can be found in Tables 6.3 and 6.4.

6.3.3 Numerical Modeling of the Hybrid Bilayer Beam

This section presents the numerical models used to analyze the hybrid beam design, followed by the numerically calculated F-SSTA responses of the hybrid beam. Before proceeding to the numerical simulation of the entire hybrid beam, we performed an initial assessment of the static CTE of the fundamental building block (Fig. 6.8 (a.2, down)) at the basis of the

truss layer. The CTE α_{z1} of such block in the z_1 direction (Fig. 6.8 (a.2)) was extracted by numerical simulations performed using the commercial software COMSOL Multiphysics. In these simulations, a uniform $\Delta T = 10$[K] static temperature difference (with respect to the ambient temperature) was applied on the building block. The resulting static strain ϵ_{z1} in the z_1 direction was used to extract the CTE $\alpha_{z1} = \epsilon_{z1}/\Delta T = -41.9 \times 10^{-6}$[1/K], which was found consistent with the theoretical prediction in [68]. Following this initial validation of the equivalent CTE, the entire hybrid beam was assembled and used to evaluate the F-SSTA response.

Numerical Models

To simulate the hybrid beam, we considered two different modeling strategies based on different physical assumptions. One model was based on a three-dimensional (3D) elasticity formulation, hence capturing the full geometry of both the links, or the truss members, in the truss layer and the solid layer, as shown in Fig. 6.9(a, top). The 3D model was discretized using 3D tetrahedral elements. The second model leveraged simplified 1D and 2D structural mechanics theories in an effort to capture the same mechanical and dynamic behavior while reducing the size of the resulting model. In this reduced model, the truss members in the truss layer were modeled based on the Euler-Bernoulli (EB) beam formulation while the solid layer was modeled according to the Kirchhoff plate theory (Fig. 6.9 (a, bottom)). The cross-sectional parameters listed in Table 6.3 were entered as input data. These two models, are hereinafter referred to as the full 3D model and the reduced model, respectively. It is highlighted that, although the full 3D model provides a more accurate representation of the actual geometry of the hybrid beam, it leads to a large number of degrees of freedom. In cases where the truss layer includes many unit cells (e.g. $N_z \times N_y = 80 \times 2$) and the transient response is sought, this approach can result in a drastic increase in size that becomes rapidly unmanageable from a computational perspective. On the other side, the reduced model offers a much more efficient option to simulate the response the F-SSTA hybrid beam system. Therefore, in the following section, we will first perform a numerical analysis to compare the performance of both modeling approaches in terms of both the static and the modal

response. For this task, we will use a hybrid beam having a small number of unit cells (i.e. $N_z \times N_y = 20 \times 2$) so to allow an efficient solution with both methods. This initial model validation will be followed by a time-dependent analysis of a full scale hybrid beam (i.e. $N_z \times N_y = 80 \times 2$) performed using the reduced model.

Validation of the Reduced Numerical Model

To validate the reduced model and show its ability to capture all the relevant features of the hybrid beam, we compared its static and modal response with that of the full 3D model. The test model for this validation phase consisted in a hybrid beam counting $N_z \times N_y = 20 \times 2$ units. The 3D model was discretized into $\sim 4,840,000$ 3D quadratic tetrahedral finite elements, corresponding to ~ 20 million degrees of freedom (DOFs), while the reduced model only used $\sim 170,000$ 2D quadratic triangular elements and $\sim 100,000$ 1D linear edge elements, corresponding to ~ 2.5 million degrees of freedom. The large discrepancy in DOFs already suggests the significant saving in computational resources offered by the reduced model. The comparison between the physical responses predicted by the two models is presented in Fig. 6.9 (b) and (c) in terms of both the thermoelastic static deformation produced by a 10[K] temperature difference, and of the modal characteristics of the fundamental mode (accounting both the frequency and the modal deformation). Note that the static deformation (Fig. 6.9(b)) was induced by imposing a spatially-uniform static temperature difference (with respect to the ambient temperature) $\Delta T = 10$[K] on the entire structure. Figure 6.9(b) shows that the static displacement profile obtained with both models. Aside from an evident visual resemblance, the maximum displacement of the free end is calculated at 9.7×10^{-5}[m] for the reduced model, and at 9.9×10^{-5}[m] for the full 3D model; a maximum error of 2%. Concerning the modal analysis (Fig. 6.9(c)), the eigenfrequency of the fundamental mode were also found to be very close (41.52 Hz for the reduced model compared with 42.24 Hz for the full 3D model) and within a maximum error of 1.7%. Remembering that the F-SSTA response is dominated by the thermoelastic response and by the fundamental mode of the structure, these results confirm the validity of the reduced model and the fact that it can

be used as an effective surrogate model. In the following, we will only exploit the reduced model to simulate the time-dependent F-SSTA response of the hybrid beam.

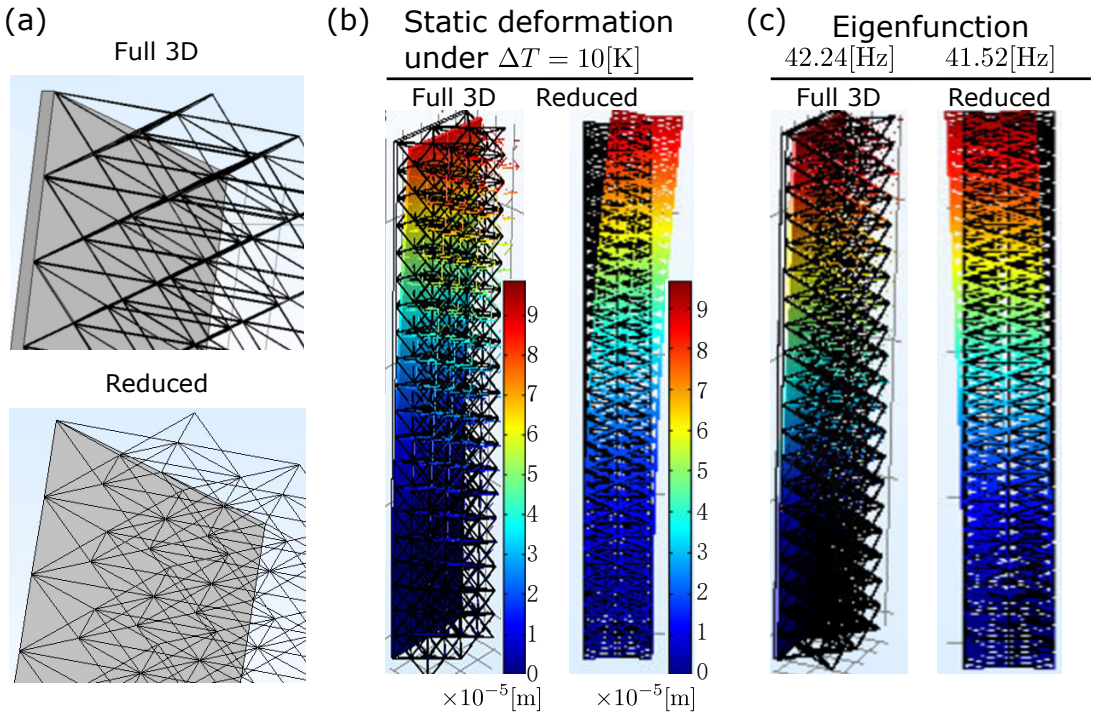

Figure 6.9. (a) Zoomed-in view showing some geometric detail of the two hybrid beam models. Full 3D model: based on complete 3D geometry and elasticity formulation. Reduced model: based on a 1D Euler Bernoulli beam formulation for the members in the truss layer and 2D Kirchhoff plate formulation for the flat solid layer. Using a hybrid beam composed of 40 ($N_z \times N_y = 20 \times 2$) and constrained in cantilever configuration (bottom end in figure), the two models were compared both in terms of their static thermoelastic and modal response. (b) Static deformation under a spatially uniform temperature difference of 10[K]. (c) Eigenfrequency and eigenfunction
corresponding to the fundamental flexural mode of the hybrid beam.

Time-Dependent Simulation of NTE-aided F-SSTA Beam

In order to assess the F-SSTA performance of the hybrid beam, we performed a time-dependent analysis of a beam assembled based on 160 units ($N_y \times N_z = 80 \times 2$), subject to inward surface heat flux in the form of $q = Q\text{sgn}(v)$. In the following, this hybrid beam with 160 units will be referred to as the NTE beam (as in Negative Thermal Expansion) Note that, owning to the low frequency involved in the TA driven oscillatory response of the beam,

we neglected the time lag associated with heat conduction process. This assumption is well justified by the fact that the dimensions in the transverse direction of the truss members and the continuous layer are much smaller than the thermal penetration depth $\delta_k = \sqrt{2\kappa/\omega}$, where κ is thermal diffusivity of the materials and ω is the angular frequency. Under this assumption, the surface heating at the boundaries of each element in the beam is converted to an effective volumetric heating source with no time lag. The volumetric heating source p is expressed as:

$$p[\mathrm{W/m^3}] = \frac{S}{V}(q[W/m^2]) \tag{6.60}$$

where S and V are the surface area and the volume of that element, respectively. The time evolution of the temperature field in the beam and plate elements are expressed as:

$$\frac{dT}{dt} = \frac{p}{\rho c_\varepsilon} = \frac{S}{V}\frac{Q}{\rho c_\varepsilon}\mathrm{sgn}(v) \tag{6.61}$$

The thermo-mechanical coupling was completed by including the thermal stress resulting from the temperature field calculated via Eqn. (6.61) in the structural analysis.

In order to assess the performance of the NTE beam design, we considered two additional bilayer beams that will serve as baseline (or reference) configurations: 1) a bilayer beam (aluminum and Ti-6Al-4V) where both layers are continuous, and 2) a hybrid bilayer beam where the continuous layer is made out of aluminum and the truss layer shares the same geometry used for the NTE beam but made out of a single material Ti-6Al-4V, hence not capable of NTE (see Fig. 6.10). In the following, we will refer to these reference models as RB1 and RB2, respectively. The length of both reference beam models was slightly modified in order to match the fundamental frequency to that of the NTE beam that was found to be approximately 2.6 Hz.

Figure 6.10 shows the displacement envelop of the free end of each beam as a function of time, under the surface heat flux $q = Q\mathrm{sgn}(v)$ with $Q = 77[\mathrm{W/m^2}]$. In order to trigger the flexural motion of the bilayer beam, an initial perturbation is needed. In a practical experiment, even the ambient-induced vibration could be sufficient. In our numerical simulations, we applied the perturbation in the form of a displacement initial condition over the entire

beam; the displacement profile was scaled following the fundamental mode shape. While any initial displacement profile would have had the required effect of triggering the instability, the chosen initial condition has the added benefit of minimizing the initial transient. Recall that the thermoacoustic response is driven by the fundamental mode, so by choosing the initial condition in the form of a displacement profile scaled as the fundamental mode we can target directly this mode. Finally, we chose a scaling that resulted in a free-end displacement equal to 1[mm]. In an undamped beam, any initial perturbation regardless of its magnitude will be amplified by the periodic thermal loading $q = Q\text{sgn}(v)$. However, in a damped beam under a fixed Q, there exists a critical value of the amplitude of the initial perturbation such that the response can be seen either growing (if starting below the critical value) or attenuating (if starting above the critical value). Despite this initial behavior both responses will evolve towards the same limit cycle response (which is controlled exclusively by the self-sustained oscillation). This aspect will be further clarified in Section 6.4 when addressing the energy conversion mechanism. Equivalently, for a fixed initial condition, there exists a critical Q value such that only above this value the initial perturbation can be amplified, because a larger Q represents more energy production.

Getting back to the analysis of the results in Fig. 6.10, in order to highlight the contribution of the NTE property we neglected any form of dissipation (including structural damping and thermoelastic damping). The damped F-SSTA response will be shown later in this section, and will be discussed more in detail in Section 6.4. It is well visible from the results that the motion of RB1, in the absence of any damping, grows linearly as predicted by the model proposed in Section 6.2 (See Fig. 6.4). The motion of RB2 remains practically unaltered, showing no significant signs of amplification. Although the effective CTE of the Ti-6Al-4V truss layer is positive (only one constituent material is used in the truss layer), the lower effective stiffness of the cellular structure limits significantly the stress contributing to the thermal moment.

To understand this behavior more in detail, we revisit the instability criterion developed in Section 6.2 and reported in Eqn. (6.59). Note that, in Eqn. (6.59), we consider a negative

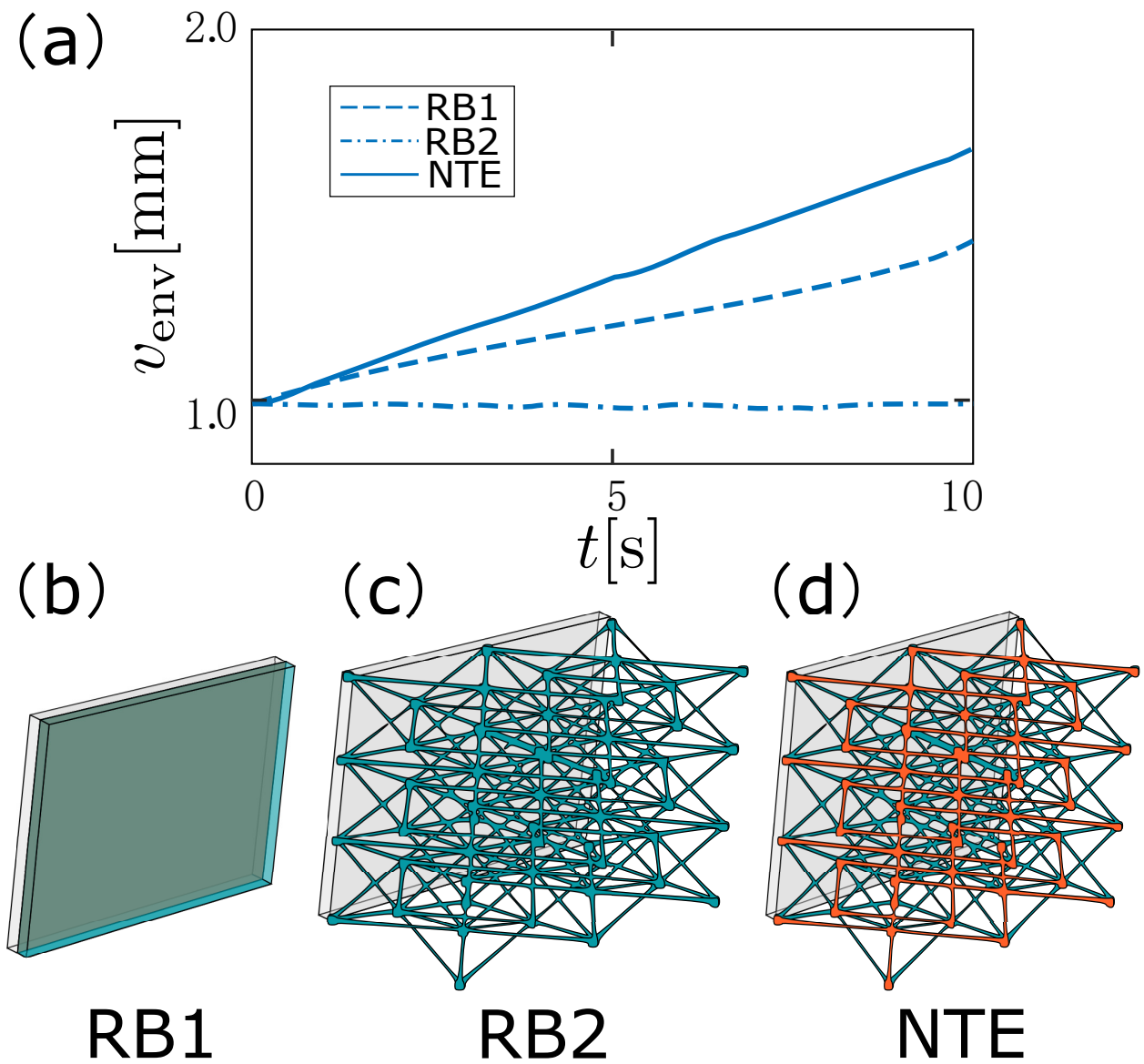

Figure 6.10. (a) Time history of the envelope of the free-end displacement of the beams ensuing from a thermal load $Q = 77[\text{W/m}^2]$. View of a few unit cells for the (b) RB1 beam, (c) RB2 beam, and (d) the NTE beam. Damping is neglected in all three cases.

$\text{Im}[c_A]$ as a necessary condition for F-SSTA instability. The expression of D, originally derived in Section 6.2 (Eqns. 6.13), is also recast into the following form:

$$D = \frac{1}{96} E_2 h^3 \frac{n^2 + 14n + 1}{n + 1} \tag{6.62}$$

Recall that $n = E_1/E_2$ is the Young's modulus ratio of the two layers. Incorporating Eqns. (6.59) and (6.62), Eqn (6.58) is further simplified as:

$$\beta/\omega \sim -48\frac{B(H_1 - H_2)}{\omega}\frac{\lambda^2}{h^2}\phi(n) \tag{6.63}$$

where

$$\phi(n) = \frac{n}{n^2 + 14n + 1} \tag{6.64}$$

Note that the material of the two layers of the beam is selected so that $H_1 - H_2 < 0$, which guarantees the negativity of $\mathrm{Im}[c_A]$ (Eqn. (6.59)) and therefore a positive β/ω (Eqn. (6.63)), and that as $n \to 0$, $\phi(n) \sim n \to 0$ (Eqn. (6.64)).

Recall that the qualitative discussion about the role of c_A and $\phi(n)$ is based on the $q = Bv$ type thermal load (See also Section 6.2), which facilitates the analytical interpretation. Given that numerical calculations were not performed using the $q = Bv$ thermal load, the numerical value of B was not provided. All the quantitative (numerical) simulations presented in this paper are based on a more realistic thermal load $q = Q\mathrm{sgn}(v)$.

For RB2, the Ti-6Al-4V truss layer is much less stiff than the aluminum continuous layer ($n \ll 1$), hence resulting in a near-zero growth-rate-to-frequency ratio. Qualitatively speaking, when the bilayer beam is heated, the axial stretching of the continuous layer dominates the weak thermal expansion effect of the Ti-6Al-4V truss layer. As a result, the Ti-6Al-4V truss layer provides a weak contribution to the thermal bending of the overall bilayer beam. The truss layer ends up acting as an appendix whose motion is dominated by the axial expansion and contraction of the continuous layer.

Despite the relatively low stiffness of the NTE truss layer leading to small n, the NTE beam still exhibits a pronounced effect of the thermal bending of the continuous layer due to the strong contraction associated with the significantly negative CTE. It turns out that the motion of the NTE beam grows linearly with time faster than the motion of RB1. In fact, the two-constituent truss layer can be seen equivalently as a continuous compliant material that shrinks when heated. These results confirm the possibility of using a NTE material to enhance the F-SSTA instability, hence suggesting a promising pathway towards

the experimental realization of a self-sustained flexural motion driven by a spatial thermal gradient.

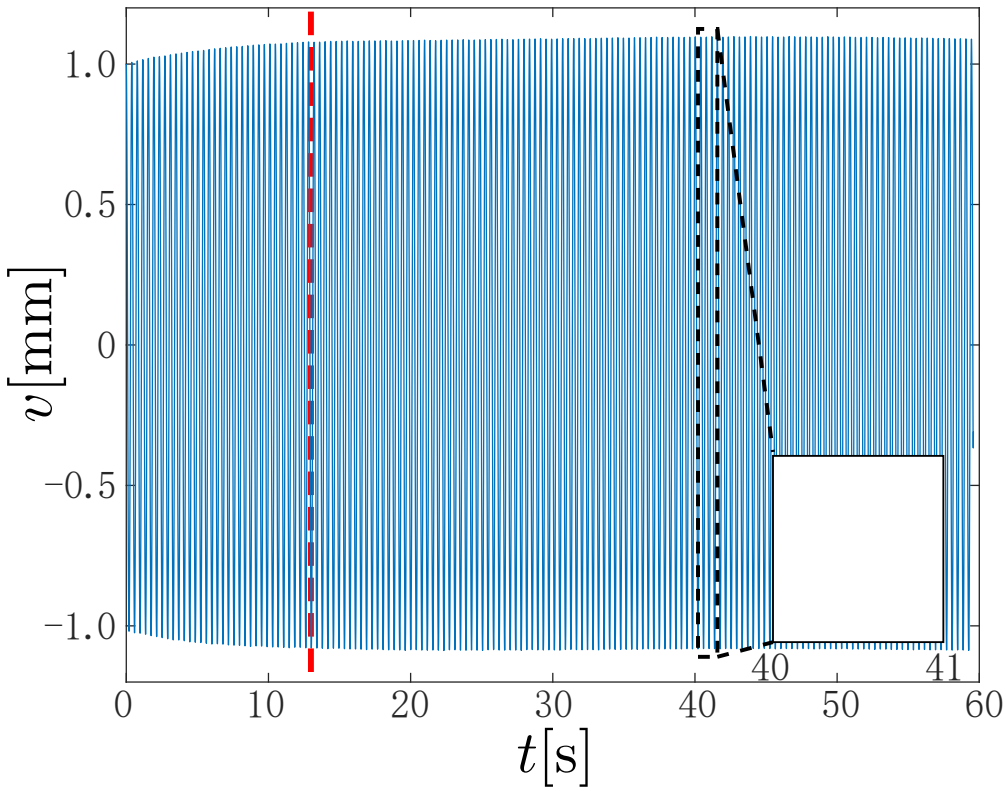

Figure 6.11. Sustained oscillation of the free end of the NTE beam in the presence of 1% damping. First, the motion grows (up to the red dashed line), and then it saturates to limit-cycle oscillation due to the presence of damping. The inset shows that the limit-cycle oscillation is quasi-harmonic.

When dissipative effects are neglected, the F-SSTA response of a bilayer beam can grow unbounded regardless of the amplitude of the spatial thermal gradient. Recall that the former condition assumed that the heating region and the layer with larger CTE were in the same half plane (See also Section 6.2). However, when a dissipation mechanism (e.g. structural damping) is present, there exists a critical magnitude of the thermal gradient above which the self-sustained flexural motion is possible. Figure 6.11 shows the self-sustained flexural motions of the NTE beam subject to the thermal load amplitude $Q = 230[\mathrm{W/m^2}]$ and in the presence of Rayleigh damping [76]. The effective damping ratio ζ at the fundamental frequency ω_r is 1%, achieved by setting the two Rayleigh damp-

ing coefficients equal to each other $a_M = a_K = a$. The damping ratio can be written as $\zeta = 0.5(a_M/\omega_r + a_K\omega_r) = 0.5a(1/\omega_r + \omega_r) = 1\%$, and the relation can be inverted to find the coefficient a. Unlike the undamped case, the flexural motion cannot grow unbounded due to the energy dissipation associated with structural damping. Initially, the response grows linearly while slowly reaching steady-state oscillation (Fig. 6.11), hence suggesting the attainment of an energy balance between the thermoacoustic gain and the damping-induced dissipation. Further considerations on the energy balance are provided in Section 6.4. Figure 6.11 also reveals that the critical value Q to trigger self-sustained flexural instability is approximately $Q = 230[\mathrm{W/m^2}]$, since the saturation happens rapidly after the initial growth. As described above, the motion is initiated by a perturbation of the free-end corresponding to a 1[mm] displacement, and it rapidly saturates. This behavior indicates that, under a fixed thermal load $Q = 230[\mathrm{W/m^2}]$, the critical initial free-end displacement necessary to achieve an amplifying motion is slightly over 1 [mm], as also discussed earlier in this section. Any initial perturbation that is smaller than the critical value (here approximately identified at $v = 1[\mathrm{mm}]$) will be amplified at first and eventually saturate and reach limit cycle behavior. Regardless of the value of the initial perturbation, the response always reaches the limit-cycle oscillation. However, the initial transient can show either a growing or an attenuating response depending on the amplitude of the initial perturbation with respect to the critical value. The energy conversion process will be further analyzed in the next section.

6.4 Analysis of Energy Conversion in F-SSTA systems

The previous discussion clearly highlighted that the thermo-mechanical energy conversion mechanism is key for the performance of the F-SSTA system. It follows that, from a design perspective, a simplified qualitative model capable of capturing the most important functional dependencies contributing to the energy conversion process could significantly enhance the understanding of the system and the design of F-SSTA architectures. In Section 6.3.3, we presented a numerical strategy to accurately simulate the response of the F-SSTA hybrid beam and to capture its multi-physics dynamics. Despite the development of a re-

duced model, the computational burden is not negligible and the purely numerical nature of the model is not amenable to an analytical study of the energy conversion mechanism. For these reasons, we introduce a lumped-parameter one Degree Of Freedom (1DOF) model that is capable of capturing the phenomenological behavior of both the undamped and the damped motion of the F-SSTA beam under the $q = Q\text{sgn}(v)$ type thermal load. This simplified approach is possible because the F-SSTA response of the bilayer beam is driven by its fundamental resonance. As it is often the case in classical modal analysis of continuous systems, the response of the system around well-isolated modal resonances can be approximated by 1DOF oscillators. Note also that the use of such a discrete 1DOF model further facilitates the analytical derivation of perturbation energy budgets. The energy budgets method is a well-established theoretical framework to interpret the energy production and dissipation in the thermoacoustic process. Energy budgets have found successful applications in both fluid-based [28], [77] and axial-mode solid-state thermoacoustics [60]. In the following, we apply the concept of energy budget to the F-SSTA system based on the reduced order 1DOF model. Although using a simplified model, the rigorous derivation of the thermoacoustic gain and the damping-induced loss contributions to the energy budget greatly improves the understanding of the underlying energy conversion mechanism in F-SSTA systems.

As previously stated, in the case of well separated resonances (such as typically a fundamental mode), the flexural response of the beam can be qualitatively modeled as a 1DOF spring-mass-damper system. In the context of F-SSTA, the mass represents the bending inertia of the bilayer beam, the spring coefficient represents the flexural rigidity of the beam, and the damping coefficient represents the intrinsic dissipation in the beam (e.g. structural damping). The unstable flexural motion induced by the thermo-mechanical coupling can be modeled as a forcing term in the equivalent 1DOF model. Consider a spring-mass-damper system in Fig. 6.12. The equation of motion (EOM) is expressed as:

$$m\hat{u} + c\hat{u} + k\hat{u} = F\text{sgn}(\hat{u}) \tag{6.65}$$

where $\hat{u}$ is the mass displacement, m, c, k and F are mass, viscous damping coefficient, stiffness coefficient, and force amplitude, respectively. The prime symbol denotes derivation with respect to time.

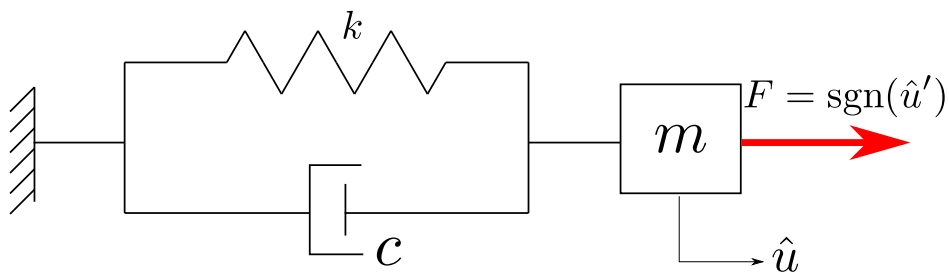

Figure 6.12. A 1DOF spring-mass-damper model qualitatively representing the fundamental flexural motion of a bilayer beam under inward heat flux $q = Q\mathrm{sgn}(v)$.

With reference to the system shown in Fig. 6.8, the first flexural mode of the bilayer beam is simplified and qualitatively captured by the 1DOF spring-mass-damper. The density, stiffness, and damping characteristics are simplified as three lumped parameters m, k, and c, respectively. Note that the forcing term is taken as a sign function of velocity $\hat{u}$, instead of displacement $\hat{u}$. Recall the expression of the one dimensional stress σ including the thermal component: $\sigma = E(\epsilon - \alpha\Delta T)$, where ϵ is the strain and E is the Young's modulus. In the F-SSTA system, the effective "thermal force" that directly drives the bilayer beam is proportional to the temperature difference ΔT, which is 90 degree out of phase with the heat input q (Eqn. (6.61)) in a quasi-harmonic motion (Figure 6.13 (a) and (c) insets). Therefore, when the beam is subject to a thermal load which is in phase with the displacement (e.g. $q = Q\mathrm{sgn}(v)$), the resulting temperature fluctuation is in phase with velocity, because velocity and displacement are 90 degree out of phase. Hence, in the 1DOF model, we use a sign function of velocity, as the direct forcing term, to represent the thermal load in the F-SSTA system. It is highlighted that due to the nonlinear excitation, whether $q = Q\mathrm{sgn}(v)$ in the F-SSTA system or $F = f\mathrm{sgn}(\dot{u})$) in the 1DOF system, the response cannot be exactly sinusoidal, or harmonic. However, due to the resonant nature of the system, the motion is still dominated by the fundamental frequency with low amplitude super-harmonics. Hence, the response is quasi-harmonic, as shown in the insets of Fig. 6.13(a) and (c).

Following the non-dimensionalization of Eqn. (6.65) yields:

$$\ddot{u} + \xi\dot{u} + u = f\text{sgn}(\dot{u}) \tag{6.66}$$

where u is the dimensionless displacement, $\xi = \omega_0 c/k$ and $f = F/kL$ are the dimensionless damping coefficient and forcing amplitude, and $\omega_0 = \sqrt{k/m}$. The dot symbol indicates the dimensionless time derivative $\dot{()} = ()/\omega_0$.

Figure 6.13 (a) and (c) show the undamped ($\xi = 0$) and damped ($\xi = 0.004$) responses of the 1DOF system under the load $f = 0.05$ with initial conditions given as $u = 1$ and $\dot{u} = 0$. In analogy with the continuous bilayer beam analyzed in Section 6.2 and with the configurations shown in Fig. 6.10 (a), the undamped response of the 1DOF system grows linearly without saturation. The damped response initially grows linearly, then it saturates and reaches a steady-state oscillation.

The dimensionless EOM (Eqn. (6.66)) can be recast to yield the perturbation energy budget [28]:

$$\mathcal{P} = \dot{\mathcal{E}} + \mathcal{D} \tag{6.67}$$

where

$$\mathcal{P} = \frac{1}{2}f\dot{u}\text{sgn}(\dot{u}) = \frac{1}{2}f|\dot{u}| \tag{6.68}$$

$$\mathcal{E} = \frac{1}{2}(u^2 + \dot{u}^2) \tag{6.69}$$

$$\mathcal{D} = \frac{1}{2}\xi\dot{u}^2 = \frac{1}{2}\xi|\dot{u}|^2 \tag{6.70}$$

denote the instantaneous thermoacoustic production, instantaneous energy, and instantaneous dissipation, respectively.

The energy dissipation $\mathcal{D}$ originates from the constant damping coefficient ξ adopted in the 1DOF model. In reality, the energy loss associated with the F-SSTA response can be due to multiple causes, including structural damping, thermoelastic damping, and flow-induced damping [78]. Modeling all these different sources of damping independently is a complicated task (especially when using a 3D model) and leads to computationally heavy

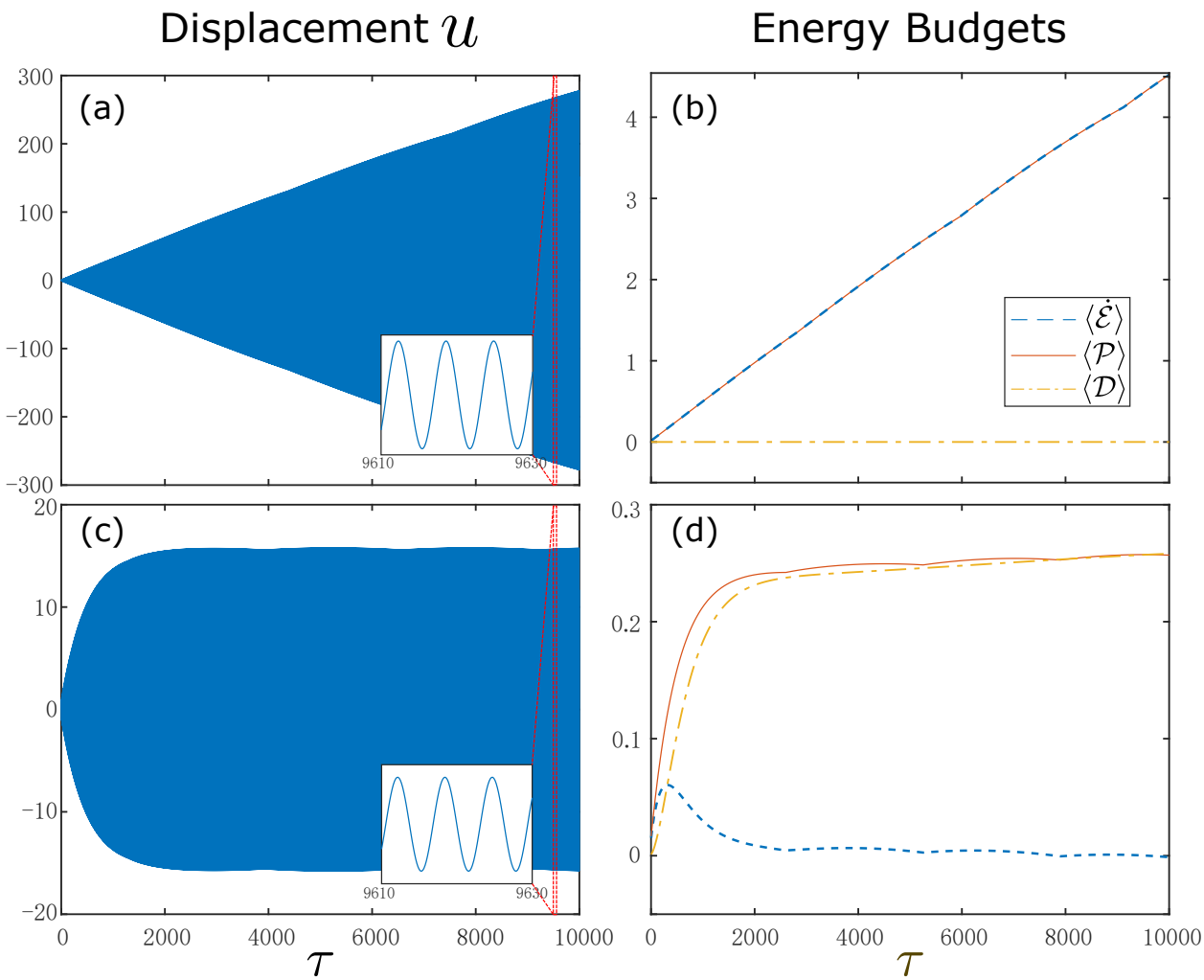

Figure 6.13. Dimensionless displacement u of the (a) undamped and (c) damped 1DOF systems. Insets show that the motion, whether unstable (a) or stable (c), is quasi-harmonic. The cycle-averaged perturbation energy budgets of the (b) undamped and (d) damped 1DOF systems. τ is the dimensionless time. Note that the blue dashed line $\langle\dot{\mathcal{E}}\rangle$ is the time derivative of the cycle-averaged mechanical energy. $\langle\dot{\mathcal{E}}\rangle = 0$ indicates that the cycle-averaged mechanical energy is unchanged due to energy balance.

models. Therefore, the use of simplified models (e.g. Rayleigh damping [76]) to represent losses is widely accepted. Given that the 1D model is a simplified mechanical equivalent of the beam vibrating at its fundamental frequency, it is reasonable to simplify the energy loss as a constant damping coefficient. In addition, from a qualitative perspective, this

representation of damping is sufficient to describe a linear dissipation independently of the possible causes.

Equation (6.67) reveals that in the F-SSTA system, part of the thermoacoustic production term $\mathcal{P}$ leads to an accumulation of energy, that is the rate of change of $\mathcal{E}$, while the rest is dissipated by the damping term, represented by $\mathcal{D}$. Observing the expressions for $\mathcal{P}$ and $\mathcal{D}$ (Eqns. (6.68) and (6.70), respectively), we conclude that the production $\mathcal{P}$ increases linearly with the magnitude of velocity, while the dissipation $\mathcal{D}$ increases quadratically with the magnitude of velocity, as shown in Fig. 6.14. Therefore, if the system is initiated by a perturbation that is smaller than $|\dot{u}|_{\mathrm{cr}}$ (defined in Fig. 6.14), as the amplitude of the F-SSTA oscillation grows, it is expected that the two competing factors $\mathcal{P}$ and $\mathcal{D}$ eventually become identical, hence giving rise to a limit cycle (Equilibrium point in Fig. 6.14). Alternatively, if the system is initiated by a perturbation that is larger than $|\dot{u}|_{\mathrm{cr}}$, the motion will at first decay (after the initial release) while eventually reaching the limit cycle equilibrium, where $\mathcal{P} = \mathcal{D}$. As a result, regardless of the initial perturbation, a steady-state oscillation can always be self-sustained. However, it is the growth-saturation motion (i.e. initiation below the critical value of the velocity) that more closely resembles the classical thermoacoustic oscillation observed in fluids [8], [27], [28], [33], [79]–[82].

Figure 6.13 (b) and (d) show the cycle-averaged thermoacoustic production, energy accumulation rate, and dissipation. In the undamped case ($\xi = 0$), all the input thermoacoustic production is devoted to building up the energy level without losses, hence leading to an unbounded growing motion. In the damped case ($\xi \neq 0$), the production exceeds the dissipation, at first, hence causing an accumulation of energy ($\langle \dot{\mathcal{E}} \rangle > 0$). This positive $\langle \dot{\mathcal{E}} \rangle$ leads to a linearly growing motion that is well visible in the simulation results of the bilayer beams (Fig. 6.10). The difference between $\langle \mathcal{P} \rangle$ and $\langle \mathcal{D} \rangle$ keeps decreasing until $\langle \dot{\mathcal{E}} \rangle$ becomes zero; at this point, the energy level remains unchanged and a steady-state oscillation ensues, as shown in Figure 6.13 (c). Similar results are also observed in the damped response of the bilayer beam in Fig. 6.11.

Therefore, we conclude that despite the simplicity of the 1DOF model, it successfully captures the main features of both the undamped and damped F-SSTA response of a bilayer beam. Moreover, the 1DOF system allows the derivation of the energy budgets based on

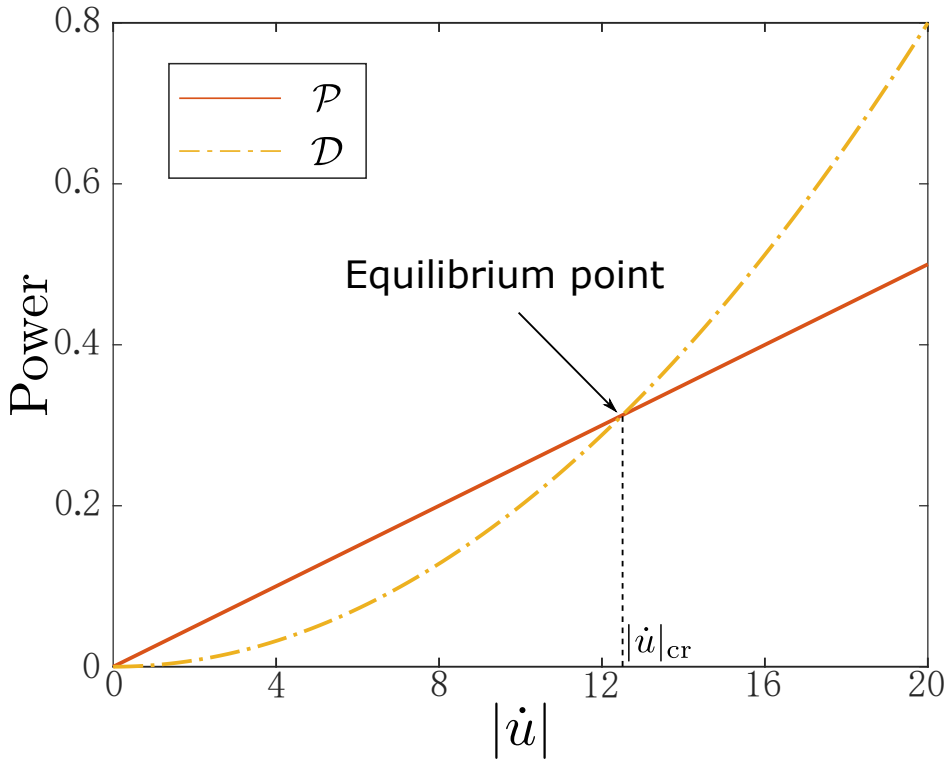

Figure 6.14. The instantaneous thermoacoustic production $\mathcal{P}$ and the instantaneous dissipation $\mathcal{D}$ as a function of the dimensionless velocity magnitude $|\dot{u}|$ of the 1DOF system, obtained by Eqns. (6.68) and (6.70), $f = 0.05$, $\xi = 0.004$. Note that $\mathcal{P}$ and $\mathcal{D}$ contribute to the time rate of increase and decrease of energy (Eqn. 6.67), respectively, so they have the unit of power. The intersection of these two curves is the equilibrium point indicative of a steady-state motion. The equilibrium point corresponds to a critical value of the perturbation $|\dot{u}|_{\mathrm{cr}}$ that separates two different transient behaviors that, however, lead to the same limit cycle response. If the system is initiated by a value below $|\dot{u}|_{\mathrm{cr}}$, the motion will be amplified due to $\mathcal{P} > \mathcal{D}$. On the contrary, if the system is initiated by a value above $|\dot{u}|_{\mathrm{cr}}$, the motion will initially attenuate.

simple mathematical manipulation of the governing equation, which provides interesting insights in the energy conversion process that takes place in F-SSTA systems.

6.5 Discussion

In this section, we discuss several relevant topics related to F-SSTA, including (1) a conceptual comparison between the concept of F-SSTA presented in this study and the concept of thermal flutter that was explored in the late 1960s [71]; (2) a comparison between

natural and architectured NTE materials; (3) stiffness matching for further improvement of F-SSTA systems; and (4) thoughts on manufacturing architectured lattice structures.

6.5.1 Comparison Between F-SSTA and Thermal Flutter

The thermal flutter phenomenon was discovered in the study of the dynamic thermoelastic response of boom-like structures operating in outer space environment. In thermal flutter, one side of a thin-walled boom with open annular cross section was subject to direct radiation from sunlight, while the other side remained in the dark hence radiating heat to deep space. Under these conditions, the boom exhibited either torsional or flexural instability depending on the specific design of the boom's cross section. By revisiting Eqn. (6.3), we observe that in both configurations a non-zero thermal moment gradient ($\partial^2 m_T/\partial x^2$) is necessary to achieve a heat-induced flexural instability. This condition further requires $m_T(x) \neq 0$ and $\partial m_T(x)/\partial x \neq 0$. The differences between F-SSTAs and the thermal flutter are mainly reflected in how these two conditions are satisfied.

In the flexural thermal flutter configuration, two main causes contribute to the occurrence of the instability: (1) the existence of a local thermal moment due to an asymmetric temperature distribution across the cross section of the beam which results from a single side exposure to the heat source ($m_T(x) \neq 0$); (2) as the beam bends, the non-uniform distance from the heat source of points located along the beam longitudinal axis leads to a non-uniform heat absorption, creating a non-zero thermal moment gradient along the beam ($\partial m_T(x)/\partial x \neq 0$). The thermal moment gradient effectively contributes to a thermal-induced motion.

In the context of F-SSTA, both sides of the beam experience identical heating (cooling), but the local thermal moment is achieved by utilizing two layers of distinct materials. Different thermal properties of both layers give rise to asymmetric temperature distribution over the cross section, while the difference in thermal expansion coefficients contribute to a distinct thermal strain. The combination of both these effects leads to a non-zero local bending moment ($m_T(x) \neq 0$). The thermal moment gradient ($\partial m_T(x)/\partial x \neq 0$) is formed by the spatially-varying and dynamically-changing neutral axis location h_0, under the effect of the localized thermal gradient.

Despite both phenomena rely on a non-uniform thermal moment distribution, we emphasize the necessity of a spatial thermal gradient in the F-SSTA configuration which is the foundation of the thermoacoustic instability.

6.5.2 Natural and Architectured NTE materials

While in the analysis above we have considered artificial structures designed to exhibit negative CTE, we note that there exist natural materials that can contract upon heating. However, most of these materials have some significant disadvantages that limit their application, especially to F-SSTA systems. For example, ZrW_2O_8 and related ceramics are brittle and subject to abrupt failure induced by thermal stresses [83]. Invar is robust, but it exhibits low CTE only in a very limited temperature range [84]. More specifically, for the application to SSTA systems, the intrinsic dissipative mechanism in the candidate material should be as low as possible so that the unstable TA motion can be triggered with a lower thermal gradient. This requirement is better met by architectured materials composed of metal constituents. Moreover, the truss-like NTE structure made out of aluminum and Ti-6Al-4V, as shown in Fig. 6.8 can achieve NTE with very large magnitude (CTE= -60×10^{-6}[1/K] as θ approaches 45 degree).

6.5.3 Stiffness Matching for Further Improvement of F-SSTAs

In this study, we focus on the potential of NTE materials to enhance the F-SSTA instability. Equation (6.64) further entails that it is beneficial to the flexural instability if the two layers have comparable stiffness ($n \sim 1$). On the contrary, if one layer is much stiffer than the other ($n \to 0$ or $n \to \infty$), the growth-rate-to-frequency ratio is reduced because $n \to 0$, $\phi(n) \sim n \to 0$, while as $n \to \infty$, $\phi(n) \sim 1/n \to 0$. In both cases, the low-stiffness layer acts as an appendix to the high-stiffness layer, which results in its motion being dominated by the axial motion of the high-stiffness layer and in negligible overall thermal bending. As a result, the flexural thermoacoustic instability is limited. It is worth noting that the design of the hybrid beam used in this study was not optimized for stiffness matching. The study intended to show how the use of tailored NTE properties, achieved via engineered material

design, can significantly help achieving experimentally sustainable F-SSTA instability. It is possible to envision enhancing the performance by matching the stiffness of the two layers. For example, the continuous (aluminum) layer could be replaced by a truss layer composed of a single-constituent tetrahedron octet. In such way, the layer would maintain a positive CTE while lowering the overall stiffness to a value comparable with that of the NTE layer. As a result, when heated, the different yet comparable thermal stresses in the two layers could give rise to a strong thermal moment.

6.5.4 Thoughts on Manufacturing Architectured NTE Materials

We note that, from a fabrication perspective, the introduction of an architectured material design certainly increases the manufacturing complexity. Indeed, the truss like structure combined with the presence of two material constituents in the octet truss design is not a challenge to be taken lightly. However, recent advances in additive manufacturing and 3D printing (either with single or multiple materials) indicate that, while single material designs are already achievable, multi-material designs could soon become viable. Recall that the octet design was already built and experimentally validated in [85] and [68] via a traditional fabrication approach. However, this latter approach was not deemed viable for the present study due to the large number of units to be fabricated, to the difficulty of achieving high quality (low friction) joints in the octet truss, and to the complexity in joining the two layers to form the hybrid design.

6.6 Concluding Remarks

In this chapter, the science of thermoacoustics is extended to include self-sustained instabilities of flexural waves (F-SSTAs); a unique response modality typical of solid media. The mathematical framework of F-SSTAs was established and used to analyze the instability of the transverse bending motion in a bilayer slender beam. By employing a simplified heating strategy, both an analytical modal solution and a criterion to determine the onset of the flexural instability were obtained. According to this criterion, in natural materials, the layer with higher ratio of thermal expansion coefficient to heat capacity should be placed on the

side where heat is provided (i.e. the hot region). However, for engineered materials in which unconventional properties can be achieved (e.g. negative thermal expansion coefficient) extreme thermoacoustic performance could be anticipated. This is a unique opportunity opened by solid-state thermoacoustics and could be particularly relevant for device applications. Numerical simulations indicated that a hybrid bilayer beam composed of a layer made out of natural material and the other layer made out of an NTE engineered material exhibited an significantly improved F-SSTA response. Numerical simulations in both the frequency and time domains helped revealing the mechanism of motion amplification due to flexural instability. More specifically, the time dependence of the location of the neutral axis under thermoacoustic coupling was observed and found to be a key aspect in the development of the instability. An experimental setup was also developed in order to validate the theoretical framework of F-SSTAs. Although no evident self-sustained motion was observed, due to the limited heating and cooling capacity, the ultra-low effective damping was found to be a confirmation of the thermal-to-mechanical energy conversion due to the F-SSTA process. Nonetheless, with the numerical evidences of the significant improvement of NTE-aided F-SSTA responses, it is anticipated that a successful experimental realization can be achieved leveraging the tunable thermo-mechanical properties of engineered materials. The energy conversion process of the F-SSTA system was explored analytically by exploiting a perturbation energy budget approach based on the simplified equivalent 1DOF model. It was found that the thermal energy input is either converted into internal energy (accumulated in the system) or dissipated due to structural damping. While the introduction of engineered materials is certainly accompanied by additional complexities from a fabrication perspective, results suggest that they also provide one of the most likely viable routes to realize practical F-SSTA systems capable of self-sustained oscillations.

Compared to its axial counterpart, flexural thermoacoustic vibrations are easier to excite in slender structures, and are associated with lower fundamental frequencies and larger amplitude of the response. All these aspects can result in significantly easier implementation and higher power density, both aspects of key relevance for the fabrication of thermoacoustic devices.

7. CONCLUSIONS AND FUTURE WORK

Thermoacoustic technology possesses several characteristics that could make it a key technology to promote the next generation of energy-conversion devices. The most immediate of these characteristics is their eco-friendliness. However, the development of TA devices has been severely hindered by various limitations, such as low efficiency and low scalability. These drawbacks arise from the intrinsic nature of the gaseous working substances. This thesis provides the first systematic study of solid-state thermoacoustics, as an attempt to explore opportunities to bypass certain limitations of traditional fluid-based thermoacoustics, thus potentially facilitating the commercialization of thermoacoustic devices. This study also presents a new paradigm of thermoacoustic research. Although in its infancy, it is anticipated that the SSTA technology could grow based on the theoretical foundation established in this thesis, and eventually leading to the development of solid-state thermoacoustic devices. More importantly, the author believes that the fast-growing knowledge of solid-state engineered materials, whose thermo-mechanical properties can be more easily tailored, shall be properly combined with the development of SSTA, in order to improve the performance of SSTA systems for practical applications.

In this chapter, we will first summarize the key contributions of this thesis in Section 7.1, followed by remarks on the main benefits and limitations of using solids as thermoacoustic working media in Section 7.2. Then, Section 7.3 will discuss thoughts about possible future directions that may be worth exploring to further the understanding and design capabilities of SSTA devices.

7.1 Summary of Key Contributions

In this thesis, the study of SSTA systems are divided in two categories: 1) A-SSTA and 2) F-SSTA. A-SSTA refers to the thermoacoustically unstable axial motion of slender structures (e.g., 1D bars) subject to a spatial temperature gradient. Due to the resemblance between the axial-mode elastic waves in solids and the pressure waves in gases, A-SSTA shares significant similarities with the conventional fluid-based thermoacoustics. On the other side, F-SSTA is a thermoacoustically unstable mode unique to solid media. This modality, which

refers to the excitation of unstable flexural mode, was realized in a bilayer slender beam subject to a spatial thermal gradient. Compared to its axial counterpart, flexural thermoacoustic vibrations are easier to excite in slender structures, and are associated with lower fundamental frequencies and larger amplitude of the response. All these aspects can result in significantly easier implementation and higher power density, both aspects of key relevance for the fabrication and use of thermoacoustic devices. The key contributions presented in this thesis regarding A-SSTA and F-SSTA are summarized here below:

1. Development of the quasi-1D theory of A-SSTA. Following the classical Rott's theory of thermoacoustics, a quasi-1D theory of A-SSTA was derived in Chapter 3. The theory only took into account the cross-sectionally averaged fluctuating quantities in the TA process. The A-SSTA theory successfully predicted the unstable axial standing-wave mode that exists in a finite straight bar and the axial traveling-wave mode that exists in a continuous loop-shaped bar, respectively (Chapter 4). The development of the quasi-1D theory 1) facilitates the stability analysis; and 2) allows conducting optimal design of solid-state thermoacoustic systems.

2. Comparative study of the standing- and traveling-wave A-SSTA. Similar to fluid-based TA, traveling-wave SSTA supports a more efficient thermo-mechanical energy conversion process, which is reflected by a more pronounced TA instability.

3. Systematic analysis of energy conversion. A perturbation energy budget is proposed in order to systematically understand the energy conversion mechanism in both standing- and traveling-wave SSTA.

4. Comparative discussion between A-SSTA and fluid-based TA. Important differences between A-SSTA and fluid-based TA were also observed. Among them, the most significant stems from the dissimilar thermal expansion mechanism in the two classes of working media. Unlike fluids, solids are less sensitive to heat and temperature gradients due to their smaller coefficient of thermal expansion (CTE). This aspect is intrinsically not in favor of a strong TA instability. However, the advent of engineered materials provides a means to tailor the CTE of solid materials, which can potentially take any

positive or negative real value. The possibility to manipulate of the thermo-mechanical properties of engineered materials offers a unique opportunity in SSTA devices. These ideas were explored in Chapter 5.

5. Development of the theory of F-SSTA. The F-SSTA theory was established based on the classical Euler-Bernoulli beam theory, incorporating the thermo-mechanical coupling terms in the governing equations. The F-SSTA theory suggests that to successfully leverage the thermo-mechanical coupling to obtain unstable F-SSTA responses, an asymmetric temperature distribution over the cross section has to be established. This study was performed in Chapter 6 by using a bilayer beam as a prototypical system to illustrate the operating mode.

6. Development of an analytical criterion for F-SSTA instability. By employing a simplified heating strategy, both an analytical modal solution and a criterion to determine the onset of the flexural instability were obtained. According to this criterion, in natural materials, the layer with higher ratio of thermal expansion coefficient to heat capacity should be placed on the side where heat is provided (i.e. the hot region).

7. Experimental assessment of the F-SSTA mechanism. An experimental investigation of the F-SSTA modality was conducted. The setup consisted of a properly designed continuous bilayer beam. Although self-sustained motion was not observed, the reduced effective damping clearly suggested the existence of the thermo-mechanical energy conversion associated with the flexural motion of the bilayer beam.

8. Numerical study of NTE-aided F-SSTA. The instability criterion suggested the possibility of replacing one of the two continuous layer by an engineered layer with negative thermal expansion (NTE) coefficient to significantly enhance F-SSTA instability. Careful numerical simulations confirmed this hypothesis and showed the distinctive role of engineered materials in the SSTA systems. It is anticipated that by leveraging the tunable NTE properties of engineered materials, a successful experimental realization of F-SSTA responses could be achieved.

7.2 Remarks on Benefits and Limitations of SSTA

Having summarized the main achievements of this thesis, we first highlight the most significant benefits of using solids as working media for thermoacoustics as follows:

1. High robustness. Conventional fluid(gas)-based thermoacoustic devices may experience leakage issues, which requires complex sealing design. However, the use of solid materials naturally prevents the leakage problem.

2. More direct electro-mechanical energy conversion. In gas-based thermoacoustic energy harvester, a dedicated energy harvesting element, e.g., a piezoelectric element, has to be integrated with the thermoacoustic conversion component. This coupling involves a fluid-structure interaction that converts the mechanical energy carried by the pressure wave in the gaseous working medium into the mechanical energy carried by the elastic wave in the solid structure. Then the mechanical energy of the structure is further converted into electricity. Such multi-step energy conversion is inevitably associated with energy losses and a more elaborate design. However, by using solids as working media, the serial thermo-mechanical-electrical energy conversion can be simplified by integrating the piezoelectric element directly within the solid. The removal of the fluid-structure conversion step allows reducing the energy loss, thus facilitating an easier implementation of energy harvesting.

3. Enhanced tailoring and tuning ability of solids. To optimize a conventional thermoacoustic device, researchers have proposed numerous ideas to improve the design of each individual component of the system. However, in the case of a gas or liquid working medium, the capability to alter the material properties is very limited. Solids offer more opportunities to tailor their characteristics, especially when leveraging architectured material concepts, mainly attribute to the ongoing development of engineered materials. With solid materials as constituents, the macroscopic structure can be deliberately designed to possess thermo-mechanical properties that favor thermoacoustic instability (e.g. large thermal expansion coefficient). The ease of tailoring and tuning material properties allows controlling more system parameters, thus enhancing the

performance of thermoacoustic devices. This is a unique opportunity provided by solid materials, which could greatly benefit the design of SSTA.

4. High scalability. The application of gas-based thermoacoustic devices are also hindered by their bulky size. The low frequency oscillation, which is in favor of the heat transfer process in thermoacoustic, can be only achieved with a large acoustic resonator. However, the possibility to manipulate the (dynamic) density and stiffness of solid structures that translates to a more manageable sound speed opens the window to achieving desired low frequency with a more compact geometry. This aspect may also promotes the future application of thermoacoustic devices.

Based on the above mentioned benefits of solids as main working media for thermoacoustics, the author anticipates that SSTA could promote further practical application of thermoacoustic-based energy-conversion technology. To foster the development of SSTA, a few considerations on the limitations of SSTA should also be kept in mind:

1. Heating a moving solid with conduction. The TA instability in both the fluid and solid systems exists in an oscillatory working medium that is provided heat at a proper phasing. In fluid systems, this process takes place in a porous material, or regenerator (REG), where the gaseous parcel oscillates cyclically while heat exchange occurs via conduction mechanisms. However, for solid systems, exchanging heat with the external environment by conduction during oscillatory motion of the solid is not a trivial task. Conceptually, for an A-SSTA system, one can surround the 1D bar by a large thermal inertia, e.g., a copper jacket as shown in Fig. 4.1(a), but this idea poses a challenging requirement for the selection of the interface material in between the copper jacket and the 1D bar. The interface must be simultaneously highly thermally conductive (to achieve an effective isothermal boundary condition) and able to provide negligible shear forces. Future effort can be dedicated to either the synthesis of an interface material of this kind, or an alternative heating strategy, which is more appropriate for oscillating solids. In the experimental attempt conducted in Chapter 6, we used two infrared lamps to provide radiative heat. We were able to see a reduction of the

effective damping, as a sign of positive thermo-mechanical energy conversion associated with the flexural motion. Yet, a self-sustained vibration was still not obtained, because the heat leakage from the hot region to the cold region greatly reduced the strength of the thermal gradient.

2. Low sensitivity to heat. In general, the response of natural solid materials is less sensitive to heat, compared to gaseous media. This aspect, which is characterized by a lower coefficient of thermal expansion (CTE), could be detrimental to thermoacoustic instability. While certain composites have CTE that is multiple orders of magnitude higher than that in metals, the high dissipation in composites is another harmful aspect that should be carefully considered because it prevents the establishment of powerful thermoacoustic instabilities. Overall, this limitation of homogeneous solid materials can be overcome by artificially engineering the material's CTE. With a dedicated selection of constituent materials and elaborate topological design, an artificial truss structure can possess tunable CTE which allows unbounded positive or negative value. This unique chance provided by solids could greatly benefits thermoacoustic instability in solid media. The performance enhancement in A-SSTA and F-SSTA systems through the use of engineered materials have been discussed more in details in Chapter 5 and Chapter 6, respectively.

3. Nonlinearity in SSTA. The motion in a solid system which is thermoacoustically unstable initially grows with time. As the amplitude of oscillation grows, the nonlinear effects in the system become more prominent. From the knowledge of gas-based thermoacoustic systems, it could be inferred that the nonlinear effects associated with SSTA are another source that could limit the strength of thermoacoustic instability in solids. This aspect was not explored in this thesis and should be further investigated.

7.3 Future Work

This thesis merely lays the theoretical foundation of SSTA. Although some preliminary experimental studies have been conducted on F-SSTA, more experimental investigations

need to be performed to better understand the thermoacoustic coupling in solids, and to validate the theoretical framework proposed in this study. For experimental studies in the future, one may consider the following strategies to pursue optimal thermoacoustic energy conversion, thus facilitating a successful experimental operation.

1. Experimentation at the micro- or nano- scales. At the micro- or nano- scales, it is anticipated that the thermal gradient achieved by radiation could be better managed. For example, a strong light beam could be shed onto a non-uniformly perforated screen. The screen, placed in between the solid structure and the light source, acts as an intensity filter of the light. The non-uniform perforation shall enable the light, which is refracted onto the solid structure, to create an effective spatial thermal gradient, along the direction of motion. This shall apply to the experiments of both A-SSTA and F-SSTA.

2. Construction of cellular structures. This strategy considers an SSTA system which is made from cellular structures so that the additional surfaces that are exposed to air can facilitate a more effective thermo-mechanical energy exchange. Additionally, the cellular structure can be deliberately designed to be more compliant than continuous solids, so to effectively lower the resonant frequencies; a useful factor for TA processes. It is also remarkable that the thermo-mechanical properties (e.g., CTE) of cellular materials can be optimally tailored for the benefits of SSTA, as shown earlier in this thesis. Overall, this seems a promising route towards a successful experimental demonstration of SSTA phenomena.

3. Stiff matching of the F-SSTA bilayer beam. In Chapter 6, we derived an approximate analytical expression of the F-SSTA growth-rate-to-frequency ratio, which suggested that matching the stiffness of the two layers of the hybrid bilayer beam can further enhance the F-SSTA instability. Therefore, further exploration can involve the numerical and experimental studies of a hybrid bilayer beam that is composed of two truss layer, one being NTE and the other being regular positive CTE material. As a result, despite the large difference of CTE, which is beneficial to F-SSTA responses, the stiffness of the two truss layers is comparable.

The above-mentioned aspects are some of the immediate extensions that could be made, based on the author's knowledge of the fundamental SSTA theory, as well as the conclusions drawn in the initial numerical and experimental explorations. It is noteworthy that, although SSTA is a promising technology for the future development of solid-state energy conversion devices (e.g., engines and refrigerators), the exploration of SSTA is still at its inception. Extensive efforts have to be made in the future to look into all practical aspects relevant to the application of SSTA systems more in detail.

Other than exploiting thermoacoustic coupling's capability of energy conversion, it is merely suggested by the author that exploring the possibility of manipulating sounds by leveraging thermoacoustic coupling may lead to a promising route to the design of exotic acoustic metamaterials and functional acoustic devices. A preliminary work shows the numerical observation of several peculiar phenomena in a thermoacoustically coupled waveguide, such as non-reciprocal sound propagation, one-way energy transport, and effective zero refractive index [86].

REFERENCES

[1] G. Swift, "Thermoacoustic engines," J. Acoust. Soc. Am., vol. 84, no. 4, pp. 1145–80, 1988, ISSN: 0001-4966. [Online]. Available: http://dx.doi.org/10.1121/1.396617.

[2] P. Ceperley, "A pistonless stirling engine-the traveling wave heat engine," J. Acoust. Soc. Am., vol. 66, no. 5, pp. 1508–1513, 1979. [Online]. Available: http://dx.doi.org/10.1121/1.383505.

[3] [Online]. Available: https://en.wikibooks.org/wiki/Engineering_Acoustics/Thermoacoustics.

[4] M. Tijani and J. Zeegers, "Design of thermoacoustic refrigerators.," Cryogenics, vol. 42, no. 1, pp. 49–57, 2002. [Online]. Available: https://doi.org/10.1016/S0011-2275(01)00179-5.

[5] [Online]. Available: www.http://www.aster-thermoacoustics.com.

[6] G. W. Swift, Thermoacoustics A Unifying Perspective for Some Engines and Refrigerators, eng, 2nd ed. 2017. 2017.

[7] G. Chen, L. Tang, B. Mace, and Z. Yu, "Multi-physics coupling in thermoacoustic devices: A review," Renew. Sustain. Energy Rev., vol. 146, p. 111 170, 2021, ISSN: 1364-0321. DOI: https://doi.org/10.1016/j.rser.2021.111170. [Online]. Available: https://www.sciencedirect.com/science/article/pii/S1364032121004597.

[8] T. Yazaki, A. Iwata, T. Maekawa, and A. Tominaga, "Traveling wave thermoacoustic engine in a looped tube," Phys. Rev. Lett., vol. 81, no. 15, pp. 3128–3131, 1998. [Online]. Available: http://dx.doi.org/10.1103/PhysRevLett.81.3128.

[9] S. Backhaus and G. Swift, "A thermoacoustic-stirling heat engine: Detailed study," J. Acoust. Soc. Am., vol. 107, no. 6, pp. 3148–3166, 2000. [Online]. Available: http://dx.doi.org/10.1121/1.429343.

[10] A. A. Putnam and W. R. Dennis, "Survey of organ-pipe oscillations in combustion systems," J. Acoust. Soc. Am., vol. 28, no. 2, pp. 246–259, 1956. [Online]. Available: https://doi.org/10.1121/1.1908253.

[11] C. Sondhauss, "Ueber die schallschwingungen der luft in erhitzten glasr¨ohren und in gedeckten pfeifen von ungleicher weite," Ann. Phys., vol. 155, pp. 1–34, 1850.

[12] J. B. S, A. K. R, and S. V. S, "Mechanical response of ti–6al–4v octet-truss lattice structures," Int. J. Sci. Res., vol. 3, 7 2013.

[13] K. Feldman, "Review of the literature on rijke thermoacoustic phenomena," Journal of Sound and Vibration, vol. 7, no. 1, pp. 83–89, 1968, ISSN: 0022-460X. [Online]. Available: https://doi.org/10.1016/0022-460X(68)90159-4.

[14] J. W. S. Rayleigh, The theory of sound, eng, 2d ed., rev. and enl. New York: Dover Publications, 1945.

[15] H. Kramers, "Vibrations of a gas column," Physica, vol. 15, no. 11, pp. 971–984, 1949, ISSN: 0031-8914. [Online]. Available: https://doi.org/10.1016/0031-8914(49)90061-0.

[16] H. RVL., Electric power source. U.S. Patent No. 2,549,464, 1951.

[17] M. WA., Heat-controlled acoustic wave system. U.S. Patent No.2,836,033, 1958.

[18] N. Rott, "Damped and thermally driven acoustic oscillations in wide and narrow tubes," Zeitschrift fur Angewandte Mathematik und Physik, vol. 20, no. 2, pp. 230–43, 1969, ISSN: 0044-2275. [Online]. Available: http://dx.doi.org/10.1007/BF01595562.

[19] N. Rott, "Thermally driven acoustic oscillations. ii. stability limit for helium," Zeitschrift fur Angewandte Mathematik und Physik, vol. 24, no. 1, pp. 54–72, 1973, ISSN: 0044-2275. [Online]. Available: http://dx.doi.org/10.1007/BF01593998.

[20] N. Rott, "The influence of heat conduction on acoustic streaming," Zeitschrift fur Angewandte Mathematik und Physik, vol. 25, no. 3, pp. 417–21, 1974, ISSN: 0044-2275. [Online]. Available: http://dx.doi.org/10.1007/BF01594958.

[21] N. Rott, "Thermally driven acoustic oscillations. iii. second-order heat flux," Zeitschrift fur Angewandte Mathematik und Physik, vol. 26, no. 1, pp. 43–9, 1975, ISSN: 0044-2275. [Online]. Available: http://dx.doi.org/10.1007/BF01596277.

[22] N. Rott, "Thermoacoustics.," Advances in Applied Mechanics, vol. 20, pp. 135–175, 1980, ISSN: 00652156.

[23] N. Rott, "Thermoacoustic heating at the closed end of an oscillating gas column," J. Fluid Mech. (UK), vol. 145, pp. 1–9, 1984, ISSN: 0022-1120. [Online]. Available: http://dx.doi.org/10.1017/S0022112084002792.

[24] N. Rott and G. Zouzoulas, "Thermally driven acoustic oscillations. iv. tubes with variable cross-section," Z. Angew. Math. Phys. (Switzerland), vol. 27, no. 2, pp. 197–224, 1976, ISSN: 0044-2275. [Online]. Available: http://dx.doi.org/10.1007/BF01590805.

[25] M. Guedra and G. Penelet, "On the use of a complex frequency for the description of thermoacoustic engines," Acta Acust united Ac., vol. 98, no. 2, pp. 232–241, 2012. [Online]. Available: http://dx.doi.org/10.3813/AAA.918508.

[26] C. Scalo, S. Lele, and L. Hesselink, "Linear and nonlinear modelling of a theoretical travelling-wave thermoacoustic heat engine," J Fluid Mech., vol. 766, pp. 368–404, 2015. [Online]. Available: http://dx.doi.org/10.1017/jfm.2014.745.

[27] J. Lin, C. Scalo, and L. Hesselink, "High-fidelity simulation of a standing-wave thermoacoustic–piezoelectric engine," J. Fluid Mech., vol. 808, pp. 19–60, 2016. DOI: 10.1017/jfm.2016.609.

[28] P. Gupta, G. Lodato, and C. Scalo, "Spectral energy cascade in thermoacoustic shock waves," J. Fluid Mech., vol. 831, pp. 358–393, 2017. [Online]. Available: http://dx.doi.org/10.1017/jfm.2017.635.

[29] G. Chen, L. Tang, and B. Mace, "Theoretical and experimental investigation of the dynamic behaviour of a standing-wave thermoacoustic engine with various boundary conditions," Int. J. Heat Mass Transf., vol. 123, pp. 367–381, 2018. [Online]. Available: https://doi.org/10.1016/j.ijheatmasstransfer.2018.02.121.

[30] K. De Blok, "Low operating temperature integral thermo acoustic devices for solar cooling and waste heat recovery," The Journal of the Acoustical Society of America, vol. 123, no. 5, pp. 3541–3541, 2008. DOI: 10.1121/1.2934526. [Online]. Available: https://doi.org/10.1121/1.2934526.

[31] Novel 4-Stage Traveling Wave Thermoacoustic Power Generator, vol. ASME 2010 3rd Joint US-European Fluids Engineering Summer Meeting: Volume 2, Fora, Fluids Engineering Division Summer Meeting, Aug. 2010, pp. 73–79. DOI: 10.1115/FEDSM-ICNMM2010-30527. [Online]. Available: https://doi.org/10.1115/FEDSM-ICNMM2010-30527.

[32] T. Biwa, D. Hasegawa, and T. Yazaki, "Low temperature differential thermoacoustic stirling engine," Applied Physics Letters, vol. 97, no. 3, p. 034 102, 2010. DOI: 10.1063/1.3464554. [Online]. Available: https://doi.org/10.1063/1.3464554.

[33] Z. Yu, A. J. Jaworski, and S. Backhaus, "Travelling-wave thermoacoustic electricity generator using an ultra-compliant alternator for utilization of low-grade thermal energy," Applied Energy, vol. 99, pp. 135–145, 2012, ISSN: 0306-2619. [Online]. Available: https://doi.org/10.1016/j.apenergy.2012.04.046.

[34] J. Smoker, M. Nouh, O. Aldraihem, and A. Baz, "Energy harvesting from a standing wave thermoacoustic-piezoelectric resonator," Journal of Applied Physics, vol. 111, no. 10, p. 104 901, 2012. DOI: 10.1063/1.4712630. [Online]. Available: https://doi.org/10.1063/1.4712630.

[35] M. Nouh, O. Aldraihem, and A. Baz, "Energy Harvesting of Thermoacoustic-Piezo Systems With a Dynamic Magnifier," Journal of Vibration and Acoustics, vol. 134, no. 6, Oct. 2012, 061015, ISSN: 1048-9002. DOI: 10.1115/1.4005834. [Online]. Available: https://doi.org/10.1115/1.4005834.

[36] T. Biwa, T. Takahashi, and T. Yazaki, "Observation of traveling thermoacoustic shock waves (l)," The Journal of the Acoustical Society of America, vol. 130, no. 6, pp. 3558–3561, 2011. DOI: 10.1121/1.3658444. eprint: https://doi.org/10.1121/1.3658444. [Online]. Available: https://doi.org/10.1121/1.3658444.

[37] D.-H. Li, Y.-Y. Chen, E.-C. Luo, and Z.-H. Wu, "Study of a liquid-piston traveling-wave thermoacoustic heat engine with different working gases," Energy, vol. 74, pp. 158–163, 2014, ISSN: 0360-5442. DOI: https://doi.org/10.1016/j.energy.2014.05.034. [Online]. Available: http://www.sciencedirect.com/science/article/pii/S0360544214005830.

[38] P. Murti, H. Hyodo, and T. Biwa, "Suppression of liquid surface instability induced by finite-amplitude oscillation in liquid piston stirling engine," Journal of Applied Physics, vol. 127, no. 15, p. 154 901, 2020. DOI: 10.1063/5.0003921. [Online]. Available: https://doi.org/10.1063/5.0003921.

[39] Z. Liu, X. Zhang, Y. Mao, Y. Y. Zhu, Z. Yang, C. T. Chan, and P. Sheng, "Locally resonant sonic materials," vol. 289, no. 5485, pp. 1734–1736, 2000, ISSN: 0036-8075. DOI: 10.1126/science.289.5485.1734. [Online]. Available: https://science.sciencemag.org/content/289/5485/1734.

[40] S. H. Lee, C. M. Park, Y. M. Seo, Z. G. Wang, and C. K. Kim, "Composite acoustic medium with simultaneously negative density and modulus," Phys. Rev. Lett., vol. 104, p. 054 301, 5 Feb. 2010. DOI: 10.1103/PhysRevLett.104.054301. [Online]. Available: https://link.aps.org/doi/10.1103/PhysRevLett.104.054301.

[41] W. Nowacki, in Progress in Thermoelasticity: VIIIth European Mechanics Colloquium. Warsaw, 1969, pp. 9–61.

[42] P. Chadwick, J. Mech. Phys. Solids, vol. 10, no. 2, pp. 99–109, 1962.

[43] A. Eringen, Mechanics of Continua. John Wiley & Sons, New York, 1967, pp. 9–61.

[44] G. Zouzoulas and N. Rott, "Thermally driven acoustic oscillations. v. gas-liquid oscillations," Z. Angew. Math. Phys. (Switzerland), vol. 27, no. 3, pp. 325–34, 1976, ISSN: 0044-2275. [Online]. Available: http://dx.doi.org/10.1007/BF01590505.

[45] E. M. L. (M. Landau L. D. (Lev Davidovich), Fluid mechanics, eng, 2nd ed., repr. with corrections 1997., ser. Landau, L. D. (Lev Davidovich), 1908-1968. Teoreticheskai a fizika. English ; v. 6. Oxford: Butterworth-Heinemann, 1997.

[46] P. M. Morse, Thermal physics. W. A. Benjamin, 1962, ISBN: 0805372024. [Online]. Available: http://hdl.handle.net/2027/uc1.b4277188.

[47] H. Schlichting (Deceased), Boundary-Layer Theory, eng, 9th ed. 2017. 2017.

[48] G. K. (K. Batchelor, An introduction to fluid dynamics, eng. Cambridge: U.P., 1967.

[49] M. Biot, "Thermoelasticity and irreversible thermodynamics," Journal of Applied Physics, vol. 27, no. 3, pp. 240–253, 1956. [Online]. Available: http://dx.doi.org/10.1063/1.1722351.

[50] R. Barron, Design for thermal stress. Hoboken, N.J.: Wiley, 2012, p. 210.

[51] H. Hao, C. Scalo, M. Sen, and F. Semperlotti, "Thermoacoustics of solids: A pathway to solid state engines and refrigerators," J. Appl. Phys., vol. 123, no. 2, p. 024 903, 2018. [Online]. Available: http://dx.doi.org/10.1063/1.5006489.

[52] B. Lazan, Damping of materials and members in structural mechanics. Oxford, UK, 1968, pp. xiv+317–.

[53] S. Backhaus, E. Tward, and M. Petach, "Thermoacoustic power systems for space applications," AIP Conference Proceedings, vol. 608, no. 1, pp. 939–944, 2002. DOI: 10.1063/1.1449822. [Online]. Available: https://aip.scitation.org/doi/abs/10.1063/1.1449822.

[54] S. L. Garrett, D. F. Gaitan, D. K. Perkins, and D. A. Helseth, "Thermoacoustic life sciences refrigerator," The Journal of the Acoustical Society of America, vol. 93, no. 4, pp. 2364–2364, 1993. DOI: 10.1121/1.406185. [Online]. Available: https://doi.org/10.1121/1.406185.

[55] P. S. Spoor and C. Fellows, "The world's first thermoacoustic appliance, after one year running," International Refrigeration and Air Conditioning Conference, 2008.

[56] G. Penelet, S. Job, V. Gusev, P. Lotton, and M. Bruneau, "Dependence of sound amplification on temperature distribution in annular thermoacoustic engines," Acust. Acta Acust., vol. 91, no. 3, pp. 567–577, 2005, ISSN: 1610-1928.

[57] G. Swift, "Thermoacoustic engines," J. Acoust. Soc. Am., vol. 84, no. 4, pp. 1145–1180, 1998. [Online]. Available: http://dx.doi.org/10.1121/1.396617.

[58] S. Cummer, J. Christensen, and A. Alu, "Controlling sound with acoustic metamaterials," Nat Rev Mater., vol. 1, no. 3, p. 16 001, 2016. [Online]. Available: https://doi.org/10.1038/natrevmats.2016.1.

[59] G. Ma and P. Sheng, "Acoustic metamaterials: From local resonances to broad horizons," Sci Adv., vol. 2, no. 2, 2016. [Online]. Available: https://10.1126/sciadv.1501595.

[60] H. Hao, C. Scalo, M. Sen, and F. Semperlotti, "Traveling and standing thermoacoustic waves in solid media," J. Sound Vib., vol. 449, pp. 30–42, 2019. [Online]. Available: https://doi.org/10.1016/j.jsv.2019.02.029.

[61] H. Hao, C. Scalo, and F. Semperlotti, "Axial-mode solid-state thermoacoustic instability: An analytical parametric study," J. Sound and Vib., vol. 470, p. 115 159, 2020, ISSN: 0022-460X. [Online]. Available: https://doi.org/10.1016/j.jsv.2019.115159.

[62] A. Trapp, F. Zink, O. Prokopyev, and L. Schaefer, "Thermoacoustic heat engine modeling and design optimization," Appl Therm Eng., vol. 31, no. 14-15, pp. 2518–2528, 2011. [Online]. Available: https://doi.org/10.1016/j.applthermaleng.2011.04.017.

[63] H. Huang, C. Sun, and G. Huang, "On the negative effective mass density in acoustic metamaterials," International Journal of Engineering Science, vol. 47, no. 4, pp. 610–617, 2009, ISSN: 0020-7225. [Online]. Available: https://doi.org/10.1016/j.ijengsci.2008.12.007.

[64] R. S. Lakes, T. Lee, A. Bersie, and Y. C. Wang, "Extreme damping in composite materials with negative-stiffness inclusions," Nature, vol. 410, no. 6828, pp. 565–567, 2001. [Online]. Available: https://doi.org/10.1038/35069035.

[65] R. S. Lakes, "Cellular solid structures with unbounded thermal expansion," J Mater Sci Lett., vol. 15, no. 6, pp. 475–477, 1996. [Online]. Available: https://doi.org/10.1007/BF00275406.

[66] C. Zener, "Internal friction in solids II. General theory of thermoelastic internal friction," Phys. Rev., vol. 53, pp. 90–99, 1 Jan. 1938. [Online]. Available: https://doi.org/10.1103/PhysRev.53.90.

[67] R. Lakes, "Cellular solids with tunable positive or negative thermal expansion of unbounded magnitude," Appl Phys Lett., vol. 90, no. 22, p. 221 905, 2007. [Online]. Available: https://doi.org/10.1063/1.2743951.

[68] H. Xu and D. Pasini, "Structurally efficient three-dimensional metamaterials with controllable thermal expansion," Sci Rep., vol. 6, no. 1, 2016. [Online]. Available: https://doi.org/10.1038/srep34924.

[69] K. Takenaka, "Progress of research in negative thermal expansion materials: Paradigm shift in the control of thermal expansion," Front. Chem., vol. 6, pp. 267–267, 2018. [Online]. Available: doi.org/10.3389/fchem.2018.00267.

[70] F. Rimrott and R. Abdel-Sayed, "Flexural thermal flutter under laboratory conditions," T Can Soc Mech Eng, vol. 4, no. 4, pp. 189–196, 1976. [Online]. Available: https://doi.org/10.1139/tcsme-1976-0027.

[71] R. M. Beam, "On the phenomenon of thermoelastic instability (thermal flutter) of booms with open cross section," NASA TN-D5222, 1969. [Online]. Available: https://ntrs.nasa.gov/archive/nasa/casi.ntrs.nasa.gov/19690020211.pdf.

[72] B. A. Boley, "Thermally induced vibration of beams," Journal of Aeronautical Sciences, vol. 23, no. 2, pp. 179–181, 1956.

[73] N. D. Jadeja and T.-C. Loo, "Heat induced vibration of a rectangular plate," J Eng Ind, vol. 96, no. 3, pp. 1015–1021, 1974. [Online]. Available: https://doi.org/10.1115/1.3438401.

[74] G. Manolis and D. Beskos, "Thermally induced vibrations of beam structures," Comput Method Appl M, vol. 21, no. 3, pp. 337–355, 1980. [Online]. Available: https://doi.org/10.1016/0045-7825(80)90101-2.

[75] J. Zhang, R. Perez, and E. Lavernia, "Documentation of damping capacity of metallic, ceramic and metal-matrix composite materials," J Mat Sci, vol. 28, pp. 2395–2404, 1993. [Online]. Available: https://doi.org/10.1007/BF01151671.

[76] H. Sönnerlind. (2019). How to model different types of damping in COMSOL Multiphysics, [Online]. Available: https://www.comsol.com/blogs/how-to-model-different-types-of-damping-in-comsol-multiphysics/.

[77] X. Lu, R. Martinez-Botas, and J. Hey, "Analytical framework for disturbance energy balance in thermoacoustic devices," J. Fluid Mech., vol. 885, A21, 2020. DOI: 10.1017/jfm.2019.948.

[78] H. Hao, C. Scalo, and F. Semperlotti, "Flexural-mode solid-state thermoacoustics," Mech. Syst. Signal Process., vol. 148, p. 107 143, 2021, ISSN: 0888-3270. [Online]. Available: https://doi.org/10.1016/j.ymssp.2020.107143.

[79] G. Chen, Y. Wang, L. Tang, K. Wang, and Z. Yu, "Large eddy simulation of thermally induced oscillatory flow in a thermoacoustic engine," Appl. Energy, vol. 276, p. 115 458, 2020. [Online]. Available: https://doi.org/10.1016/j.apenergy.2020.115458.

[80] G. Chen, L. Tang, and B. R. Mace, "Modelling and analysis of a thermoacoustic-piezoelectric energy harvester," Appl. Therm. Eng., vol. 150, pp. 532–544, 2019, ISSN: 1359-4311. [Online]. Available: https://doi.org/10.1016/j.applthermaleng.2019.01.025.

[81] J. Tan, J. Wei, and T. Jin, "Onset and damping characteristics of a closed two-phase thermoacoustic engine," Appl. Therm. Eng., vol. 160, p. 114 086, 2019, ISSN: 1359-4311. [Online]. Available: https://doi.org/10.1016/j.applthermaleng.2019.114086.

[82] M. T. Migliorino and C. Scalo, "Real-fluid effects on standing-wave thermoacoustic instability," J. Fluid Mech., vol. 883, A23, 2020. DOI: 10.1017/jfm.2019.856.

[83] H. Xu, A. Farag, and D. Pasini, "Routes to program thermal expansion in three-dimensional lattice metamaterials built from tetrahedral building blocks," J. Mech. Phys. Solids, vol. 117, pp. 54–87, 2018. [Online]. Available: https://doi.org/10.1016/j.jmps.2018.04.012.

[84] C. A. Steeves, S. L. dos Santos e Lucato, M. He, E. Antinucci, J. W. Hutchinson, and A. G. Evans, "Concepts for structurally robust materials that combine low thermal expansion with high stiffness," J. Mech. Phys. Solids, vol. 55, no. 9, pp. 1803–1822, 2007. [Online]. Available: https://doi.org/10.1016/j.jmps.2007.02.009.

[85] L. Dong, V. Deshpande, and H. Wadley, "Mechanical response of ti–6al–4v octet-truss lattice structures," Int. J Solids Struct., vol. 60-61, pp. 107–124, 2015. [Online]. Available: https://doi.org/10.1016/j.ijsolstr.2015.02.020.

[86] H. Hao, C. Scalo, and F. Semperlotti, Band structure and effective properties of one-dimensional thermoacoustic bloch waves, 2021. eprint: arXiv:2102.02961.

VITA

Haitian Hao obtained a Bachelor of Science degree in Mechanical Engineering in July 2016 from Shanghai Jiao Tong University, Shanghai, China. He was admitted to the School of Mechanical Engineering, Purdue University as an exchange student in August 2015, and was later enrolled as a graduate student in the same department in Fall 2016. During his graduate study, he was co-advised by Prof. Fabio Semperlotti and Prof. Carlo Scalo. In December 2017, he obtained a Master of Science degree in Mechanical Engineering. His research interests focus on thermoacoustic phenomena, including solid-state thermoacoustics, and thermoacoustic metamaterials.

PUBLICATIONS

First-author Journal Articles:

H. Hao, C. Scalo, M. Sen, and F. Semperlotti, "Thermoacoustics of solids: A path way to solid state engines and refrigerators," J. Appl. Phys., vol. 123, no. 2, p. 024903,2018.

H. Hao, C. Scalo, M. Sen, and F. Semperlotti, "Traveling and standing thermoacoustic waves in solid media," J. Sound Vib., vol. 449, pp. 30–42, 2019.

H. Hao, C. Scalo, and F. Semperlotti, "Axial-mode solid-state thermoacoustic insta-bility: An analytical parametric study," J. Sound and Vib., vol. 470, p. 115 159, 2020.

H. Hao, C. Scalo, and F. Semperlotti, "Flexural-mode solid-state thermoacoustics,"Mech. Syst. Signal Process., vol. 148, p. 107 143, 2021.

H. Hao, C. Scalo, and F. Semperlotti, "On the use of negative thermal expansion engineered structures in flexural-mode solid-state thermoacoustics," in review.

H. Hao, C. Scalo, and F. Semperlotti, "Band Structure and Effective Properties of One-Dimensional Thermoacoustic Bloch Waves," in review.

First-author Conference Proceedings and Abstracts:

H. Hao, C. Scalo, M. Sen, and F. Semperlotti, "Thermoacoustic instability in solid media," J. Acoust. Soc. Am. , vol. 143, no. 3, p. 1753, 2018.

H. Hao, C. Scalo, M. Sen, and F. Semperlotti, "Solid-State Thermoacoustics," Proceedings of Inter-Noise 2018, Chicago (INCE, 2018), vol. 258, no. 7, p. 432-439, 2018.

H. Hao, C. Scalo, M. Sen, and F. Semperlotti, "Standing-wave and traveling-wave thermoacoustics in solid media," J. Acoust. Soc. Am. , vol. 144, no. 3, p. 1712, 2018.

H. Hao, C. Scalo, M. Sen, and F. Semperlotti, "Thermoacoustic Instability in the flexural motion of a bilayer beam," J. Acoust. Soc. Am. , vol. 149, no. 4, p. A44, 2021.

Patent:

H. Hao, C. Scalo, M. Sen, and F. Semperlotti, "Thermoacoustic device and method of making the same," US Patent App. 16/556,228, 2020.